Engineering Characterisation of a Rocked Bag Bioreactor for Improved Process Development and Scale-Up

An EngD Thesis submitted to

University College London

by

Douglas Trevor James Marsh

Declaration

I, Douglas Marsh, confirm that the work presented in this thesis is my own. Where information has been derived from other sources, I confirm that this has been indicated in this thesis.

Acknowledgements

I would like to thank my supervisors from UCL, Gary Lye and Martina Micheletti for their support and guidance throughout this project. Additionally, I would like to thank Matthew Osborne for his help and advice, for welcoming me into the MS/TS group and for providing such a fantastic collaborative opportunity. This work would not have been possible without the funding from the EPSRC and Eli Lilly.

I would like to thank everyone from UCL, especially those in the Mammalian Cell Group; Akin, Lourdes, Nav, John, Rich, Kate and Sara. I'd like to thank those who welcomed me into Roberts 115; Owen, Kane, Kristina, Shaz and of course Rooney, and in Cloisters; Anand, Greg, Alex T, Matt and Aminat. Vishal's help with PCR was essential.

My lunchtimes were never complete without the 'quick' crossword, for which I am indebted to Chris and Rhys.

I am inclined to thank Rob for predicting this almost a decade ago and Ben for his incredible friendship.

I would like to thank Daria for Pilot Plant Week.

I would like to thank everyone from Eli Lilly MS/TS, in particular Gary, Ann Maria, Liam, Ciara O'D, Sinead and Ronan for their endless patience and training, Anthony for his incredible statistical tutelage and Ambrose for his analytical knowledge. I was considerably safer thanks to Ciara T. I'd also like to thank Graham for introducing me to The Spaniard, which remains my favourite pub.

Finally, I would like to thank all of my family and those friends not listed above. I would not have been able to do any of this without you.

Abstract

Thorough characterisation is essential for efficient and knowledge-led cell culture process development in biomanufacturing. Despite diverse applications of rocked bag bioreactors, there is currently little understanding of the fundamental determinants of fluid mixing and mass transfer, and the effects that these would have on cell culture kinetics, product quality and cell physiology.

A rocked bag bioreactor has been fully evaluated at 10 to 50 L scale. Under typical operating conditions, single-use rocked bag bioreactor t_m were found to vary from 7-71 s, $k_La(O_2)$ from 3.5-29 h^{-1} and $k_La(CO_2)$ from 0.6-2.7 h^{-1}, with the rocking rate found to cause gas entrainment above 20 min^{-1}. A GS-CHO cell line cultured under controlled fed-batch conditions at low rocking rate to produce surface aeration achieved significantly higher cell specific antibody productivities. However, these cells were significantly less robust at harvest than cells cultured in the presence of a dispersed gas phase in rocked bags or stirred tanks.

A fabricated rocked bag mimic was fluid dynamically characterised using particle image velocimetry. It was found that increasing rocking rate from 25 to 42 min^{-1} produced an 8-fold increase in turbulence kinetic energy, giving the rocked bag similar fluid dynamic characteristics to a stirred tank. The gas entrainment noted at higher rocking rates was connected to the fluid transitioning out of phase at higher rocking rates.

A detailed cell culture kinetic, physiological and transcriptomic evaluation demonstrated that cells cultured in the rocked bag operated to entrain gas matched very closely those cultured in a stirred tank. Cells cultured in a bubble free environment exhibited several indications of higher stress, despite identical cell culture kinetics to the stirred tank.

In a second industrial GS-CHO cell line, the specific productivity of the cells cultured in entrained gas phase bags was again found to be lower than those cells cultured in surface aerated bags, however the product quality was not significantly impacted.

In summary, this work demonstrates the flexibility of rocked bags as alternative single-use bioreactor designs.

Table of Contents

List of Figures

List of Tables

Nomenclature

Abbreviation	Description
2-D	2-Dimensional
ADCF	Animal derived component free
ATR	Attenuated total reflectance
BY	*Nicotiana tabacum* cultivar bright yellow
CD	Chemically defined
CDR	Complementarity-determining region
CFD	Computational fluid dynamics
CHO	Chinese hamster ovary
CIP	Clean-in-place
CMOS	Complementary metal-oxide semiconductor
dhfr	Dihydrofolate reductase
DAPI	4',6-diamidino-2-phenylindole
DVR	Dynamic velocity range
EF-L	Embryonic feline lung fibroblast
EVA	Ethylene-vinyl acetate
EVOH	Ethylene-vinyl alcohol
FBS	Foetal bovine serum
FDA	Food and Drug Administration
FO	Fibre optic
GHT^-	Glycine hypoxanthine thymidine deficient
GS	Glutamine synthetase
HPLC	High performance liquid chromatography
ICH	International conference on harmonisation
IgG	Immunoglobulin G
IVC	Integral viable cell count
LDA	Laser 22oppler anemometry
LDPE	Low density polyethylene
LSV	Laser speckle velocimetry

mAb	Monoclonal antibody
MDCK	Madin-Darby canine kidney epithelial
mRNA	Messenger ribonucleic acid
MSX	Methylamine sulphoximine
MTX	Methotrexate
NS0	Nonsecreting murine myeloma
OTR	Oxygen transfer rate
PBT	Pitched blade turbine
PF-68	Pluronic F-68
PDI	Protein disulphide isomerises
PE	Polyethylene
PI	Propidium iodide
PIV	Particle image velocimetry
PP	Polypropylene
PVA	Poly(vinyl acetate)
PTV	Particle tracking velocimetry
QbD	Quality by Design
qPCR	Quantitative polymerase chain reaction
Sf	Spodoptera frugiperda
SIP	Sterilise-in-Place
STR	Stirred tank bioreactor
SUB	Single-use bioreactor
UPR	Unfolded protein response
USP	United States Pharmacopeia
VCC	Viable Cell Count

Symbol	Description	Unit
A	Cross sectional area of stirred tank	m^2
C^*	Oxygen saturation concentration	$mmol.L^{-1}$
C_s	Smagorinsky constant filter width	
C_L	Liquid oxygen concentration	$mmol.L^{-1}$
D	Impeller diameter	m
dCO_2	Dissolved carbon dioxide concentration	mmHg
dO_2	Dissolved oxygen concentration	mmHg
DO	Dissolved oxygen concentration	% air saturation
D_i	Impeller diameter	m
D_t	Tank diameter	m
EDR	Energy dissipation rate	$W.kg^{-1}$
H	Height of bag	m
H_f	Height of fluid in bag	m
H_i	Height of impeller from base of tank	m
H_t	Height of tank	m
IVC	Integral viable cell count (VCC)	Viable cells.day.mL^{-1}
k_La	Volumetric mass transfer coefficient	h^{-1}
$k_La(CO_2)$	Carbon dioxide volumetric mass transfer coefficient	h^{-1}
$k_La(O_2)$	Oxygen volumetric mass transfer coefficient	h^{-1}
L	Length of bag	m
N	Bag rocking rate	min^{-1}
N_i	Impeller revolution rate	s^{-1}
N_s	Image source density	-
P	Power	W
ppm	Parts per million	$million^{-1}$
Q	Volumetric gas flowrate	m^3s^{-1}
Q_{Amm}	Cell specific ammonium production rate	$pM.cell^{-1}.day^{-1}$

Q_{Glc}	Cell specific glucose consumption rate	pM.cell^{-1}.day^{-1}
Q_{Gln}	Cell specific glutamine consumption rate	pM.cell^{-1}.day^{-1}
Q_{Glu}	Cell specific glutamate consumption rate	pM.cell^{-1}.day^{-1}
Q_{Lac}	Cell specific lactate production rate	pM.cell^{-1}.day^{-1}
Q_P	Cell specific production rate of recombinant molecule	pg.cell^{-1}.day^{-1}
R_p	Pumping rate	m.s^{-1}
Re	Reynolds number, ratio of inertial to viscous forces	Dimensionless
RFU	Relative fluorescence units	-
rpm	Revolutions per minute	min^{-1}
t	Time	S
t_m	Mixing time	S
U	Instantaneous velocity of the of the flow at a single point	m.s^{-1}
u_s	Superficial gas velocity, $\frac{Q}{A}$	ms^{-1}
$\bar{u}$	Mean velocity of the of the flow at a single point	m.s^{-1}
u'	Fluctuating component of the flow at a single point	m.s^{-1}
$\tilde{u}$	Root mean squared of u’	m.s^{-1}
u_i	Horizontal velocity vector	m.s^{-1}
u_j	Vertical velocity vector	m.s^{-1}
$\bar{\bar{u}}$	Spatial average velocity over flow field of $\bar{u}$	m.s^{-1}
V	Volume	m^3
v	Volume	L
VCC	Viable cell count	Viable cells.mL
v_{tip}	Velocity of impeller tip	m.s^{-1}
vvh	Volume gas per volume liquid per hour	hour^{-1}
vvm	Volume gas per volume liquid per minute	min^{-1}
w	Weight	kg
W	Width of bag	m
x,y,z	Direction of Cartesian co-ordinates	m

x_λ	Longitudinal position of fluid centroid from x/L=0	m

Greek Letter	Description	Unit
α	Angle and direction of travel of rocking platform relative to horizontal	$\pm N^{o} \pm$
β	Angle between longitudinal average gradient of fluid surface in bag compared to gravitational horizontal	^{o}
$\overline{\lvert\beta\rvert}$	Average magnitude of β	^{o}
Δ	Filter width	m
ΔH_i	Spacing between impellers	m
Δ-t	Time between captured image pairs	µs
μ	Dynamic viscosity	Pa.s
ρ	Density	$kg.m^{-3}$

Chapter 1. Introduction

1.1. Cell Culture

The biopharmaceutical industry is in a period of sustained growth, and is estimated to be worth in excess of $160 billion p.a., having grown by 8% in 2012. (Otto *et al.* 2014). The biggest selling class of biopharmaceutical within this sector is monoclonal antibodies (mAbs) (Aggarwal, 2014), which now represent more than half of the entire biopharmaceutical sector. mAbs are almost exclusively produced in mammalian host cells, because these provide the most human-like post translational glycosylation patterns (Walsh & Jefferis 2006). Foremost among mammalian host systems is the Chinese Hamster Ovary (CHO) cell, which exhibits very high genetic plasticity and adaptability to different culture conditions (Jayapal *et al.* 2007). It is estimated to cost $1.6-6.3 billion to develop each biopharmaceutical product, therefore, despite several decades of wide adoption, there is continued pressure to reduce development time and cost, while increasing productivity (Drakeman 2014).

1.2. Upstream Cell Culture

The exploitation of living systems for the production of useful molecules is defined here as 'bioprocessing'. This is divided into upstream and downstream operations. Upstream operations involve all cell growth and production cell culture up until the point of harvest. Downstream operations involve the clarification of the broth by centrifugation and depth filtration and subsequent purification of the product by chromatography. Formulation involves exchanging the buffer around the product for one which is patient compatible and promotes product stability.

1.3. Production Cell Culture

Production cell culture occurs at scales of up to 25 m^3, and is typically executed in stirred tank bioreactors using CHO cells in suspension in chemically defined media (Wurm 2004). A bioreactor is defined as a device or system designed to support a biologically active environment (IUPAC 1997). Chmiel (2006) extends this definition

to include active control of the environment. Lab (>2 L) to large-scale production cell culture is predominantly carried out in stirred tank bioreactors, whose design and operation is adapted from microbial stirred tanks (Marks 2003). A fed-batch process would be expected to last for approximately 14 days, with cells inoculated at low concentration into fresh medium, growing initially exponentially to a peak cell density and then moving into a stationary and eventual death phase. The harvest point is typically determined by the rate of product accumulation versus the accumulation of impurities due to cell lysis and degradation in the quality of secreted product.

1.4. Bioreactors

For successful cell culture, conditions such as temperature, dissolved oxygen (DO) and pH must be controlled within relatively tight boundaries to maximise the volumetric productivity of the culture; this is the role of the bioreactor. There are generally defined windows of operation for cell culture determined by cellular requirements and cellular sensitivities (Marks 2003) although the importance of the impeller for promoting mixing and gas mass transfer compared to its potential for cell damage are subject to some debate (Sieck et al 2013, Nienow 2014)

1.4.1. Homogeneity of Cell Culture Environment

Good mixing is essential for mammalian cell culture, since it dictates the size of the concentration gradients felt by the cells (Nienow 1996) as well as the efficiency of the control systems. Concentration gradients can lead to reduced cell growth (Osman 2002) and ineffective parameter control, such as pH (Langheinrich & Nienow 1999). Despite early fears that mammalian cells would be highly shear sensitive due to their lack of a structural cell wall (Marks 2003), the majority of modern commercial cell culture takes place in suspension in stirred tank bioreactors (STR) (Hu 2011). Stirred tank bioreactors offer acceptable mixing even at large scale due to the use of multiple impellors (Nienow 1996). The most efficient mixing occurs during turbulent flow, which is defined in a stirred tank as when the impeller Reynold's number, which is the dimensionless ratio between the inertial and viscous forces in a fluid flow (Equation 1.1), exceeds $1x10^4$ (Sinnott

2005). In mammalian cell culture, the viscosity and density of the liquid phase are considered to be very similar to water (Michaels 1995) and do not change significantly over the duration of the culture, Reynolds number is determined by impellor geometry and rotation rate, as well as the density and viscosity of the liquid. In a stirred tank the Reynolds number, Re, is defined as:

$$Re = \frac{\rho N D^2}{\mu} \qquad (1.1)$$

Where ρ is the density of the liquid, $kg.m^{-3}$, N is the rotation rate of the impeller, s^{-1}, D is the diameter of the impeller, m, and μ is the dynamic viscosity of the liquid, $kg.m^{-1}s^{-1}$.

Due to fears of impeller mediated cell damage, impeller tip speed has historically been kept below 1.5 ms^{-1}, which is a significant constraint on impeller rotation rate when scaling up. However, there is little reported work to support this (Nienow 2006). Axially pumping impellers and turbines are increasingly replacing flat-bladed Rushton turbines for routine mammalian cell culture, due to their superior mixing efficiency at lower power input, especially in higher aspect ratio tanks (Vrabel 2000, Nienow 2006). Baffles are still generally not used, despite their presence increasing mean power input (and therefore improving mixing) at a given impeller speed (Nienow 2014). They also complicate cleaning-in-place operations (Marks 2003).

There remains a generally poor understanding of where the upper limit for shear stress lies for CHO cells; while there are many values of energy dissipation rate for lethal levels, sub-lethal levels of mammalian cell damage of any type are not well characterised (Sieck *et al.* 2013; Hu *et al.* 2011). It is generally considered that if the scale of the Kolmogoroff eddies (the flow structures responsible for the ultimate dissipation of the energy input by the impeller) are larger than the scale of the cells (which for CHO cells are 16-19 µm) then cell damage will not occur (Croughan 1987). The Kolmogoroff eddy scale during typical cell culture conditions is of the order of 50-150 µm, which explains why cell damage from agitation alone is not generally seen (Papoutsakis 1991). This theory fits with the increased damage seen

in microcarrier cultures, which are of the order of 1-200 µm and are much more shear sensitive, with reduction in their size reducing this sensitivity (Cherry and Papoutsakis 1989). This uncertainty has led to the use of very low agitation rates at large scale, with the focus being on sufficient oxygen transfer characteristics (Nienow & Langheinrich, 1996).

A summary of the literature published around the physical condition limitations of contemporary cell culture can be found in Tab.1.1.

Table 1.1: Suggested physical condition limits for CHO cell culture in a bioreactor.

Factor	**Ideal range**	**Justification**
Impeller tip speed	<1.5 ms^{-1}	Above this value, a reduction in cell specific productivity was reported by Sieck et al. (2013)
Sparge gas flowrate	<0.1 vvm	Above this value, a reduction in cell specific productivity was reported by Sieck (2012).
Volume averaged EDR	<<1x10^2 kWm^{-3}	To avoid direct cell destruction (Ma et al. 2002)
	<60 Wm^{-3}	To avoid reduced cell specific productivity (Sieck et al. 2013)
Local EDR	<<1x10^4 kWm^{-3}	These values could be exceeded by the bursting of small (1.7mm) bubbles, shown to cause cell destruction by (Ma et al. 2002)
Shear stress	<<10 Pa	Equivalent to Volume averaged EDR value quoted above (Ma et al. 2002)
Reynolds number	>3x10^3	Microscale vessel with low Reynolds number showed very comparable performance to lab scale vessel with Re of 1.2x10^4 (Nienow et al. 2014)
Sparger gas exit velocity	<25ms^{-1}	Growth inhibition of NS0 cells seen at gas exit velocities of 30ms^{-1} (Zhu et al. 2008)

1.4.2. Gas Mass Transfer

Compared to microbial fermentations, mammalian cells have a low oxygen demand in the range of $1x10^{-17}$ to $1x10^{-16}$ mol s^{-1} $cell^{-1}$ (Nienow & Langheinrich 1996) and can grow adequately between 5 and 100 % air saturation (Oh *et al.* 1989). Gas is added to the cell culture directly under the impeller by a variety of sparger designs and, as far as gas transfer is determined, the impeller rotation is thought to be responsible for determining the level of bubble dispersion, bubble size (Alves 2002), dissolved oxygen homogeneity (Nienow 1996) and liquid film thickness (Danckwerts 1951).

The volumetric oxygen mass transfer coefficient, k_La, coupled with the concentration gradient for mass transfer, defines the ability of an individual bioreactor to deliver oxygen to a cell culture. Superficial gas velocity (u_s) and total mean specific energy dissipation rate can be used to predict the k_La in a stirred tank of standard geometry (Van't Riet 1979), however, the addition of antifoam or cell protectants to the medium can also have a significant influence (Mostafa & Gu 2003; Lavery & Nienow 1987).

Large scale cell culture is typically operated in the k_La range 1-15 h^{-1} (Langheinrich *et al.* 2002). The oxygen transfer capability must be above that required by the cells to prevent oxygen depletion, beyond this, gas addition by sparging should be minimised since bubble bursting is currently thought to be the primary means for cell damage during cell culture (Hu 2011). Because of fears of gas sparging causing damage, cell cultures are typically sparged with oxygen enriched air or even pure oxygen, which can lead to issues of carbon dioxide accumulation (Sieblist *et al.* 2011).

Sintered, micro or frit spargers with pore sizes of less than 100 µm can be employed to produce significantly smaller bubbles which maximise interfacial surface area per sparged volume, however the smaller the bubble, the greater the energy dissipation as it bursts (Bolton-Stone & Blake 1993). The Kolmogoroff scale of smaller bubble bursts is also in line with the diameter of freely suspended cells. Capturing the contents of the upward jet produced when small bubbles burst at the

liquid surface, Trinh *et al.* (1994) determined that the majority of the cells contained within were dead.

Shear protectants have been added to cell culture to reduce the effects of bubble mediated shear damage, primarily Pluronic F-68 (PF-68), which is an amphiphilic triblock copolymer consisting of poly(propylene oxide) center and two poly(ethylene oxide) tails (Hu 2011). There are a several theories proposed for PF-68's protectant effect, including biological explanations such as cytoplasmic reinforcement (Gigout *et al.* 2008) and cell membrane reinforcement (Zhang *et al.* 1992) and physical theories such as the reduction in interfacial tension resulting from PF-68 addition reducing bubble burst energy dissipation and cell-bubble adhesion (Michaels *et al.* 1995). Regardless, PF-68 addition of 1 gL^{-1} appears to significantly protect cells from bubble mediated shear damage (Velez-Suberbie *et al.* 2013) while significantly higher concentrations of PF-68 do not impact productivity or product quality but have not been demonstrated to provide additional benefits (Tharmalingam & Goudar 2015).

While too much gas sparging can reduce homogeneity in microbial cultures (Gray et al 1996), due to the much lower impeller energy input and volumetric gas flow rates used for mammalian cell culture, aeration can actually help mixing beyond the circulation loops of the impeller (Langheinrich *et al.* 1998).

1.4.2.1. Carbon Dioxide Removal

It is also important to consider dissolved carbon dioxide (CO_2) levels, although they are rarely directly controlled. If small (<1 mm) bubbles or oxygen enriched air are employed, the ability of the bubble to add oxygen to the liquid phase can be significantly greater than its ability to remove CO_2 (Gray *et al.* 1996). Especially at larger scale, where poor mixing (Section 1.4.1) as well as higher hydrostatic pressures, can produce high local concentrations of CO_2 in solution; levels beyond 100mmHg can be reached which can negatively affect cell growth (Gray *et al.* 1996). The issue is that cells produce approximately as much CO_2 as the oxygen they consume, and also that oxygen movement from the gas to the liquid phase is interfacial area limited while CO_2 is concentration gradient limited. Smaller bubbles

provide more interfacial area for oxygen transfer but are more rapidly saturated with CO_2 (Sieblist *et al.* 2011) and can dissolve entirely in larger vessels (Gray *et al.* 1996). Oxygen enrichment further reduces the necessary volumetric flowrate of the gas for oxygen and therefore reduces the CO_2 stripping capability. Strategies to limit CO_2 accumulation at large scale are based on sparging larger bubbles (5 mm), using higher volumetric gas flow rates and not enriching the air with pure oxygen to balance the oxygen addition against the CO_2 removal (Sieblist *et al.* 2011; Nienow 2006; Gray *et al.* 1996).

1.5. Scale Translation and Technology Transfer

Scaling-up mammalian cell culture is complex, because culture performance is dependent on a number of interrelated properties of agitation and the operating window for successful mammalian cell culture narrows as the scale increases (Nienow 2006; Marks 2003; Varley and Birch 1999). Parameters such as power input, impeller tip speed, impeller shear rate and specific impeller pumping rate are commonly used as a basis for successful scale-up (Varley & Birch 1999). Despite positive indications, the use of mixing time as a scale up criterion at large scale is considered impractical due to the very high tip speeds necessitated (Yang *et al.* 2007). It is currently believed that oxygen transfer, bulk mixing, and CO_2 removal are the barriers to equivalent performance at full scale versus lab scale culture (Xing *et al.* 2009). Xing *et al.* (2009) found that a 5,000 L stirred tank bioreactor operating under typical conditions was oxygen transfer rate limited and had significant axial pH and oxygen concentration gradients, as well as higher dCO_2 levels. Concerns with shear stress during scale-up are becoming less prominent, since the adoption of cell protectants such as PF-68, although the precise mechanism by which this occurs is poorly understood (Section 1.4.2). With an advancing limit on the upper bound of impeller rotation rate (Nienow 2006), scale-up is likely to become easier as improved agitation positively impacts on culture environment and control. Several processes have been scaled successfully by various approaches to beyond 10,000L (Jayapal 2007), indicating that there is not a single correct approach. A successful scale-up will produce a comparable amount of product of comparable quality profile, with particular attention paid to critical quality attributes.

Scale-down, or lab-scale model creation of a production-scale process represents an economic and parallelisable investigational tool. Such models can allow time efficient design space investigation for process optimisation or window of operation establishment. Scaling-down involves all the same issues as scaling-up, except in this case the challenge is in making the small scale perform as 'poorly' as the large scale, since cell culture kinetics and product quality comparability must be demonstrated (Berridge *et al.* 2009).

Technology transfer is defined as "a logical procedure that controls the transfer of any process together with its documentation and professional expertise between development and manufacture or between manufacture sites" (World Health Organization 2010), therefore this includes scale-up and scale-down. Since several biopharmaceutical manufacturers have their research and development and production sites separately, processes are developed in one location or technology before being deployed in another. Non-identical bioreactor designs, such as that encountered by Abraham *et al.* (2004) can complicate the process, since the transfer is dependent on the critical process parameters being maintained, however in non-identical bioreactors this becomes a significant challenge (Rice et al 1993). In this case, it must be established that despite the differences, the product molecule is comparable (Berridge *et al.* 2009; Osman *et al.* 2002).

1.6. Bioreactor Engineering Characterisation

Engineering characterisation is essential for knowledge led process optimisation. During aerobic fermentation, the healthy state of the living cells is governed by the local delivery of nutrients such as oxygen and carbon sources and concentration of toxins such as lactate and ammonium. In order to ensure that these parameters are maintained within optimal levels during the most demanding point of the process, usually at peak cell density, it is necessary to characterise systems to evaluate at what levels the many adjustable inputs need to be set at to provide the necessary conditions for the cells for optimal productivity.

1.6.1. Oxygen Mass Transfer Rate Quantification

Oxygen delivery and control is important for successful mammalian cell culture as described in Section 1.4.2. Cell culture at 3 % oxygen saturation results in 4 % lower cell specific productivity of recombinant human erythropoietin produced in CHO cells compared to that conducted 10 % oxygen saturation (Restelli *et al.* 2006). Oxygen is typically delivered to stirred tank bioreactors as bubbles of dispersed gas, directly into the liquid phase, and underneath the impeller, but surface aerated bioreactors are feasible (Zhang *et al.* 2009). For oxygen to pass from the gas phase to the site of oxidative phosphorylation in the cell itself, it must pass through the gas film, the liquid film which surrounds the bubbles, the bulk liquid, the liquid film which surrounds the cells, and then diffuse through the cytoplasm to the point of need within the cell. Diffusion from the bubble to the bulk liquid is modelled by the two film theory (Whitman 1962), which simplifies the rate of transfer from bubble to bulk liquid around the perceived bottleneck of the liquid film transfer ($1/k_L$) with the gas phase resistance (k_G) neglected due to the very low solubility of oxygen in water. This reciprocal resistance (k_L), combined with the surface area of gas-liquid interface (a) and the concentration gradient between bubble or gas phase oxygen saturation (C*) and liquid oxygen saturation (C_L) produces the equation for oxygen transfer rate:

$$OTR = k_L a \times (C^* - C_L) \qquad (1.2)$$

This can be measured experimentally in a number of ways (Van't Riet 1979). One of the most popular methods is the static gassing-out method (Wise 1951), which involves the deoxygenation of the liquid by nitrogen followed by a measurement of the rate of reoxygenation under aeration. Since:

$$OTR = \frac{dC_L}{dt} \qquad (1.3)$$

Combining equation 1 and 2, integrating and taking the natural logarithm gives:

$$Ln(C^* - C_L) = -k_L a \times t \qquad (1.4)$$

Hence the negative gradient of a plot of $\ln(C^*-C_L)$ against t equals kLa k_La is expressed in units of reciprocal time (usually $hour^{-1}$ for cell culture applications) and represent the ability of a system to deliver oxygen to the liquid in its current configuration at a given concentration gradient. This value is very useful as a comparison between different bioreactor systems but should not be used as the sole basis for determining a bioreactor's ability to deliver oxygen to the liquid since this is also dependent on the capability of the gas addition controller.

Liquid composition is important during k_La evaluations, the addition of solutions which affect the viscosity and surface tension will have an impact on the resistance to mass transfer as well as the mean bubble size and therefore total interfacial area (Koetsier & Thoenes 1972). Care must be taken when conducting k_La measurements to either use the intended cell culture media or a reasonable mimic thereof. In spite of this, the dynamic nature of the liquid phase during cell culture, due to the increasing cell density, cell debris, extracellular protein secretion and liquid additions will cause changes in viscosity and surface tension which will impact upon measured k_La values.

1.6.2. Liquid Phase Homogeneity

Liquid homogeneity is important during cell culture to minimise local variations of solutes (Section 1.1.1). Just as k_La (Section 1.3.1) deals with the ability of a bioreactor to transfer oxygen from the gas to the liquid phase, the mixing time could cause a bottleneck in slowing the diffusion of the oxygen through the bulk liquid, potentially allowing oxygen depletion (Nienow 1996).

Mixing efficiency can be predicted in a variety of ways (Particle Image Velocimetry, Computational Fluid dynamics, power input correlations etc.), but the most popular means of estimation is known as the mixing time evaluation. This involves measuring the time taken for a traceable substance added to the liquid phase to reach a given level of homogeneity, typically >95 %. Measured mixing times range from 10 to several hundred seconds depending on energy dissipation rate (EDR, $W.kg^{-1}$) and tank scale and geometry (Magelli *et al.* 2013; Langheinrich *et al.* 1998; Nienow 1997; Nienow *et al.* 1996). Longer mixing times are usually seen at

production scale (>1,000L) due to a reluctance to scale-up on the basis of maintained energy dissipation rate (Nienow 2006). Subcategories of mixing time can be split into two types, with local methods which use a perturbation and then measure the response at a single point in the liquid with a relevant probe (pH, conductivity, temperature) and global methods, which rely on a visual change in the liquid coupled with image analysis to locate and potentially quantify the quality of mixing (Cabaret *et al.* 2007). While the visual methods provide more information on the mixing, they are significantly more difficult to apply, especially as scale increases, and they rely on the chemical reaction time required to produce the colour change being negligible with respect to the overall mixing time. Mixing times are generally divergent when making comparisons between different authors because of subtle differences in the application of the methodology and the sensitivity of turbulent mixing thereto (Kawase *et al.* 1989). Like k_La, mixing times are best used as a comparative tool between systems.

1.7. Strategies for Process Development

Effective control of cell culture process inputs results in favourable process outputs. The primary objective of cell culture is the production of the product molecule within the product quality specification; however this is achieved through a balance of maximising cell growth and cell specific productivity. Mammalian cell culture harvest titres have increased from 50 mgL^{-1} in 1984 to >10 gL^{-1} as of 2009 (Wurm 2004, Kelly 2009) though a combination of increased cell densities and higher productivity per cell (Wurm 2004). Advances have been brought about in four areas; medium formulation, feeding strategy, cell line engineering and cell culture process changes (Tab.1.2).

Table 1.2: Process development strategy overview for CHO cell based macromolecule production.

Strategy	Current position	Future potential	Contribution
Medium optimisation	Chemically defined media which support high growth and productivity across a range of host cells and clones. Improveents in cell culture medium	Tailored medium using metabolic flux analysis (Xing et al. 2011).	Wurm (2004) attributes the 100-fold increase in productivity to medium development
Feed formulation and delivery	Fed-batch additions extend culture viability and balance nutrient and trace element levels leading to increased productivity (Section 1.7.1).	Widespread adoption of advanced nutrient feedback control or perfusion based culture could lead to extended and more highly productive cell cultures.	An optimised fed-batch is generally able to offer up to 10x improvement over a batch process (Reinhart et al. 2015, Kim Do et al. 2013).
Cell line engineering	Improvements in selection pressure design have accelerated and improved the cell line selection process (Section 1.8.1). Anti-apoptotic genes and growth promoting genes have increased culture duration and cell densities (Wurm 2004)	Targetted integration for clone to clone similarity and unfolded protein response engineering for higher productivity (Section 1.8).	GS-KO cells were 2 to 3-fold more productive than non KO GS cells (Fan et al. 2012).
Cell culture process changes	Temperature and pH shifts	Directed changes to cell culture conditions to influence factors measured online	1.4-1.85 fold increase in final product concentration in bioreactors *Yoon et al. 2006, Trummer et al. 2006).

Medium for mammalian cell culture was initially formulated using foetal bovine serum (FBS) at a concentration of 1-20 % $v.v^{-1}$. This allowed reasonable cell growth

without the need for understanding the exact metabolic requirements of mammalian cells. However, it was quickly realised that the chemically undefined nature of serum and batch to batch variability was reducing culture consistency (Barnes & Sato 1980) and had safety implications.

Substitution of chemically defined alternatives to serum was a complex process (Tab.1.3). Serum has a number of benefits to cells in culture, including providing trace amounts of essential hormones, minerals, proteins and fatty acids, acting as a cell protectant and functioning as a H_2O_2 detoxifier (Liu & Chang 2006; Barnes & Sato 1980; Sandstrom *et al.* 1994). Chemically-defined medium became increasingly attractive to the biopharmaceutical industry due to the reduced chance of contamination and increased batch consistency.

Table 1.3: Serum-free medium components (adapted from Barnes & Sato 1980).

Component type	Example	Purpose
Non-hormonal Proteins	Albumin	pH buffering, nutrient transport, medium detoxification, iron binding
Hormones	Insulin	Cell metabolic regulation
Lipids	Cholesterol, free fatty acids, phospholipids	Energy source; growth stimulator
Nutrients	Various amino acids depending on cell needs	Energy sources

Increasingly, animal derived component-free (ADCF) medium is becoming popular, because of the risk of even secondarily derived animal products producing contamination of the product (Wong *et al.* 2003). Modern medium formulations for mammalian cell culture contain over 70 ingredients and the relative amounts can be optimised on a per-process basis using either spent medium analysis or a larger-scale high-throughput screen involving statistical experimental design (Liu & Chang 2006; Hodge 2005). Given the time consuming process of medium

optimisation, a 'platform' approach is sometimes adopted, in which a medium is developed to give acceptable but not optimal performance for a number of cell lines (Li *et al.* 2010).

1.7.1. Feeding Strategy

Initially, cell culture was conducted as a single batch, with the cells consuming the nutrients and then rapidly dying. Feeding was introduced as a means of maintaining the cells in a viable state once a desired cell density had been achieved, increasing productivity. Fed-batch operation is currently the primary means of production cell culture. The addition of nutrients at one or more time points over the course of the cell culture extends the maintenance of nutrients and adjusts the balance, increasing productivity and extending culture duration. Longer and more productive cell cultures result in less downtime and fewer seed train operations per unit product.

Optimising feed composition and timing is highly complex. Integrative systems biology approaches, which combine several assays to build understanding about the metabolic and product quality impacts of feeding are insightful but resource intensive (Fan *et al.* 2015). Better results can be achieved using a continuous feed, in which the nutrient mix is added gradually after a certain point in the culture (Hedge *et al.* 2012), however, this is generally considered too complex compared to the benefits over bolus feeding (Li *et al.* 2010). An alternative approach is a controlled fed-batch, in which the concentration of relevant metabolic substrates are monitored online or at line and feed addition is based on the measured level (Zhang *et al.* 2015). This approach mitigates some of the batch-to-batch inconsistency by responding directly to cellular needs but does not deal with the accumulation of toxins. Perfusion culture, which involves the gradual turnover of the culture broth while retaining the cells and product, has been adopted by some manufacturers, due to its potentially higher volumetric productivity (Pollock *et al.* 2012). This has the benefit of removing and diluting toxins as well as enriching nutrients, and can achieve cell densities almost an order of magnitude greater than fed-batch to $>2x10^8$ cells.mL^{-1} (Clinke *et al.* 2013). Cell separation is the key

engineering challenge for perfusion and currently limits the maximum scale (Warnock & Al-Rubeai 2006, Clincke *et al.* 2013). Despite a reduction in cost of goods (Pollock *et al.* 2012), there is still reluctance to widespread adoption of perfusion technology at manufacturing scale due to the increased risk of failure, looser batch definition and reducing cost benefit at larger scale (Bosch *et al.* 2008).

1.8. Cell Line Engineering

Improvements in the genetic engineering of cell lines have brought about significant increases in cell culture peak cell density and productivity. The methodology for inserting the product transgene into the host cell genome has been significantly optimised (Kayser *et al.* 2006). Improved expression vectors increase the level of expression and selectability of transfectants (Lucas *et al.* 1996).

Significant variability in transgene expression is generated by the random nature of the insertion site (Kayser *et al.* 2006). Additionally, the chromatin structure around the insertion site impacts upon accessibility of the gene inserted there (Liu *et al.* 2001) so exploiting accessible regions of the genome can also increase productivity (Kayser *et al.* 2006). Adding DNA elements from chromatin domain borders such as boundary elements and scaffold and matrix attachment regions can also improve productivity. Increased specificity in insertion site can result in more robust and consistent expression (Thyagarajan & Calos 2005). Technology such as Zinc Finger Nucleases, FLP-In or CRISPR/Cas9 can be used to insert the vector into certain identified transcriptional hotspots in the genome (Lee *et al.* 2015, Orlando et al 2010, O'Gorman *et al.* 1991).

Direct genetic improvements to the cells themselves have focussed around cell longevity and cellular productivity. Overexpression of anti-apoptotic factors such as XIAP have been shown to reduce the levels of apoptosis in culture (Sauerwald *et al.* 2003). This should maintain viabilities for longer, and could therefore increase productivity, however, antiapoptotic genes have also been associated with lower gene expression (Kondragunta *et al.* 2012). Lactate accumulation during cell culture has also been found to inhibit cell growth (Irani *et al.* 1999), using siRNA (Kim & Lee 1999) reduced lactate production to 45-79% of the control production rate. Cellular

protein production involves the transcription of mRNA and translation to form the protein precursor followed by the folding, post translational modification and secretion (Kayser *et al.* 2006). It is currently considered that mAb production is limited post-transcriptionally (Dinnis & James 2005), with the bottleneck occurring during the folding and assembly. An investigation into a poorly expressing cell line found that inefficient folding was a bottleneck despite abundance of light chain polypeptides (Reinhart *et al.* 2014). Improvements in the expression of intracellular protein disulphide isomerises (PDI) has led to 37 % increased cell specific productivity (Borth *et al.* 2005). A current area of interest is the unfolded protein response, chemically inducing endoplasmic reticulum stress, and therefore invoking the unfolded protein response has been found to increase productivity of the cells without changing the amount of heavy or light chain being translated.

1.8.1. Selection Pressure Optimisation

As part of the vector which carries the transgene of interest, a selection gene is also included to allow the chemical environment of the cell culture to be adjusted to promote only the survival of high copy number transfected cells. Dihydrofolate reductase (*dhfr*) used to be the dominant selection pressure in CHO cells (Wurm 2004), however, the GS-CHO (Glutamine Synthetase) system (Bebbington 1991) is increasingly being adopted by industry.

The *dhfr* system involves the culture of cells in media deficient in glycine, hypoxanthine, and thymidine (GHT-) and the addition of methotrexate (MTX), which blocks the activity of DHFR. After 2-3 weeks of 'amplification', any cells which do not significantly overexpress DHFR will have died, leaving only high copy number transfectants (Wurm 2004). One issue is that the amplification extends the timeline for cell line generation, and leads to genetic stability risk once the selection pressure is removed (Fan *et al.* 2012). The Glutamine Synthetase (GS) system is an attractive alternative, because this amplification step is generally not required and because the increased GS activity acts to reduce ammonia concentrations during cell culture, which is a toxin known to affect cell culture performance (Lao & Toth 1997). The addition of 10-100uM Methylamine Sulphoximine (MSX), which

downregulates GS activity to a glutamine deficient medium is designed to reduce the survival rate of cells which have not been transfected. One issue with the GS system is the wild type activity of GS in CHO cells. This reduces the stringency of the selection system allowing some untransfected cells to survive the selection environment (Sanders & Wilson 1984) and reduce the mean productivity of surviving clones passed on to cell line evaluation. A solution to this was to use CHO cells which have had their GS gene knocked out prior to transfection, allowing higher productivity cell lines to be selected from a smaller pool of candidates (Fan 2011).

1.9. Cell Culture Process Changes

Dynamically changing the operating conditions of cell culture has also led to improvements in cell culture productivity (Tab.1.4). Mild hypothermic conditions for cell culture or 'cold shocks' have been extensively studied as a way of improving recombinant protein productivity in CHO cells with up to a five-fold improvement in specific productivity (Ducommun *et al.* 2002). However the extent of the positive effect is variable and appears to be temperature, product and cell line specific (Al-Fageeh *et al.* 2006). Cold shocks have resulted in changes in the expression levels over 100 genes (10 % of those assayed), in particular, those involved in proliferation, cholesterol synthesis and several from the cytoskeleton family (Beer *et al.* 2003) as well as G0/G1 cell cycle arrest. It is thought that this arrest could be responsible for the higher cell specific productivities, as was found by Fussenegger (2001). One issue with this approach is that the cell density reduction may offset the specific productivity increase sufficiently to lead to no net change in overall product yield, however the delay in the onset of apoptosis may result in a longer production period (Al-Fageeh *et al.* 2006). Temperature reductions are best deployed in a biphasic cell culture, with the cells allowed to grow at physiological temperature for a period of time before the temperature is reduced to promote protein production and delay apoptosis (Trummer *et al.* 2006).

A similar effect can be observed from changes in the culture pH with pH values of 6.1 to 8 having been tested for CHO cells, which are typically cultured between pH

6.8 and 7.2. For one CHO cell line, it was found that the optimum growth rate was in the 7-7.2 range, the optimum antibody productivity was in the range of 6.7-6.9 (Trummer 2006). Cell viability is also maintained for longer with a pH below 7.1. With this knowledge, it is then possible to conduct biphasic cell culture in which the pH is kept at higher levels to promote growth until a target cell density is reached, and then switch to a lower pH to promote viability maintenance and productivity for the remainder of the culture (Trummer 2006).

Table 1.4: Summary of process changes that have been reported to improve cell culture outcomes.

Strategy	Method details	Mechanism	Improvement
Temperature reduction	Operate at 37^{o}C to promote cell growth and then switch to 28-35^{o}C to extend culture viability (Trummer et al. 2006) and increase cell specific productivity (Yoon et al. 2003).	PDI, a folding chaperone levels increase by 7-fold at 33^{o}C.	0-1.5 fold increase in final product concentration, partially due to elongated culture (Trummer et al. 2006, Yoon et al. 2003).
pH reduction	Lower pH can favour protein production and culture longevity while higher pH can favour cell growth (Trummer et al. 2006).	Unknown	Effect not measured in isolation (Trummer et al. 2006).
Osmolality increase	Higher osmolality (>500 mosm/kg vs ~300mOsm/kg) slows cell growth and increases cell specific productivity.	Theorised effect might be mediated via increased intracellular immunoglobulin mRNA expression (Kim et al. 2002).	Doubling (1-fold increase) of final product concentration in same duration.
Chemical addition	Sodium Butyrate or Valeric acid addition at or before peak cell density (Kim et al. 2002).	Sodium butyrate increases heavy and light chain gene accessibility, enhancing transcription, effect more pronounced for lower productivity cell lines. (Jiang et al. 2008). Valeric acid results in ~10% more cells in the G1 stage of the cell cycle, suppressing cell division and increasing protein production (Park et al. 2016).	Sodium Butyrate addition results in a -0.3 to +1-fold increase in final product titre over same culture duration, depeding on the cell line (Jiang et al. 2008). Valeric acid resulted in a 1.5-fold increase in final product titre, largely due to culture elongation, 0.8-fold higher at same time point. (Park et al. 2016).

1.10. Product Quality Characteristics

A typical mAb process involves the thawing of a frozen vial of cells from the master cell bank into growth medium in shake flasks, with the cells passaged every 3-4 days and total culture volume expanded to seed a lab scale bioreactor or rocked bag, which is then itself used to seed progressively larger stirred tanks until production scale is reached. Typical fed-batch mode mammalian cell culture production lasts approximately 14 days, after which the culture broth is harvested and depth filtered or centrifuged to separate the now unwanted cells and cell debris from the secreted product. This product stream is then filtered and passed through a series of chromatographic and virus removal or inactivation steps designed to purify, concentrate and polish the product into an ideal therapeutic state. This is then filtered, filled and finished (Liu 2010; Birch & Racher 2005). With cell culture harvest titres now reaching as high as 15 gL^{-1} (Huang *et al.* 2010), there is increasingly a drive to understand and improve the product quality because of the potential impact on the efficacy and stability. The three major effectors of product quality are considered to be cell line (Zhu 2012), process conditions (Hossler *et al.* 2009) and culture media (Bruhlmann *et al.* 2015).

1.10.1. Product Charge Heterogeneity

Charge heterogeneity of recombinant proteins is a measurement that detects modifications to the protein by chemical degradation mechanisms such as oxidation, deamination, isomerisation and fragmentation (Liu *et al.* 2008). Deamidation of asparagine residues to aspartic and iso-aspartic acid reduces the stability of the protein and it may also be immunogenic to the patient (Chelius *et al.* 2005).

During highly productive cell cultures, it is possible for misfolded protein degradation machinery to become overwhelmed and for aggregated and misfolded proteins to become released alongside correctly folded product (Schroeder *et al.* 2002). Aggregated protein may also elicit an immunogenic response in patients so is highly undesirable.

The hinge region of a mAb can be enzymatically or chemically cleaved during production or subsequent processing, resulting in fragments of various sizes and charges. This has a significant effect on the potency, since Fc-mediated effector function is disrupted, and also reduces *in-vivo* half-life (Vlasak & Ionescu 2011).

Specific bioreactor configuration (shake flasks compared to controlled stirred tanks) appears to have a significant impact on charge heterogeneity (Marino *et al.* 1997, Hsu *et al.* 2012), however there appears to be little published data investigating the relative importance of different operational inputs.

1.10.2. Product Glycosylation

The glycosylation profile of recombinant proteins is a key product quality attribute investigated, because of the well described impact on efficacy and *in-vivo* half-life (Hossler *et al.* 2009). See Tab.1.5 for a summary of the reported cell culture effects on N-linled glycan distribution.

Protein N-linked glycoslylation begins in the ER and involves the addition of a polysaccharide block to the protein followed by the stepwise removal or addition of monosaccharides (Butler 2006). Protein glycosylation is a key regulatory concern (FDA 1997) since the composition of monosaccharides can affect the immunogenicity and pharmacokinetics of the glycoprotein (Sethuraman & Stadheim 2006). Hypothermic conditions, such as those produced after temperature reductions, were found to produce more incompletely glycosylated immunoglobulins. It was found that culture at 32 ^{o}C reduced the activity of key N-linked glycan branching and elongation enzymes, while increasing the specific productivity of immunoglobulins, resulting in a glycosylation bottleneck and secretion of product with pre-mature glycan structure (Sou *et al.* 2015). Cell culture dissolved oxygen concentration can affect the quantity of digalactosylated immunoglobulins which is thought to be due to the availability of UDP-Gal (Butler 2006). Elevated dissolved CO_2 concentration was found to reduce Neural Cell Adhesion Molecule (NCAM) polysialylation. pH effects on galactosylation of an IgG_3 mAb were observed by Muthing *et al.* (2003), with higher pH resulting in more complete galactosylation. Shear effects have been found to impact site occupancy

in a glycoprotein, and the proportion of higher order glycan species possibly due to physical distortion of the cell affecting the ER (Godoy-Silva *et al.* 2009). Since bioreactor configuration impacts both on the homogeneity of the chemical environment and the consistency of chemical and physical parameters, this should be a key consideration when designing a process.

Table 1.5: Summary of factors found to effect protein N-linked glycan species distribution in CHO cell culture.

Factor	Host cell	Effect	Mechanism	Reference
High impeller EDR	CHO	Increased galactosylation	Theorised to be physical effect on Golgi morphology via integrin signalling causing actin polymerisation	Godoy-Silva et al. 2009, Sieck et al. 2013
Insufficient extracellular glutamine concentration	CHO DG44	Increased Man5	Limited UDP-GlcNAc biosynthesis	Fan et al. 2015
High extracellular NH4+ concentration	CHO DG44	Increased Man5	Low α-1,3-mannosyl-glycoprotein 2-β-N-acetylglucosaminyltransferase (GnTI) and UDP-GlcNAc transporter activities	Fan et al. 2015
Extracellular glucose and glutamine concentration	CHO DG44	Increased galactosylation	Intracellular UDP-Gal	Fan et al. 2015
Extracellular Uridine, Manganese and Galactose	GS-CHO	Increased galactosylation	Favouring addition of galactose by galactosyltransferase	Gramer et al. 2011
Manganese concentration	CHO-S	Increased galactosylation	Increased α-1,3-mannosyl-glycoprotein 2-β-N-acetylglucosaminyltransferase I and II and β-1,4 galactosyltransferase enzyme kinetics	Villiger et al. 2016
High extracellular NH4+ concentration	CHO-S	Reduced galactosylation	Reduced glycosyl transfer activities due to increased pH_{golgi}	Villiger et al. 2016
Process conditions – pH, culture temperature, DO, impeller rpm, glucose and glutamine concentration in medium	CHO-K1	<1.5% for any given glycan species	Process variables did not significantly affect high impact enzyme reaction rates	St Amand et al. 2016

1.11. Single-Use bioreactors

Single-use bioreactors (SUB) are bioreactors whose product contacting components are typically constructed from pre-sterilised plastic, used once and then disposed of (Eibl 2006). Single-use bioreactor designs have diversified since the introduction of the wave bioreactor in the late 1990s. This has been driven by a demand for a more flexible alternative to conventional reusable bioreactors. Single use bioreactors offer a number of benefits but also come with their own associated challenges (Rao *et al.* 2009)

1.11.1. Advantages of Single-Use Bioreactors

Biopharmaceutical products need to be brought to market as quickly as possible to make a return on the investment (Farid *et al.* 2005). However, this increased speed cannot be effectively achieved at the expense of increasing costs (Dimasi & Grabowski 2012).

Single-use systems are typically purchased off-the-shelf, meaning that lead times in starting a new project are reduced. Validation load is also reduced, since products come pre-validated and cleaning and sterilisation protocols are unnecessary. Unit operations become more rapid and with lower workload, with no time needed for cleaning or sterilisation reducing equipment downtime. The elimination of clean-in-place (CIP) and steam-in-place (SIP) utility within a facility can reduce the water requirement by 19 % and facility size by 4 %, which accelerates and economises production and operation (Sinclair *et al.* 2008).

Companies and contract manufacturers are increasingly moving towards multi-product facilities to satisfy a larger product portfolio (Siganporia *et al.* 2014). In addition, large pharmaceutical companies are currently relying on small scale start-up companies to feed the pipeline, for which more flexible approaches to manufacture are desirable. The smaller floor space requirements and very low cross contamination risk of single-use technology make multi-product facilities more viable. In addition to this, the continued increase in volumetric productivity

of processes (Huang *et al.* 2010) and shrinking of product niches may combine to necessitate smaller commercial production volume. Additionally, the recent drive for Process Analytical Technology (PAT) favours single use, since the technology is highly modifiable, allowing additional probes or probe mounting positions to be installed without the expensive modification of fixed equipment.

Single-use technology allows a more evenly distributed expenditure over a product life-cycle than stainless steel (Sinclair 2007). The scale of the operation can be more easily altered. The use of single-use systems in a biochemical engineering process can increase the net present value and reduce the economic sensitivity of the project (Novais & Hoare 2001). The cost efficiency of single-use is likely to rise as adoption broadens.

1.11.2. Disadvantages of Single-Use Bioreactors

With single-use plastic culture ware, there is an increased risk of leachables and extractables due to the chemical additives such as plasticisers during fabrication and degradation due to gamma irradiation during sterilisation (Hammond *et al.* 2013). This raises issues in the subsequent use of the product as a therapeutic because the leached or extracted compounds can reduce the potency and purity of the product as well as being toxic or immunogenic to the patient (Jenke 2007). Leachables within the bioreactor can be growth inhibitory (Hammond *et al.* 2013), potentially stalling process development or manufacturing.

Consequently, efforts are made by the manufacturer to assess the levels and reactivity of the plastics and leachables and to keep these within specified limits. Plastics are tested for their biocompatibility, to prove that they are not toxic or biologically reactive using elution (*United States Pharmacopeia* (USP) <87>) and culture (USP <88>) methods. Additionally, the levels of leachables must be quantified and risk assessed as to whether the levels are acceptable regarding product interaction and patient safety. The *International Conference on Harmonisation* (ICH) Q3C has guidelines for the maximum allowable levels of residual solvents. The Food and Drug Administration (FDA) is increasing interested in leachables and extractables as part of its Quality by Design (QbD) initiative (Yu *et*

al. 2008). This was initially the most controversial aspect of single-use bioreactors but standardisation in testing methods and agreed upon acceptable limits should work to reduce this (Ding *et al.* 2014).

Single-use equipment, being made from plastic, has a lower maximum culture capacity than stainless steel equivalents with single-use bioreactors still not routinely going beyond 2,000 L working volume (Loffelholz *et al.* 2014) compared to 25,000 L production capacity in stainless steel stirred tanks (Nienow 2006). This is due to the lower tensile strength of single-use plastics compared to stainless steel. The single-use bags themselves are routinely tested for their robustness in terms of pressure, integrity, gas permeability, tensile strength and puncture resistance, but leaks can still occur due to incorrect installation.

Novel technology represents a significant training challenge to manufacturers who have a workforce well used to stainless steel bioprocessing (Eibl *et al.* 2009). There is also very scarce information on typical operating parameters for non impeller-agitated bioreactors (Section 1.12.5).

Although the product contacting surfaces are single-use, significant proportions of larger scale single-use technology are re-usable, such as the skids, control towers and motors. These come at considerable cost and may lock the user to the particular vendor. Supplier dependence is not an issue exclusive to single-use bioreactors, but the expansion of consumable equipment adds risk to a bioprocess and mitigating this risk by stockpiling or seeking alternative suppliers can be time consuming and costly (Challener 2014).

There was initial concern over greater waste production as a result of disposable bioprocessing, however, this was found to be offset by the reduction in cleaning and sterilisation, which reduces water and energy consumption and reduces the overall cost (Sinclair *et al.* 2008, Rawlings & Pora 2009, Flanagan *et al.* 2014).

1.11.3. Types of Single-Use bioreactors

The interest in single-use bioprocessing and bioreactors has led to a number of single-use bioreactor designs emerging, which are summarised in Table 1.2.

Table 1.6: Summary of various single-use bioreactor designs currently available. *Stirred bags are made from flexible plastic bags, which sit inside a steel manifold for support. These are typically used at scales of 10L and above. ** Stirred tanks made from rigid plastic. These are typically used at scales of up to 10L.

Bioreactor design	Key example(s)	Advantages	Disadvantages
Rocked bags	Sartorius Stedim BIOSTAT CultiBag RM, Applikon Appliflex, GE Healthcare Wave Bioreactor	Potential for cell culture in a low shear, bubble free environment (Genzel *et al.* 2006). Potentially high oxygen transfer capacity (Yuk *et al.* 2011).	Unfamiliar agitation makes system configuration a challenge. Maximum working volume 500L.
Stirred bags*	XDR Xcellerex, Sartorius Stedim BIOSTAT CultiBag STR	Familiar agitation and geometry ease technology transfer, maximum scale 2,000L.	2,000L working volume requires several systems for large scale manufacturing.
Stirred tanks**	Millipore Mobius Cellready, Sartorius UniVessel SU, TAP Biosystems ambr15	Familiar agitation and geometry, allow highly parallelised cell culture at 15mL (Nienow *et al.* 2014) or replace existing lab scale vessels (Odeleye *et al.* 2014).	Lab scale (2L) systems costly on a per operation basis.
Orbitally shaken bags	ExcellGene Kuhner Orbshake	Familiar agitation and geometry. Available up to 2000L, well characterised (Zhang *et al.* 2009).	Low oxygen transfer capacity at large scale due to surface aeration. (Zhang *et al.* 2010).
Hollow Fibre	BioVest Acusyst systems	Supports high cell densities; up to 10^8 viable cells.mL^{-1} (Brecht 2010).	Maximum per cartridge volume limited to 2.5L.

Bioreactor design	Key example(s)	Advantages	Disadvantages
Paddle tank	PBS Biotech Pneumatic Bioreactor System	Supplier quotes excellent scalability from 3 to 500L.	Unfamiliar agitation makes system configuration a challenge.
Orbitally shaken plates	Pall micro24, Applikon micro-Matrix, RoboLector L	Inexpensive system with high throughput cell screening potential at 10mL scale (Betts *et al.* 2014).	Sampling represents a handling challenge, well-to-well variation.

1.12. Rocked Bag Single-Use Bioreactors

1.12.1. Development

The first single-use, rocked bioreactor was developed in 1996 by Singh (1999) in response to a perceived lack of single-use culture ware beyond the lab scale that could satisfy the oxygen transfer rates necessary for current suspension cell culture demands. Singh also postulated that stirred tanks are inherently unsuitable for mammalian cell culture due to their complexity and high levels of shear from the impeller and gas sparging.

1.12.2. Design and Operation

The rocked bag bioreactor was designed to be simple to operate, produce low shear and be predictably scalable from lab to small pilot scale. A flexible FDA approved polyethylene (PE) bag was used as the culture chamber, which was mounted on a rocking platform. The bag is partially filled with culture medium and the remainder has pressurised gas continuously passed over it. The very low aspect ratio of the bag allows for a high surface area, which combined with the waves generated by the rocking motion, produces sufficient oxygen transfer for mammalian, plant and insect cell culture. The rocking motion also provides bulk mixing and maintains the cells in suspension. A list of the key features of the rocked bag can be found in Tab.1.7. Systems exist ranging in scale from 0.1L up to 500L working volume (Eibl 2008).

Rocked single-use bioreactors can be operated in batch, fed-batch (Eibl *et al.* 2009) and perfusion modes (Clinke *et al.* 2013), with cell densities reaching in excess of 2 $x10^8$ cells.mL^{-1}. Fed-batch is the most popular mode of operation because it is relatively simple, yet avoids the potential for overflow metabolism, substrate and product inhibition during batch operation (Section 1.7.1).

Table 1.7: Summary of the key features of the rocked bag bioreactor design.

Feature	Advantage(s)	Disadvantage(s)
Rocking based agitation	Able to deliver sufficient oxygen transfer for standard density cell culture without the complication of an impeller.	Large mobile object has health and safety implications. Rocking motion can compromise probe mounting and tubing attachment. Rocking rate, angle and velocity profile adjustments can make optimisation a multivariate challenge.
Headspace aeration	No dispersed gas phase reduces risk of foaming or cell damage.	Growth and productivity performance may not be representative of stirred tank performance.
Single-use	Rocked bag installation is simple compared to stirred tanks because no mechanical impeller connection needs to be made.	Flexible plastic film carries a leachables/extractables risk.
Single-use probes	No breach in sterile system. Fewer possibilities to use novel probe designs.	Single-use pH probe reliability is medium and feed sensitive.
Simple operation	pH and DO control are unnecessary provided a suitable rocking rate is selected for seed train cell expansion operations.	

1.12.3. Fabrication

Brecht (2009) provides a design of a Hyclone BPC bag as shown in Fig.1.1. Plastic used for bioreactors in bioprocessing is typically composed of several films bonded together, since no single film can satisfy all the requirements. Ethylene-vinyl-acetate (EVA) is robust and flexible, but is gas and liquid permeable. Ethylene-vinyl-alcohol (EVOH) is gas impermeable allowing leak testing and finer gas control. Low density polyethylene (LDPE) has the lowest leachable/extractable levels. These polymers are used together to ensure structural integrity, gas impermeability and biocompatibility (Jenke and Barge 2014). Each layer of plastic polymer is rarely used without additives, poly(vinyl chloride) (PVC), a product contacting polymer used in blood storage bags, is used with plasticisers to allow flexibility, while antioxidants are added to polypropylene (PP) to protect it during the gamma irradiation necessary for sterilisation (Barbaroux *et al.* 2014). These additives themselves can degrade during processing and gamma irradiation, potentially becoming process impacting leachables (Section 1.11.2).

Figure 1.1: Cross section through the typical layers in a bag. Polyester (dark grey), bonding agent (light grey), Ethylene Vinyl Alcohol (white), bonding agent and Polyethylene (black). Taken from Brecht (2009).

1.12.4. Measurement and Control

In modern bag designs, measurement is typically via single-use optical sensor patches, which allow non-invasive measurement of DO and pH. Gassing and inoculation attachments are mounted on the top of the bag away from the liquid surface and can be controlled conventionally. Pressure is controlled by a pressure control valve mounted at the gas inlet. Temperature is typically controlled by heating the rocking platform beneath the bag, with fluid mixing relied upon to distribute the heat evenly throughout the culture.

1.12.5. Engineering Characterisation of Rocked Bags

There is a need to gain insight into the engineering characteristics of the rocked bag bioreactor if it is to be accurately compared to existing stirred tank technology. In terms of oxygen transfer, traditional rocking provides k_La values in the region of 1-40 h^{-1} (Rao *et al.* 2009), with the majority reporting 1-1 $0h^{-1}$ (Zhang *et al.* 2009; Knevelman *et al.* 2002; Mikola *et al.* 2007), which are above those provided by spinner flasks and shake flasks of 5-10 h^{-1} (Ries *et al.* 2010, Vallejos *et al.* 2011) but below those achievable through sparging in single-use stirred bags of 100 h^{-1} (Loffelholz *et al.* 2014). With additional horizontal displacement, it is possible to achieve mass transfer of up to 700 h^{-1} in a rocked bag at 10L scale (Oosterhuis & van der Heiden 2010). Factors affecting the oxygen transfer in wave bags are believed to be rocking rate and angle, gas flow rate and oxygen concentration and lqiuid fill volume of the bag. Rocking rate is considered the most significant effector, with rocking angle becoming more significant at lower rocking rates. Fill volume is inversely related to k_La (Eibl *et al.* 2010). During development, Singh (1999) predicted that a k_La of 4 h^{-1} would limit mammalian cell density to <7 $x10^6.mL^{-1}$, so the current values should theoretically support current commercial mammalian cell growth without becoming oxygen limited (Nienow 2006).

Experimental mixing time studies have also been carried out in rocked bags, again these were found to be inversely proportional to rocking rate and with a variable response to rocking angle. Lower fill volumes were found to decrease mixing time. Mixing time was shown to increase with scale from 2-200 L but only by one order of magnitude at equivalent operational parameters (Eibl *et al.* 2009).

1.12.6. Applications

Rocked bags have proved versatile, being applied to a variety of organisms and purposes. These are summarised in Table 1.8.

Table 1.8: Applications of single-use rocked bioreactors. See footnote for nomenclature.

Application	Host cell	Author(s)	System
Seed train or production cell culture	CHO[1], NS0[2]	Singh 1999, Knevelman *et al.* 2002	Biowave 2L, Wave Biotech
Perfusion cell culture	Hybridoma, CHO	Tang *et al.* 2007, Yuk *et al.* 2011	2L Wave Bioreactor, Wave Biotech
Virus production on microcarriers	MDCK[3], E-FL[4]	Genzel *et al.* 2006	2L Wave Bioreactor, Wave Biotech
Baculovirus/Insect cell based r-protein production	Sf-9[5]; Sf-21	Kadwell & Hardwicke 2007	20-200L Wave bioreactor, Wave Biotech
Plant cell cultivation and antibody expression	BY-2[6]	Eibl & Eibl 2006	2L Wave Bioreactor, Wave Biotech
Yeast fermentation	*Saccharomyces cerevisiae* S279Y	Mikola *et al.* 2007	20L Wave Bioreactor, Wave Biotech
Microbial fermentation	*Escherichia coli*	Mahajan *et al.* 2010	10L Wave bioreactor, Wave Biotech

1 Chinese Hamster Ovary
2 NonSecreting Murine Myeloma
3 Madin-Darby Canine Kidney Epithelial
4 Embyronic Feline Lung Fibroblast
5 Spodoptera frugiperda-9
6 Nicotiana tabacum cultivar Bright Yellow-2

1.13. Single-Use Sensing Technology

In general there are two approaches to process monitoring in single use bioreactors. These either use re-usable or single-use sensor technologies or. Re-usable dissolved oxygen probes are based on a Clark electrode, which reduce oxygen on a catalytic platinum surface protected from fouling by a silicon

membrane protected. This reduction causes a current to flow, creating a potential difference which, at 0.7 V, changes linearly with oxygen partial pressure provided the solution is well mixed (Clark *et al.* 1953). Re-usable pH probes are based on a single package dual electrode design, using sensing and reference silver chloride electrodes. Both electrodes sit within a pH 7 buffered solution. When the probe is placed in a solution of lower pH, the hydrogen ions in this solution occupy the hydrogel layer on the outside of the probe. This displaces some sodium ions which can move across the dry glass of the probe casing and into solution around the sensing electrode. The inverse happens when the probe is placed in higher than reference pH solution. This creates a change in positive sodium ion concentration around the sensing electrode in response to external pH, generating a potential between the sensing and reference electrode, which is linearly correlated with the pH in the range of pH 2-12 (Reilley 1965).

Single-use DO sensors use a silicone matrix immobilised luminescent transition-metal complex. Under excitation, this produces light at a longer wavelength and lower energy than the excitation frequency via a Stokes' shift mechanism, however, in the presence of oxygen, this process is collision quenched, resulting in a reduced photoluminescence intensity proportional to dissolved oxygen tension (Quaranta *et al.* 2012). Single-use pH patches use a fluorescent dye (8-hydroxy-1,3,6-pyrene trisulfonic acid) immobilized onto an anion-exchange resin, embedded in a proton-permeable hydrogel layer. This is backed onto filter material to protect the measurement from optical interference from the culture broth. The emission intensity ratio at 515nm when excited at 468 compared to 408nm correlates with pH over the range of pH 6-9 (Kermis *et al.* 2002).

These sensors can be immobilised onto the inner side of bioreactor prior to sterilisation and then fibre optic cables attached on the adjacent outer surface to photometrically interrogate these sensors without any need to compromise the sterile closure of the bioreactor. The development of disposable optical sensing patches is tied to the development of single-use technology, since as single-use systems become more advanced and larger scale, the demand for suitable and reliable single-use online monitoring is increasing. Using existing online sensor

technology in conjunction with single-use systems does somewhat reduce the associated benefits since these require sterilisation but is possible using pre-sterilised 'bellows', which allow the aseptic insertion of a reusable probe into a bioreactor. Single-use sensors which are sterilised with the bioreactor are the alternative. These must be low cost and reliable but do not need to be last significantly beyond the length of time of the culture (Rao *et al.* 2009). The key drawback with single-use probes is the optical pH sensor, which has been shown to drift versus an electrochemical probe over even relatively short cell culture times, especially at lower pH values (Hanson *et al.* 2007). As mentioned in Section 1.5, mammalian cells are sensitive to even small changes in pH, so accurate probes are critical to consistent cell culture execution.

1.13.1. Online Single-Use Sensors

There are a variety of single-use sensing technologies currently available, summarised in Table 1.9.

Table 1.9: Current online single-use sensors (Glindkamp *et al.* 2009). See footnotes for nomenclature.

Basis for sensor	Requirements	Detects	Limitations
Optical oxygen sensors	Integrated fibre optic with metal complex in silicone matrix	Oxygen	Long-term photobleaching, minor cross-sensitivity to other ions.
Optical pH sensors	Integrated fibre optic with aminofluorescein in PVA[1] matrix	pH	Cross-sensitive to ionic strength, dynamic range of only 3 pH units.
Infrared Spectroscopy	ATR[2] crystal integrated into bioreactor for contact with liquid phase. Measuring cell at gas outlet for gas phase.	Carbon dioxide	High cost of ATR crystal limits use in liquid phase measurement.
Fluorometry	Fibre optic connection and transparent observation window	Proteins, vitamins, coenzymes, biomass, glucose, various metabolites	
Optical Chemosensors	Transducer inside bioreactor and observation window.	Sensors can be designed to respond optically to analyte concentration.	
Electrolytic pH probes	Dry storage tolerant pH probe	pH	Relatively high cost

1 Poly(vinyl acetate)
2 Attenuated total reflectance

1.14. Characterisation and Quantification of Bioreactor Fluid Dynamics

Fluid dynamics describes the nature of the flow at scales ranging from the largest to the smallest. The extraction of the velocity component of the flow at high resolution allows the description of turbulence scale and intensity, shear, vorticity, and pressure gradients, all of which can have implications for cell culture performance (Peube 2009).

1.14.1. Relevance to Bioprocessing

Fluid dynamics is especially pertinent to the process industries because these rely on efficient mixing during production and processing. It was estimated that in excess of $600 million is lost by the pharmaceutical industry per year due to poor mixing (Paul *et al.* 2004). Bioprocessing has an additional level of complexity because the use of living cells potentially imposes upper limits on mixing quality and therefore energy dissipation due to fears of cell damage and product quality impact (Sections 1.4.1 and 1.10).

It is currently understood that the maximum energy dissipation rate from the impeller rotation in the bioreactor may be responsible for cell damage and is an important consideration when moving between scales (Sieck *et al.* 2013). There are numerous techniques employed to measure and estimate the mean impeller power input, such as the use of clay polymer particle size, computational fluid dynamics (CFD), impeller motor torque measurements and power number based calculations. Measuring the maximum power dissipation is considerably more difficult, yet this number is considered very important when quantifying the effect on the cells. Energy dissipation values taken from Zhou & Kresta (1996) were used by Godoy-Silva *et al.* (2009) as the basis for testing the effect of various levels of energy dissipation that could be recreated in their 'torture chamber'. The 'torture chamber' is a capillary of various diameters (225, 1,500 and 2,000 µm) attached to the bioreactor in a sterile circulation loop which also includes syringe pumps. As the cells pass through the narrow capillary, energy dissipation rates up to 1.1 $x10^{8}Wm^{-3}$ are predicted by CFD. The fluid dynamics involved during the bursting of bubbles at the fluid surface is also a separate but important consideration to

impeller power input in terms of cell damage (Sieck *et al.* 2013; Nienow 2006) (Section 1.4.2).

1.14.2. Computational Fluid Dynamics

CFD utilises computer modelling to predict the flow of fluid in a given system. It is able to predict velocity and flow direction, and consequently the shear and power input can be estimated within the flow. Currently, bioreactors can be modelled using a Eulerian approach, with the gas and liquid phases considered dispersed and continuous respectively. Inter-phase momentum transfer is estimated using the Ishii-Zuber drag model, turbulent closure using the k-e model and bubble size distribution using the Multiple Size Group (MUSIG) model (Wang *et al.* 2014). CFD is a popular technique used to characterise velocity vectors and power input in bioreactors with novel geometries (Nienow *et al.* 2014; Oncul *et al.* 2009) but being theoretical, CFD must be validated or assisted by experimental measurements, such as mixing time, photography or anemometry (Oberkampf 2002).

1.14.3. Particle Image Velocimetry

PIV allows the indirect measurement of fluid dynamics by recording the movement of visible particles in a fluid flow. Using a double pulsed sheet of laser light perpendicular to one or several synchronised cameras, the advancement of incidental or seeded particles in the fluid can be measured over a defined time interval. This image is then divided into interrogation areas, and the movement of the particles within each of these is cross-correlated to provide 2 or 3-Dimensional (3D) velocities (U) at high resolution over the illuminated fluid. Repeated measurements (<500) can then be used to quantify the mean ($\bar{u}$) and fluctuating (u') velocity components at each point, which can then be used to extract several fluid dynamic properties from the flow (further details can be found in Section 4.2).

PIV evolved from simpler methods of laser analysis of fluid flow, due to a need to sample a greater area of the flow field in turbulent complex flows at the cost of temporal resolution. One such method was Laser Doppler Anemometry (LDA), which utilised two laser beams (often a single split beam) which intersect at a single

point in a flow field. A detector, such as a photodiode records the wavelength of light refracted by particles crossing the intersecting laser beams and the Doppler effect is used to measure the velocity of the flow at that point. Laser Doppler Anemometry allows very precise measurements at single points in the velocity flow fields, but is incapable of resolving coherent structures in unsteady flows due to the sample size limitation. This led to the development of techniques that were capable of sampling the entire flow field, starting with Laser Speckle Velocimetry (LSV) (Barker & Fourney 1977).

LSV was based on laser speckle measurements in solid mechanics. The nature of some solid surfaces is their uneven refraction of light, or speckle, which can be used to optically track the movement of solid surfaces provided that movement is greater than the size of the speckle diameter, but low enough to allow correlation (Krothapalli 1991). LSV utilised very high concentrations of tracer particles in the fluid, which when intersected by a two dimensional sheet of laser light (parallel to the mean flow), effectively create a plane of overlapping speckles, which are recorded over two time spaced frames by a camera perpendicular to the light sheet (Adrian 1984). LSV is capable of describing velocities at any point in the flow field, but does have some limitations. When using LSV, the correlation and resultant velocity estimates are less accurate if the speckle pattern is not maintained, which is common in turbulent fluid flows, or in flows with a significant velocity component perpendicular to the light sheet. Additionally, the high seeding density of tracer particles can affect the properties of the flow and has cost implications at larger scale (Krothapalli 1991).

Soon after the development of LSV, it was discovered that by lowering the concentration of seeding particles, more precise velocity readings could be extracted (Adrian 1984). This would allow the observation of individual particles as they moved within interrogation windows (subdivisions of the total viewed area), and therefore chaotic flows could be more easily tracked, albeit at a resolution defined by the size of the interrogation areas. This was termed Particle Image Velocimetry. Moving to even lower seeding densities results in Particle Tracking Velocimetry (PTV), in which the position of discreet particles is tracked over a

number of time separated frames. This method is very accurate but due to the low seeding densities, there is significant 'drop-out', in which velocity information is sparsely available over a given observation area. PIV is a very popular measurement tool for bioreactor fluid dynamics (Weheliye *et al.* 2014; Odeleye *et al.* 2014; Figueredo-Cardero *et al.* 2012; Sucosky *et al.* 2004).

1.14.4. Particle Image Velocimetry Operation

The current setup for monoscopic PIV is as in Fig.1.2. A pulsed light laser, such as an Nd:Yag, is focussed into a sheet approximately 1mm wide using a spherical and a cylindrical lens. This sheet passes through the fluid system of interest, parallel to the direction of the dominant flow. This fluid contains tracer particles which diffract the light and this is recorded by a digital Complementary Metal-Oxide Semiconductor (CMOS) camera perpendicular to the plane of the light sheet. The laser and the camera are synchronised to fire and record an image pair respectively with an external repetitious flow event such as an impeller blade passing a given point, or a time interval. These image pairs are spaced at a time distance known as Δ-t (Section 1.18). Typically, several hundred repeated image pairs are then transferred to a computer software package for analysis.

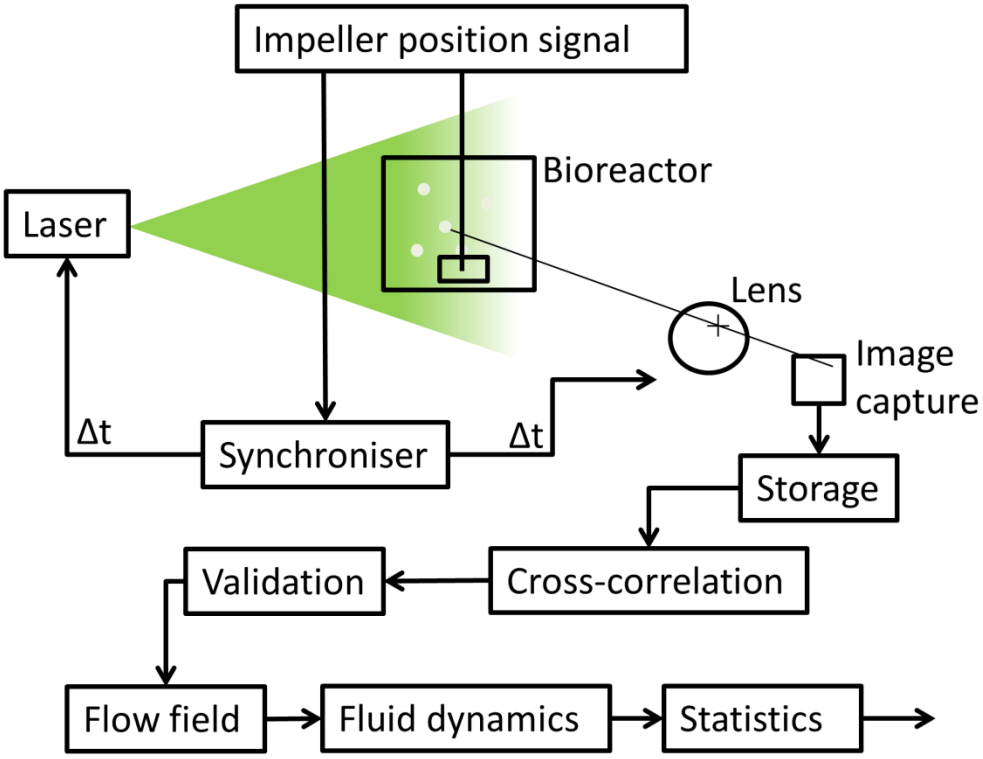

Figure 1.2: Schematic of PIV operation adapted from Adrian (2005).

1.14.5. Practical Considerations of PIV

The Δ-t between image pairs must be set according to the maximum particle velocity, such that a particle travelling at the maximum velocity will travel one quarter of the interrogation area (Adrian 1987). Since modern PIV still has a relatively limited Dynamic Velocity Range (DVR) of approximately 200, Δ-t should be set as large as possible while still conforming to the above rule in order to resolve the smallest vectors.

PIV requires the presence of small (1-50 µm) tracer particles within the flow, these can be made from metal oxides, glass or polymers, but must be smaller than the smallest eddies in the flow and of similar density to the fluid (Melling 1997). PIV operates optimally in the range of 2 $x10^{10}$ – 2 $x10^{11}$ tracer particles.m^{-3} bounded above and below by LSV and PTV respectively.

The lower limit for PIV is two particle image pairs per interrogation area, however such a low sample size leaves the analysis open to significant fringe cross-interference and a minimum of four particle image pairs are feasible, with upwards of 7-10 recommended (Adrian 2005; Krothapalli 1991). The upper limit is defined as before there is overlap of particle images, or when the source density (N_S) is still significantly less than one.

1.14.6. Data Acquisition and Processing

Westerweel (1993) divides the analysis of PIV into three sections: Interrogation, validation and derivation.

For PIV analysis, the image pairs are divided into a grid of square interrogation areas, in which the locations of the particles are compared. These two image pairs are statistically correlated using Fast Fourier Transforms to find the most likely transformation between the two. Using the Δ-t, this displacement and direction can be converted into one velocity vector per interrogation area per image pair.

Modern correlation techniques, known as adaptive correlations, initially use very large interrogation windows to obtain approximate vectors, and then use this vector to set the offset of smaller windows within, increasing the likelihood of a good correlation at higher spatial resolution, and increasing the dynamic velocity range of the technique to 200 compared to 5-10 when using standard cross-correlation (Hart 2000). Deforming windows can also be used, which allow more accurate capture of rotations and extensions of the flow (Huang *et al.* 1993). Sub-pixel accuracy is used when estimating the centre of particles, allowing better correlations to be drawn. This technique uses a Gaussian fit of pixel intensities of the correlation (interrogation) window, which prevents the correlation peak locking to a pixel centre and therefore tending to return velocities that are pixel integers.

Spurious vectors, known as outliers are generated both during acquisition and interrogation of PIV data. In terms of the flow, outliers can be generated by spatial variations in particle density, or excessive out of plane motion. Operationally, noise in the image generated by the camera alignment, focussing and ambient light

pollution may also contribute to outliers. During correlation, the finite resolution of the image, coupled with the limited dynamic spatial range can also result in outliers being produced (Nogueira *et al.* 1997).

Validation is designed to remove the outliers generated by the limitations of the acquisition, and limitations of the correlation technique (Nogueira *et al.* 1997). Range validation removes all of the vectors from a vector map outside a specified range. This is usually used as an initial high pass filter, with only the upper bound set at a velocity beyond which it is highly unlikely that real vectors will exist. This could be set based on the fastest component in a system; taken from the impeller tip speed, literature values or preliminary findings. This technique is unable to substitute reasonable vectors for outliers.

Moving average validation can be used after range validation and exploits the likelihood of vectors to be similar to neighbouring vectors (Nogueira *et al.* 1997). This technique compares each vector to neighbouring vectors and if they are found to be significantly different, they can be considered outliers and removed. The area of sampling around a given vector can be varied, as well as the tolerance for difference within the sampled vector field. This technique is especially useful, since it can be used to replace outlying vectors with a reasonable substitute.

Peak validation is less common but can be used with classical cross-correlation, and effectively checks that the height of the highest peak in the correlation map is significantly higher (ideally at least 5-fold higher) than the second highest peak, this rules out ambiguous or erroneous correlations and therefore vectors. As with range validation, this is unable to substitute reasonable vectors for outliers (Keane & Adrian 1992)

Derivation is defined as further analysis carried out on the validated vector field. It allows the extraction of parameters of the flow relevant to mixing and cell damage. Typical parameters that can be ascertained include fluid velocity, shear stress and turbulence kinetic energy. These are discussed in more detail in Section 4.2.

1.15. Aims and Objectives

In the previous sections, various single-use bioreactor designs have been described (Section 1.12.2) along with current knowledge regarding their engineering characteristics (Section 1.12.5). Despite this, a fundamental understanding of single-use bioreactor hydrodynamics is still missing, in particular the understanding of how single-use bioreactor design and operation impacts on mixing, gas-liquid mass transfer and culture performance.

With regard to gas-liquid mass transfer (Section 1.4.2) there is currently no general consensus on the effects of rocked bag agitation inputs (rocking rate and angle, fill volume and gas flowrate) on volumetric gas mass transfer. While there is agreement on the importance of rocking rate (Yuk *et al.* 2011; Mikola *et al.* 2007) there are contradictory findings over the effect of gas flow rate (Yuk *et al.* 2011; Singh 1999). Furthermore, there is no published work to date describing the effect of scale or liquid fill volume on volumetric O_2 and CO_2 mass transfer.

Equally, established and reliable bases for designing and operating stirred tanks at lab and large scale (Nienow 2006) do not exist for rocked bioreactors. Furthermore, demonstrations of cell culture performance, significantly productivity, changes in response to rocked bag configuration are scarce. It is also not established how cells might respond to the different hydrodynamic environment produced by the rocking-based agitation. Suspension CHO Cells have been shown to respond to different levels of bubble induced shear stress in a stirred tank bioreactor in terms of mechanical robustness (Velez-Suberbie *et al.* 2012) but correlations between dispersed gas phase and culture performance have not been established.

At a more fundamental level, detailed analyses of flow regimes, e.g. velocity, frequency, shear, turbulence etc., within stirred tanks have resulted in a good understanding of regions of high and low liquid homogeneity (Odeleye *et al.* 2014; Gabriele *et al.* 2009). While fluid velocities within rocked bags have been measured under laminar conditions with invasive probes (Oncul *et al.* 2010; Kalmbach *et al.* 2009) there are currently no detailed measurements of fluid velocity or bulk position over the course of the rock.

In general terms, for both conventional STR and SUB, sub-lethal cell biological responses to energy dissipation rate as a result of bubble bursting are not well understood (Hu *et al.* 2011). Various effects on cells in suspension have been measured over 6 orders of magnitude (Mollet *et al.* 2004), however there are only two reports of sub-lethal effects (Sieck *et al.* 2013; Godoy-Silva *et al.* 2009). Oxygen mass transfer coefficients reported in rocked bags at higher rocking rates (Yuk *et al.* 2011) strongly suggest gas entrainment, meaning the rocked bag is able to produce potentially stressful cell culture environments with unknown cellular response. Similarly, cell culture productivity and glycosylation impacts have been previously reported in response to shear stresses (Sieck *et al.* 2013; Kondragunta *et al.* 2012; Godoy-Silva *et al.* 2009), however a broader analysis of the product with respect to its product quality in terms of therapeutic efficacy has not been carried out.

Given this current lack of engineering knowledge on rocked bioreactors, the aim of this thesis is to produce the first thorough engineering characterisation of single-use, rocked bioreactors over a range of scales and to establish the impact of bioreactor configuration and operation on the physiology, productivity and product quality of an industrially relevant cell lines. GS-CHO cell lines have been selected for use in this study because they are the most commonly used hosts for industrial recombinant protein production (Section 1.1). The specific objectives of the research are described below.

- To characterise the effects of rocking rate, rocking angle, gas flow rate, fill volume and rock motion acceleration on the volumetric oxygen mass transfer coefficient ($k_La(O_2)$), CO_2 stripping rate and liquid phase mixing time (t_m) in rocked bags of 10 L up to 50 L scale. On the basis of this evaluation, the cell culture impact in terms of growth, productivity and cellular mechanical robustness to changes in the most significant input will then be demonstrated. This work is described in Chapter 3.
- To understand the observations from the characterisation, the fluid flow within the rocked bag will be investigated using a fabricated structural mimic and rocking platform to allow phase resolved Particle Image Velocimetry to measure 2-Dimensional (2-D) velocity vectors at high spatial

resolution over the course of a rock. The movement of the bulk fluid within the bag during rocking will also be analysed in greater detail. These data will be used to observe a change in fluid behaviour with respect to rocking rate. This work is described in Chapter 4.

- To understand the mechanisms of response to bubble induced shear stress during rocked bag cell culture. Using flow cytometry and gene expression levels to infer the cellular response in terms of cell cycle progression, apoptotic state and transcriptomic changes to cytoskeleton, DNA damage, glycosylation and cholesterol retention pathways. This work is described in Chapter 5.
- To establish the generic nature of the findings in the previous chapters by investigation of a second industrial cell line producing a therapeutically relevant product. Having characterised how the cell responds to bubble induced shear stresses, a state-of-the-art process will be used to investigate the effect of rocked bag bioreactor configuration on the product quality characteristics using an array of chromatographic purity and quality assays and glycosylation profile analyses. This work is described in Chapter 6.

In addition to the above, Chapter 2 provides detail of the bioreactors used in this work, cell culture methods and related analytical techniques. Finally, Chapter 7 will summarise the novel insights gained during this work and will attempt to draw some generic conclusions from the results obtained. This Chapter will also consider options for future work.

Chapter 2. Materials and Methods

2.1. Cell Culture Lines and Passaging

All cell culture work was performed aseptically, using standard cell culture techniques in a Class II biological safety cabinet. The cell line used in Chapters 3 and 5 (cell line A) was a stably transfected Glutamine Synthetase – Chinese Hamster Ovary (GS-CHO) cell line expressing an IgG_4. This cell line was kindly provided by Lonza Biologics Ltd. (Slough, UK). Frozen vials of this cell line were revived at passage 9 (relative to the master cell bank) and then expanded in CD-CHO media (Life Technologies, Paisley, UK) supplemented with 100µM Methylamine Sulphoximine (Sigma-Aldrich, Gillingham, UK) in Erlenmeyer shake flasks (Corning Life Sciences, NY, USA) shaken at 150 rpm, 37 ^{o}C and air supplemented with 5 % CO_2 in an Galaxy S incubator (Wolf Laboratories, York, UK).

The cell line used for the work described in Chapter 6 (cell line B) was a stably transfected GS-CHO expressing a recombinant therapeutic protein. This was supplied by Eli Lilly SA (Kinsale, Ireland) and certain details cannot be reported here for reasons of commercial confidentiality. Frozen vials of cells were thawed and expanded in Erlenmeyer flasks in Multitron incubators (Infors HT) under controlled conditions of temperature and CO_2 and passaged periodically in proprietary expansion medium. Expansion was continued in pH and DO controlled Biostat B-DCU II (Sartorius Stedim) 5L bioreactors in seed medium for a single passage before the broth was used to inoculate the production bioreactors (Section 2.2.2.2) containing production medium at defined split ratios.

2.2. Fed-Batch Cell Culture

2.2.1. Cell Line A

For cell line A, fed-batch cell culture was carried out at 37 ^{o}C with the DO setpoint at 30 % and the pH setpoint at 7.1±0.05. Cells passaged as described in Section 2.1 were inoculated in mid-exponential phase at 2 x10^5 viable cells.mL^{-1} as counted using an automated trypan blue exclusion method by ViCell XR (Beckman Coulter,

High Wycombe, UK) and cultured for 14 days. 10 x concentrated media supplemented to 150 gL^{-1} glucose was added up to once per day to maintain a concentration of 2 gL^{-1} glucose in the medium. 1 % $v.v^{-1}$ Antifoam Emulsion C (Sigma-Aldrich) was added as necessary to control foam accumulation, typically less than 60ppm was added over the duration of the cell culture.

2.2.1.1. Rocked Bag Configuration

An Applikon EZ controller system (Applikon, Tewkesbury, UK) was used for the work with cell line A (Section 2.2.1). This system works in conjunction with the Appliflex rocking platform onto which the bags are mounted. The Appliflex bags are available in 3 sizes; 10, 20 and 50 L total volume. The platform can rock at up to 25 min^{-1} at angles up to 13 ^{o}, and provides various angular velocity profiles through the rocking acceleration and deceleration adjustment. This model supported re-usable autoclavable probes for dissolved oxygen and pH measurement (Section 2.4.1 and 2.4.2). The maximum working volume of the bags is 50 % of the total volume.

The rocked bag was operated with a constant airflow of 0.04 vvm (200 $mL.min^{-1}$) to maintain bag shape and prevent CO_2 accumulation. Bags were rocked at the specified rocking rate (*N*) to an angle of 10^{o} above and below the horizontal. Control of DO and pH is by gas mixing into the headspace with liquid base addition. O_2 (<200 $mL.min^{-1}$) can be added to maintain DO above 30%. Addition of 100 mM $NaHCO_3$ (<17 $mL.min^{-1}$) and CO_2 (<100 $mL.min^{-1}$) were used to control pH. The gas outlet was pressurised to 20 mbar using head of water.

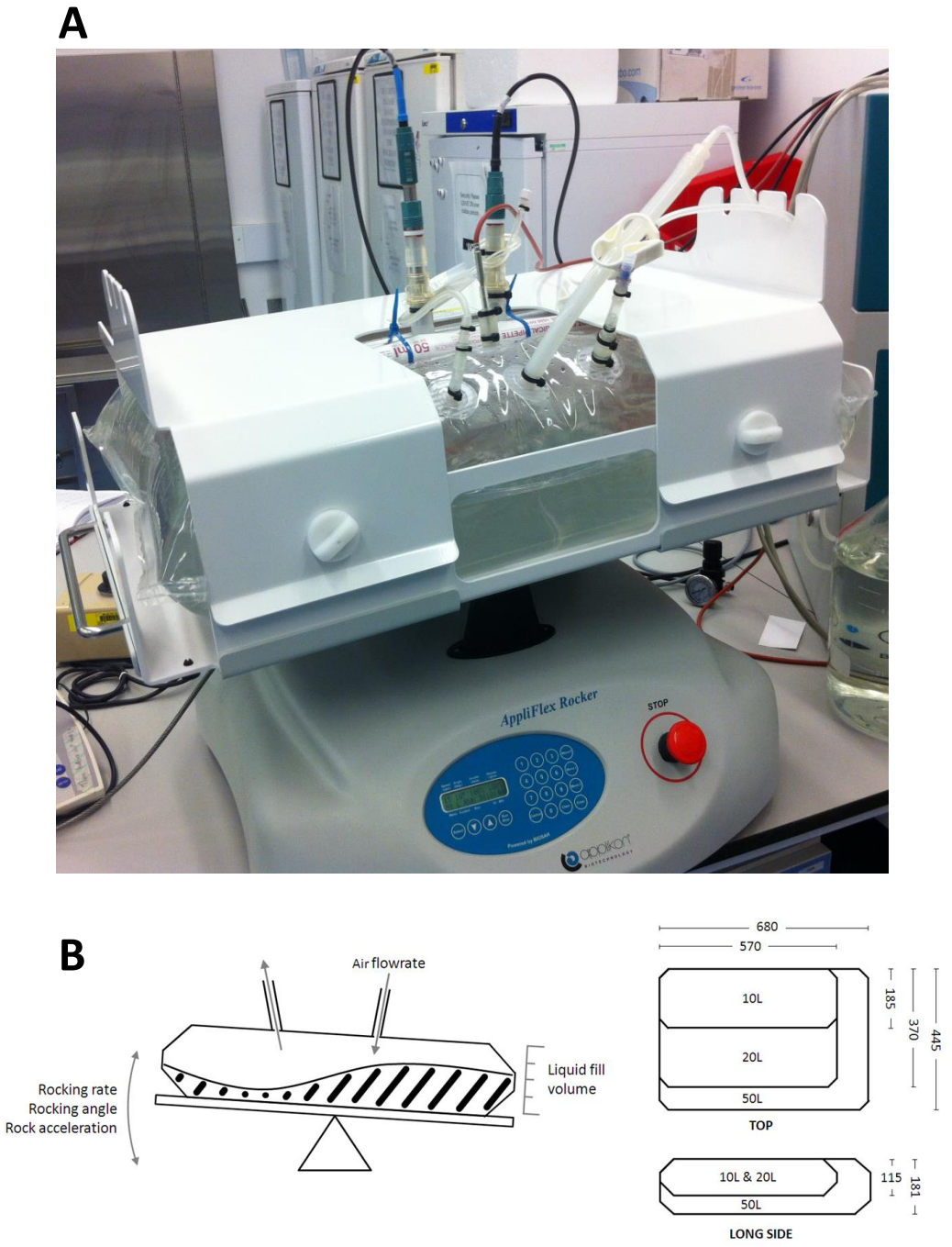

Figure 2.1: (A) Appliflex 50 L rocked bag installed on rocking platform. (B) Schematic diagram of the engineering inputs of the Applikon Appliflex. Dimensions of the inflated bags at the three scales evaluated in mm – the height of all bags and width of the 20 and 50 L bags are dictated by the steel restraint and can be measured precisely, other measurements are more likely to vary with installation and measurement point. Refer to Section 2.3 for further details.

2.2.1.2. Stirred Tank Configuration

A controlled stirred tank bioreactor was used for the work described in Chapter 5. This was a Sartorious Biostat B-DCU control system, with a 5 L (3.4 L working) stirred tank agitated by a single 62 mm 3-blade pitched blade turbine (PBT) (45^{o} blade angle) at 260 rpm (Fig.2.2A). The vessel was sparged from an 8 hole, 0.9 mm hole diameter horseshoe sparger at a constant gas flowrate of 150 mL.min^{-1}. The composition of this gas flow is adjusted to control pH with CO_2 addition and dissolved oxygen with a mix of air, pure nitrogen and pure oxygen. Upward pH control was provided by the pumped addition of 100 mM $NaHCO_3$ (<17 mL.min^{-1}). Online DO measurement was performed using an polarographic oxygen sensor (Mettler Toledo, Leicester, UK) while online pH measurement used an electrolytic pH probe (Mettler Toledo).

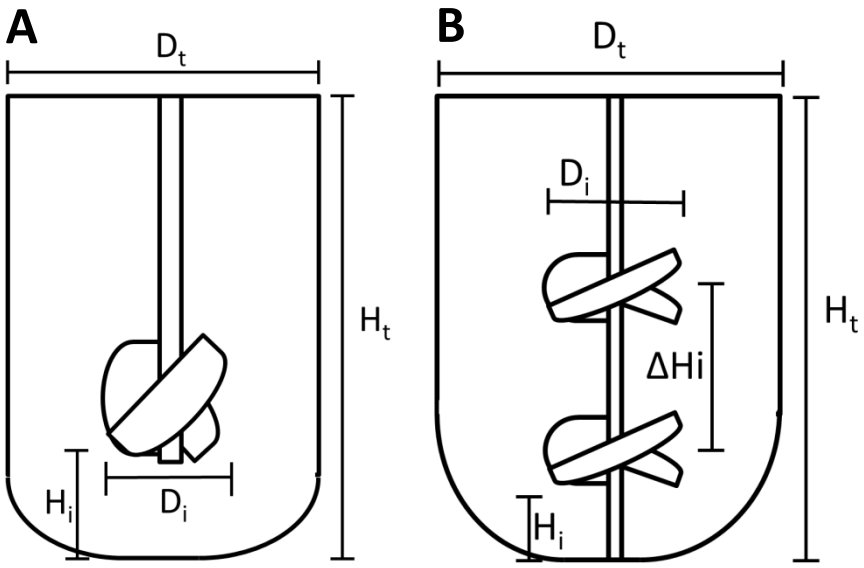

Figure 2.2: Key dimensions of (A) 5 L and (B) 50 L stirred tank bioreactors. For the 5L (A), in mm, D_t = 62, H_t = 345, D_i = 62 and H_i = 70. For the 50 L (B), in mm, D_t = 370, H_t = 666, D_i = 143, H_i = 120 and ΔHi = 186. Refer to section 2.3.1.2 for further details.

Cell culture was also conducted in a 50 L CultiBag Single-Use Bag (SUB) STR (Sartorius Stedim) for the work described in Section 3.3.1. This was agitated by a pair of 120 mm 3-blade PBT (4 5^{o} blade angle) at 120 rpm (Fig.2.2B). As in the B-DCU, the vessel was sparged from an 8 hole, 0.9 mm hole diameter horseshoe

sparger at a constant gas flowrate of 2.5 L.min^{-1}. The composition of this gas flow is adjusted to control pH with CO_2 addition and dissolved oxygen with a mix of air, pure nitrogen and pure oxygen. Upward pH control was provided by the pumped addition of 500 mM NaOH (<17 mL.min^{-1}). pH and DO were measured online every 150 and 15 s respectively using the built in Pre-Sens single-use sensor patches (Sartorius).

2.2.2. Cell Line B

For cell line B, cells were inoculated in mid-exponential phase based on a defined split ratio and cultured for a defined period. Cell culture was performed with defined temperature, DO and pH setpoints. A proprietary nutrient feed was added at a defined point as well as glucose supplementation at defined periods of time. CO_2 gas addition and 500 mM NaOH (<17 mL.min^{-1}) were used to control pH.

2.2.2.1. Rocked Bag Configuration

For cell line B (Section 2.2.2), a 10 L Sartorius Cultibag RM system was used (Sartorius Stedim, Epsom, UK). This platform supports gamma presterilised Sartorius CultiBags from 2, 10 and 20 L total volume and rocks at up to 42 min^{-1} at angles up to 10 ^{o}. This controller uses single-use Pre-Sens patches for oxygen and pH measurement. The maximum working volume of the bags is 50 % of the total volume.

10 L total volume CultiBag RM rocked bags were configured to rock at either 13 or 28 min^{-1} at 10^{o} and filled to 5 L (50 % total volume). For fed-batch cell culture, these were operated as described in Section 2.2.2. Gas flowrate was set at 0.04 vvm (200 mL.min^{-1}), with the oxygen and nitrogen mix altered to control DO by addition to the headspace of the rocked bag. CO_2 was added in addition to this to control pH. At 13 min^{-1}, visual observation indicated that there is no bubble formation due to the rocking of the bag, however oxygen transfer experiments (detailed in Section 2.4.1, results discussed in Section 6.2) established that this would still be capable of supporting the cell culture requirements, provided the gas mix was dynamically enriched with oxygen. At 28 min^{-1}, gas entraining wave

formation was observed due to the rocking of the bag, which produces a dispersed gas phase similar to a sparged bioreactor. This configuration has a significantly higher oxygen transfer rate (Section 6.2), however by varying the concentration of O_2 in the gas added by the control system, the same dissolved oxygen value could be maintained at both rocking rates.

To mitigate against potential effects from leachables (Wood *et al.* 2013; Hammond *et al.* 2013) and probe instability (based on company experience) an additional step was added to rocked bag preparations with this cell line. Bags were filled with 2.9 L (897 $mL.cm^{-2}$, Wood *et al.* 2013) of production medium 3 days prior to inoculation and heated to process temperature, gassed to process pH (5 % CO_2 in air $v.v^{-1}$) and rocked at 13 min^{-1}. After 1 day, the CO_2 and air gas mix was adjusted to achieve an offline pH of 6.83 (BioProcess Analyser 400, Nova Biomedical, Runcorn, UK) and this was used to calibrate the pH probe offset. The offline dCO_2 concentration determined (BioProfile Analyser 400) was subtracted from 100 % and used to calibrate the DO probes, since CO_2 and oxygen are the only gasses present relevant to the calibration. Systems were checked again 48 hours later to assess drift. On the day of inoculation, this 'soaked' medium was drained from the bags and replaced with fresh production medium.

An additional stirred tank was operated as described in Section 2.2.2 but used this 'soaked' production medium. Cell culture data kinetics not show any statistically significant differences in all measured aspects of cell culture performance compared to the controls.

2.2.2.2. Stirred Tank Configuration

For the work described in Chapter 6, the BioStat B-DCU II (Sartorius Stedim) 5L bioreactor and control system was used to operate control cell culture. This 4L working volume autoclavable glass bioreactor was configured with a single downward pumping 60mm diameter 3 blade (300 blade angle) PBT positioned above an 0.9 mm open pipe sparger. The dissolved oxygen concentration was controlled by the addition of pure O_2 through the sparger. To control pH, 100 % CO_2 or 1 M NaOH are added through the sparger or by peristaltic pump. The bioreactor

is dual walled and temperature control is achieved by the addition of water from a heating and cooling loop.

Two such bioreactors were used to establish that the cell culture experiments described in Section 2.2.2.2 fell within historical norms and allowed comparison to a larger control dataset (Section 2.3.2.1).

2.3. Cell Culture Analytical Techniques

2.3.1. Bioreactor Sampling

For cell line A, fed-batch cell cultures, as described in Section 2.2.1, were sampled daily and cell viability and number was measured using a ViCell XR (Beckman Coulter). Glucose, Lactate, Ammonium, Glutamine and Glutamate concentration, dCO_2 and dO_2 partial pressure and pH were measured a Bioprofile Analyser 400 (Nova Biomedical). The online pH reading of the bioreactor was corrected if the difference was greater than 0.04 pH units from the offline reading. The particle size distribution of samples was measured using a CASY Model TTC (Roche Diagnostics Ltd., Burgess Hill, UK). The CASY Model TTC uses electric current exclusion and pulse area analysis to count and size cells and cell debris. Cells are passed down a narrow capillary and the electrical resistance of the cell membrane is used to detect the particle size.

Samples were centrifuged at 1 $x10^4$ g and cell-free culture supernatant frozen for subsequent high performance liquid chromatography (HPLC) analysis. For the subsequent PCR analysis, samples were stored on ice during the cell count and then a volume containing approximately 3 $x10^6$ viable cells was centrifuged at 500 g and supernatants discarded. 70 µL of buffer RLT (Qiagen) was then added on top of the pellets. Buffer RLT contains Guanidine Isothiocyanate, which acts to reduce the rate of RNA degradation by RNases (Pasloske 2001). These samples were stored at -80 ^oC. Samples for staining were also stored on ice for up to 1 hour before the staining procedure was started.

For cell line B, during the fed-batch cell cultures described in Section 2.2.2, cell count, viability and cell size was measured daily using a ViCell (Beckman Coulter),

metabolite concentration, liquid phase gas composition and offline pH was also measured daily and corrected if the difference was greater than 0.04 pH units using a Bioprofile 400 (Nova Biomedical). Supernatant samples were frozen every two days from day 8 onwards for product quantification and product quality analysis.

2.3.2. Product Quantification

For cell line A (Section 2.2.1), IgG_4 concentration was determined by HPLC (Agilent Technologies, UK) using a 1 mL HiTrap™ Protein G column (GE Healthcare, UK). 100 µL of undiluted sample was loaded at a flowrate of 2 $mL.min^{-1}$. Sodium phosphate equilibration buffer (10 mM NaH_2PO, 10 mM Na_2HPO_4, adjusted to pH 7.0 by 2 M NaOH addition) and a glycine elution buffer (20 mM, adjusted to pH 2.8 by 10 M HCl addition) were used. Detection was carried out at 280 m and the sample concentration was measured by integrating the elution peak and generating a standard curve (as shown in Appendix, Section 8.1) using known quantities of IgG_4 depending on the sample tested.

For cell line B (Section 2.2.2), product titre was measured using Protein A HPLC on an Applied Biosystems Poros A/20 2.1x30 mm column running on an Agilent 1200. Samples were loaded in a pH 6.5 buffer and eluted using a pH 2.5 buffer (buffer details are excluded due to commercial sensitivity). Elution profiles at 280 nm were integrated and compared to a standard using a reference protein concentration to determine product concentration.

2.3.3. Derived Cell Culture Parameters

2.3.3.1. Integral Viable Cell Concentration

The integral viable cell concentration (IVC) is a measure of the total number of cells present in that culture up to a given time. It is calculated by an approximation of the area under a plot of viable cell count against time.

$$IVC_{i+1} = \left(\frac{C_i + C_{i+1}}{2}\right) \times (t_{i+1} - t_i) \qquad (2.1)$$

Where C is the viable cell count (VCC) and t is the culture age. The units of IVC are cells.day.mL^{-1}.

2.3.3.2. Cell Specific Productivity

Cell specific productivity (Q_p) is calculated by taking the slope of a plot of titre (pg.mL^{-1}) against the IVC (cells.day.mL^{-1}), at the same timepoint, typically harvest. The units of Q_p are pg.cell^{-1}.day^{-1}.

2.3.3.3. Cell Specific Metabolite flux

Cell specific metabolite fluxes (Q_X, where x is any metabolite) are calculated by taking the slope of a plot of that metabolite concentration (pg.mL^{-1}) against the IVC (cells.day.mL^{-1}) at the same timepoint, typically harvest.

2.3.4. Cell Mechanical Robustness Assay

The day 14 harvest material from cell line A was passed through a rotating disc device designed to mimic the levels of shear encountered in the feed zone of a large scale centrifuge (Tait *et al.* 2009; Hutchinson & Bingham 2006). It should be noted that all samples were 75±1 % viability at the point of harvest. Samples were exposed to three levels of energy dissipation; none, 1.9 x10^{4}Wkg^{-1} and 3.7 x10^5 Wkg^{-1} corresponding to disc rotational speeds of 0, 6,000 and 12,000 rpm for a duration of 12 s . The latter two have been previously demonstrated to mimic the shear experienced in the feed zones of hemetic and non-hemetically sealed centrifuges respectively. The particle size distribution of samples was then analysed using a CASY Model TTC (Roche Diagnostics Ltd.) (Section 2.3.1).

2.3.5. Transcriptomic Analysis

2.3.5.1. RNA Extraction

RNA extraction was carried out using an RNeasy mini kit (Qiagen, Manchester, UK) with the additional on-column DNase digestion (RNase-Free DNase set, Qiagen). Cell culture (Section 2.2.1) supernatant collected as described in Section 2.3.1 was sampled daily and centrifuged to remove supernatant. Pellets of 3-4 x10^6 viable

cells were stored under 4 µL buffer RLT (Qiagen RNeasy Mini kit, Qiagen) at -80 ^{o}C. Pellets were thawed on ice and cells disrupted by addition of 310 µL of buffer RLT (Qiagen RNeasy Mini kit, Qiagen) and vortexing. Cells were homogenised by centrifuging at 16,000 g in QiaShredder spin columns (Qiagen). 350 µL of 70 % v.v^{-1} ethanol was added to the flow-through and mixed by pipetting. Samples were transferred to RNeasy spin columns and washed with a series of buffers to remove contaminating DNA and proteins as well as an on-column DNA digestion step. Purified samples of RNA were eluted by the addition of RNA free water and RNA quantity and purity were measured using a Nanodrop 1000 Spectophotometer (Thermo Ltd., Hampshire, UK) at 260 and 280 nm wavelength.

2.3.5.2. cDNA Synthesis

Purified samples of RNA were converted to cDNA using a Quantitect Reverse Transcription kit (Qiagen). Per sample, 1µg of RNA was added to a mix of 2 µL of gDNA Wipeout buffer and a variable volume of RNase-free water to make 14 µL total volume and incubated at 42 ^{o}C for 2 min to eliminate any residual DNA in the sample. 1 µL of Quantiscript Reverse Transcriptase, 4 µL of RT buffer and 1 µL of RT Primer Mix were added to the samples on ice to make the total volume up to 20 µL and this was incubated at 42 ^{o}C for 15 min followed by 95 ^{o}C for 3 min to inactivate the RT. Samples were stored at -20 ^{o}C prior to qPCR. No-template controls were generated here by the above method substituting RNase-free water for RNA addition. No-enzyme controls were generated by the above method substituting RNase-free water for Quantiscript Reverse transcriptase.

2.3.5.3. Quantitative Polymerise Chain Reaction

For each 25 µL well, 12.5 µL of SYBR green PCR Master Mix (Qiagen) was combined with 33.3 ng (diluted to 5 µL for pipetting accuracy) of cDNA, 2.5 µL of (5 µM) forward and reverse primer mix and 5 µL of RNase free water. No template and no enzyme control wells were established for each primer and sample respectively. A BioRad CFX Connect PCR machine (BioRad, Hemel Hempstead, UK) was used to conduct the qPCR. Temperature was initially raised to 95 C for 15 min to activate the DNA polymerase and then cycled between 94 ^{o}C (denaturation), 55 ^{o}C

(annealing) and 72 ^{o}C (extension) for 15, 30 and 30s respectively, with fluorescence measured at 72 ^{o}C.

2.3.5.4. Primer Design and Amplification Product Validation

Primers were designed for targets of <200 bp using NCBI gene and primer-blast online tools with *The Sequence Manipulation Suite* (Stothard 2000) used to screen for self-annealing primer sets and ordered from Eurofins Genomics MWG (Ebersberg, Germany). Primer sequences can be seen in Table 2.1. PCR products were tested for specificity by 1 % w.v^{-1} agarose gel electrophoresis. 1 g UltraPure Agarose (Invitrogen) was dissolved by boiling in 100 mL of 1X TAE buffer (Sigma-Aldrich) to which 0.4 µg.mL^{-1} of Ethidium Bromide (Sigma-Aldrich) was added. 10 µL of each PCR product was combined with 2 µL of Fermentas 6X DNA Loading Dye & SDS solution (Life Technologies) and loaded onto the gel. The ladder used was BIOLINE HyperLadder 1kb (BIOLINE, London, UK). The gel was operated at 120 Volts and 400 mA on a Bio-Rad PowerPac Basic (Bio-Rad). After 60 min, the gel was transferred to a Bio-Rad Gel Dock 2000 (Bio-Rad) for imaging, using Quantity One analysis software version 4.6.8 (Bio-Rad). Gel imaging showed single bands of the expected product size for each primer set (Appendix, Section 8.6).

Table 2.1: Forward and reverse primer sequences for genes of interest and reference gene (Actb). Refer to section 2.3.5.4 for further details.

Gene	Forward	Reverse
Abca1	GTCTCGCCTGTTCTCAGATG	GAACGGGAGGGTTTTGCTTA
Sod1	CGAACAATGGTGGTACGTTT	GAAAGTAGTTTGACCATGAAGTC
Arpc3	CCCTCTTGTGAACCACACTC	ACTCCAAGTCCTCCCCATAC
Apex1	CACGCCGATCTTGTTGGC	TCAGGAGTGCTGTGATTGGT
Ddost	CTTCACGCCTGATAGGTAAGC	AAAATGTTAAGGGCTGGGACT
Actb	TCCGAAAGTTGCCTTTTATG	CGAAGAAAGAGCTGCGAA

2.3.6. Flow Cytometric Assays

2.3.6.1. Cell Cycle Analysis

Cell cycle distribution was determined for days 0, 2, 4 and 6 to 14 using a propidium iodide DNA stain combined with flow cytometry for cells cultured as described in Section 2.2.1. Cell culture samples were first centrifuged at 500 g for 5 min at 20 ^{o}C and washed and centrifuged again with PBS with the supernatant being discarded. The cells were then fixed by addition of 7 0% v.v^{-1} ice cold ethanol to a concentration 5 x10^{6} cells mL^{-1} and incubation at 4 ^{o}C for 30 min. Samples were then centrifuged at 1,500 g at 20^{o}C for 5 min, supernatant discarded, then resuspended in 0.5 mL PBS and centrifuged at 800 g for 5 min at 20 ^{o}C. The supernatant was again discarded and 75 µL of 100 µgmL^{-1} Ribonuclease A (Sigma-Aldrich, Gillingham, UK) solution was added. This was incubated for 5min at room temperature, 0.75 mL of 50 µL.mL^{-1} Propidium Iodide (PI) solution (Life Technologies) was then added followed by a final 5 min room temperature incubation. The samples were analysed by flow cytometry (Coulter Epics XL-MCL, Beckman Coulter) at 488 nm excitation and a 675 nm band-pass filter for detection. The cell cycle distribution was obtained by analysing the cell count versus PI intensity histogram with Cylchred (Cardiff University, Cardiff, UK). Measurements were performed in duplicate.

2.3.6.2. F-Actin Intensity Analysis

F-actin intensity was measured using a phalloidin stain quantified by flow cytometry (Wulf *et al.* 1979). After sampling, cell culture broth was centrifuged at 500 g for 5 min and the supernatant discarded. Cell pellets were resuspended in 3.7 % v.v^{-1} formaldehyde solution (Sigma-Aldrich) containing 0.2 % v.v^{-1} TWEEN-20 (Sigma-Aldrich) at a concentration of 1-2 x10^{6} cells.mL^{-1}. 12.5 µL of Alexa Fluor 488 Phalloidin (Life Technologies) was added and the solution incubated in the dark at 4 ^{o}C for 15 min. Samples were then washed by two successive 5 min centrifugations at 300 g and 4 ^{o}C followed by resuspension in PBS (Sigma-Aldrich). Cell pellets were then resuspended in 300 µL of 300 nM 4' 6-diamidino-2-phenylindole dihydrochloride (DAPI) (Invitrogen) and incubated in the dark at 25 ^{o}C for 5 min.

Finally, the cells were once again centrifuged at 300 g and 4 ^{o}C for 5 min and pellet resuspended in PBS twice to wash away residual DAPI. The samples were analysed by flow cytometry (Coulter Epics XL-MCL, Beckman Coulter) at 488 nm excitation and a 515-545 nm band-pass filter for detection. The mean intensity of actin fluorescence per cell was taken as a measure of F-actin intensity. Measurements were performed in duplicate.

2.3.6.3. Apoptosis Assay

Cell apoptotic state was determined using an Annexin V-FITC and 7-ADD Kit (Beckman Coulter) (van Engeland *et al.* 1998). After sampling, cell culture broth was centrifuged at 500 g for 5 min at 4 ^{o}C and the supernatant discarded. Cell pellets were resuspended in PBS and centrifuged again at 500 g for 5 min at 4 ^{o}C. Cells were then resuspended in 1X binding buffer (Beckman Coulter) to a concentration of 5-10 x10^{6} cells.mL^{-1}. 100 µL of this cell suspension was gently mixed with 10 uL Annexin V-FITC and 20uL 7-AAD and then incubated on ice in the dark before being diluted with 400 µL of 1X binding buffer. Positive controls were generated by incubation with 3 % v.v^{-1} Formaldehyde (Sigma-Aldrich) replacing the initial PBS addition in the above method. The samples were analysed by flow cytometry (Coulter Epics XL-MCL, Beckman Coulter) at 488 nm excitation and a 525-655 nm band-pass filter for detection. Excitation at these two wavelengths places the cells into one of 4 quadrants relating to the extent of apoptotic or necrotic state of the cells. Gates was set using unstained cells as a negative control, and annexin V-FITC stained cells and 7-ADD stained cells as single positives. As the double positive control, cells were incubated at 0 ^{o}C for 30 min in 3.7 % v.v^{-1} formaldehyde (Sigma-Aldrich), centrifuged, resuspended in binding buffer and stained and analysed as above. Measurements were performed in duplicate.

2.3.7. Cell line B Product Quality Assays

Product quality was analysed using various chromatographic techniques applied to cultures performed at Eli Lilly with cell line B (Section 2.2.2). Because of the commercial nature of this work only brief details can be provided of the methods used. Samples were first purified using Vivapure Maxiprep A (Sartorius) centrifugal

columns to bind and wash (neutral pH) and elute (low pH) purified product for further analysis. Size exclusion chromatography was carried out using an isocratic gradient on a YMCpack DIOL-200 8.0x300 mm column to measure purity and aggregation levels (Hong *et al.* 2012). Purity was further assessed using reverse phase chromatography (Vlasak & Ionescu 2008). Samples were first reduced and denatured using a 24:1 ratio DTT:protein incubation at 37 ^{o}C for 30 min. Samples were then injected into a c4-300 4.6x150 mm reverse phase HPLC column in aqueous conditions and then an organic gradient was used to elute product and modified forms separately, allowing quantification. Post translational modifications were assessed using a digest followed by reverse phase chromatography. The product was divided up into specific sections using a specified time and temperature incubation with trypsin (Life Technologies). The digested product was then passed down a TSK Gel ODS-100V 4.6x150 mm Reverse Phase HPLC column. Variants elute separately based on known modifications. CE-LIF was used to characterise the N-linked glycans attached. Samples were treated with PNGaseF to cleave oligosaccharides from the protein. These were then fluorescently labelled with APTS and passed down a capillary electrophoresis column. Laser induced fluorescence was used to characterise the glycan form.

2.3.7.1. Statistical Analysis of Cell Culture Kinetics and Product Quality

To compare the performance of the different cell culture configurations, JMP version 8 (SAS, Dublin, Ireland) was used to conduct ANOVA, tolerance intervals and Tukey-Kramer Honest Significant Difference tests on various cell culture outputs (as performed in Section 2.2.2): harvest point culture duration integral viable cell count, harvest point titre, cell specific productivity (Section 2.3.3.2), seven product quality attributes and the glycosylation profiles of the product molecule (Section 2.3.7). The Tukey-Kramer Honest Significant Difference tests is similar to a student's t test but is conservative when there are different sample sizes (Tukey 1949), as was the case here given the large historical data set.

Tolerance intervals were generated based on 15 historical 5 L stirred tank cell cultures conducted at Eli Lilly with the same cell line at identical conditions. These

established that the control stirred tanks run as part of this experiment were comparable with the historical data in terms of all cell culture outputs measured (Fig.2.3).

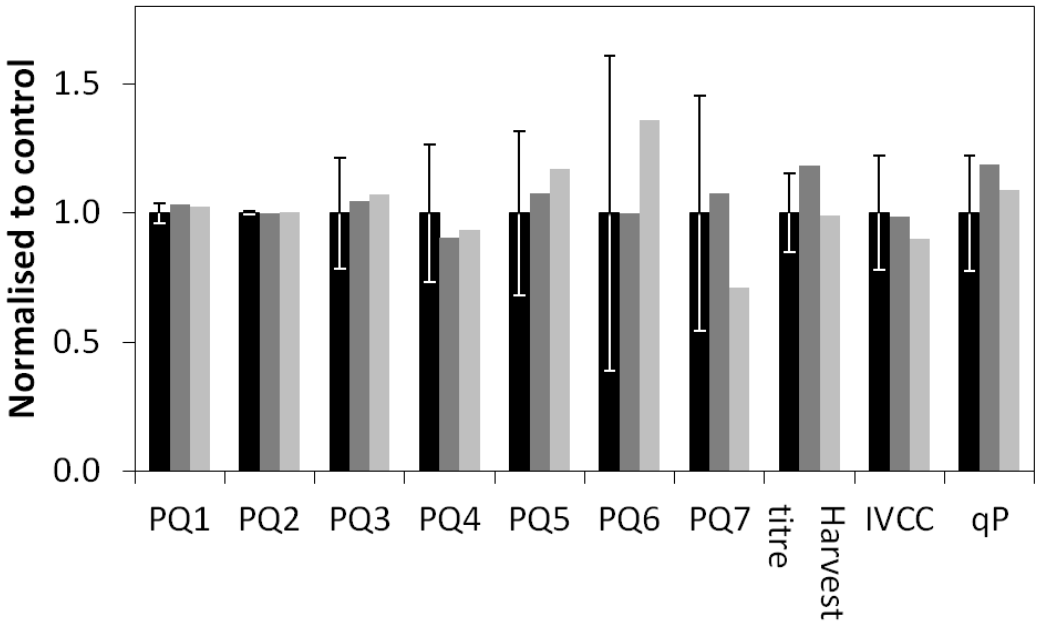

Figure 2.3: Relative performance of historical stirred tank runs (black bars, n = 15) and two stirred tank controls (dark and light grey bars) operated as part of the experiment in Section 5.3. Error bars represent 95 % confidence.

2.4. Quantification of Rocked Bag Engineering Parameters

2.4.1. Oxygen Mass Transfer Rate

Oxygen transfer rate measurements in the Applikon Appliflex (Section 2.2.1.1) were carried out using the built-in polarographic dissolved oxygen probe (AppliSens Z010023525, Applikon, Inc., Holland). The liquid phase used was designed to mimic the gas transfer properties of the medium used during cell culture and was 11.5 $g.L^{-1}$ NaCl (Sigma-Aldrich, Co., MO, US), 1 gL^{-1} Pluronic F-68 (AppliChem GmbH, Darmstadt, Germany) and 20 ppm Antifoam Emulsion C (Sigma-Aldrich, Co., MO, US). This composition was found to generate a dispersed gas phase (As observed in Section 3.2.1) at the same conditions as the CD-CHO media used in cell culture and provided identical values of oxygen mass transfer (Appendix, Section 8.2).

Antifoam had to be added at rocking rates above 16 min^{-1} to prevent foaming which, due to the surface aeration, can negatively affect oxygen transfer.

A modified version (Singh 1999) of the static gassing-out method was used (Van't Riet 1979), suitable for use with rocked bag bioreactors. In this case the headspace of the bag was filled with nitrogen and the bag agitated to reduce the DO down to <10 %. The bag headspace was then evacuated by compression to remove the nitrogen and then rapidly refilled with air in the absence of agitation. When the bag was up to operating outlet pressure (20 mbarg, Section 2.2.1.1), the air flowrate was reduced to 0.04 vvm (unless otherwise stated) and agitation begun. The DO was recorded every 20s and the rate at which the liquid phase was oxygenated between 20 % and 80 % DO was used to estimate $k_La(O_2)$ by taking the negative gradient of the plot of $\ln(C_L^*-C_L)$ against time (Section 1.6.1). The probe response time (0-62.5 %) was found to be 9 s, which is negligible for the purposes of this study (Van't Riet 1979). When reducing the fill volume, complete and consistent bag evacuation and at the larger scale probe submergence became an issue. For this reason, there is a larger error at the lowest fill volume in the 10L bag, and no reading recorded at 20 % fill volume in the 20 L bag. See Appendix, Section 8.3 for example raw data. All measurements were performed in triplicate.

For evaluation of the Sartorius RM (Section 2.2.2.1) described in Section 6.2.1, the above approach was reproduced using the single use oxygen probes. Data were collected between 10 and 60 % DO. A one factor at a time approach was used with inputs kept at a rocking rate of 25 min^{-1}, a rocking angle of 10 ^{o}, a fill volume of 50 % total volume and an air flowrate of 0.04 vvm unless otherwise stated. Repeat readings were taken at a range of rocking rates to quantify the error over the range of oxygen transfer rates investigated (Table 2.2).

Table 2.2: Error measurements at various rocking rates for oxygen mass transfer data collected in Section 6.2.

Rocking rate (min^{-1})	Number of repeats (N)	Coefficient of Variance (%)
15	2	3.2
25	6	6.1
35	2	9.6
40	3	11.4

2.4.2. Carbon Dioxide Mass Transfer Rate

For CO_2 mass transfer rate measurement in the Appliflex, the media mimic solution used in the oxygen mass transfer determination (Section 2.4.1) had to be adapted slightly. To this end, 2 gL^{-1} of $NaOCO_3$ (Merck KGaA, Darmstadt, Germany) was substituted for 2 gL^{-1} NaCl, to allow realistic levels of CO_2 in the liquid at physiological pH CO_2 concentration was measured indirectly using the standard electrolytic pH electrode (Applisens Z001023551 pH+ sensor, Applikon, Inc., Holland) compatible with the bag. Using a similar method to the oxygen mass transfer evaluation, the headspace was evacuated and replaced with 100 % CO_2 and agitation begun to drive CO_2 into the liquid phase. When the liquid pH reached 6.9 the agitation was stopped and the headspace was rapidly evacuated and refilled with air. Agitation and gassing inputs were started at this point and the pH response with respect to time was recorded. The experiment was run for 60 minutes. By taking offline liquid samples and rapidly passing them through a BioProcess Analyser 400 (Nova Biomedical) it is possible to generate a calibration curve for online pH against offline liquid phase CO_2 partial pressure (Appendix, Section 8.4). This conversion can then be applied to the pH readings recorded under various conditions to convert from pH readings into a CO_2 saturation. From the change in CO_2 saturation over time, the $k_La(CO_2)$ can be calculated by taking the negative gradient of the plot of $\ln(C_L^*-C_L)$ against time. All measurements were performed in triplicate.

After the agitation was begun, there was a short period of apparent rapid CO_2 'stripping' as the liquid and gas phase equilibrated. This was due to the liquid phase being approximately 13 % CO_2 saturated, while the gas phase was <1 % (Fig.2.4).

Since this concentration gradient would not occur during normal cell culture, this portion of the experiment was ignored from the evaluation.

The above method was validated by comparing the gas and liquid phase readings (Fig.2.4). In this case (20 min^{-1}, 8 ^{o}, 50 % fill volume and 0.036 vvm air flowrate), over the first 15 minutes of the experiment the gas and liquid phase CO_2 saturation levels converge, before trending downwards together as the air entering the bag displaces the CO_2 enriched air in the bag and equilibrates with the liquid phase. This early stage is not relevant to this investigation, given that this concentration gradient is very unlikely to occur during cell culture due to the low metabolic rate of mammalian cells and the necessity for a constant airflow during rocked bag cell culture. The rate of CO_2 transfer was measured from 20 minutes after the experiment was started to allow equilibration of the gas and liquid phases to occur.

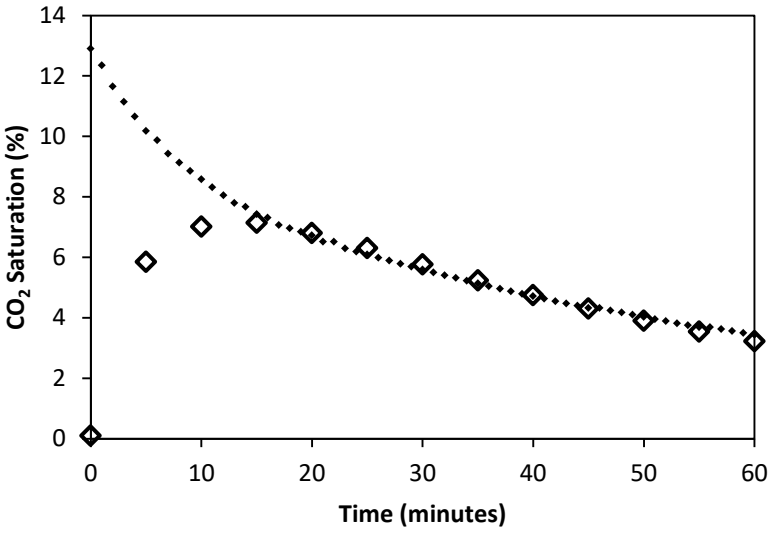

Figure 2.4: Liquid phase (by pH probe, filled diamonds) and gas phase (by mass spectroscopy, open diamonds) measured over the course of a CO_2 transfer rate determination experiment.

For the CO_2 stripping experiments in the Sartorius CultiBag RM (Section 2.2.2.1), the technique employed above was modified and involved the direct offline sampling of the liquid phase using the Bioprocess Analyser 400 (NOVA Biomedical). This was possible due to the proximity of the rocked bag systems to the Bioprocess 400,

meaning that analysis could be begun within 30 s of the sample being taken, and repeated at least every 3minutes, allowing 8-10 readings per experiment.

2.4.3. Liquid Mixing Time

Liquid Mixing time was measured by measuring the time taken for pH to stabilise after an acid addition at given system inputs (Bryant 1977). The system was filled with water to the desired level and the agitation begun. After a delay of at least 60 s for the flow pattern to reach steady state, 1.2 5mL of 2 M HCl (Sigma-Aldrich) was added at the fluid surface at a fixed stationary point (port f, see Fig.2.5) in the rocking cycle (at the change of direction). The built-in glass electrode pH probe (Applisens Z001023551 pH+ sensor, Applikon) positioned in port e (Fig.2.5) was attached to a Mettler-Toledo SevenEasy pH meter (Mettler-Toledo, Beaumont Leys, UK) with 1 Hz logging capability. The response time of the probe to acid addition was found to be <1 s over the range of the measurements. The mixing time was taken as the time needed to pass 95% homogeneity. See Appendix, Section 8.5 for example raw data. Experiments were performed in quintuplicate due to the high variability inherent in mixing time measurements.

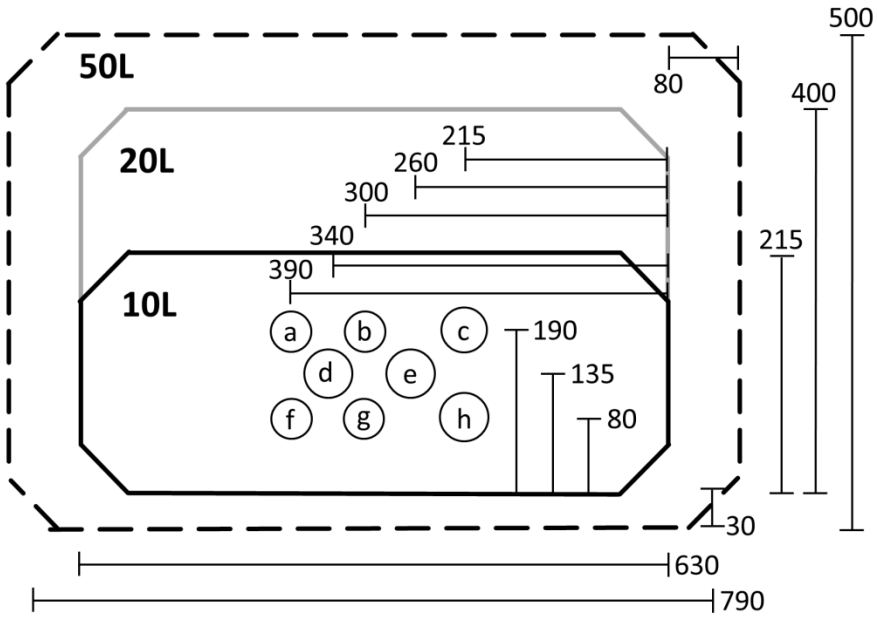

Figure 2.5: Dimensions and port positions of uninflated Applflex bags of 10, 20 and 50 L total volume. All measurements in mm. Ports; (a) Addition port 1, (b) Temperature probe sleeve, (c) Gas inlet, (d) 12mm Probe port 1, (e) 12mm probe port 2, (f) Addition port 2, (g) Gas outlet and (h) Sample port.

Since the above method relies on a probe at a single position, and repositioning the probe was not feasible, the values obtained were validated using the optical iodine-thiosulphate decolourisation method (Cronin et al 1994). Mixing times at 20 and 25 min^{-1} fell within standard error of the pH trace method's results. It was observed that while there was no clear stagnant zone in the liquid, the central region of the fluid near the fluid surface was most poorly mixed (Fig.2.6B), so the pH values recorded by the probe positioned here represent mixing times above the spatial average.

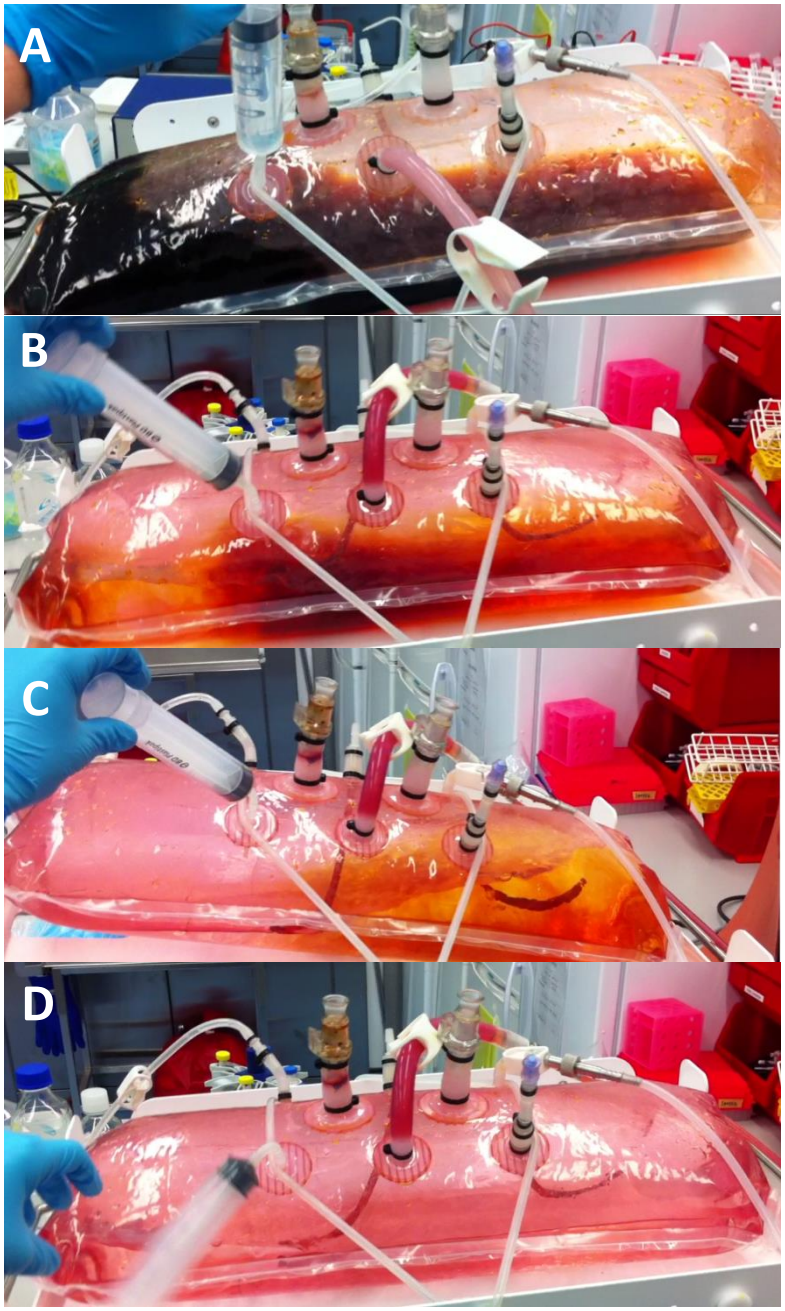

Figure 2.6: Photographs illustrating the principle of the iodine thiosulphate method for mixing time determination. This show the decolourisation of the solution over time: (A) 0; (B) 4; (C) 8 and (D) 12 s. Experimental conditions: rocking rate 20rpm, rocking angle 10^{o} and 50 % fill volume. Experiments performed as described in Section 2.4.3.

2.4.4. Rocking Angular Velocity Profile

An L3G4200D (STMicroelectronics, Geneva, Switzerland) gyroscope was positioned longitudinally and centrally on the rocking platform (Section 2.1). Since this device measures angular velocity, absolute positioning is not required for accurate measurement. Rocking was started and then logging was begun at 20 Hz (maximum available, 48 data points per rock). This was carried out at 50 % and 100 % acceleration and deceleration on the Appliflex Rocker at setpoints of 25 min^{-1} and 8^{o} and on the Sartorius RM platform at 25 min^{-1} and 80 for comparison. It was found that the Appliflex Rocker could not actually achieve 25 min^{-1} at 50% acceleration and was actually rocking at ~21 min^{-1}. The data are therefore presented normalised over one rock, rather than with respect to time. The data from the first 5 complete rocks were averaged to remove noise. Integration of the data reveal that the total angular distance reported for the three configurations differs by <2 %.

2.5. Fluid dynamic Characterisation of Rocked bag

2.5.1. Rocked Bag Mimic

Phase-resolved Particle Image Velocimetry (PIV), as described in Section 1.14.3, was used to characterize the flow in a specially-made Perspex mimic of a 2 L RM CultiBag (Sartorius). In order to minimise diffraction through the curved walls of the real bag-shaped bioreactor, a plaster of Paris cast of the real bag was laser scanned to digitise its shape and such information was then used to create a 1:1 scale mimic. This was achieved by milling the top and bottom 'halves' of the structure out of two Perspex cuboids, which were then polished and bolted together.

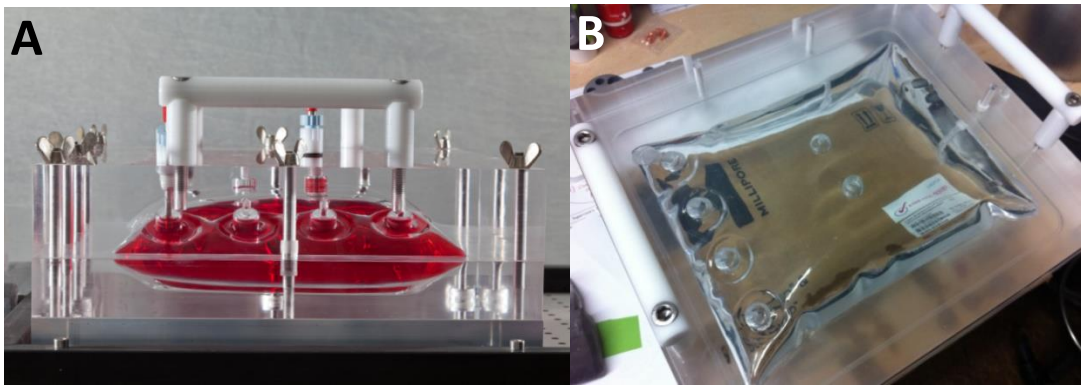

Figure 2.7: Photographs of completed PMMA structural mimic of Sartorius CultiBag RM 2L. (A) shows a photograph of the end of the PMMA bag mimic, filled with dyed water. (B) shows the top section from above during fabrication. For further details, see Section 2.6.1.

2.5.2. Rocking Platform Mimic

The rocking platform used in these experiments was fabricated in-house from welded stainless steel and powered by a PM10C 50 rpm 5.9 Nm motor (Parvalux, Dorset, UK). The platform was designed to allow the PIV camera to be mounted in-phase with the bag mimic and in order to have optical accessibility from all angles (Fig.2.8). A U-shaped through beam sensor (PMY44P, Panasonic Electric Works, NJ, USA) was occluded at a single point in each rock by a rotating spar attached to the motor. The position of this timing signal relative to the platform position could be adjusted manually based on the inclination of the platform by adjusting the position of this spar on the crank shaft shown in Fig.4.1.

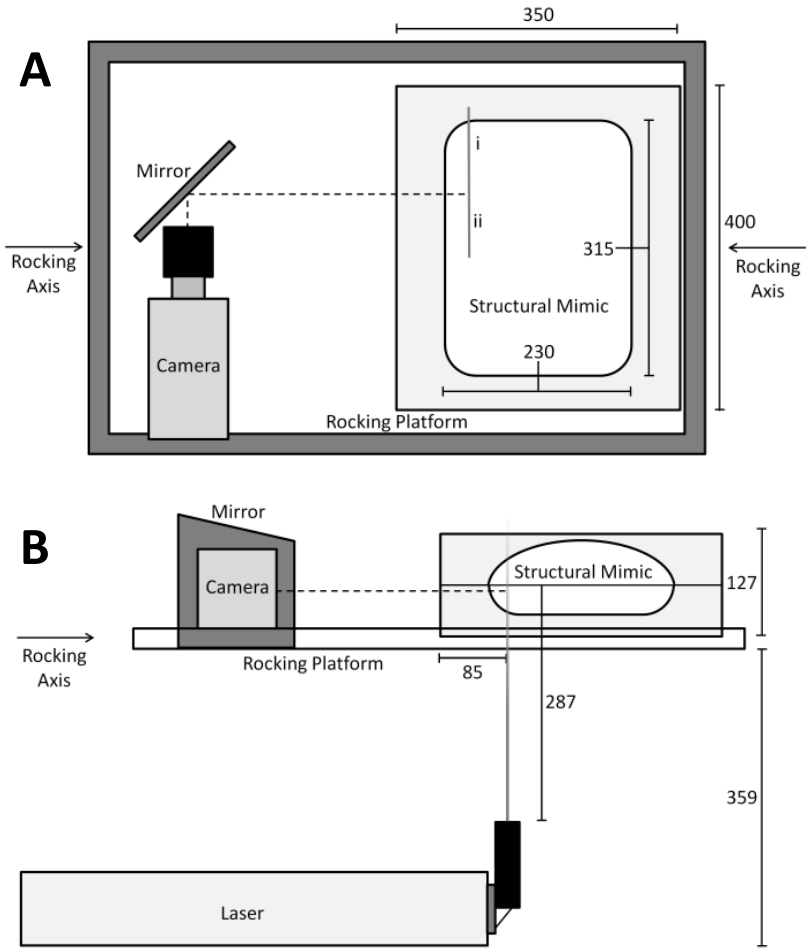

Figure 2.8: Schematic configuration to measure velocities in the vertical plane: (A) top view; (B) side view.

2.5.3. PIV equipment configuration

The PIV equipment used consisted of a dual head 532nm Nd:YAG laser, a NanoSense MkII camera with a resolution of 1260x1024 (Dantec Dynamics, Bristol, UK), a mirror and a 532 nm filter. With the exception of the laser, the equipment was mounted on a dedicated rocking platform as described in Section 2.5.2 and Fig.2.8. The movement of the rocking platform was synchronised with the PIV acquisition system using an analogue Timing Box (Texas Instruments Inc., Texas, USA) interfaced with the timing sensor (Section 2.5.2), laser and camera.

The Perspex (Poly(methyl methacrylate), PMMA) mimic was filled with deionised water and seeded with 10 µm diameter silver coated hollow glass spheres (Dantec

Dynamics), 500 image pairs were taken at eight phase resolved points in the rocking cycle at each *N*. The Δ-t (Section 1.14.4) was set for each acquisition to allow the fastest particles to advance approximately one third of each interrogation area and was varied between 1500 and 3200 μs (Adrian 1986). Each interrogation area was sized as a 16x16 pixel square with 50 % interrogation area overlap - one interrogation area centre every 8 pixels.

Recorded data were passed into DynamicStudio (Dantec Dynamics) where cross correlation was performed at 16x16 pixel interrogation area resolution. This data was then imported into to *MatLab* (MathsWorks, Cambridge, UK) for the extraction of the mean and fluctuating components of the per interrogation area fluid velocities, using purpose written *MatLab* scripts for calculation and figure plotting (Appendix, Section 9.1-9.4 for the code used).

Experiments were carried out for the platform set to rock to 8^{o} above and below the horizontal. The rocking rate was varied between 25 and 42 min^{-1}. A Cartesian coordinate system (x, y, z) was used with the origin positioned at the intersection of a vertical line drawn down from the leftmost tip of the end and a horizontal line drawn to the left from the base of the bag. Bag or platform angle at a given point (α) is measured in degrees above and below the horizontal with the direction of travel of the bag at that point also indicated. E.g. α=+4^{o}- indicates that the bag is 4 degrees above the horizontal but is heading back towards the horizontal. The angle of the surface of the fluid compared to gravitational horizontal is denoted by β.

2.5.4. Fluid flow characterisation

In order to carry out flow visualization experiments, the camera and timing system used for the PIV system were employed (Fig.2.8). The bag-shaped mimic (Fig.2.7) was filled with 0.5 gL^{-1} aqueous methyl blue in deionised water at 50% fill volume and illuminated with a 650 W lamp. The camera was configured to capture 360 images per rock at N = 25, 33.5 and 42rpm (150, 201 and 252Hz, respectively). Data were acquired for five consecutive rocks at each N and the timing system (Section 2.5.2) was used to start each acquisition at the same point during the rocking cycle. The images obtained were then processed using a purposely-developed *MatLab*

(MathsWorks) script (Appendix, Section 9.5) to establish both the position of the bulk of the liquid and the mean angle of the free surface at 360 points over the rocking cycle. Measurements were performed in quintuplicate.

2.6. Statistical Testing

2.6.1. Students t-test

The student's t-test is a statistical hypothesis test used to determine if two sets of data are significantly different from one another. For equal sample sizes and equal variance the t-statistic is calculated as:

$$t = \frac{\bar{X}_{1-}\bar{X}_2}{s_{x_1x_2}.\sqrt{\frac{2}{n}}}$$

Where 1 and 2 indicate the two groups, $\bar{X}$ is the mean of the group, $s_{x_1x_2}$ is the pooled standard deviation, and n is the group size. As the difference in the means gets larger, the sample size gets larger and the pooled standard deviation gets smaller, the t statistic gets larger. The degrees of freedom are $2n - 2$.

2.6.2. Linear regression t-test

It is possible to statistically test for a correlation between two variables by applying a t-test to the linear regression of an x by y dataset. A linear regression model in the form:

$$\hat{y_i} = \hat{B}_0 + \hat{B}_1 x_i \qquad (2.1)$$

Where $\hat{y_i}$ is a given dependent variable, x_i is a given independent variable and $\hat{B}_0$ and $\hat{B}_1$ are parameters for intercept and gradient respectively. $\hat{B}_0$ and $\hat{B}_1$ can be estimated by the least squares method as:

$$\hat{B}_1 = \frac{\sum(x_i-\bar{x})(y_i-\bar{y})}{\sum(x_i-\bar{x})^2} \qquad (2.2)$$

$$\hat{B}_0 = \bar{y} - \hat{B}_1\bar{x} \qquad (2.3)$$

Where $\bar{x}$ and $\bar{y}$ are the mean of the x and y values respectively.

A two tailed t-test can then be performed on the gradient ($\hat{B}_1$) to compare this to 0, see Section 2.6.1.

Chapter 3. Engineering Characterisation of a Rocked Bag Bioreactor

3.1. Introduction and Aim

Rocked bioreactors are an example of a single-use upstream technology that has attracted significant interest and investigation since their inception in 1999 (Singh 1999). As described in Section 1.13.6, various applications have been reported including: fermentation of *S.cerevisiae* (Mikola *et al.* 2007) and *E.coli* (Mahajan *et al.* 2010), culture of plant (Eibl & Eibl 2007), insect (Weber *et al.* 2002) and adherent mammalian cells (Genzel *et al.* 2006), suspended mammalian cells in perfusion mode (Tang *et al.* 2007) and using transient transfection (Haldankar *et al.* 2006).

One of the posited benefits of rocking as a mechanism to induce fluid flow and mass transfer is low hydrodynamic shear (Section 1.13.2). This was hypothesised early on in the design of these systems but only recently demonstrated (Kalmbach *et al.* 2011). The low shear and unsteady flow environment were considered to be responsible for the attainment of higher cell densities compared to a stirred tank bioreactor during microcarrier culture of Madin Darby Canine Kidney cells (Genzel *et al.* 2006).

Aspects of the engineering characterisation of rocked bag bioreactors have appeared in a number of publications as described in Section 1.13.5. Hot wire anemometry has been used to measure fluid velocity at fixed points within a rocked bag. The fluid flow regime was found to be laminar at 2 and 20 L scale albeit at relatively low rocking rate and rocking angle (Oncül *et al.* 2010). Subsequent work with additional sensors showed that fluid velocity was greatest towards the centre of the bag and the bottom of the liquid (Kalmbach *et al.* 2011). Mixing time evaluations have tended to show stirred tank equivalent mixing times (Singh 1999; Eibl *et al.* 2010). In terms of gas mass transfer, published literature agrees that the largest effectors are rocking rate and to a lesser extent rocking angle (Mikola *et al.* 2007) with aeration rate being least important (Yuk *et al.* 2011).

As described in Section 1.5, knowledge of the fundamental engineering characteristics has been used as a basis for scale-up and for translation of results between bioreactors with alternate geometries and different methods of mechanical agitation (power input). For microbial systems, oxygen transfer rate (OTR) was used as the basis for scaling between *E. coli* cultures in a stirred miniature bioreactor (Gill *et al.* 2008) and an orbitally shaken microplate system (Micheletti *et al.* 2006) up to laboratory scale stirred tanks. Power per unit volume ($P.V^{-1}$) was also used as a basis for achieving equivalent cell culture performance in shaken microplates and laboratory stirred tanks (Barrett *et al.* 2010). To date, however, no thorough analysis of how all the effectors of fluid agitation in rocked bag geometries affect the basic engineering requirements for cell culture (k_La, mixing time etc.) has been reported in the scientific literature. Current investigations have also not attempted to explain the mechanisms by which these changes are affected and there is also a relatively poor understanding of how scale affects the basic characteristics of rocked bioreactors.

As described in Section 1.16, the aim of this chapter is to characterise the effects of rocking rate, rocking angle, gas flow rate, fill volume and rock motion acceleration on on mass and gas transfer characteristics volumetric oxygen mass transfer coefficient ($k_La(O_2)$), CO_2 stripping rate ($k_La(O_2)$) and liquid phase mixing time (t_m) at 10L up to 50L scale. The cell culture impact in terms of growth, productivity and cellular mechanical robustness of small changes to the most significant input will then be demonstrated.

The specific objectives of this chapter are:

- To characterise the effect of rocking rate, rocking angle, fill volume, platform acceleration and air flowrate on the volumetric oxygen and carbon dioxide mass transfer coefficient and the time to liquid phase homogeneity in rocked bag bioreactors.
- To characterise the scalability of rocked bag bioreactors.
- To use the characterisation data to design and operate fed-batch cell culture across various agitation configurations to evaluate the effect of the physical

environment on the cell culture growth, productivity and metabolite profiles.

- To compare the mechanical robustness of cells cultured in rocked bags under various agitation configurations to cells cultured in a stirred tank bioreactor.

3.2. Engineering Characterisation of Rocked Bag Bioreactors

The first experiments focused on the quantification of key engineering parameters of the rocked bag bioreactor, such as volumetric O_2 and CO_2 gas mass transfer rates and mixing times in the 10 L bag (Figure 2.1). These are discussed together in the following sections for each of the identified effectors of rocked bag bioreactor performance. The relative significance of each effector is considered in Section 3.2.6.

3.2.1. Rocking Rate

The k_La describes the ability of a bioreactor to transfer O_2 from the gas to the liquid phase under standardised initial liquid and gas phase compositions. The $k_La(O_2)$, together with the oxygen saturation of the liquid and gas phases, define the overall oxygen transfer rate. Cell culture is typically operated in bioreactors with oxygen mass transfer coefficient between 1-10 h^{-1} (Nienow 2006).

The standard static gassing-out method was modified as described in Section 2.4.1 to make the method more accurate in the case of rocked bag bioreactor experiments. Increasing rocking rate was found to have the greatest impact on $k_La(O_2)$ (Fig.3.1A) over the range of rocking rates investigated. This agrees with the majority of previous evaluations (Yuk *et al.* 2011; Mikola *et al.* 2007). Singh *et al.* (1999) proposed that gas transfer occurs by surface renewal, as the liquid present at the interface is exchanged due to agitation, however this does not explain the non-linear increase in gas transfer being seen here and by other workers in Fig.3.1A. At 10 L scale, up to a rocking rate of 18 min^{-1}, the rocking of the platform brought about ripples on the fluid surface, above 20 min^{-1} a more recognisable wave was formed which increasingly entrained the gas phase as the rocking rate

was further increased to 25 min^{-1}. At 16 min^{-1} and above, there is clear bubble formation within the bulk fluid despite initially very little apparent wave formation. It is proposed here that up to approximately 18 min^{-1}, the proportional increase in $k_La(O_2)$ is due to the increasing fluid surface turnover. Above 18 min^{-1}, where bubble development becomes significant, the $k_La(O_2)$ appears to increase exponentially, with interfacial area, as the bubbles become both smaller and more numerous.

Liquid phase mixing in cell culture bioreactors is also important because it impacts on the homogeneity of the nutrients, extracellular metabolites and bioreactor control substances in the cellular environment. In this work, mixing time was also found to be significantly impacted by rocking rate (Fig.3.1B). The pH trace method was used due to the quantifiable results provided and this was validated by an orthogonal visual method (Section 2.4.3). In contrast to what was noted with the $k_La(O_2)$, the relationship between rocking rate and mixing time was found to be linear, with mixing times reducing from 23 s at 15 min^{-1} to 6.6 s at 25 min^{-1}. In the range of 15-22 rocks.min^{-1}, the mixing time was between 4.9-5.7 rocks but at 25 min^{-1}, the mixing time was 2.75 rocks. Over the range of rocking rates investigated (15-25 min^{-1}), the mixing time fell by 71 % (from 22.8-6.6 s). Eibl *et al.* (2010) also found mixing time to depend significantly on rocking rate, with the mixing time falling from 140 to 70 s when rocking rate was increased from 16 to 20 min^{-1} at 200 L scale.

Interestingly, the measured increase in $k_La(O_2)$ (Fig.3.1A) was not matched by the measured decrease in mixing time (Fig.3.1B). This substantiates the hypothesis that while the rate of mixing in the bulk fluid is increasing linearly, it is the bubble entrainment which is causing the apparent exponential increase in $k_La(O_2)$.

In addition to the rate of oxygen transfer, the rate of CO_2 stripping from the culture is important because this impacts on cell growth and productivity (Gray *et al.* 1996) (Section 1.4.2.1). Adequate CO_2 removal rate is a major issue particularly in larger scale cell culture bioreactors (Xing *et al.* 2009). The $k_La(CO_2)$ was measured here indirectly using the change in the online pH measurement of a carbonate buffered liquid phase in response to a change in dissolved CO_2 concentration (Section 2.4.2).

The $k_La(CO_2)$ was found to be only minimally affected by rocking rate (Fig.3.1C). Increasing the rocking rate from 15 to 25 min^{-1} increased the CO_2 stripping rate by 20 %. While this is a significant change, given the very high sensitivity of $k_La(O_2)$ to rocking rate, CO_2 stripping should be a secondary consideration when selecting a rocking rate. Previous investigations into stirred tanks have also shown a very low sensitivity of CO_2 stripping rate to agitation inputs (Sieblist *et al.* 2011). This is thought to be because of the significant concentration gradient, CO_2 moves rapidly from the liquid to the gas phase and therefore the interfacial area is less of a bottleneck for CO_2 transfer (Sieblist *et al.* 2011). Since higher agitation tends to influence the interfacial area by reducing bubble size (Mayinger & Heldinger 2004) this has little effect on CO_2 transfer.

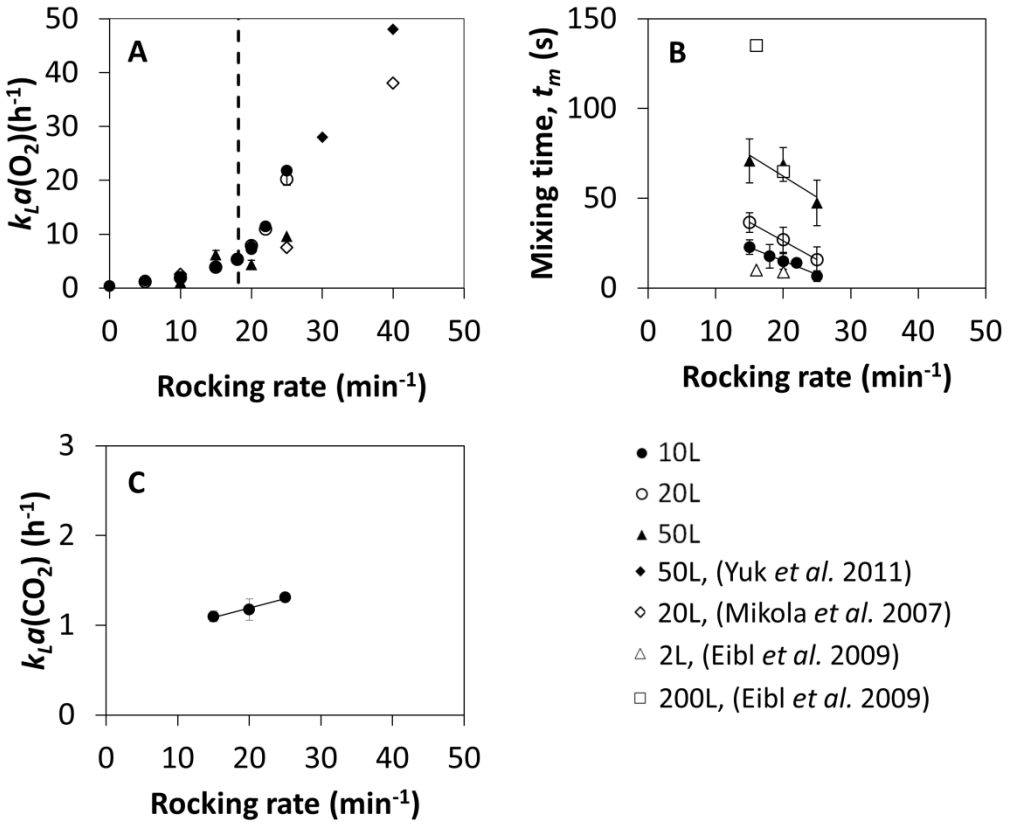

Figure 3.1: Effect of rocking rate on (A) volumetric oxygen mass transfer coefficient, $k_La(O_2)$ (n = 3 at 10 and 20L and n = 2 at 50L), (B) fluid mixing time, t_m (n = 5), (C) volumetric CO_2 mass transfer coefficient, $k_La(CO_2)$ (n = 3) and comparison to literature data. Filled circles; 10 L scale, open circles; 20 L scale, filled triangles; 50 L scale. Literature data, filled diamonds, Yuk *et al.* (2011); 50 L scale, open diamonds, Mikola *et al.* (2007) 20 L scale, open triangles, Eibl *et al.* (2009); 20 L scale, open squares, Eibl *et al.* (2009); 200 L scale. Error bars represent 95 % confidence about the mean. Solid lines fitted by linear regression, (B) R^2 = 0.98, (C) R^2 = 0.97, 1.00 and 0.81 for 10, 20 and 50 L respectively. Measurements performed as described in Section 2.4.

3.2.2. Rocking Angle

In rocked bioreactors, the rocking angle dictates that maximum angular displacement of the bag from the horizontal and therefore the gradient down which fluid flows. In this work it was found that rocking angle had a linear effect on measured $k_La(O_2)$ values varying from 4.0-9.7 h^{-1} over angles from 6 to 130 (Fig.3.2A). While this work and the work of Yuk *et al.* (2011) record an approximate 1.25 h^{-1} $k_La(O_2)$ increase for every one degree the rocking angle is increased, Mikola *et al.* (2007) only reported an approximately 0.16h^{-1} increase per degree (Fig.3.2A).

Rocking angle was less effective than rocking rate in influencing $k_La(O_2)$, and was not found to interact with rocking rate; the ratio of k_La at 13° compared to 10° at 20 min^{-1} and 25 min^{-1} differed by 0.05 %. The greater rocking angle should affect the flow linearly by two mechanisms: (i) it will cause a greater mean velocity of liquid, due to the platform having to move over a greater angular distance to complete a rock; (ii) it will also increase the accelerating force acting on the liquid due to gravity at any point in the rocking cycle, due to the greater rocking angle. At 20 min^{-1}, gas entrainment was noted from 8-13° and became more significant at higher rocking angles. The increase in bubble entrainment was not, however, as significant as that observed with increasing rocking rate.

Mixing time was found to be proportionately affected by rocking angle (Fig.3.2B). Over the range of rocking angles investigated (6-13°), the mixing time fell by 57 % (23-10 s) meaning that, as with the $k_La(O_2)$, the mixing time is more dependent on rocking rate than rocking angle. In contrast, Eibl *et al.* (2009) report a ~4-fold increase in mixing time when moving from 10° to 5° at 2 L scale. This discrepancy may be due to differences in the technique applied to measure the mixing time as well as the means of tracer delivery (Section 1.6.2).

Finally, rocking angle has no measurable effect on $k_La(CO_2)$ (Fig.3.2C). Comparison of $k_La(CO_2)$ values at 7 and 13° rocking angles indicate that there is not a statistically significant difference ($p = 0.15$, regression analysis, Section 2.6.2).

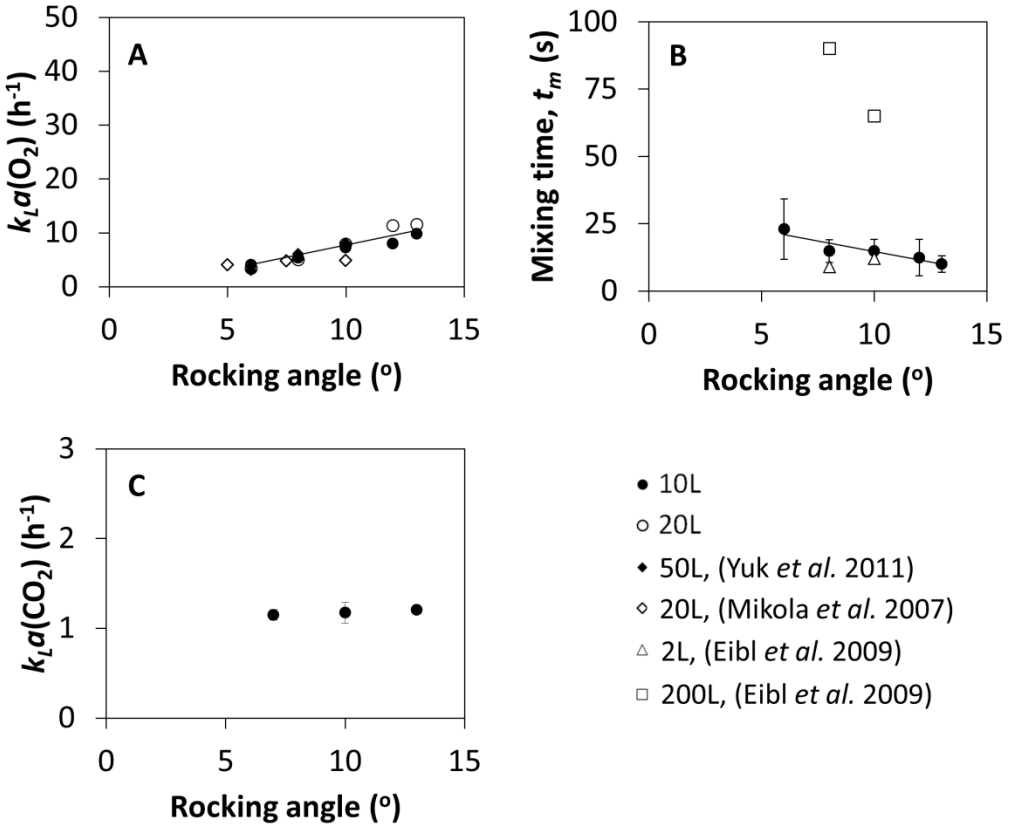

Figure 3.2: Effect of rocking angle on (A) volumetric oxygen mass transfer coefficient, $k_La(O_2)$ (n = 3), (B) fluid mixing time, t_m (n = 5), (C) volumetric CO_2 mass transfer coefficient, $k_La(CO_2)$ (n = 3) and comparison to literature data. Filled circles; 10 L scale, open circles; 20 L scale. Literature data, Filled diamonds, Yuk *et al.* (2011); 50 L scale, open diamonds, Mikola *et al.* (2007) 20 L scale, open triangles, Eibl *et al.* (2009); 20 L scale, open squares, Eibl *et al.* (2009); 200 L scale. Error bars represent 95 % confidence about the mean. Solid lines fitted by linear regression, (A) Internal data R^2 = 0.90, (B) Internal data R^2 = 0.86. Measurements performed as described in Section 2.4.

3.2.3. Fill Volume

The fill volume represents the proportional liquid (medium) fill of the rocked bag compared to the total volume. Rocked bags are not typically operated above 50% fill volume (Singh 1999). Fill volume was found to have a very significant proportional effect on $k_La(O_2)$ (Fig.3.3A) which is believed to be due to two mechanisms. Because of the relatively vertical sides of the bag (as shown in Fig.2.1), the lower volume of liquid does not have a significant effect on the gas transfer surface area (a) in the absence of a dispersed gas phase but requires a lower mass of oxygen to pass into it to reach saturation. This is in contrast to a

bottom sparged stirred tank, in which a greater volume of liquid increases liquid height and therefore bubble residence time, increasing the interfacial area. Secondly, the energy input by the rocking platform is passing into a smaller volume of liquid, which could have implications for the liquid film thickness as well as bubble entrainment. The level of entrained gas was seen to be equivalent at 30 % fill volume and 20 min^{-1} to that at 50 % fill volume and 25 min^{-1}. It should be noted that the $k_La(O_2)$ at 25 min^{-1}, 50 % fill and 20 min^{-1} 30 % fill are very similar, being 23.0 h^{-1} and 21.8 h^{-1} respectively. At 20 % fill volume, the $k_La(O_2)$ was ~4-fold that at 50 % fill volume. Hanson *et al.* (2009) did not find any significant effect on $k_La(O_2)$ brought about by a change from 20 to 35 % fill volume.

The effect of fill volume on mixing time is less evident than the effect on $k_La(O_2)$ (Fig.3.3B). Over the range investigated (50-20 %) the mixing time fell by 33 % (from 12.75±4.9 s to 8.6±4.5 s), while the rocking rate increased by 370%. While the energy input per unit mass potentially increases, a component of the mixing is thought to derive from the momentum built by the fluid as it flows down the pitched bag (Fig.4.7). Since this will scale with fill volume, this may be why the mixing time does not change dramatically with fill volume at this scale. This overall effect is in agreement with Eibl *et al.* (2010), who also find small but measurable effects on mixing times from small volume changes.

Fill volume was found to have only a small effect on $k_La(CO_2)$ (Fig.3.3C). Decreasing the fill volume from 50 % to 30 % in a 10 L bag increased the $k_La(CO_2)$ by 17 %. While decreasing the fill volume of the rocked bag reduces the total amount of CO_2 that must be gassed out for a given reduction in liquid phase saturation, it also reduces the gas turnover rate of the headspace at a given air flowrate. These two effects work against one another and reduce the overall increase in $k_La(CO_2)$ that would occur from a volume reduction of the liquid and gas phase at fixed air flowrate.

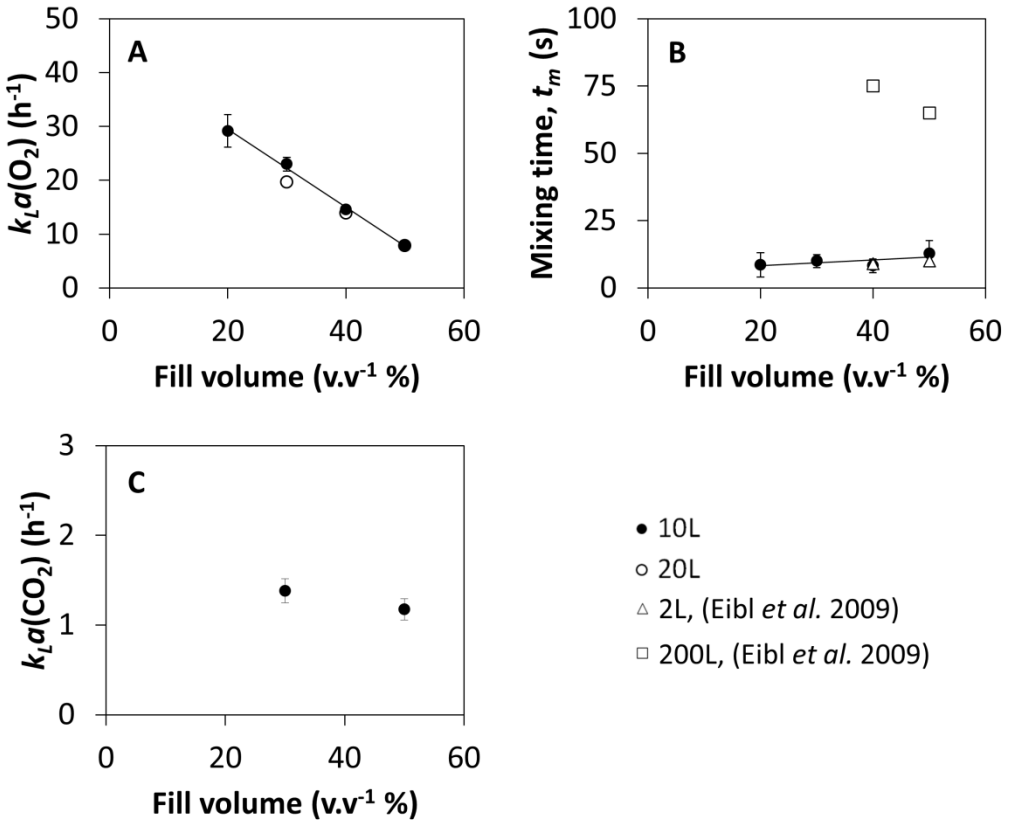

Figure 3.3: Effect of fill volume on (A) volumetric oxygen mass transfer coefficient, $k_La(O_2)$ (n = 3), (B) fluid mixing time, t_m (n = 5), (C) volumetric CO_2 mass transfer coefficient, $k_La(CO_2)$ (n = 3) and comparison to literature data. Filled circles; 10 L scale, open circles; 20 L scale. Literature data, open triangles, Eibl *et al.* (2009); 20 L scale, open squares, Eibl *et al.* (2009); 200 L scale. Error bars represent 95 % confidence about the mean. Solid lines fitted by linear regression, (A) R^2 = 0.98, (B) R^2 = 0.44. Measurements performed as described in Section 2.4.

3.2.4. Rocking Platform Acceleration and Deceleration

The adjustment of acceleration and deceleration of the rocking platform affects the acceleration of angular velocity over the course of the rock. Higher values result in the platform accelerating more rapidly after the rocking direction change and decelerating more rapidly prior to the next platform direction change. For the purposes of this study, these values were always adjusted together. 50 % represents an acceleration over 50 % of each half rock and then deceleration over the remaining 50 % to a momentary stationary point at the end of the half rock before the direction change, mimicking the sinusoidal velocity profile of some other

rocking platforms. 100 % involved accelerating and then decelerating more rapidly after a rock direction change.

It is important to quantify the effect that this may have on the $k_La(O_2)$, since some alternative platforms do not offer this adjustment, while this platform only operates over its full range of rocking speeds and rocking angles at 100 % acceleration. 100 % acceleration was expected to produce the greatest gas transfer due to the more aggressive change in direction compared to 50 % acceleration and deceleration. However, 50 % acceleration at 20 min^{-1} and 10^o and 50 % fill volume (10 L bag) had a $k_La(O_2)$ 27 % greater than an identical setup at 100 % acceleration (9.6 h^{-1} and 7.6 h^{-1} respectively, Fig.3.4A). Angular velocity data revealed that at 50 % acceleration, the peak angular velocity was 29 % greater than at 100% (Fig.3.4D). Visual observation suggested that this greater velocity mid-rock increased the acceleration of the surface of the liquid along the bag, creating a larger, higher wave, entraining more of the gas into the liquid phase. This is described further in Section 4.11.1. Measurement of the platform angular velocity by the gyroscope (Section 2.4.4) also confirmed that 50 % acceleration and deceleration produces angular velocity profiles which closely match other sinusoidal rocking platforms (Fig.3.1D).

Additionally, acceleration and deceleration rate was not found to have a statistically significant effect on mixing time: p=0.39, regression analysis (Fig.3.4B). This is likely in part due to the relatively low sensitivity of the mixing time methodology. Likewise, measurement of $k_La(CO_2)$ is not sensitive enough to agitation inputs to detect any change with respect to rocking acceleration: p = 0.12, regression analysis (Fig.3.4C).

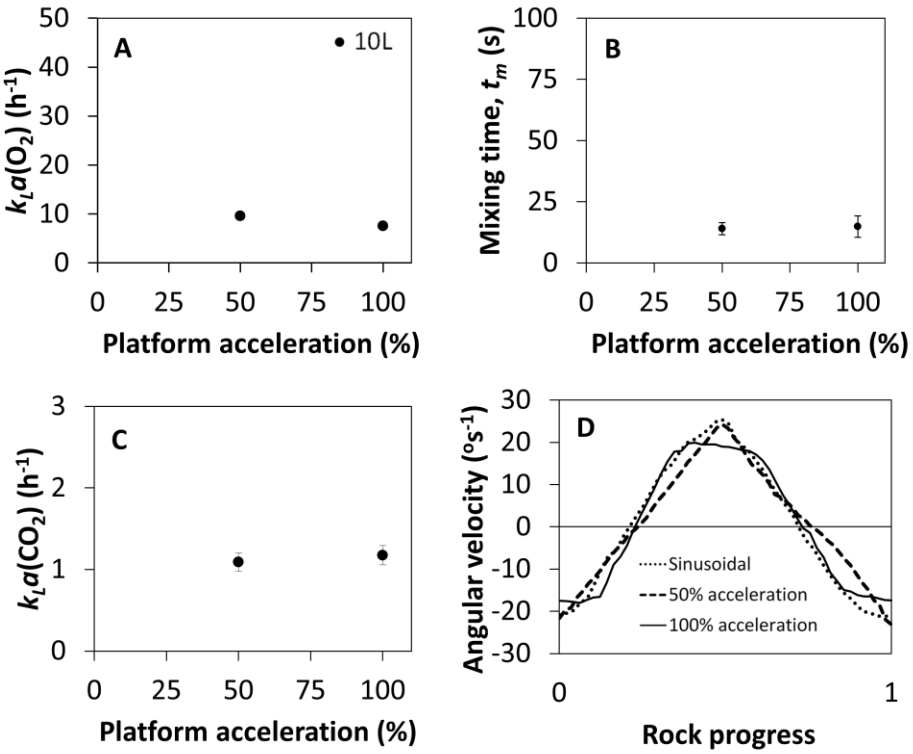

Figure 3.4: Effect of rocking platform acceleration and deceleration on (A) volumetric oxygen mass transfer coefficient, $k_La(O_2)$ (n = 3), (B) fluid mixing time, t_m (n = 5), (C) volumetric CO_2 mass transfer coefficient, $k_La(CO_2)$ (n = 3) and comparison to literature data. Filled circles; 10 L scale. Error bars represent 95 % confidence about the mean. Measurements performed as described in Section 2.4. (D) shows the angular velocity profile of the rocking platform over a single rock at different acceleration rates compared to a sinusoidal rocking platform. Solid line; 100 % acceleration, dashed line; 50 % acceleration, dotted line; Sinusoidal rocking platform.

3.2.5. Air Flowrate

Air flowrate is the volumetric flow rate of air entering the headspace of the rocked bag bioreactor, equivalent to an overlay in a stirred tank. Air flowrate was not found to have a significant effect on $k_La(O_2)$ (Fig.3.5A). At 0.015 vvm the $k_La(O_2)$ was 27.5±2.7 h^{-1} (n = 5) compared to 29.6±2.7 h^{-1} at 0.100vvm (n = 4). This difference was not found to be statistically significant (p = 0.13, regression analysis). This finding does, however, contradict Singh (1999), who found air flowrate to be the most important input for $k_La(O_2)$, but is supported by Yuk *et al.* (2011), who also found air flowrate to be insignificant for oxygen transfer in a cell-free environment. Under cell culture conditions a reasonable air flowrate would still be necessary to

replenish the O_2 consumed by the cells, CO_2 stripping, additional control gas turnover and bag pressure maintenance.

Air flowrate was not found to have a significant effect on mixing time (Fig.3.5B); at 0.0 and 0.1vvm, the mixing time was 10.4±3.2 s and 11.0±4.3 s respectively, regression analysis showed no significant relationship: p=0.72. This rules out any significant disturbance of the fluid surface as a result of air flow which might be affecting liquid flow patterns.

Air flowrate was, however, found to have a linear effect on $k_La(CO_2)$ (Fig.3.5C). This is to be expected, given that CO_2 mass transfer is typically limited by the gas phase turnover rather than the interfacial area available at typical cell culture energy inputs (Sieblist *et al.* 2011). At the centre point conditions investigated, the $k_La(CO_2)$ was approximately 1.2 h^{-1}. Given that CHO cells consume O_2 and produce CO_2 at approximately the same rate (Goudar *et al.* 2011), the CO_2 stripping rate is surprisingly low compared to the oxygen transfer rate (7.5 h^{-1} at standard conditions). However, characterisation of a 50 L Cultibag (SUB) stirred tank (Section 2.2.1.2) indicates that at a given volumetric air flowrate, the $k_La(CO_2)$ are very similar in this stirred tank to the rocked bag (Fig.3.5C).

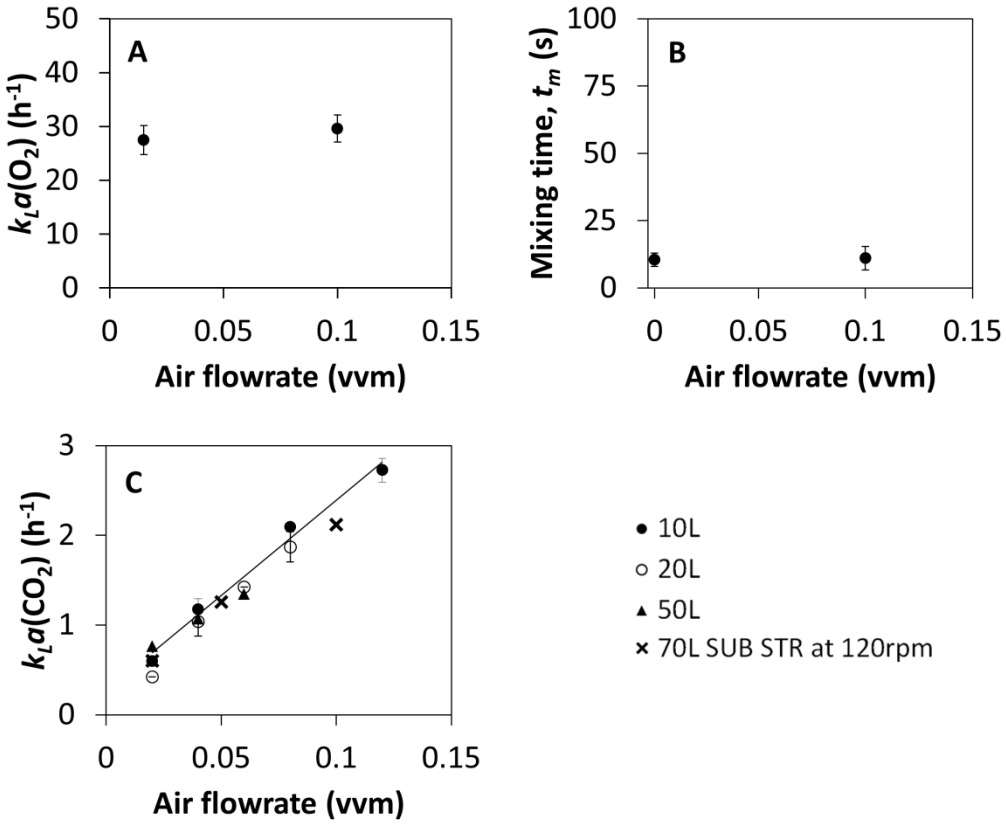

Figure 3.5: Effect of air flowrate on (A) volumetric oxygen mass transfer coefficient, $k_La(O_2)$ (n = 3), (B) fluid mixing time, t_m (n = 5), (C) volumetric CO_2 mass transfer coefficient, $k_La(CO_2)$ (n = 3 at 10 L, n = 2 at 20 L and n = 1 at 50 L) and comparison to 70L SUB data (n = 1). Filled circles; 10 L scale, open circles; 20 L scale, filled triangles; 50 L scale, crosses; 70L SUB STR (Section 2.2.1.2). Error bars represent 95 % confidence about the mean. Solid lines fitted by linear regression, (C) Internal data R^2 = 0.97. Measurements performed as described in Section 2.4.

3.2.6. Summary of Bioreactor Engineering Characterisation

Based on the findings in Sections 3.2.1 to 3.2.5 it can be concluded that rocking rate had the most significant effect on both $k_La(O_2)$ (Fig.3.1A) and mixing time (Fig 3.1B). From 15 to 25 min^{-1}, the $k_La(O_2)$ increases rapidly by over 5-fold. Similarly, increasing the rocking rate from 15 to 25 min^{-1} results in a 3.4-fold reduction in mixing time. Fill volume also had a significant effect on the $k_La(O_2)$ (Fig.3.3A), reducing the fill volume from 50 to 20 % resulted in a 3-fold increase in $k_La(O_2)$. Air flowrate was the most significant input in determining the $k_La(CO_2)$, producing a 4.5-fold increase in rate from 0.02 to 0.12 vvm (Fig.3.5C).

Moderate effects were observed from adjustments in the rocking angle, which had a linear proportional positive effect on $k_La(O_2)$ and negative effect on mixing time when adjusted from 6 to 13^o (Fig.3.2A & 3.2B respectively). Fill volume had an approximately proportional effect on mixing time with mixing times falling by 50 % in response to a reduction from 50 to 30 % fill volume (Fig.3.3A & 3.3B respectively).

Reducing the rocking platform acceleration from 100 to 50 % was found to increase the $k_La(O_2)$ by 27 % (Fig.3.4A). Likewise, rocking acceleration was not found to affect the mixing time or $k_La(CO_2)$ (Fig.3.4B & C). Increasing the rocking rate from 15 to 25 min^{-1} resulted in a 19 % increase in $k_La(CO_2)$ (Fig.3.1C) while reducing the fill volume from 50 to 30 % increased the $k_La(CO_2)$ by 17 % (Fig.3.3C). Rocking acceleration and rocking angle did not have measurable effects on the $k_La(CO_2)$ (Fig.3.4C). No effect on $k_La(O_2)$ or mixing time was observed from adjusting the air flowrate (Fig.3.5A & B).

3.2.7. Impact of Scale

Rocked bags are currently available from a variety of manufacturers at scales between 2 to 1,000 L total volume. It is important to understand how the physical environment within a bioreactor changes with scale if cell culture processes are to be rationally scaled-up. Data obtained here on rocked bags between 10 to 50 L scale was included in Figs 3.1 to 3.5.

The rate of oxygen mass transfer with respect to agitation inputs was found to behave identically in both 10 L and 20 L bags (Fig.3.1A); this is believed to be due to the very similar geometry. The 20 L bag is scaled-up from the 10 L bag by width alone, which means that the flow length, fluid depth and fluid surface area to volume ratio are all unchanged as indicated in Fig.2.1. Since there is no sparged dispersed gas phase, the fluid surface is responsible for gas transfer and therefore if this is maintained relative to volume, the gas transfer would be expected to be similar.

Comparison with other work, using rocked bags from other manufacturers (Yuk *et al.* 2011; Mikola *et al.* 2007), shows that at a given rocking rate, $k_La(O_2)$ values in 2-50 L bags rarely deviate by more than 20 % (Fig.3.1A). This is used to build a model which is tested in Section 6.2.1. The 50 L bag is scaled up from the 20 L bag in three dimensions, and the surface area to volume ratio at rest is 43% lower than the 10 and 20 L bags. This is reflected in the $k_La(O_2)$ falling by 40-50 % at a given rocking rate compared to the smaller scales. The exception to this is at 15 min^{-1}, where an unexpected phenomenon was observed. The slow rocking interacted with the ripples of the bag surface to generate a larger wave than that observed at 20 min^{-1}, this entrained gas and repeatedly produced significantly higher oxygen $k_La(O_2)$ at 15 than at 20 min^{-1}.

In contrast to oxygen transfer rates, mixing time was found to change dramatically with bag size (Fig.3.1B). At twice the fluid volume, the mixing time was approximately doubled (60-140 % greater at 20 L versus 10 L bag scale). This trend continued up to 50 L bag scale, with mixing times being 3 to 7-fold greater at 50 L compared to 10 L. It has previously been suggested that the rocked bag may have poor lateral mixing (Mikola *et al.* 2007) and since the bag here is being scaled up from 10 L to 20 L entirely in the lateral dimension, this may be highlighting a weakness in the rocked bag agitation regime. This does not explain the continued trend up to 50 L scale, where the bag is scaled in 3 dimensions. The recorded mixing times are very unlikely to affect cell culture performance over the scales characterised. Assuming this trend continues, however, this apparent lack of scalability could have implications at larger scale. Singh (1999) also noted a similarly significant 6 to 12-fold increase in mixing time from a 10-fold scale increase.

The $k_La(CO_2)$ showed no measureable change with scale (Fig.3.5C). This could be predicted from its dependencies measured at 10 L bag scale. The only input that was found to significantly affect CO_2 stripping was the volumetric air flowrate, and since this can be easily scaled over this range, it is possible to maintain the $k_La(CO_2)$ or CO_2 stripping of the bag at 10 and 50 L bag scale.

For the measurements at larger scale, fewer replicate readings were performed. At 10L scale, based on triplicate readings for $k_La(O_2)$,the coefficient of variance was on average, 5% for rocking rate, 2% for rocking angle and 5% for fill volume. For $k_La(CO_2)$, at 10L scale, based on triplicate readings, the coefficient of variance was on average, 6% for air flowrate. Given these low experimental errors, it was considered efficient to use duplicate readings at larger scale (20 and 50L bags) for the $k_La(O_2)$ and single for the $k_La(CO_2)$ readings. Because of the higher variability of mixing time readings (Coefficient of variance for rocking rate at 10L scale was 28%), quintuplicate readings were maintained at all scales.

3.3. Impact on Cell Culture Kinetics

Key findings from the engineering characterisation studies in Section 3.2 were subsequently used to design fed-batch cell culture conditions to examine the impact of rocking conditions on cell culture performance. At 10 L bag scale, mixing time would not be a concern regardless of experimental setup, since within ranges where cell culture is feasible from an oxygen transfer perspective, the mixing times were well within the normal ranges for cell culture (Fig.3.1B, 3.2B, 3.3B, 3.4B & 3.5B). Secondly, because of the lack of a sparged gas phase, there are no caveats associated with setting an air flowrate sufficient for CO_2 stripping (Fig.3.5C). Regarding oxygen transfer, the formation of bubbles at relatively low rocking rates and therefore low $k_La(O_2)$ was of interest, since it challenged whether bubble-free cell culture would be feasible in a rocked bag system. This led to the operation of the bag at a low rocking rate of 15 min^{-1}. To test how well the cell culture performed at higher rocking rates when there was a significant entrained gas phase, the bag was operated at a high rocking rate of 25 min^{-1}. Finally, repeated cell cultures were performed at an intermediate rocking rate of 20 min^{-1}, to check if there was an optimum between these two points and to establish the consistency of the process. For this work, cell line A was used (Section 2.1). This is a stably transfected GS-CHO suspended cell line producing a whole IgG_4 product molecule. Production cultures of this cell line were operated in a bolus fed-batch mode at 37^{o}C and pH 7.1±0.05 for 14 days. Bioreactors are seeded from shake flasks with cells in mid-exponential phase at passage 15-20 (Section 2.2.1).

In terms of viable cell count (Fig.3.6A), the cell cultures performed at the standard rocking rate of 20 min^{-1} were very consistent up until the onset of death phase (~200 h), where the 95% confidence boundaries move apart. The cells reached a maximum viable cell count (VCC; Section 2.3.3.1) of on average 10.5 $\times 10^6$cells.mL^{-1} and maintained a viability above 75 % until harvest at 335 h. The higher variation in the VCC and cell viability after 200 h is due to a combination of small differences in the timing of the transition from stationary to death phase and less precise cell counting in the latter part of the cell culture. Comparison with the cultures at different rocking rates shows that the viable cell counts and viabilities never deviated by a significant margin from the standard runs at 20 min^{-1}.

The integrated viable cell count (Fig.3.6B) shows that cumulatively, by the end of the cultures, there were more cells present over the course of the cell culture at 25 compared to at 15 min^{-1} respectively, albeit by a small (12 %) margin compared to the standard cultures. Antibody productivity also showed subtle differences, with the culture at 15 min^{-1} producing a 15 % higher harvest antibody titre of 0.78 gL^{-1} (Fig.3.6C) and 19 % higher cell specific productivity of 9 pg.$cell^{-1}$.day^{-1} (Fig.3.6D) than the very similar values produced at 20 and 25 min^{-1}.

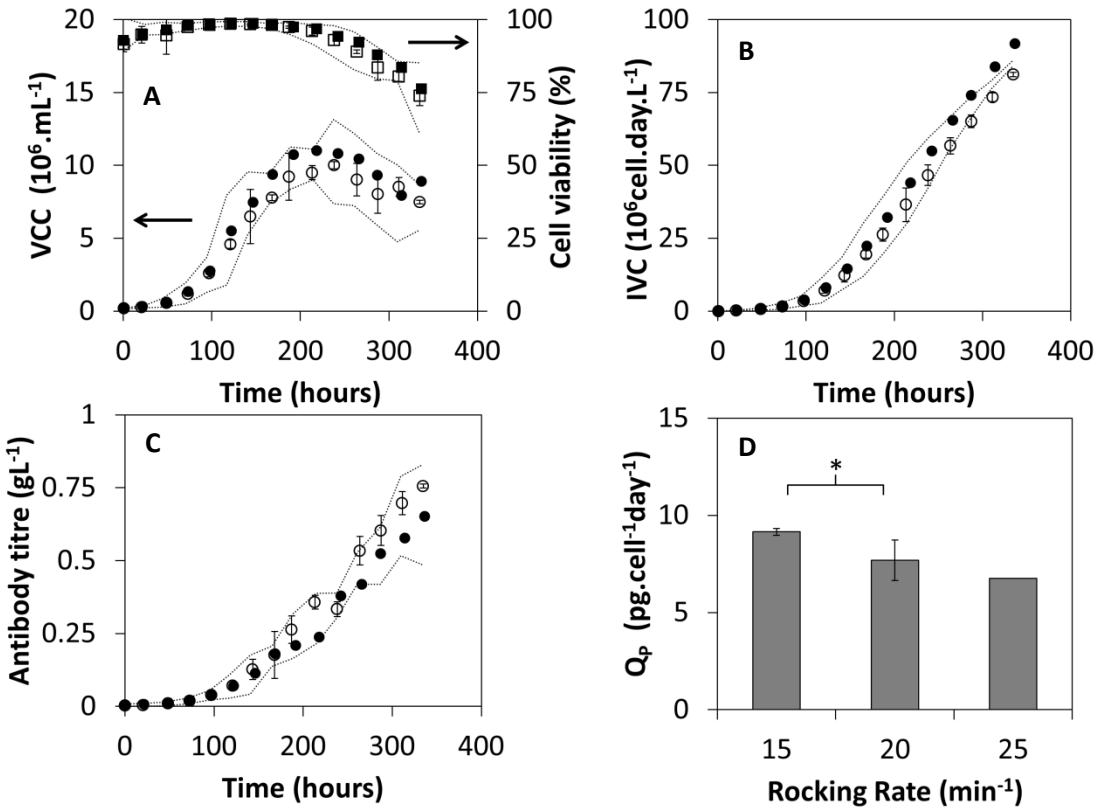

Figure 3.6: Fed-batch cell culture kinetics for cultures performed at different rocking rates: open symbols; 15 min^{-1} (n = 2); filled symbols; 25 min^{-1} (n = 1). (A) viable cell count (circles) and cell viability (squares) over time; (B) integrated viable cell count over time (Section 2.3.3.1); (C) antibody titre over time and (D) cell specific productivity (Section 2.3.3.2). Dotted lines represent 95 % confidence boundaries based on three cultures at a standard rocking rate of 20 min^{-1}. Error bars represent 95 % confidence about the mean. *p = 0.036, *t*-test, Section 2.4.1. Cell cultures performed as described in Section 2.2.1.

While the cell counts and antibody titre were similar across all runs, bigger variations were found in other indicators of cell culture performance notably in metabolite concentrations. In terms of cell size (Fig.3.7A), which has been inversely related to energy dissipation rate (Godoy-Silva *et al.* 2009), the modal diameter of the cells cultured at 20 and 25 min^{-1} fell from 15 µm at inoculation to 13 µm over the first 150 h of the culture before increasing to 18 µm at harvest. Larger cells may be more prone to cell damage based on the Kolmogorov theory of energy dissipation based on eddy size (Papoutsakis 1991). The specific glucose consumption rate of the cells cultured at 15 min^{-1} was significantly higher than at 20 and 25 min^{-1} (Fig.3.7B). While the runs at 20 and 25 min^{-1} showed very small net changes in lactate concentration (Fig.3.7C) over the last half of the cell culture. Lactate continued to accumulate throughout the run conducted at 15 min^{-1}, resulting in a final lactate concentration of 4.8 gL^{-1}, compared to 3.2 gL^{-1} and 2.6 gL^{-1} at 25 and 20 min^{-1} respectively. A similar trend was noticed with ammonium concentration, again resulting in a 100 % higher peak value at the lower rocking rate (Fig.3.7D).

Glucose consumption and lactate production have not previously been found to be affected by even significant changes in hydrodynamic stress in bioreactors when using suspended CHO cells (Sieck *et al.* 2013; Godoy-Silva *et al.* 2009). These observations bear similarity to G1 cell cycle arrest data shown by Carvalhal *et al.* (2003) in which p27 overexpression in adherent CHO cells led to higher cell specific productivity alongside higher specific oxygen, glucose and glutamine consumption rates and higher lactate and ammonium production rates.

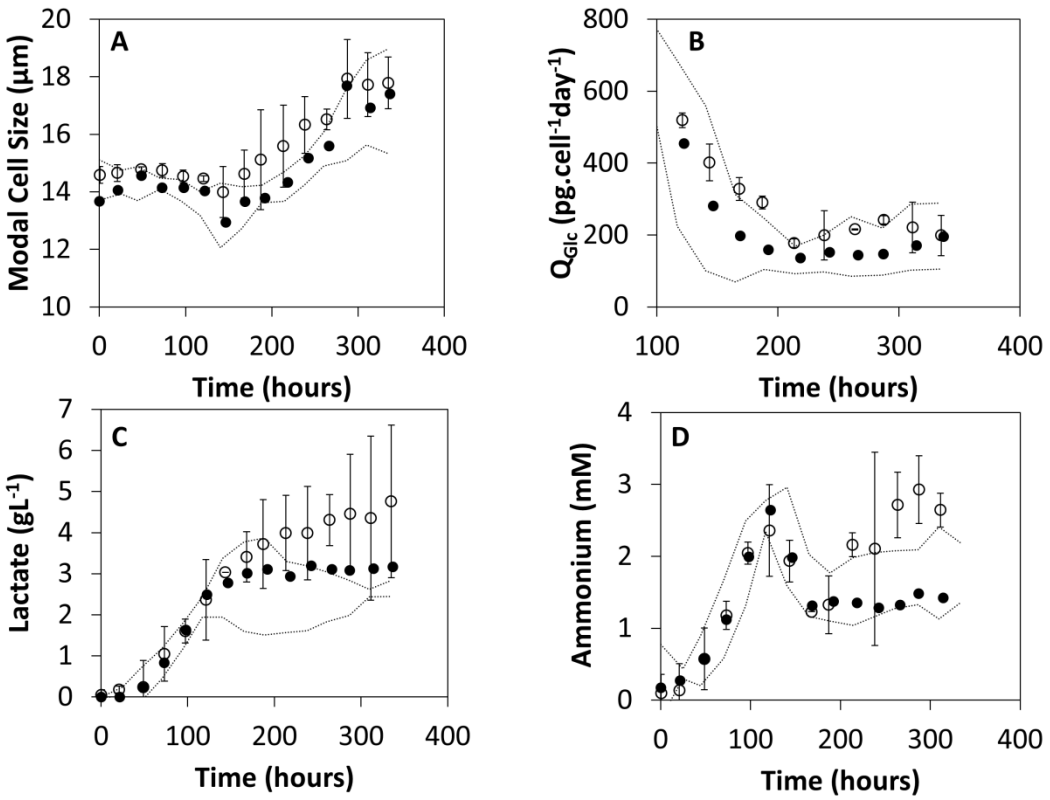

Figure 3.7: Cell culture metabolite and cell size profiles for cultures operated at different rocking rates: open circles; 15 min^{-1} (n = 2); filled circles; 25 min^{-1} (n = 1). (A) modal cell size, (B) specific glucose consumption rate, Q_{Glc} , (C) lactate concentration and (D) ammonium concentration. Dotted lines represent 95 % confidence boundaries based on three cultures at a standard rocking rate of 20min^{-1}. Error bars represent 95% confidence about the mean. Cultures performed as described in Fig. 3.4.

As a consequence of the lower OTR and lower mixing efficiency at the lower rocking rate it was found that more control substances (oxygen, base and CO_2) had to be added to the bioreactor by the control loop to maintain set point values for pH and DO (Fig.3.8). While 6 L of pure oxygen were mixed into the gas inlet over the course of the cell culture to maintain the DO setpoint of the standard culture at 20 min^{-1}, >900 L had to be added at the lower rocking rate of 15 min^{-1}. A significant proportion of this addition occurred directly after the daily feeds, where the DO would fall to below the 30 % air saturation set point for up to an hour, falling below 20 % on five occasions. In this case the agitation regime was not providing a sufficiently high $k_La(O_2)$ for adequate bioreactor DO control. Additionally, approximately double the volume of base was added to the culture at the lower

rocking rate. This is likely due to a combination of the extra lactate production of the cells (Fig.3.7C), the extra CO_2 production from the larger feeds necessitated by the greater glucose consumption and the slightly reduced CO_2 stripping capability (Fig.3.1C) at 15 min^{-1} compared to at 20 min^{-1}. CO_2 addition over the cell culture was 17% higher at 25 min^{-1} vs. 15 min^{-1}. The majority of the CO_2 is added by the control system over the first 75-100 h of the culture to compensate for the CO_2 stripped from the liquid phase by the constant air flowrate. This 17 % additional CO_2 added at a rocking rate of 25 compared to 15 min^{-1} (Fig.3.8) supports the measured CO_2 stripping rate, $k_La(CO_2)$, being 19 % higher (Fig.3.1C).

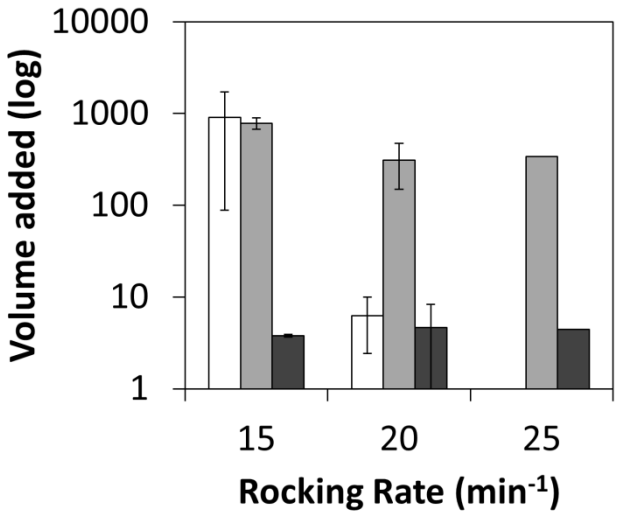

Figure 3.8: Total volume addition of control substances for culture duration performed at different rocking rates as shown in Fig. 3.4. White bars are 0.1 M Sodium Bicarbonate addition (mL), grey bars are O_2 addition (L) and black bars are CO_2 addition (L). Error bars represent 95 % confidence about the mean, n = 2 at 15 min^{-1}, n = 3 at 20 min^{-1} and n = 1 at 25 min^{-1}.

3.3.1. Impact on Mechanical Robustness of Cells at Harvest

The mechanical robustness of cells produced at the different rocking rates with different levels of dispersed gas was also investigated. This is important because cell mechanical robustness at harvest will impact upon the clarification performance over primary recovery unit operations (Tait *et al.* 2013). For comparison, the same cell line was cultured in a 50 L SUB STR operated as in Section 2.2.1.2 and harvested at the same cell viability. For pH and DO control in

the SUB, gas is sparged from an 8 hole 0.9 mm horse-shoe sparger at 2.5 L.min^{-1} beneath two downward pumping impellers, so this system has a permanent dispersed gas phase. In terms of cell culture kinetics, this bioreactor performed within the boundaries established by the triplicate runs at 20 min^{-1} in the rocked bag, which are reproduced in Fig.3.9.

Fig.3.10 shows the particle size distribution of the material from the 15 min^{-1} run (white bars) compared to that at 25 min^{-1} (black bars) and material from a 50 L SUB SUB after being exposed to different levels of energy dissipation rate indicative of levels experienced in large scale centrifuges (Hutchinson *et al.* 2006). Comparing the particle size distributions at 1.9 x10^{4} Wkg^{-1} (Fig.3.10A), indicative of a low shear centrifuge with an hermetically sealed feed zone, the 15 min^{-1} culture material produces 30 % more <5 µm particles than the material from the 25 min^{-1} culture or from the stirred tank. This suggests that the 15 min^{-1} material is more susceptible to shear-induced damaged under reasonable processing conditions.

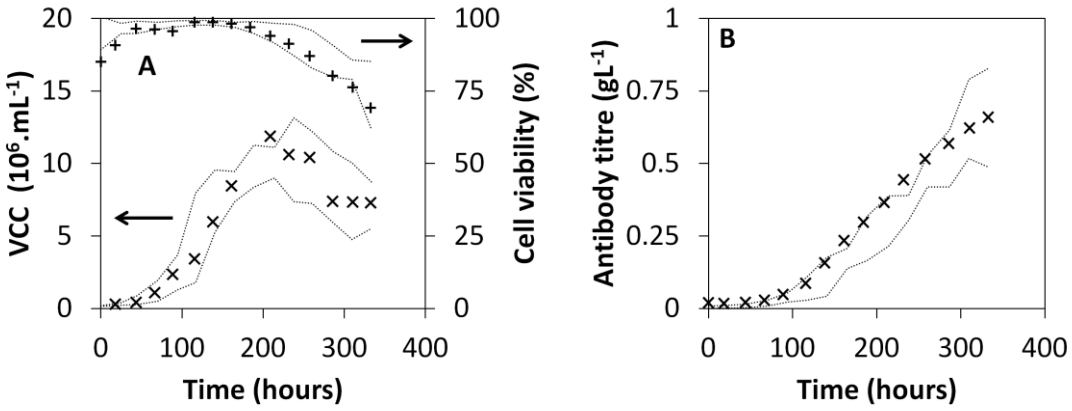

Figure 3.9: Fed-batch cell culture kinetics for a 50 L SUB STR (Section 2.2.1.2) compared to intermediate (20 min^{-1} rocking rate) rocked bag data presented in Fig.3.6. (A) diagonal crosses; viable cell count, crosses; cell viability, (B) antibody titre. Dotted lines represent 95 % confidence boundaries based on three cultures at a standard rocking rate of 20 min^{-1}. Cell culture in the 50 L SUB STR was performed as described in Section 2.2.1 (n=1).

At the higher energy dissipation rate of 3.7 x10^5 Wkg^{-1} (Fig. 3.8B), equivalent to a 'high shear' centrifuge, there is also clearly a population of viable cells remaining from the 25 min^{-1} rocked bag and SUB culture that is not present for the 15 min^{-1} material. This again suggests that at equivalent levels of hydrodynamic shear the cell produced in the cultures rocked at 15 min^{-1} are less mechanically robust than those produced in rocked bags or stirred tanks with an entrained gas phase. As described in Section 1.4.2, the energetic bursting of bubbles entrained in a liquid is believed to be a major source of hydrodynamic shear stress. Operating rocked bags at rocking rates which entrain gas into the liquid is likely to contribute significantly to the shear stress experienced by the cells. This may cause adaptation of the cells to the environment. These adaptations may come at the cost of some protein productivity but produce cells better able to withstand the high hydrodynamic stress levels experienced during primary recovery. Further investigation of the cell biological and product quality impacts of the presence of a dispersed gas phase is conducted in Chapters 5 and 6.

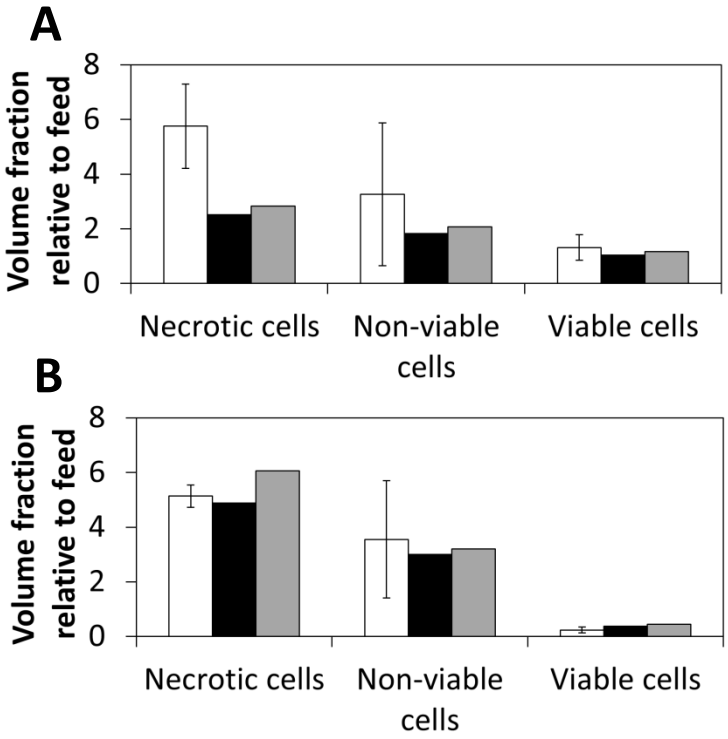

Figure 3.10: Particle size distributions of harvested material showing the extent of cell damage for cultures performed at different rocking rates: 15 min^{-1} rocked bag (white bars, n = 2), 25 min^{-1} rocked bag (black bars, n = 3) and stirred 50 L SUB (grey bars, n = 1). Volume fraction of necrotic cells/cell debris (<7 µm), Non-viable cells (7-12.5 µm) and viable cells (12.5-40 µm) relative to un-sheared feed material after exposure to (A) 1.9 $x10^4$ Wkg^{-1} and (B) 3.7 $x10^5$ Wkg^{-1}. Cell cultures kinetics are described in Fig.3.6. Cells exposed to different levels of shear as described in Section 2.3.4.

3.4. Summary

As described in Section 3.1, the aim of this chapter was to characterise the rocked bag and evaluate the effect of different agitation inputs on cell culture performance. The experimental results obtained have shown that when establishing conditions for rocked bag cell cultures, the overriding design consideration is the rocking rate. This has been found to have the greatest influence on the oxygen mass transfer rate (Fig 3.1A) and the liquid homogeneity (Fig 3.2A). Higher rocking rates increase fluid mixing efficiency in a linear manner and above a critical rocking rate, which for the system studied here was 20 min^{-1}, gas is entrained into the liquid as the rocking platform changes direction. This entrainment of gas causes the oxygen mass transfer rate to rise rapidly above this critical rocking rate (Fig.3.1A). CO_2 stripping rate appears to be decoupled from

oxygen transfer and liquid mixing and rises proportionately with overlay air flowrate (Fig 3.3D). A further objective was to understand the effect of scale increase on the mass transfer and mixing times within the rocked bag. As shown in Fig 3.1A, oxygen transfer was found to decrease at a rate proportional to the surface area to volume ratio, while mixing times increased proportionately with liquid volume (Fig.3.1B). CO_2 stripping rate was conserved at all scales tested by maintaining the volumetric gas flowrate (Fig.3.5C).

In terms of the objective of examining the impact of changing the most rocking rate (found to be the most important engineering input) on cell culture performance, it was found that operating the rocked bag above and below this critical gas entrainment rocking rate resulted in different cell culture kinetics. Cells cultured in a bubble free environment at 15 min^{-1}, were 19% more specifically productive (Fig.3.6D), consumed more glucose (Fig.3.7B) and produced 50 % more lactate (Fig.3.7C) and 100 % more ammonium (Fig.3.7D) with identical growth and viability profiles compared to cells cultured at 25 min^{-1} (Fig.3.6D).

The comparison of the mechanical robustness of cells cultured in rocked bags at different rocking rates to cells cultured in a stirred tank bioreactor showed significant differences in response to rocking rate. Exposure of the cell broth from rocked bags with and without a dispersed gas phase as well as a control 50 L SUB STR to shear stress equivalent to an hermetically sealed centrifuge resulted in significant differences in the particle size distribution (Fig.3.10). Cells cultured at 15 min^{-1} underwent a 5.8-fold increase in cell debris below 7 µm after exposure, compared to a 2.5 and 2.8-fold increase for the cells from a 25 min^{-1} bag and SUB respectively, indicating that cells cultured in a bubble free environment may be more fragile during subsequent processing.

The impact of the dispersed gas phase on cell phenotype and transcriptome and the quality attributes of the antibody produced will be studied further in Chapters 5 and 6 respectively. However, in Chapter 4, a more detailed characterisation of bioreactor fluid dynamics at different rocking rates will be performed.

Chapter 4. Detailed Fluid Dynamic Characterisation of a Rocked Bag Bioreactor

4.1. Introduction and Aim

In the previous chapter, physical characterisation of a rocked bag bioreactor at multiple scales revealed significant changes in oxygen mass transfer in response to changes in rocking rate (Fig.3.1A). The volumetric oxygen mass transfer coefficients achieved at lab scale in the rocked bag were found to be similar to those achieved in more conventional bioreactor designs such as stirred tanks. It was therefore considered important to further investigate the basis for some of the phenomena observed. In the case of gas mass transfer, it was found that there was a rocking rate beyond which bubbles became entrained in the gas phase and the volumetric gas transfer coefficient increased rapidly. In contrast, it was also found that there was an apparent linear relationship between fluid mixing time and rocking rate (Fig.3.1B). A fundamental understanding of the fluid dynamics within the bag as it rocks will provide a basis for the effective selection of rocked bag bioreactor operating conditions for different applications.

As discussed in Section 1.15.1, fluid dynamics are known to have an impact on cell culture performance (Schmalzriedt *et al.* 2003; Marks 2003). Increased understanding of the fluid flow characteristics of bioreactors results in improved efficiency in their utilisation (Barrett *et al.* 2009; Micheletti *et al.* 2006). If the fluid dynamic conditions are too turbulent, especially in the presence of bubbles (Chisti 2000), this can result in shear stress effects which negatively impact on the cell density and cell viability attained (Oh *et al.* 1992). Poor mixing leads to inhomogeneity, which exposes cells to fluctuations in pH, DO, nutrient and toxin concentrations which can increase cell death (Section 1.4.1).

There is currently little understanding of rocked bags from a fluid dynamic standpoint, especially under suspension cell culture conditions (Section 1.13.5). Modelling work based on characteristic length of the bag supported by mixing time measurements has been carried out by Eibl *et al.* (2009), which estimates that

rocking rate and fill volume are important inputs and that bag geometry and scale could also significantly impact upon the fluid dynamics. Velocity measurements have been made at five points and used to validate CFD models for 2 and 20 L bags (Oncül *et al.* 2010). It was found that under what the authors described as 'laminar conditions' at low rocking rates (15 min^{-1}), liquid velocities fluctuated between 0 and 0.2 ms^{-1} in a 2L bag and between 0 and 0.6 ms^{-1} in a 20L bag over the course of the rock. The greatest velocities were measured towards the centre of the bag longitudinally with very little lateral gradient in velocity. Further work was conducted using the same system with 19 probe mounting points (Kalmbach *et al.* 2011), which measured low shear stress values (<0.2 Pa) and increased velocity fluctuation at 20 L compared to 2 L scale.

However, the actual flow pattern, as well as the basis for generating the wave observed under certain rocking configurations has not yet been described. The aim of this chapter is to use Particle Image Velocimetry (PIV) to measure the 2-Dimensional (2-D) phase resolved longitudinal vector field over the course of the rock over a range of rocking rates, which were previously found to have the largest impact on liquid homogeneity (Section 3.2.6). This will allow quantification of fluid velocity, turbulence and shear stress over the course of the rocking cycle (Section 4.2). Additionally, the bulk fluid position and conformation with respect to the rocking position will be measured at high temporal resolution using a novel technique. These techniques will be used together to explain the basis for wave formation observed in Section 3.2.1.

The specific objectives are as follows:

- To design and construct a precise, 3D mimic of a rocked back suitable for laser-based PIV investigation.
- To describe the 2-Dimensional fluid dynamics in a lab scale rocked bag over the course of the rock at several rocking speeds.
- To investigate the source of the wave formation observed at higher rocking speeds in Section 3.2.1.

- To understand the basis for bulk fluid movement as a function of bag movement, with reference to the fluid and bag phase.

4.2. Extraction of Fluid Dynamic values from PIV data

In a steady turbulent system, the instantaneous velocity of the x component of the flow at any point (U_i) can be described by Equation 4.1,

$$U_i = \bar{u}_i + u_i' \quad (4.1)$$

where $\bar{u}_i$ is the mean vector and u_i' is the fluctuation from that mean vector due to turbulence. This value of U_i in two or three dimensions can be accurately measured by PIV, as described in Section 1.14.3, and this, constitutes the vector length, or the speed of flow in a given area.

Using PIV, the value of $\bar{u}_i$ and consequently u_i' can be obtained. With these turbulent fluctuations, advanced fluid dynamic properties can be extracted from the flow.

Turbulence kinetic energy is a measure of the energy being dissipated by eddies in turbulent flow and is measured by using the root mean square ($\tilde{u}$) of the instantaneous fluctuations in velocity: u_i', u_j' and u_k' in the following equation

$$k = \frac{1}{2}\left(\tilde{u}_i{}^2 + \tilde{u}_j{}^2 + \tilde{u}_k{}^2\right) \quad (4.2)$$

When using 2-D PIV, $\tilde{u}_k$ cannot be accurately measured, and an assumption of isotropic velocity is made, therefore the equation becomes:

$$k = \frac{3}{4}\left(\tilde{u}_i{}^2 + \tilde{u}_j{}^2\right) \quad (4.3)$$

Shear stress is a measure of the level of mechanical stresses within the fluid and can be related to cell damage (Papoutsakis 1991; Tanzeglock *et al.* 2009; Chisti 2000). When estimating shear in a turbulently mixed bioreactor, the level of laminar shear is negligible compared to that generated by the turbulent

fluctuations in the flow. Therefore shear stress (τ) can be estimated by the following equation:

$$\tau = -\rho\overline{u_\iota{}' u_j{}'} \quad (4.4)$$

where ρ is the density of the fluid.

The most basic method for evaluating energy dissipation into the fluid is to use the direct evaluation method (Sharp & Adrian 2001). This method measures the gradients in instantaneous velocity in all dimensions, the isotropic assumption is again employed (Atta 1991).

$$(\varepsilon_T)_{DE} = \nu\left(2\overline{\left(\frac{\delta u_i{}'}{\delta x}\right)^2} + 2\overline{\left(\frac{\delta u_j{}'}{\delta y}\right)^2} + 3\overline{\left(\frac{\delta u_j{}'}{\delta x}\right)^2} + 3\overline{\left(\frac{\partial u_\iota{}'}{\partial y}\right)^2} + 2\overline{\frac{\delta u_i{}'}{\delta y}\,\frac{\delta u_j{}'}{\delta x}}\right) \quad (4.5)$$

This gives an indication of the rate of viscous dissipation of mechanical energy in the turbulent motion. However, this does not account for the limits of the resolution of the technique being used, so the solutions are always significant underestimates (Gabriele *et al.* 2009). The application of this method is informative, since it gives a baseline against which other methods of energy dissipation can be measured.

A more accurate quantification of the energy being dissipated can be estimated using the Smagorinsky closure model (Khan 2005) as given in Equation 4.6.

$$(\varepsilon_T)_{SGS} = (C_s\Delta)^2\left(4\overline{\left(\frac{\delta u_i{}'}{\delta x}\right)^2} + 4\overline{\left(\frac{\delta u_j{}'}{\delta y}\right)^2} + 2\overline{\left(\frac{\delta u_j{}'}{\delta x}\right)^2} + 2\overline{\left(\frac{\delta u_i{}'}{\delta y}\right)}\right)^{\frac{3}{2}} \quad (4.6)$$

This attempts to account for the resolution of the technique being used for acquisition. In this case of PIV, the resolution is approximately 0.5-1mm (Gabriele *et al.* 2009, Li *et al.* 2013), which is well above the expected Kolmogorov scale of 50μm, and therefore not able to truly resolve such structures. Δ is the *filter width*, which in this case is the resolution of the velocity measurement. C_s is the Smagorinsky constant, which is usually between 0.1 and 0.2, a typical value for bioreactors is 0.173 (Gabriele *et al.* 2009).

It has been hypothesised that cell damage is likely to occur when the size of the smallest eddies, those responsible for dissipating the energy input by the impeller, are in the same scale as the cell diameter (Papoutsakis 1991).

An estimate for the length scale of the Kolmogorov eddies in metres can be obtained by:

$$\eta = \left(\frac{v^3}{\varepsilon}\right)^{\frac{1}{4}} \quad (4.7)$$

Using the previously calculated estimate for ε, and the kinematic viscosity v of the liquid is known, the scale of the Kolmogorov eddies can be estimated.

4.3. Development of a Rocked Bag and Rocking Platform Mimics

As described in Section 4.1 the first objective of this work was to design a system which would allow PIV to be applied to a rocked bag or rocked bag like system. PIV requires two planes of optical accessibility to operate; one ideally parallel to the axis of greatest velocity for the laser sheet to be fired along and one perpendicular to that, for the camera to observe the advancement of the tracer particles within the laser sheet. Rocked bags are not well suited to optical analysis due to their translucency, irregular geometry and bulky agitation apparatus as shown in Fig.2.1A and 2.6. As a result, it was decided that a mimic rocked bag would need to be fabricated in order to apply PIV to this geometry. Typically, when evaluating stirred tank bioreactors using PIV, they are submerged in water in a cuboidal tank to reduce distortion of the image by refraction (Odeleye *et al.* 2014). Given the rocking motion of bags, such an apparatus would be unfeasibly heavy and the movement of the water around the bag would be very likely to move the bag itself and interfere with the readings. Cutting the bag longitudinally in two and adding a flat transparent plate to the bag to allow side-on optical accessibility was initially considered. This would allow excellent optical accessibility in one plane, but not in a second, and there would also be potential for interference in fluid velocities from the geometric alteration of the bag.

The final design chosen, however, was a solid structural mimic of the rocked bag was fabricated from poly(methyl methacrylate) (PMMA, Perspex) as shown in Fig.2.7. This would allow 2 planes of good optical accessibility of the bag, while conserving its exact geometry. Machining out the precise internal shape of the bag from two cuboids of PMMA produced a transparent and optically accessible geometric replica of the bag with minimal refraction due to the regular outer geometry. Using a solid to mimic an inflated bag was considered reasonable given the previous observation that the surface of even large bags moves less than 1 mm during rocking (Oncul *et al.* 2009). A plaster of Paris cast of the rocked bag was made and the 3D geometry of this was digitised and was used in conjuction with a computer numerical control (CNC) milling machine to machine out two cuboids of PMMA to the precise shape of the rocked bag. See Section 2.5.2 for details of the fabrication of this mimic.

The second challenge was the rocking platform. It was determined that the laser would need optical access from below to provide the best illumination of the tracer particles flowing longitudinally within the bag. The laser could not be fired from above the bag because the free surface of the fluid would scatter the laser light, which would reduce the precision and intensity of the plane of acquisition. Off the shelf rocking platform designs mount the bag above a horizontal sheet of stainless steel, which is itself rocked from directly beneath by a motor which precludes the desired laser position. Additionally, the commercial rocking platform did not have sufficient space for the mounting of a high speed camera. Finally, for phase resolved PIV, there needs to be a timing signal which synchronises the laser firing and camera acquisition to a precise point in the rocking cycle to support the 500 repeats typically taken, the rocking platforms used with off the shelf bags do not provide an effective way to precisely mount a trigger. As with the bag, it was necessary to fabricate a bespoke rocking platform. Using a 'skeletal' design, a mimic rocking platform was built which elevated the bag by approximately 400 mm, allowing the laser to be mounted below as described in Section 2.5.2. This platform was also larger, and had a pin-board for the secure and precise mounting of the camera 'in-phase' with the bag as it rocked.

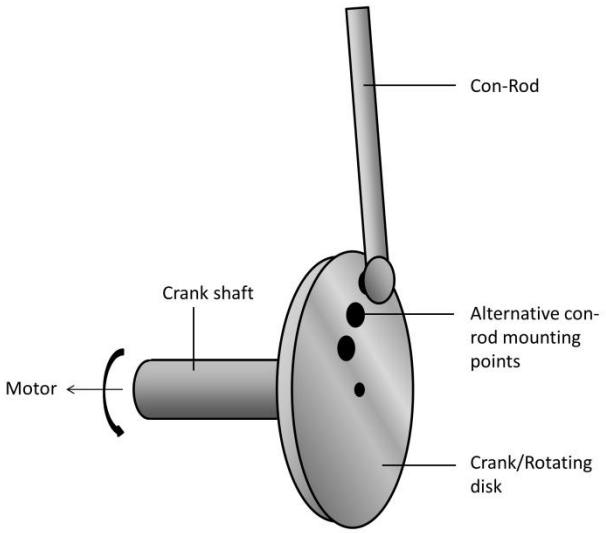

Figure 4.1: Schematic of the basis for the sinusoidal rocking of the platform. Motor speed can be used to adjust the rocking rate while adjusting radial mounting point of the con-rod on the crank adjusts the rocking angle.

The basis for the rocking motion used a rotating 'crank' to convert rotation from a motor into a vertical sinusoidal movement profile as shown in Fig.4.1. A key design specification was the relative positioning of the axis of rotation of the platform compared to the bag, since this was hypothesised to significantly affect the angles of forces acting during rocking. This platform provided adjustment of rocking rate and angle by adjusting the motor speed and con-rod radial position on a rotating disk being driven by the motor (Fig.4.1). The platform was initially specified with a motor capable of up to 100 revolutions or rocks per minute, however this could not provide consistent angular velocity at lower rocking rates and was replaced with an identical motor geared down to 50 min^{-1}. The rotating disk also had a cam to trigger a mechanical switch, but this was replaced with an optical sensor to allow more reliable and consistent triggering which could be adjusted to any point in the rocking cycle (Section 2.5.2). A photograph of the fully assembled system can be seen in Fig.4.2.

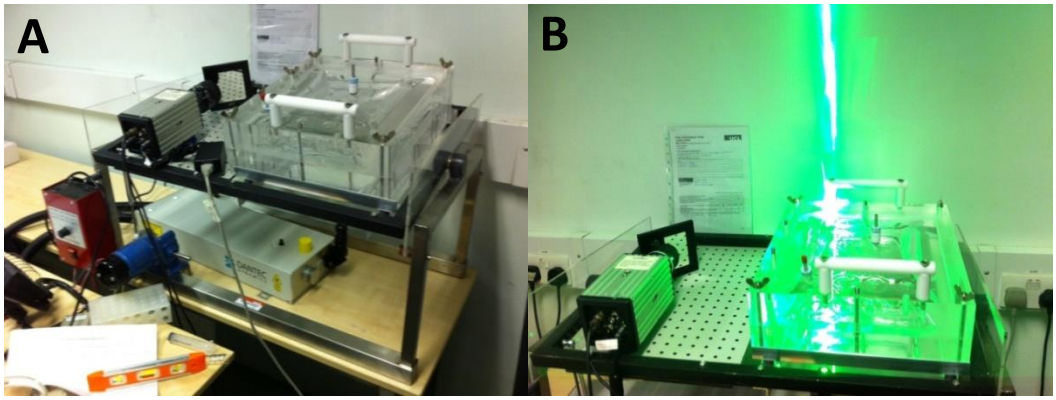

Figure 4.2: (A) Completed fully assembled mimic (Section 2.5) and (B) system in operation with laser firing vertically upwards. Fig.2.8 for schematic diagram.

4.4. Impact of Rocking Rate on Rocked Bag Fluid Velocity

Rocking rate (*N*) was found in Section 3.2.7 to have the most significant effect on the measured engineering parameters and was observed to have the greatest influence on fluid behaviour. There was a clear transition in the fluid from 'bubble-free' at lower rocking rates, to significant entrained gas at higher rocking rates. As a result, rocking rate was chosen as the primary rocked bag input to investigate in terms of its effect on the fluid dynamics. As described in Section 1.15.4, PIV requires high speed cameras, because image pairs need to be captured at small time intervals. Limitations with the high speed camera precluded rocking rates below 25 min^{-1} being investigated due to the camera (Nanosense Mk.II, Dantec Dynamics) not supporting time between image pair acquisition (Δ-t) of more than 3.15 ms. At lower rocking rates, fluid velocities are lower, which necessitates longer time intervals to capture movement of the tracer particles on a finite resolution sensor (Adrian 1997). An alternative camera (Speedsense, Dantec Dynamics) was tried, however this did not provide good image quality at mean frame capture rates *below* 30hz. In the rocked bag system, image pairs are captured once per rock (once every 2.4 s at N = 25 min^{-1}), however those image pairs need to be within 3.15 ms of one another. This makes PIV with such systems very demanding on the camera, since it needs to support a 3 log range of frame capture rates. The maximum rocking rate investigated was N = 42 min^{-1} because that is the highest rocking rate of any rocking platform currently available.

A description of the single-phase flow occurring inside the rocked bag mimic is provided in this section. In the first part, the analysis is carried out on the phase-resolved fluid flow during rocked motion at a range of rocking speeds (*N* = 25, 33.5 and 42 min^{-1}). An analysis of the results obtained and comparisons with previous works, is then presented. Finally, the fluid position and conformation is analysed at various rocking speeds. A PIV system, described in Section 2.5, was used to obtain phase-resolved velocity data, while components of the same system were used to obtain high frequency fluid images which were then analysed using a purpose-written *MatLab* script (see Appendix, Section 9.5). This data represents the first velocity vector flow field analysis of fluid velocities in rocked bags.

The two-dimensional (2-D) phase resolved velocity field over a longitudinal half of the bag, with vectors superimposed, and contour plots of the velocity magnitude are shown at *N* = 25 min^{-1} in Fig.4.3. The position and direction of the rocking platform are denoted by α. The orientation of the platform is measured in degrees such that $\alpha = +4^{o}$ indicates the platform is 4^{o} above the horizontal. The direction of movement of the platform is represented by the following symbol, so that $\alpha = +4^{o}$ - indicates that the platform is 4^{o} above the horizontal but is currently descending towards the horizontal. In Fig.4.3A, the platform is in a horizontal position and the fluid velocities are predominantly horizontal, moving from the end of the bag (x/L = 1.0) towards the centre (x/L = 0.5) at an average flow field velocity magnitude of 0.12 ms^{-1}. As the platform moves to $\alpha = +4^{o}$ (Fig.4.3B), it can be observed that the fluid moves along the inclined surface at a greater velocity (average magnitude 0.22 ms^{-1}), increasing towards the end of the bag (x/L = 0). As the platform reaches $\alpha = +8^{o}$ (Fig.4.3C), the fluid changes direction, having rebounded from the end of the bag. As the platform descends to $\alpha = -4^{o}$- (Fig. 4.3D-F), the fluid flows into the x/L = 1 end of the bag at average magnitudes within the range 0.12 - 0.16 ms^{-1}. The fluid has the lowest velocity (average magnitude 0.026 ms^{-1}) at $\alpha = -8^{o}$ (Fig. 4.3G) as it pools in the lower end of the bag while the platform is most inclined. As the platform then starts to ascend again (Fig. 4.3H), the fluid accelerates in the horizontal direction to achieve the velocity field shown in Fig. 4.3A.

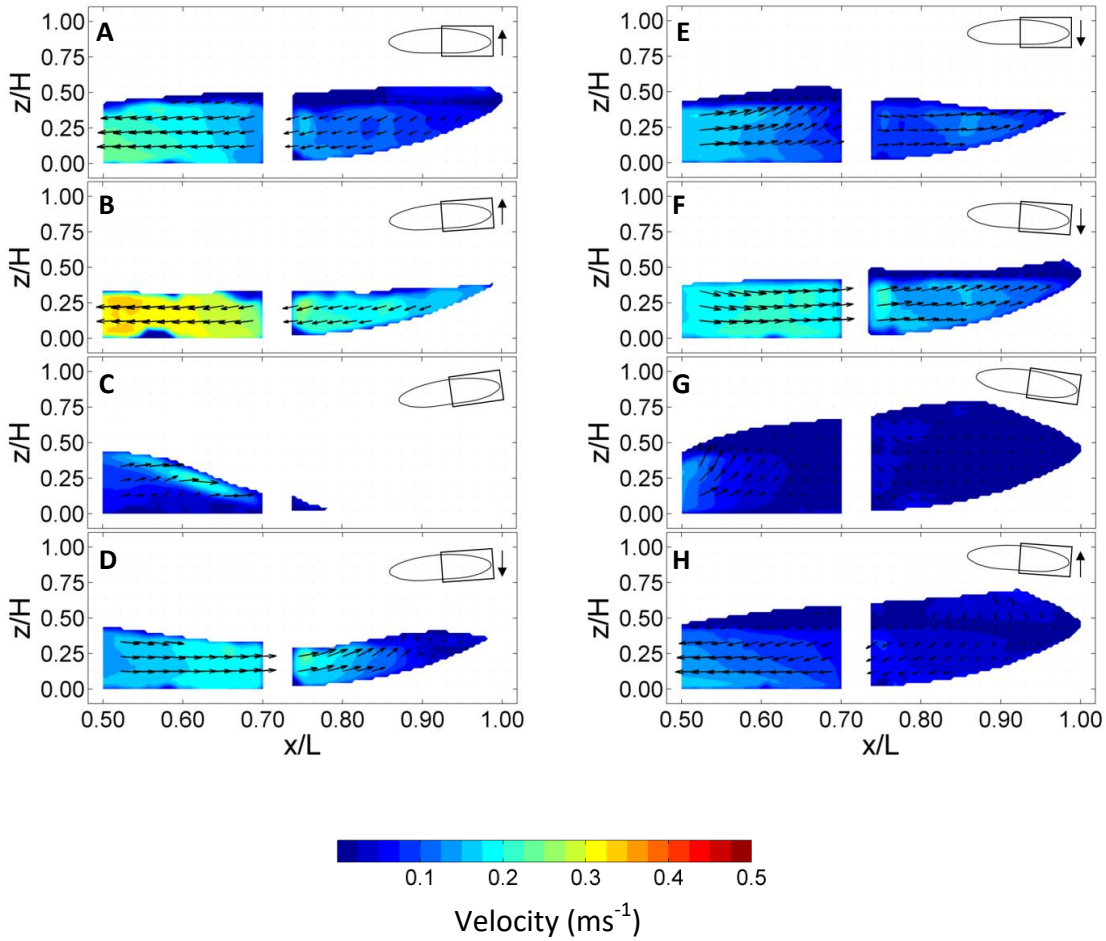

Figure 4.3: Phase resolved velocity vector fields and contour plots of the velocity magnitude in the xz plane at N = 25 min^{-1} for rocking angles through one complete rock at (A) $\alpha = 0^{o}$ +, (B) $\alpha = +4^{o}$ +,(C) $\alpha = +8^{o}$, (D) $\alpha = +4^{o}$ -, (E) $\alpha = 0^{o}$ -, (F) $\alpha = -4^{o}$ -, (G) $\alpha = -8^{o}$, (H) $\alpha = -4^{o}$. The precise orientation of the bag is $\alpha = \pm D^{o} \pm$; $\pm D^{o}$ denotes the angle in degrees above (+) or below (-) to horizontal and the second ± sign denotes whether the platform is currently ascending (+) or descending (-). Inset is a schematic of the bag showing its inclination and direction of angular movement and the field of view of the image with respect the bag. Solid colour represents fluid location. PIV performed as described in Section 2.5.3. Velocity vectors calculated as described in Appendix, Section 9.1.

While the fluid predominantly flows in the horizontal direction with respect to the platform position, there are a small number of platform positions at which a vertical velocity component is significant. In Fig. 4.3E and Fig.4.3G there is a portion of fluid with velocity values deviating significantly from the average at approximately x/L = 0.67 and x/L = 0.54, respectively. It is noteworthy that a wave is formed as the platform moves down at the horizontal level as demonstrated by a bulge in the

liquid surface in Fig. 4.3E. This wave may have a retarding effect on the bulk movement of fluid resulting in lower local velocity values and vertical velocity component as can be observed in Fig. 4.3E at x/L = 0.67. A similar wave formation is evident in Fig 4.3G at x/L = 0.54, where axial velocity components in the flow are present in correspondence to the bulge in the fluid surface. Oncul *et al.* (2009), using a hot-film velocity probe in various positions of a 2L bag at 15 min^{-1} and 7^{o} rocking angle, also noted higher velocities in the longitudinal middle of the bag compared to the end.

At N = 33.5 min^{-1}, similar trends can be observed as at N = 25 min^{-1}, with higher velocities as shown in Fig.4.4. The fluid flows out of the end of the bag as it rises (Fig.4.4A-C), before flowing back into the observed end as that end falls as part of the rock (Fig.4.4D-G). The fluid position within the bag appears to be different, however, with the fluid reaching the end of the bag at $\alpha = -0^{o}$ (Fig.4.4F), with this creating a larger wave at $\alpha = -4^{o}$ - than that observed at N = 25 min^{-1}, $\alpha = 0^{o}$- (Fig.4.4E). The point in the rocking cycle where the fluid has greatest velocity magnitude is at α = -4-, which occurs in the fluid towards the centre of the bag while the point of lowest velocity magnitude again occurs at α = -8. It is suggested that the larger wave observed at this higher rocking rate is as a result of the greater fluid velocities (0.24 and 0.10 ms^{-1} at N = 33.5 and 25 min^{-1} respectively) in the fluid prior to its deceleration by impinging on the end of the bag.

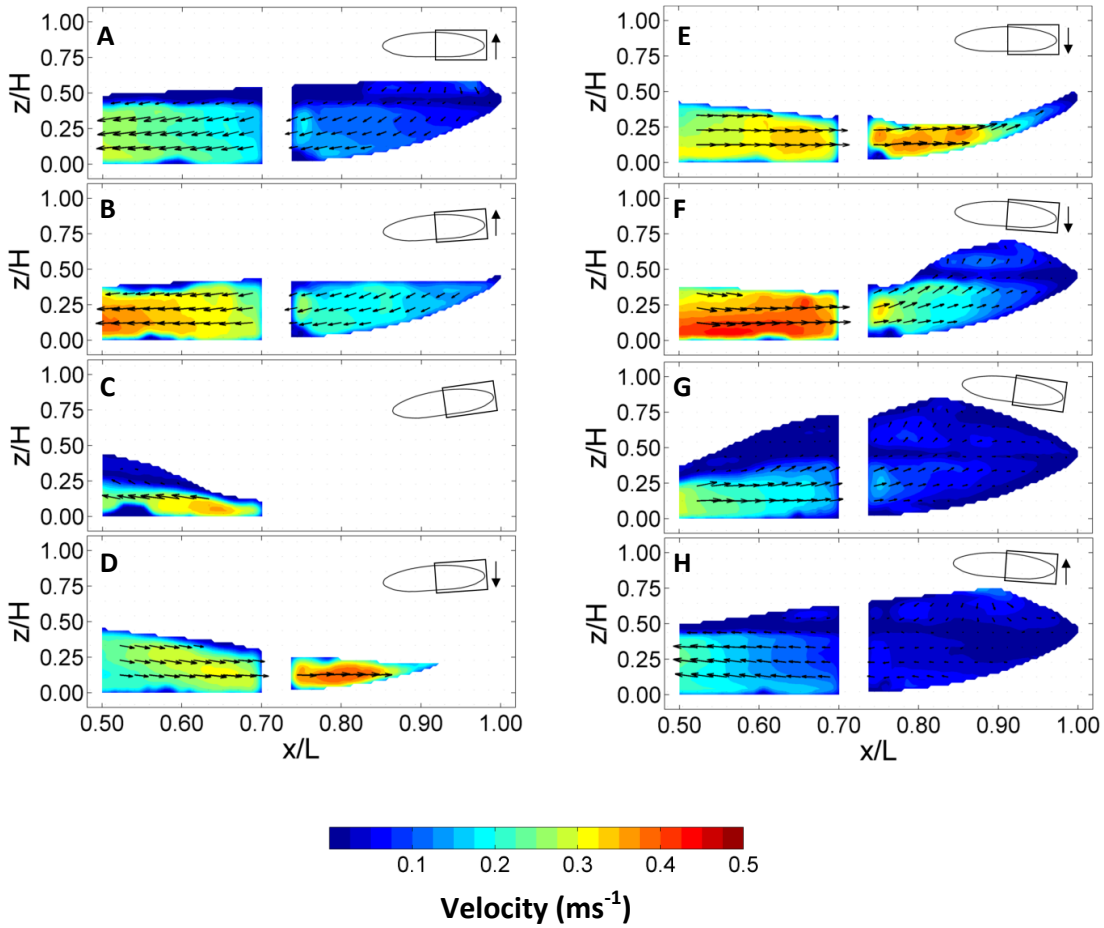

Figure 4.4: Phase resolved velocity vector fields and contour plots of the velocity magnitude in the xz plane at N = 33.5 min^{-1} for rocking angles through one complete rock at (A) $\alpha = 0^{o}$ +, (B) $\alpha = +4^{o}$ +,(C) $\alpha = +8^{o}$, (D) $\alpha = +4^{o}$ -, (E) $\alpha = 0^{o}$ -, (F) $\alpha = -4^{o}$ -, (G) $\alpha = -8^{o}$, (H) $\alpha = -4^{o}$. See Fig.4.3 for α nomenclature explanation. Solid colour represents fluid location. Inset is a schematic of the bag showing its inclination and direction of angular movement and the field of view of the image with respect the bag. PIV performed as described in Section 2.5.3. Velocity vectors calculated as described in Appendix, Section 9.1.

At the highest rocking rate investigated, N = 42 min^{-1}, the velocity magnitudes are again higher, with the fluid now appearing to be approximately one $\alpha = 4^{o}$ increment behind that at N = 25 min^{-1}. The fluid flows rapidly out of the end of the bag in Fig.4.5A-C, with fluid velocities peaking at 0.5 ms^{-1} at $\alpha = +8^{o}$ (Fig.4.5C). As the bag descends the fluid rapidly accelerates in the opposite direction (Fig.4.5D&E), however it doesn't reach the observed end of the bag until $\alpha = -2^{o}$ -. This produces significant vertical velocity which is visible at $\alpha = -4^{o}$- (Fig.4.5G) as the

fluid flows up toward the end of the bag resulting in a very large wave formation at a = -8°.

At *N* = 33.5 (Fig 4.3) and 42 min^{-1} (Fig 4.5) , in contrast to *N* = 25 min^{-1} (Fig.4.3), there are more evident velocity heterogeneities, because the fluid accumulates more velocity before being decelerated by the end of the bag, there are also consistently higher velocities towards the base of the bag compared to at the fluid surface. One of the most significant velocity gradients occurs at α = -8°, this will be discussed in more detail In Section 4.6.

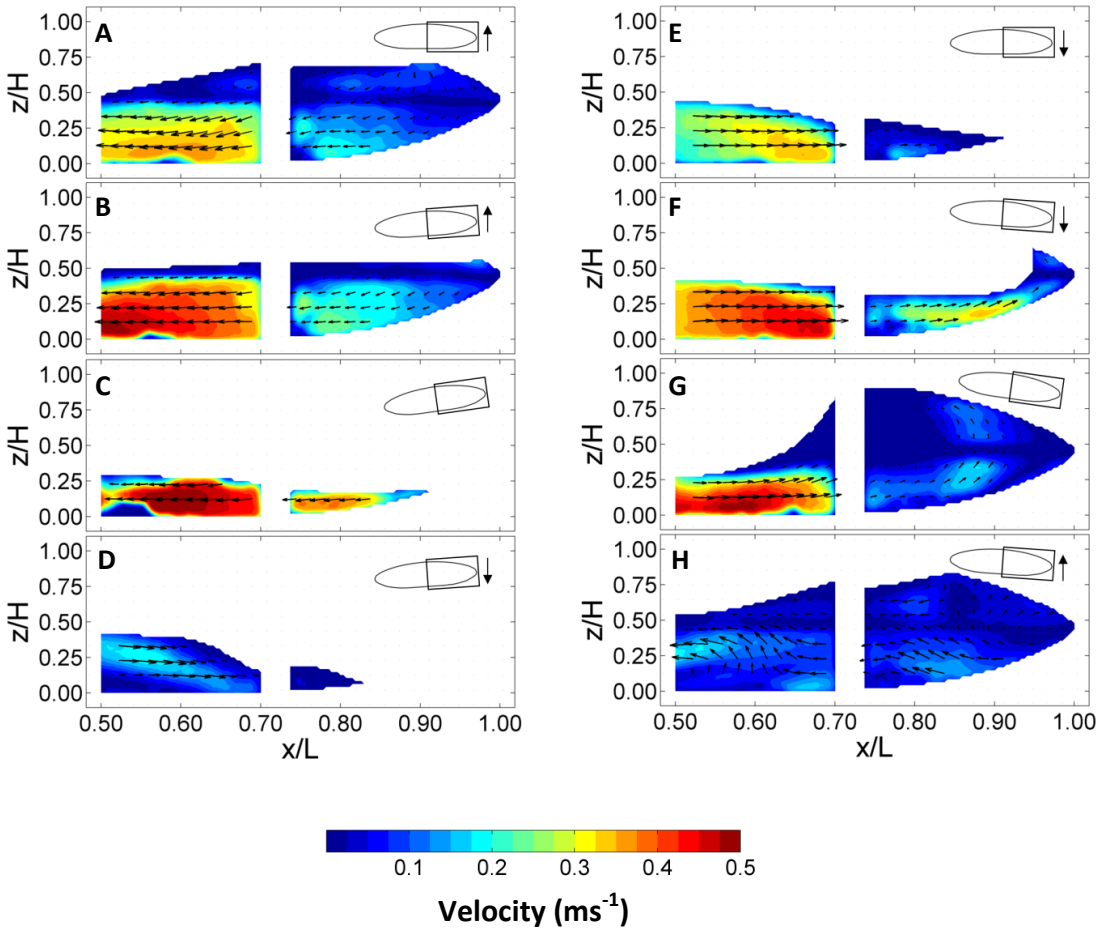

Figure 4.5: Phase resolved velocity vector fields and contour plots of the velocity magnitude in the xz plane at N = 42 min^{-1} for rocking angles through one complete rock at (A) α = 0° +, (B) α = +4° +,(C) α = +8°, (D) α = +4° -, (E) α = 0° -, (F) α = -4° -, (G) α = -8°, (H) α = -4°. See Fig.4.3 for α nomenclature explanation. Inset is a schematic of the bag showing its inclination and direction of angular movement and the field of view of the image with respect the bag. Solid colour represents fluid location. PIV performed as described in Section 2.5.3. Velocity vectors calculated as described in Appendix, Section 9.1.

4.5. Impact on Rocking Rate on Turbulence Kinetic Energy

The two-dimensional (2-D) contour plots of the phase resolved velocity magnitude with vectors superimposed are shown alongside contour plots of turbulent kinetic energy at various *N* and α = -4^{o} - in Fig.4.6. A black line has been added to Figures 4.6 and 4.7 to indicate the horizontal plane to show the extent of the fluid movement at different operating conditions. At this point in the rocking cycle, the platform has moved past the horizontal, moving downwards and the fluid is in the process of flowing towards the lower end of the bag. Fig.4.6A and D, B and E and C and F shows results obtained at different rocking speeds of *N* = 25, 33.5 and 42 min^{-1}, respectively, and at the same platform inclination with respect to the horizontal plane.

A significant effect of the rocking speed can be noted both in terms of the fluid position and the velocity magnitudes across the flow field (Fig.4.6A–C). At *N* = 25 min^{-1}, the fluid direction is mainly along the platform base, with axial velocity components present only at the far end of the bag. As the rocking speed is increased, at the same platform position, the fluid has already moved towards the end of the bag before circulating back towards the centre. At the highest rocking speed at which experiments were carried out, *N* = 42 min^{-1}, velocities are higher than at *N* = 25 min^{-1}, however, less fluid is present in the region comprised between 0.75 < x/L < 1. This could be due to the fluid moving out of phase with respect to the platform rock, with the majority of the fluid still localised at the opposite end of the bag at this point in the rocking cycle (Fig.4.5B).

Turbulent kinetic energy was calculated from the fluctuating component velocities and making the isotropic assumption (Equation 4.3). Values of turbulent kinetic energy, *k*, below 0.02 m^{2}s^{-2} can be observed in Fig. 4.5D & E at most locations for measurements obtained at *N* = 25 and 33.3 min^{-1}. The difference in fluid flow pattern observed at different rocking speeds generates differences in turbulent kinetic energy values measured in the bulk of the fluid. At N = 42 min^{-1}, values of *k* up to 0.1 m^{2}s^{-2} were measured, an order of magnitude higher than those measured at rocking speeds of *N* = 33.5 and 25 min^{-1}. At *N* = 25 min^{-1} the fluid is observed to

be largely in phase with the platform movement, causing the flow to decelerate towards the right-hand side end of the bag with velocities close to 0 ms^{-1}. The flow pattern within the bag undergoes a transition when a critical rocking speed is reached (its value being between N = 34 and 42 min^{-1} at the operating conditions used in this work), causing the fluid to move out of phase and behind the platform rock motion. This generates higher turbulence levels, indicated by higher turbulent kinetic energy values, at locations close to the right-hand side of the bag.

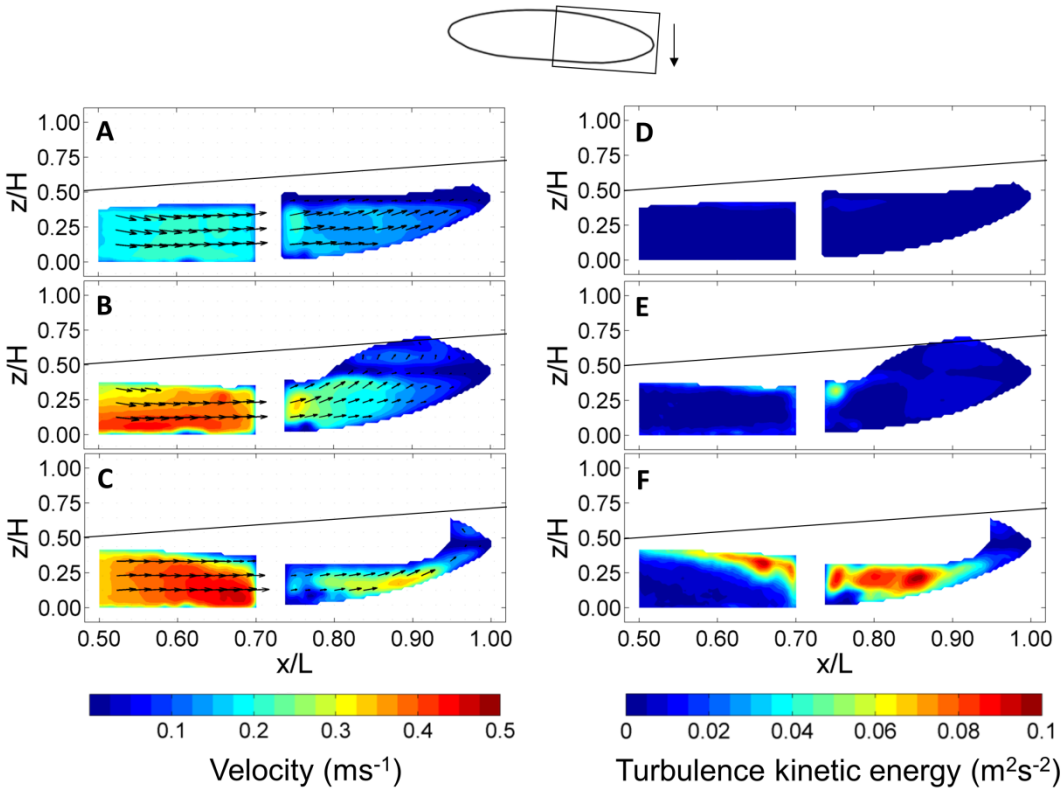

Figure 4.6: Phase resolved velocity vector fields and contour plots of: (A-C) velocity magnitude and (D-F) the turbulence kinetic energy in the xz plane at N = (A,D) 25 min^{-1} , (B,E) 33.5rpm and C,F) 42 min^{-1} at $\alpha = -4^{o}$ -. See Fig.4.3 for α nomenclature explanation. Above is a schematic of the bag showing its inclination and direction of angular movement and the field of view of the image with respect the bag. The solid black line represents the horizontal. Solid colour represents fluid location. PIV performed as described in Section 2.5.3. Velocity vectors calculated as described in Appendix, Section 9.1. Turbulence kinetic energy calculated as in Equation 4.3.

4.6. Impact on Rocking Rate on Shear Stress

The two-dimensional (2-D) contour plots of the phase resolved velocity magnitude with vectors superimposed are shown alongside contour plots of shear stress at various rocking speeds and α = -8^{o} in Fig.4.7. It should be noted that these measurements follow the results shown in Fig.4.7A-C as they were taken at the next measurement point in the rocking cycle. At *N* = 25 min^{-1} and α = -8^{o} the fluid is generally moving towards the right-hand side end of the bag although there is some axial velocity near the longitudinal centre of the bag. The fluid surface angle is parallel to the horizontal plane, as shown by the black line in Fig. 4.7A. As the rocking speed is increased, higher velocities were measured at locations from x/L = 0.5-0.8, while mean velocities towards the right-hand side of the bag are similar to those observed at *N* = 25 min^{-1}. In addition, the fluid surface angle at α = -8^{o} increases at higher rocking speeds, and a wave is formed by the fluid impinging on the right-hand side end of the bag and recirculating backwards towards its centre.

Fig.4.9E & F show contour plots of the Reynolds stress measured at *N* = 25, 33.5 and 42 min^{-1} respectively. The Reynolds stress is calculated from the 2-D turbulent components of the fluid flow (Equation 4.4). Plane averaged and maximum shear stress values vary significantly with increasing rocking speed. At *N* = 25 min^{-1} the maximum shear stress value measured over the whole rock is 3.4 Pa, and it increases to 15 Pa at N = 33.5 min^{-1} and to 21 Pa at N = 42 min^{-1}. At N = 33.5 and 42 min^{-1}, the highest shear stresses were measured at locations between x/L = 0.5-0.7 and z/H = 0.25-0.30, which is the interface between the low velocity regions described above and the higher velocity fluid moving towards the end of the bag. Kalmbach *et al.* (2011) measured shear stresses in a 2L rocked bag at N = 15 min^{-1} and rocking angle of 7^{o} using a hot-film probe. In the work of Kalmbach *et al.* (2011), values of shear stresses up to 0.11 Pa were measured, with average values based on 19 measurement points within the bag over the course of the rock being 0.02 Pa This finding is in line with the rapid increase in shear stress that was measured between N = 25 and 42 min^{-1}.

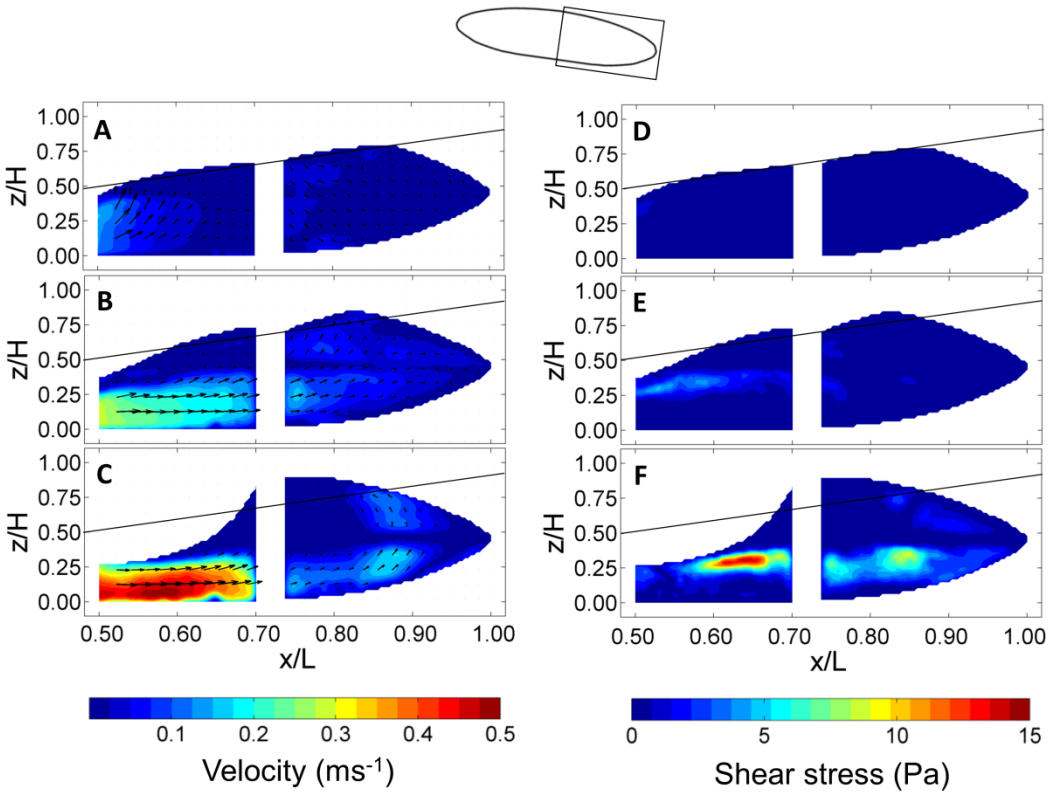

Figure 4.7: Phase resolved velocity vector fields and contour plots of: (A-C) velocity magnitude and (D-F) shear stress in the xz plane at N = (A,D) 25 min^{-1} , (B,E) 33.5rpm and C,F) 42 min^{-1} at α = -8°. See Fig.4.3 for α nomenclature explanation. Above is a schematic of the bag showing its inclination and direction of angular movement and the field of view of the image with respect the bag. The solid black line represents the horizontal. Solid colour represents fluid location. PIV performed as described in Section 2.5.3. Velocity vectors calculated as described in Appendix, Section 9.1. Shear stress calculated as in Equation 4.4.

4.7. Theoretical Mechanism of Bulk Fluid Movement

Based on observations of the fluid movement within the bag during the PIV experiments, a theory was developed for the mechanism by which the movement of the platform produces movement of the fluid within the bag. This was derived from first principles, on the basis that the rocking motion effectively pumps the fluid along the length of the bag. Pumping rate makes the assumption that as the bag rocks, the fluid surface does not move, remaining gravitationally horizontal. Therefore the fluid beneath this horizontal surface must be displaced longitudinally by the base of the bag rising at one end and falling at the other. This assumption is false at high rocking rates, but at N = 25 min^{-1}, this produces a very reasonable

prediction for bulk fluid velocity and position (Fig. 4.8A). This can be calculated by taking the volumetric displacement of one longitudinal half of the bag from its surface area and angular movement over a given time. This assumes that the bag is cuboidal and is based on mean length (*x*), width (*y*) and height (*z*) dimensions. Pumping rate would accurately describe the fluid flow in a rocked bag system in which the force of gravity was dominant; therefore, the better pumping rate describes the fluid behaviour, the more dominant is gravity in that system. Pumping rate can predict the velocity of the fluid based on the predicted volumetric displacement of the fluid in the x direction divided by the z dimension cross sectional area of the fluid at the centre of the bag at stationary. Pumping rate predicts movement of the fluid centroid position based on the predicted mean velocity of the fluid in the x direction over the time course of the rock as shown in Equation 4.8:

$$\boldsymbol{R_p} = \frac{\frac{\pi L}{360} \times \frac{d\propto}{dt} \times \frac{LW}{24}}{WH_f} \qquad (4.8)$$

where *L* is the length of the bag (*x*), *W* is the width of the bag (*y*), H_f is the height of the fluid surface from the base of the bag (*z* = 0) when the bag is stationary, □ is the bag angle and *t* is time. *P* is the pumping rate, a prediction for the longitudinal (x direction) velocity at any point in the rocking cycle (u_i).

This prediction can be compared to the bulk fluid velocities measured by PIV presented in Section 4.8, Fig.4.8 and bulk fluid positon derived from this prediction can be compared to the measured fluid centroid position in Section 4.9, Fig.4.12C.

4.8. Impact of Rocking Rate on Angle Resolved Spatially Averaged Velocity

From the results presented in Fig.4.3-4.5 it is clear that the rocked bag motion produces a characteristic fluid flow. Most importantly, the presence of a wave was observed at specific operating conditions, corresponding to a characteristic velocity field and visible from the presence of a bulge in the liquid surface. It appears that the bulk fluid flow falls further behind the platform motion at higher rocking rates (Section 4.4). In order to elucidate further the observed phenomena, the PIV

results were analysed to draw additional information on the bulk fluid motion inside the bag at different rocking rates over the course of one rock and in particular to relate this motion to the movement of the platform.

The horizontal per-vector velocity components ($\bar{u}_i$) were averaged across the measurement plane to obtain a single average value ($\bar{\bar{u}}_i$) in the positive (↑x) direction for each of the phase resolved locations of the platform in the rocking cycle at a given rocking rate (*N*). Fig.4.8A-C present this value at various rocking speeds over the course of one rock. Fig.4.8A-C also shows the pumping rate estimation at the relevant rocking speed, as described in Section 4.7. Pumping rate predicts fluid velocity and movement based on the fluid surface remaining horizontal as the base of the bag moves, therefore the movement of the base of the platform acts as a pump, moving the fluid along the line of the bag as it changes in inclination (Section 4.7). The horizontal velocity component accounts for the majority of the velocity as the bag rocks, analysis of the horizontal profile over the course of the rock should show the flow pattern of the fluid.

In order to further understand the acceleration of the fluid as it interacts with angle and position of the rocking platform over the course of the rock, the rate of change of values of $\bar{\bar{u}}_i$ was calculated as $\bar{\bar{u}}'$:

$$\bar{\bar{u}}' = \frac{d\bar{\bar{u}}}{dt} \qquad (4.9)$$

Fig.4.8D shows the corresponding horizontal fluid acceleration. Since at low rocking speeds the platform is moving relatively slowly, gravity should be the dominant force responsible for fluid motion. The pumping rate prediction shows a sinusoidal profile as the variable speed of the platform produces the variable horizontal velocity of the fluid. At *N* = 25 min^{-1} (Fig.4.8A) the average velocity follows a sinusoidal profile over one rock. The maximum absolute average velocity is achieved at α = ± 4° while the minimum is obtained at the α = ±8°. At *N* = 25 min^{-1} the average horizontal velocity component overlaps the profile of the fluid pumping rate, shown with a dotted line in Fig.4.8A, suggesting that the fluid motion is in phase and its behaviour predominantly determined by the force of gravity drawing

the fluid downwards as the bag is inclined. At N = 33.5 min^{-1}, the average horizontal velocity follows the same sinusoidal pattern, however over parts of the rocking cycle, the profile appears to be shifted towards the right by up to $\alpha = 1^{o}$ in comparison to the pumping rate curve (Fig.4.8B). The maximum $\bar{\bar{u}}$ at N = 33.5 min^{-1} is greater than that recorded at 25 min^{-1} and again occurs at $\alpha = \pm 4^{o}$, with the minimum velocity occurring at $\alpha = \pm 8^{o}$. At N = 42 min^{-1} (Fig.4.8C) a sinusoidal profile is observed which, following the trend noted at N = 33.5 min^{-1}, appears to be shifted by $\alpha = 2^{o}$ in comparison to the rocking cycle observed at N = 25 min^{-1} and with respect to the pumping rate curve. Consequently, while the maximum velocity is still measured at approximately $\alpha = \pm 4^{o}$ ±, the minimum velocity occurs at $\alpha = \pm 4^{o}$ when the platform moves towards the horizontal. As it was observed in the profile obtained at N = 33.5 min^{-1}, the maximum velocity is over predicted by the pumping rate curve, suggesting that fluid motion is no longer in phase with the platform movement.

Fluid velocities measured by Oncul *et al.* (2010), in a 2 L rocked bag at N = 15 min^{-1} showed a similar trend, with maximum fluid velocities of 0.1-0.2 ms^{-1} measured at various points at $\alpha = 0^{o}$ while being 0-0.02 ms^{-2} during the platform direction change at $\alpha = 8^{o}$. The trend being observed would predict values of approximately 0.12 ms^{-1}.

The longitudinal fluid acceleration profiles ($\bar{\bar{u}}_{l}'$) (Equation 4.9) obtained at different rocking speeds are presented in Fig.4.10D. As rocking speed is increased, significantly higher fluid accelerations are noted. A maximum value at N = 25min^{-1} of 0.43 ms^{-2} is reached, and this increases by 68% to 0.84 ms^{-2} at N = 42 min^{-1}. At N = 25 min^{-1} the profiles characterised by two local maxima, possibly as a result of the wave generation noted in Section 4.4 (Fig.4.3). The acceleration profiles follow a different trend depending on bag inclination angle. Over $\alpha = +5^{0}$ + to $+8^{o}$+ and -5 ^{o}- to -8^{o}-, the accelerations are within 0.2 ms^{-2} at all rocking speeds, while at $\alpha = 0^{o}$- and 0^{o}+, they are most different, being 0.14 ms^{-2} at N = 25 min^{-1} and 0.8ms^{-2} at N = 42 min^{-1}.

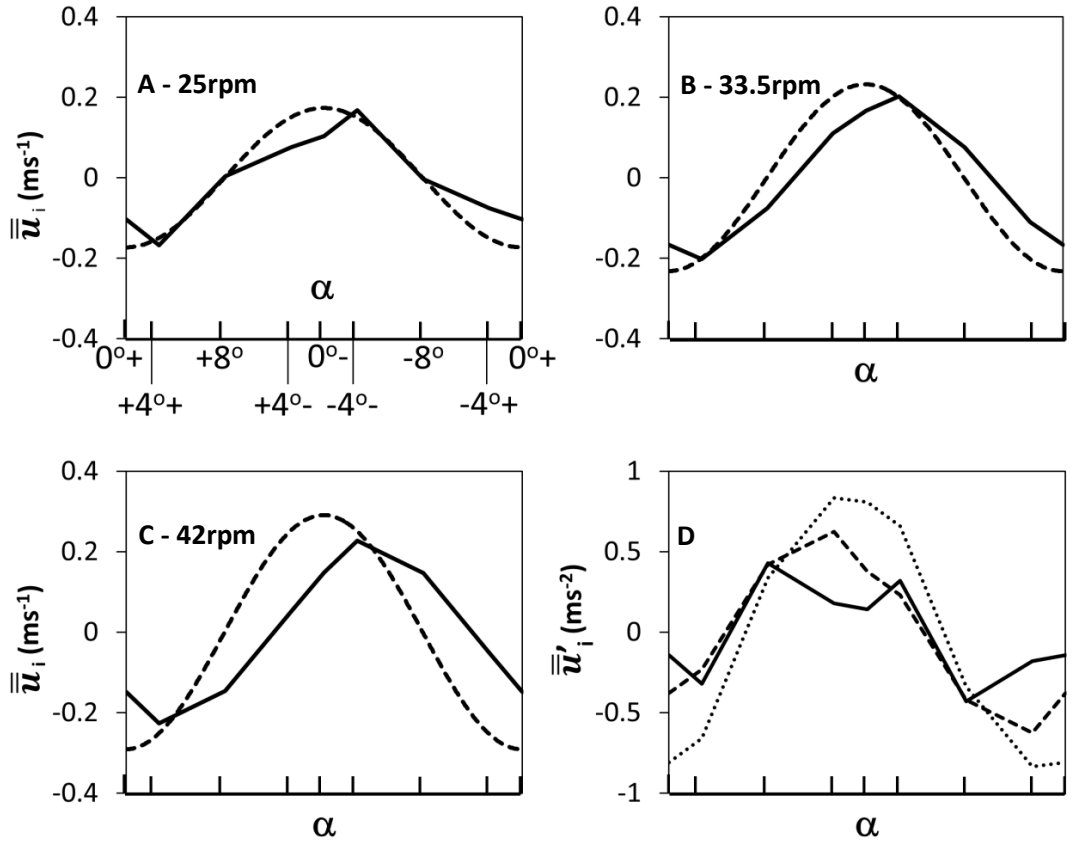

Figure 4.8: Flow field averaged horizontal velocity values over the course of a single rock at (A) 25 min^{-1}, (B) 33.5 min^{-1} and (C) 42 min^{-1}; PIV data (——) and pumping rate (R_p) (Eqn.4.8) based velocity estimate (– – –·). Values taken from the horizontal component of Equation 4.1. (D) PIV derived horizontal acceleration over the course of a single rock at 25 min^{-1} (——), 33.5 min^{-1} (– – –·) and 42 min^{-1} (·····). Values calculated from Equation 4.9. PIV performed as described in Section 2.5.3.

The spatially averaged vertical magnitudes ($\bar{\bar{u}}$) over the course of a single rock at various rocking rates are presented in Fig.4.9. Since the camera is phase-locked to the rocking platform (Fig.2.7), the presented values represent movement relative to the bag. At N = 25 min^{-1}, the fluid stays in phase with the bag, and therefore does not have a significant vertical component over the course of the rock (<0.01 ms^{-1}). The alternation between negative and positive values are at a much higher frequency than the rocking period, and reflect the wave formation from the repeated fluid interactions with the end of the bag that have been previously observed in section. At N = 33.5 min^{-1}, there is a clearer trend as the bag rocks, with the fluid vertical velocity oscillating but tending to be positive as the bag

descends and negative as the bag ascends. As the fluid predominantly flows along the base of the bag at a = +4° - (Fig.4.3-4.5), the fluid has a negligible vertical velocity before flowing up the observed end of the bag at α = 0° -. At N = 42 min^{-1}, the fluid follows a similar vertical velocity profile to that at N = 33.5 min^{-1}, however the vertical movement becomes a more recognisable wave, with sustained. The transition from the fluid at N = 25 to 42 min^{-1}, matches what was previously observed in Section 4.4, as the fluid moves from a numerous small wave regime to a single large wave regime.

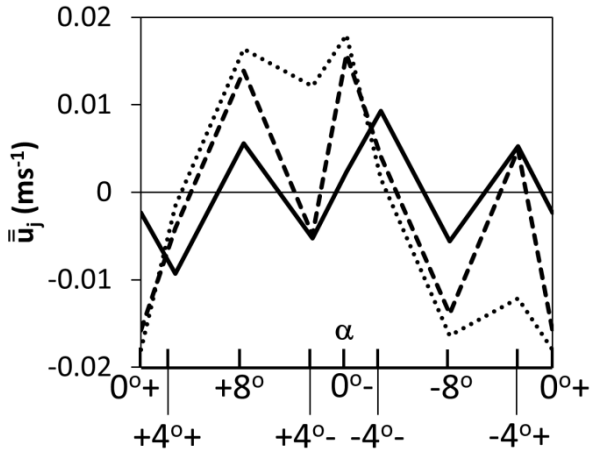

Figure 4.9: Vertical velocity profiles over the course of a single rock at 25 min^{-1} (——), 33.5 min^{-1} (– – –) and 42 min^{-1} (·····). Values calculated from the vertical component of Eqn.4.1. PIV performed as described in Section 2.5.3. Velocity vectors calculated as in Appendix, Section 9.1.

4.9. Impact of Rocking Rate on Fluid Phase

The PIV data clearly shows the different behaviour of the fluid as the rocking rate increases. The phase of the fluid appears to change with respect to the rocking platform at higher rocking rates, with the fluid motion appearing to fall behind the motion of the rocking platform. In orbitally shaken microwell plates (Buchs 2001), and rectangular cultivation bags (Ojo *et al.* 2014), above a critical orbital rotation rate the fluid was seen to move out of phase, at which point power input was found to drop dramatically. The orbital shaking frequency at which this was observed in the cultivation bag was 90 min^{-1}, significantly higher than the fastest rocking rate currently used.

The mimic bag and rocking platform developed for PIV evaluation were exploited to allow high temporal resolution tracking and quantification of the fluid position over the course of a rock at various rocking rates. By additional of methyl blue to the liquid in the rocked bag, and illuminating with a lamp instead of the laser (Section 2.5.4), the camera could be used to capture 360 frames over the course of the rock, triggered to start at $\alpha = +0^{o} +$. The powerful illumination coupled with the dark colouring of the liquid produced a high contrast ratio image which could be processed to quantify the fluid position (See Appendix, Section 9.1).

A script was written in *MatLab* (MathWorks) which polarised each image on the basis of per-pixel light intensity to produce areas of black and white representing 'liquid' and 'not-liquid' respectively, the bolts and O-ring were interpolated over in the event that liquid was present on either side and then image processing was used to remove noise from the boundary between liquid and not-liquid elements. With this analysis and produced a single region per frame captured, which represented the 2-D position of fluid in the bag at one point in the rocking cycle, shown by the red outline in Fig.4.10A. Further analysis could be applied to this fluid area: (i) The central point in the 2-D shape of fluid, the 'centroid' could be computed. (ii) The free surface of the fluid was found by plotting a line along the upper surface of the fluid. In Fig.4.10A, the fluid is higher on the right of the bag than on the left, in this case, the line of best fit (green) is plotted for all of the fluid

surface points between the left-hand-most point of the fluid and the highest point of the fluid. In the opposite case, the line of best fit is plotted for all of the fluid surface points between the right-hand-most point of the fluid and the highest point of the fluid. By applying the above analysis to all of the images in the 360 image ensemble, high temporal resolution image data could be quantified and analysed. The data captured by this technique were highly repeatable, demonstrating that both the technique and the bulk fluid behaviour at various rocking rates was consistent (Fig.4.11).

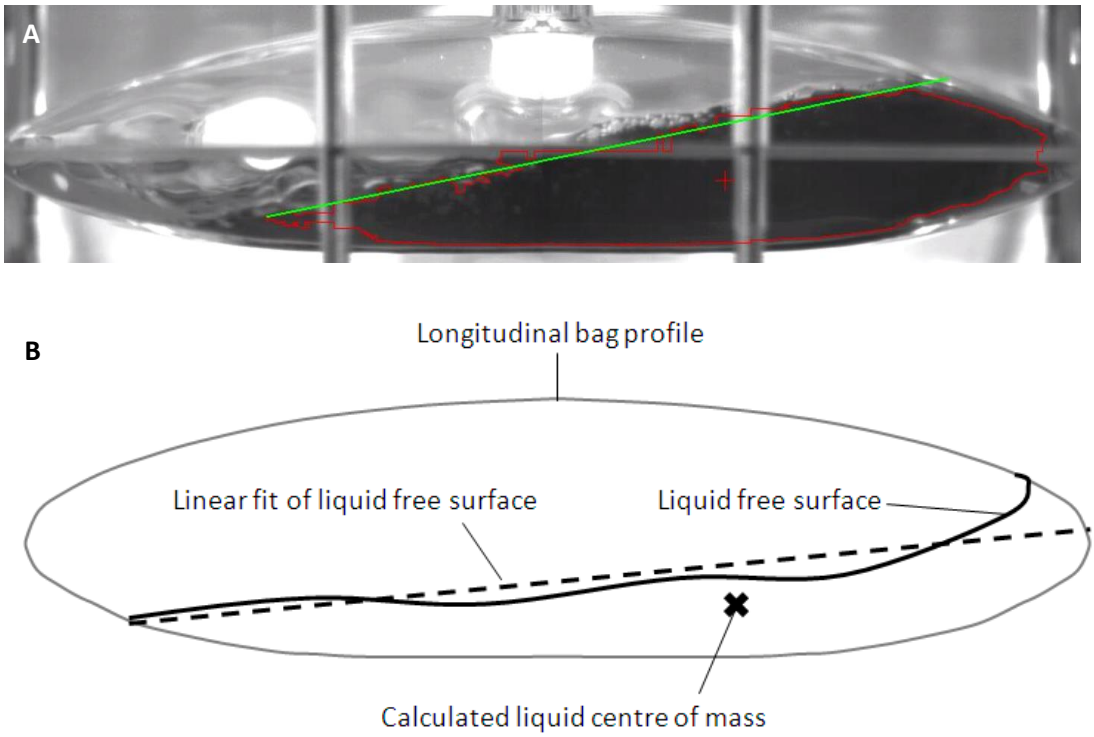

Figure 4.10: Flow visualisation in the rocked bag mimic; (A) Image of the fluid flow position in the mimic at a fixed angle and determination of the outer bound of the liquid (red line), estimation of the liquid surface position (green line). (B) Sample schematic diagram of the bag and fluid position resulting from the image analysis of A. Image analyses by *MatLab* code as described in Section 4.9 and Script itself is displayed in Appendix, Section 9.5.

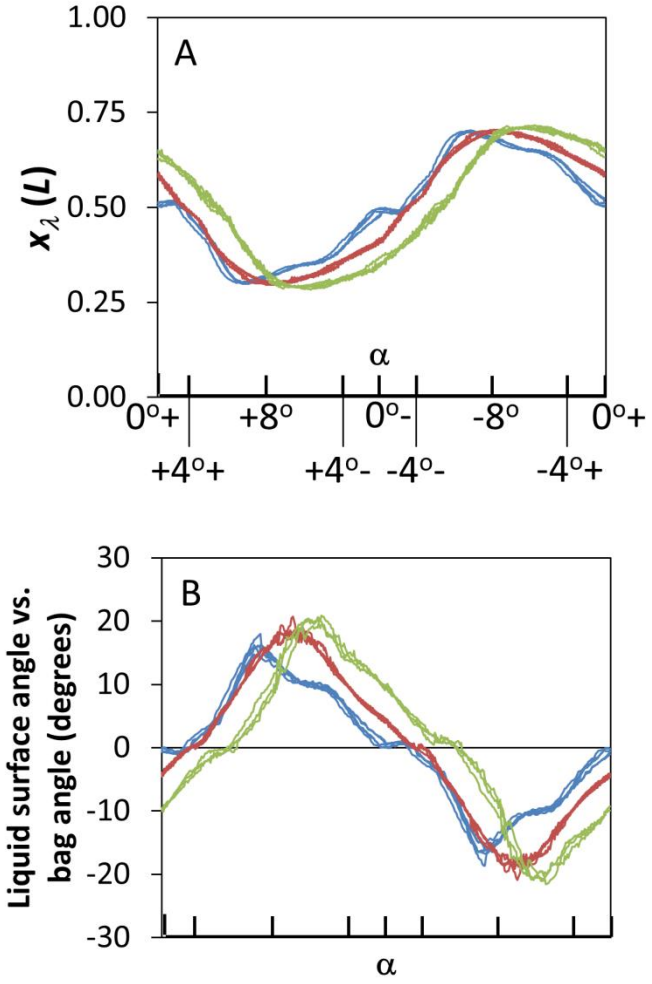

Figure 4.11: Profiles of (A) fluid centroid position and (B) liquid surface angle vs. bag angle at various rocking rates; 25 min^{-1} (solid blue line), 33.5 min^{-1} (solid red line) and 42 min^{-1} (Solid green lines) Fluid centroid position is the geometric centre of the 2-D element considered to be the fluid. Liquid surface angle is a linear gradient fit of the uppermost layer of fluid relative to the frame of reference of the bag. Further detail of these calculations can be found in Section 4.9. See Appendix, Section 9.5 for the *MatLab* code used to calculate these values. n = 5.

Flow visualisation experiments were carried out to confirm the PIV results (Section 4.4-4.6) and improve understanding of the fluid motion over the rock cycle. Analysis of the fluid position at high frequency (up to 252 frames per second, 360 images per rock) allows the quantitative determination of fluid surface angle with respect to the horizontal (β) and 2-D centre of mass (centroid, x_λ) over a single rock. Fig.4.13C shows the different longitudinal fluid surface angles at different rocking speeds over the course of a rock. Images were captured based on precise positional triggering from the rocking platform and are presented relative to gravitational horizontal, therefore if the platform was moving at infinitesimal velocity, this plot would be a horizontal line. Comparison between the different rocking speeds indicates that the fluid angle with respect to horizontal (β) is changing to a greater degree at higher rocking speeds. As the rocking speed is increased, β changes later in the rocking cycle. Maximum values of β being 8^o at α = $+8^o$ at N = 25 min^{-1} and 14^o at α =$+6^o$- at N = 42 min^{-1}. At all rocking speeds, β changes most rapidly towards the end of the rock, reflecting the high fluid deceleration at this point as shown in Fig.4.12. Taking the average magnitude of β over a whole rock ($\overline{|\beta|}$) (Fig.4.12B) can give an indication of the total extent to which the fluid surface angle differs from horizontal. In the rocking speed ranges measured, there is a linear increase in β with respect to fluid rocking speed, suggesting that the fluid moves increasingly out of phase at higher rocking speeds. The fluid centroid is the geometric centre point of the observed 2D section of the fluid position and indicates the bulk position of the fluid, longitudinal movement of the fluid centroid with respect to rocking platform position are presented in Fig.4.13C at different rocking speeds. The horizontal liquid centroid position (x_λ) was normalised against bag length, so x_λ = 0.5 would indicate the fluid centroid being in the centre of the bag longitudinally. At all rocking speeds investigated, x_λ follows a sinusoidal profile, with the fluid position changing at a rate proportional to the rocking platform movement. The maximum value of x_λ is seen after the middle of the rock, as the rapid movement of the platform propels the bulk fluid from one end of the bag to the other. Higher rocking speeds cause the x_λ wave to move with a time delay with respect to α, again suggesting a transition out of phase

as mentioned in Section 4.4 and 4.8. In Fig.4.13A and B, the more erratic profile at N = 25 min^{-1} is a reflection of small waves at the fluid surface generated after the bulk fluid interacts with the end of the bag. The single larger wave is generated at N = 33.5 and 42, produces a more recognisable sinusoidal profile. Fluid surface position has been reported using a capacitive probe by Kalmbach *et al.* (2011). In the work of Kalmbach *et al.* (2011), data from a 2L rocked bag at N = 15 min^{-1} and α = 7^{o} rock angle were used to estimate a value for the integral of β of 1.7^{o}. This value is in agreement with the data obtained in this work at higher rocking speeds, but suggests that the linear range noted between *N* = 25 and 42 min^{-1} may not continue below *N* = 25 min^{-1}.

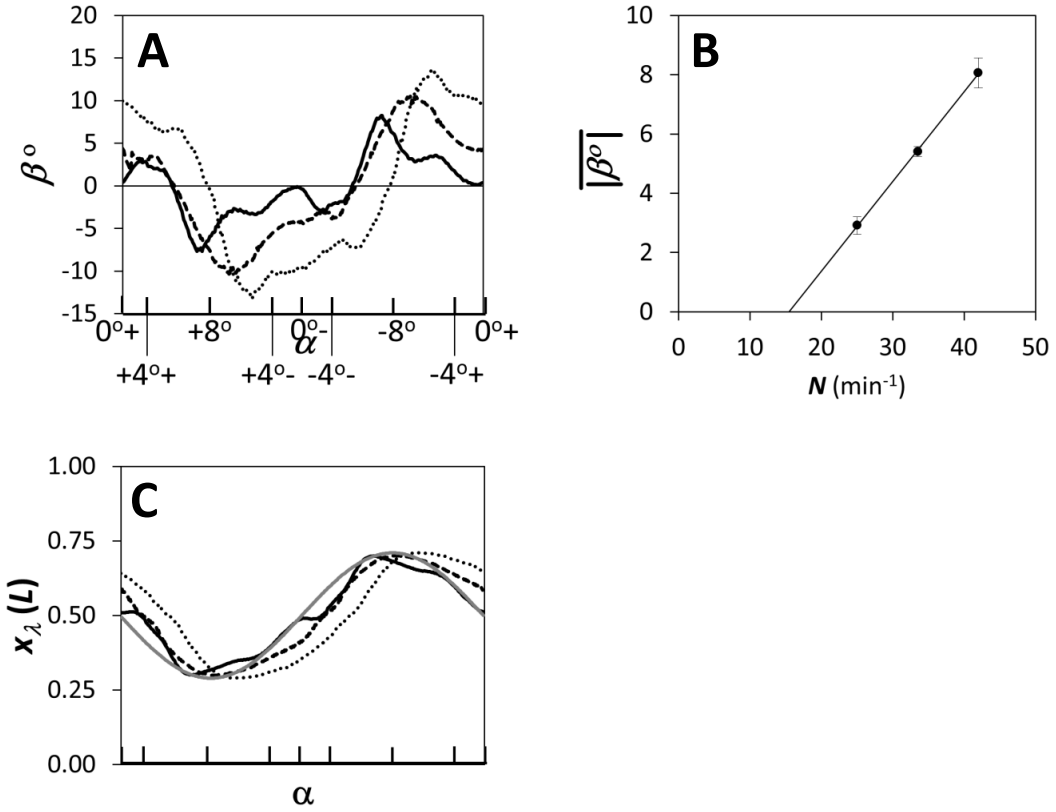

Figure 4.12: Quantification of bulk fluid behaviour. (A) Fluid surface angle compared to horizontal (β), (B) Averaged magnitude over the course of a single rock of fluid surface angle ($\overline{|\beta|}$) against bag rocking rate in min^{-1} and (C) Centroid position (x_λ) relative to bag end over the course of a single rock at 25 min^{-1} (——), 33.5 min^{-1} (– – –), 42 min^{-1} (.....) and, in (C) Pumping rate, R_P (Equation 4.8) (———). Error bars represent 95 % confidence (n = 5). β is calculated as the linear fit of the longitudinal angle of the fluid surface relative to horizontal. If the fluid is horizontal, $\beta = 0$. $\overline{|\beta|}$ is the average magnitude of β over the course of one rock, higher values represent liquid that is further out of phase (Equation 4.9). Further detail of these calculations can be found in Section 4.9. See Appendix, Section 9.5 for the *MatLab* code used to calculate these values.

4.10. Rocked Bag Fluid Velocity and Turbulence Kinetic Energy Comparison to Stirred Tank

To contextualise the findings reported in Sections 4.4 to 4.9, it is important to compare the values to those measured in other works. Fig.4.13 shows a summary of the phase-averaged and maximum phase-resolved velocity magnitudes and turbulent kinetic energy values measured at various rocking speeds, alongside comparison values from literature. Taking the N = 15 min^{-1} values from Kalmbach *et*

al. (2011), averaged velocity magnitudes are seen to increase linearly from ~0.03ms^{-1} at *N* = 15 to 0.167 ms^{-1} at *N* = 33.5, with very little measured increase beyond that point (0.173 ms^{-1} at *N* = 42). Maximum single vector velocities measured increase significantly over the range of *N* from 0.15 ms^{-1} at *N* = 15 min^{-1} to 0.51 ms^{-1} at *N* = 42 min^{-1}. Turbulent kinetic energy increases exponentially over the ranges measured, increasing from 0.0019 m^{2}s^{-2} at *N* = 25 min^{-1} to 0.019 m^{2}s^{-2} at *N* = 42 min^{-1}. Comparison of these values to those measured in a lab scale downward pumping PBT at v_{tip} = 1.06 ms^{-1} by Gabriele *et al.* (2009) show close agreement between the *N* = 42 min^{-1} bag and the tank in terms of average and maximum values of velocity magnitude and average turbulent kinetic energy. However, the rocked bag produces a greater range of turbulent kinetic energies at *N* = 33.5 and *N* = 42 min^{-1}, possibly due to the slow period of the rock compared to an impeller passage. Shear stress was found to trend identically to turbulent kinetic energy with the average and maximum at *N* = 42 being 1.7 and 20.5 Pa respectively. It appears that while rocking speeds beyond *N* = 33.5 min^{-1} do not produce significantly more fluid velocity magnitude, there is considerably more fluid turbulence generated. Comparison to the hot wire probe velocity measurements made by Kalmbach et al (2011) show that the data at *N* = 15 min^{-1} fit with the trend being observed.

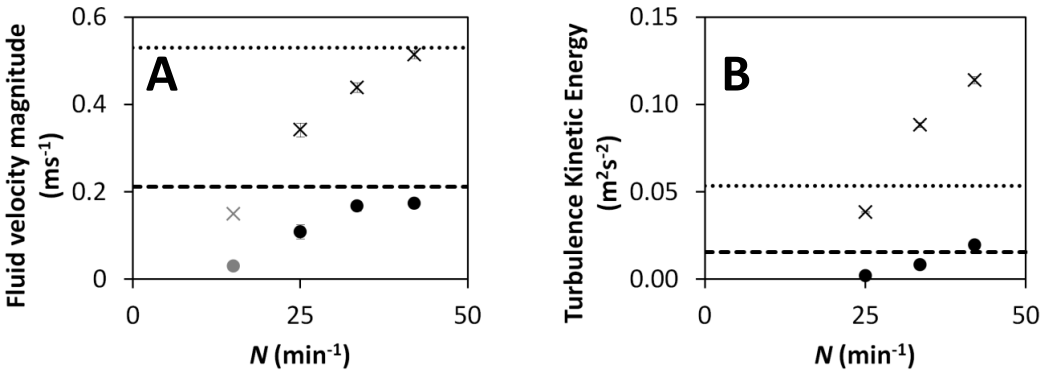

Figure 4.13: Comparison of average (●) and maximum (×) velocities and turbulent kinetic energy at different rocking rates. Grey symbols represent data extrapolated from the work of Oncul *et al.* (2011.) Dashed and dotted lines represent average and maximum values, respectively, for a 2.7L stirred tank bioreactor with downward pumping pitched blade turbine at 300rpm; v_{tip} = 1.06ms^{-1} (Gabriele *et al.* 2009). Average velocities were taken as the mean average of the 8 phase resolved spatially averaged velocities. Maximum velocities represent the largest velocity vector in the 8 phase resolved vector fields at each rocking rate. Error bars represent 95 % confidence.

4.11. Summary

The aim of this chapter was to measure, for the first time, the fluid dynamics within a rocked bag bioreactor. To this end, a structural mimic of a rocked bag and rocking platform had to be designed and fabricated, to allow visual interrogation. The bulk fluid flow was also quantified using a novel fluid tracking technique which leveraged the high speed camera and a purpose written visual analysis code.

4.11.1. Trends in Fluid Behaviour

There are a number of notable changes in fluid flow with respect to increasing values of *N*. At *N* = 25 min^{-1}, average fluid u_j velocities when the platform is moving at its greatest speed over the horizontal (α = -4+ to α = +4+) are 0.12ms^{-1} or 0.19 m over that time period. At *N* = 42 min^{-1}, average fluid u_j velocities when the bag is in motion are 0.14 ms^{-1} or 0.14 m over that time period. The fluid clearly moves more rapidly with respect to the bag angular movement at lower rocking rates. As a result, the fluid at *N* = 25 min^{-1} first reaches the far end of the bag at α =+2^{o}- (u_j = 0.09 ms^{-1}) while at *N* = 42 min^{-1} this occurs at approximately α =-2^{o}- (u_j = 0.19 ms^{-1}) (Fig.4.3D-E & 4.5E-F). Because the fluid at *N* = 25 min^{-1} is moving more slowly, due

to the bag inclination and lower bag angular velocity, when it reaches the end of the bag this causes a small vertical accumulation of fluid which propagates against the bulk fluid flow as a ripple, causing a bulk deceleration (Fig.4.10.A $\alpha = 0^{o}$). The fluid impacts the end of the bag again at $N = 25$ min^{-1} at $\alpha = -4^{o}$- (Fig.4.3F), however this again produces a small wave. This contrasts with the fluid at $N = 42$ min^{-1}, which on impacting the end of the bag at $\alpha = -2^{o}$- (Fig.4.5D-E) is redirected along the ceiling of the bag (Fig.4.5F). This fluid being forced in the other direction to the bulk flow accumulates in the upper region of the bag (Fig.4.5G) and the interaction between these two flow patterns produces significant shear (Fig.4.7F) and is responsible for visibly entraining gas into the liquid phase.

This gas entrainment is thought to be as a result of the fluid being further out of phase with respect to the rocking platform (Fig.4.12B), since the platform's relative advancement compared to the fluid is what produces this more energetic interaction between fluid flow and the ends of the bag. The fluid being out of phase is considered a function of the more rapid platform movement, since the fluid in imparted with greater momentum by the movement of the platform at higher rocking rates but would need to accelerate more rapidly to stay in phase with the rocking platform. Because the fluid moves later in the rocking cycle, it flows more rapidly because it is moving up and down the bag when the bag is more inclined, leading to higher maximum velocities. However, because the fluid is forced to change direction twice per rock, the mean velocity does not increase significantly beyond 33.5 min^{-1} (Fig.4.13A).

The wave formation appears to be a function of the internal geometry of the bag, especially the upper and lower surfaces at the end of the bag. Changes in this geometry are likely to have a more significant effect on the fluid dynamics at higher rocking rates, where the fluid is interacting with both the lower and upper side of the bags (Fig.4.5F). Given that the wave formation also determines the extent of bubble entrainment, geometry could also have a significant effect on the volumetric gas transfer co-efficient. The ends of the bag may act like the baffles of a stirred tank, impeding fluid flow and better distributing the power input from agitation.

4.11.2. Pumping Rate

Pumping rate (Equation 4.8) appears to predict the fluid displacement and fluid velocities over the course of the rock at lower rocking rates (Fig.4.8A), but because it does not account for the fluid moving out of phase, fails to adequately predict this at higher rocking rates (Fig.4.8C). The accuracy of this does support the agitation of the liquid in the bag being due to the pumping effect of the base acting alongside gravity. As the base angular velocity increases at higher rocking rates, the force of gravity does not, resulting in less predictable fluid flow. If pumping rate is predicting fluid velocities below 0.2 ms^{-1}, it appears to be a reasonable prediction for this system (Fig.4.8A). If it is predicting fluid velocities above 0.3ms^{-1}, then for this system the fluid will be flowing out of phase, and wave formation resulting in bubble entrainment will probably be occurring as well as significant turbulence (Fig.4.13B).

4.11.3. Implications for the Use of Rocked bags

The rocked bag appears to be a highly versatile system, with the capability to conduct cell culture over a very large range of turbulence levels. The results obtained in Chapter 3 suggest that the system can support moderate density cell culture at relatively low rocking rates with surface aeration (Fig.3.6), and these data show that at these lower rocking rates, the fluid dynamics are significantly more gentle than a stirred tank (Fig.4.13). At higher rocking rates however, the system produces fluid dynamics very similar to that of an equivalently scaled stirred tank bioreactor, which could ease technology transfer operations. Correlating with what was seen with oxygen transfer previously (Fig.3.1A), the fluid dynamics in rocked bag is highly sensitive to rocking rate, which means characterisation may need to be done prior to conducting cell culture.

That the rocked bag at 42 min^{-1} produces higher peak turbulence than a stirred tank at the same mean turbulence indicates less efficient disspation of the energy (Fig.4.13). This greater range of turbulence kinetic energy measured in the rocked bag may have implications for the relative cell culture performance. Sieck et al. (2013) demonstrated a reduction in cell specific productivity when cycling cells

through a range of energy dissipation rates using periodic impeller stir speed adjustments. This will be investigated further in Chapter 5 and 6.

In Chapter 3, the phenomenon of gas entrainment in a rocked system was observed in conjunction with a dramatic increase in oxygen mass transfer rate (Fig.3.1A). In Chapter 4, the basis for this phenomenon has been investigated and explained as an interaction between two subsets of the liquid during extreme platform inclination (Fig.4.5, Section 4.11.1). In Chapter 5, the impact of this flow phenomenon on cell phenotype and transcriptome during fed-batch cell culture will be investigated with comparison to a stirred tank bioreactor of equivalent scale.

Chapter 5. Impact of Dispersed Gas Phase on Cell Culture Kinetics and Cell Phenotype and Transcriptome

5.1. Introduction and Aim

It was found in Chapter 3 that the range of rocking rates required for typical cell culture applications bridges the point at which that rocking rate causes the liquid to entrain gas (Fig.3.1A). In a 5 L rocked system, increasing the rocking rate from 15 to 25 min^{-1} can result in a 5-6 fold increase in bubble interfacial area (Fig.3.1A). In addition, measurements in a structural mimic of a rocked bag (Chapter 4) indicate a ten-fold increase in turbulence kinetic energy in response to an increase from 25 to 42 min^{-1} (Fig.4.13).

The bursting of gas bubbles at the liquid surface has been found to significantly contribute to cell damage (Section 1.4.1; Papoutsakis, 1991; Chisti, 2000) even in the presence of shear protectants such as PF-68 (Ma *et al.* 2004). Shear stresses caused by bubble bursting, or equivalent energy dissipation rate (EDR) (Sieck *et al.* 2013) resulted in reduced growth (Ma *et al.* 2002) and productivity in suspended CHO cells (Keane *et al.* 2003). Sub-lethal effects of shear stresses are considerably more difficult to identify (Hu *et al.* 2011). Such effects found in various cell types include changes in membrane fluidity in hybridoma cells (Al-Rubeai *et al.* 1993), G0/G1 phase arrest in the cell cycle in adherent CHO cells (Motobu *et al.* 1998), changes in glycosylation pattern (Godoy-Silva *et al.* 2009) and increased expression of oxidative stress and anti-apoptotic genes in NS0 cells in response to excessive sparging at miniature scale (Kondragunta *et al.* 2012). Animal cells have also been found to respond differently to different types of shear flow (Tanzeglock *et al.* 2009), with cells undergoing necrosis at 1 and 500Pa for simple shear flow and extensional flow respectively.

In traditional stirred tank bioreactors, energy dissipation from impeller rotation has been widely studied using a variety of techniques (Section 1.15.1; Gabriele *et al.* 2009; Kresta and Wood 1993). Investigations into the effect of impeller rotational speed on the performance of suspended animal cells in the absence of a dispersed

gas phase has indicated very little negative impact even at high impeller rotation rates <1500 rpm (Zhang & Thomas 1993; Kunas & Papoutsakis 1990). At larger scales, the heterogeneity of the EDR increases (Ducoste & Clark 1998), and this cycling of the cells through regions of high and low EDR is thought to contribute to the poorer performance of cells (Sieck *et al.* 2013).

The rocked bag provides an alternative hydrodynamic environment, with fluid velocity and turbulent kinetic energy changing rapidly throughout the rock and in response to rocking rate (Fig.4.13) as well as gas entrainment (Fig.3.1A). By manipulating the bag rocking rate while controlling all other relevant inputs (DO, pH, glucose concentration), it is possible to conduct cell culture both with and without a dispersed gas phase (Section 3.3). The aim of this chapter is to quantify the effects on suspension CHO cells producing an IgG_4 of the presence or absence of a dispersed gas phase with respect to various aspects of cell phenotype using a hierarchy of assays to evaluate cellular responses within the culture kinetics, cellular physiology and transcription activity of 'sentinel' genes (Kondragunta *et al.* 2012).

Beyond standard cell count, viability, productivity and metabolite assays, a set of phenotypic assays were selected: Cell cycle distribution (Motobu *et al.* 1998), F-actin intensity (Velez-Suberbie *et al.* 2012) and the proportion of apoptotic and necrotic populations (Godoy-Silva *et al.* 2009) were measured using cell staining coupled with flow cytometry, since changes have previously been reported in response to different levels of shear in the cell culture environment. Kondragunta *et al.* (2012) detected changes in the expression levels of specific genes in response to a high shear cell culture environment. Using the 'sentinel' genes identified by Kondragunta *et al.* (2012) as a guide, qPCR based mRNA expression level analysis was conducted for the following genes: SOD1, which codes for an enzyme that responds to oxidative stress (McCord & Fridovich 1969), APEX1, which encodes an enzyme involved in the early stages of DNA repair (Chiarini *et al.* 2000), ARPC3, which encodes a subunit of a complex involved in actin polymerisation (Machesky *et al.* 1994), ABCA1, which codes for a cholesterol efflux pump (Schmitz & Langmann 2001) and DDOST, which encodes a glycosyltransferase enzyme involved

in post-translational glycosylation (Yamagata *et al.* 1998). By looking in more detail at the cell physiology, it should be possible to gain a better insight into the cellular response to bubble induced shear stress using an industrially relevant CHO cell line and bioreactor designs with a stirred tank bioreactor operated as a control.

The specific objectives are as follows:

- To establish an experimental design featuring a hierarchy of assays to investigate the phenotypic and transcriptomic response of GS-CHO cells to different cell culture environments.
- To compare the cell culture kinetics in three different bioreactor configurations; a rocked bag bioreactor operated at two rocking rates, with and without a dispersed gas phase, and a control stirred tank culture.
- To compare the cell phenotype over the time course of the cell culture to quantify the response of the cells actin organisation, cell cycle progression and apoptotic state to the different culture conditions.
- To compare the cell transcriptome over the time course of the cell culture to quantify the response of the cell to the differing culture environments in terms of the expression levels of key genes involved in oxidative stress, DNA repair, actin reorganisation, cholesterol retention and a key gene involved in protein glycosylation.

5.2. Impact on Cell Culture Kinetics

The impact of the presence or absence of a dispersed gas phase in a rocked bag (Section 2.2.1.1) were investigated by conducting cell cultures in rocked bags at 25 and 15 min^{-1}. As a control, a 3.5 L stirred tank (Section 2.3.1.2) was also operated. In terms of process set points and operation, cell cultures were performed as described in Section 2.2.1.

5.2.1. Cell Growth, Viability and IVC

Differences in cell growth in response to different levels of sparging have previously been reported (Oh *et al.* 1992). Conversely, a slightly higher IVC at the higher

rocking rate was previously noted (Section 3.3), in which higher levels of turbulent energy dissipation were measured (Section 4.10). A 15 % Increase in peak cell density in response to higher EDR were also reported by Godoy-Silva *et al.* (2009), although this difference was attributed to run to run variability.

For the three different bioreactor configurations studied here viable cell count, viability and integral viable cell count are shown in Fig.5.1. Cell growth curves reveal similar growth profiles between the three culture configurations. Cells immediately entered exponential phase and grew rapidly up until day 5, where cells entered a linear growth period before slowing significantly at day 7 and reaching peak density at day 8-9 of 12-14x10^6 cells mL^{-1}. The majority of the cell population then moved from stationary into death phase at day 11 with 7-9x10^6 viable cells mL^{-1} remaining by day 14. Differences between the peak cell density were within 16 %, which is within the variability of this system as quantified in Section 3.3.

Cell viability profiles were also very similar for the majority of the culture, with all systems reaching a peak viability of ~98 % at day 6-7. There was a difference noticed after day 13, where the cell population in the bag operated at 15 min^{-1} appeared to lose viability more rapidly than those in the 25 min^{-1} bag and stirred tank (Day 14 viability was 74% in the stirred tank, 67% in the 25 min^{-1} bag and 57% in the 15 min^{-1} bag). Similarly, the stirred tank showed the most rapid reduction in viable cell count from day 12-14, which is an alternate indicator of cell death rate given the inability of the trypan blue exclusion assay (Section 2.2.1) to count completely lysed cells. A significantly different rate of growth would indicate that the level of shear stress generated by bubble bursting was having a lethal effect on the cells, so this data suggests that these systems are in the sub-lethal effect range. This finding is similar to the work of Sieck *et al.* (2013), who observed no measurable difference in growth in response to 400-fold differences in impeller derived EDR.

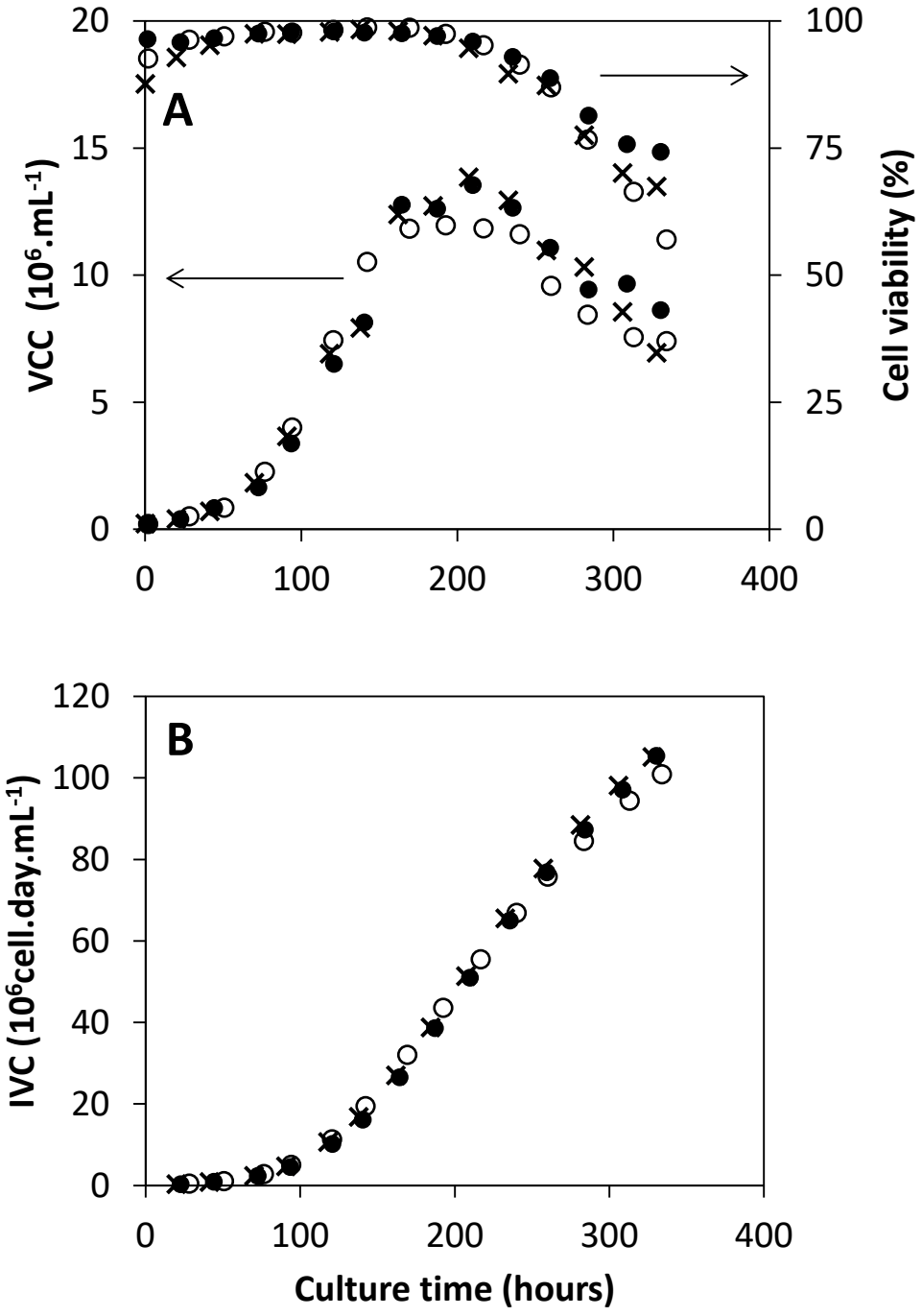

Figure 5.1: Cell culture growth, viability and integral viable cell count for surface aerated bag (open circles), dispersed gas phase bag (filled circles) and stirred tank (crosses) during fed-batch culture of GS-CHO cells: (A) Viable cell count and viability (B) integral viable cell count against cell culture time. (N = 1) Bioreactors operated as described in Section 2.2.1.1. and 2.2.1.2. and sampled as described in Section 2.3.1.

5.2.2. Antibody Production and Cell Specific Productivity

In addition to cell growth, it is also important to investigate the impact of culture conditions on antibody titre and cell specific productivity (Section 2.4.3.2). Fig.5.2 shows the measured antibody titre profiles and cell specific productivities. Antibody titre was 20 % lower over the course of the cell culture in the 25 min^{-1} bag, with antibody production in the 15 min^{-1} bag and the stirred tank effectively identical (harvest antibody concentration differed by <3 %). All systems followed a similar pattern, with production slowing towards the end of the culture as viable cell count falls. This difference is could indicate a shift of the cells grown in the 25 min^{-1} bag towards survival and away from production, as noted in response to excessive gassing by Kondragunta *et al.* (2012). A reduction in recombinant protein productivity in response to sparging has also been shown by Keane *et al.* (2003).

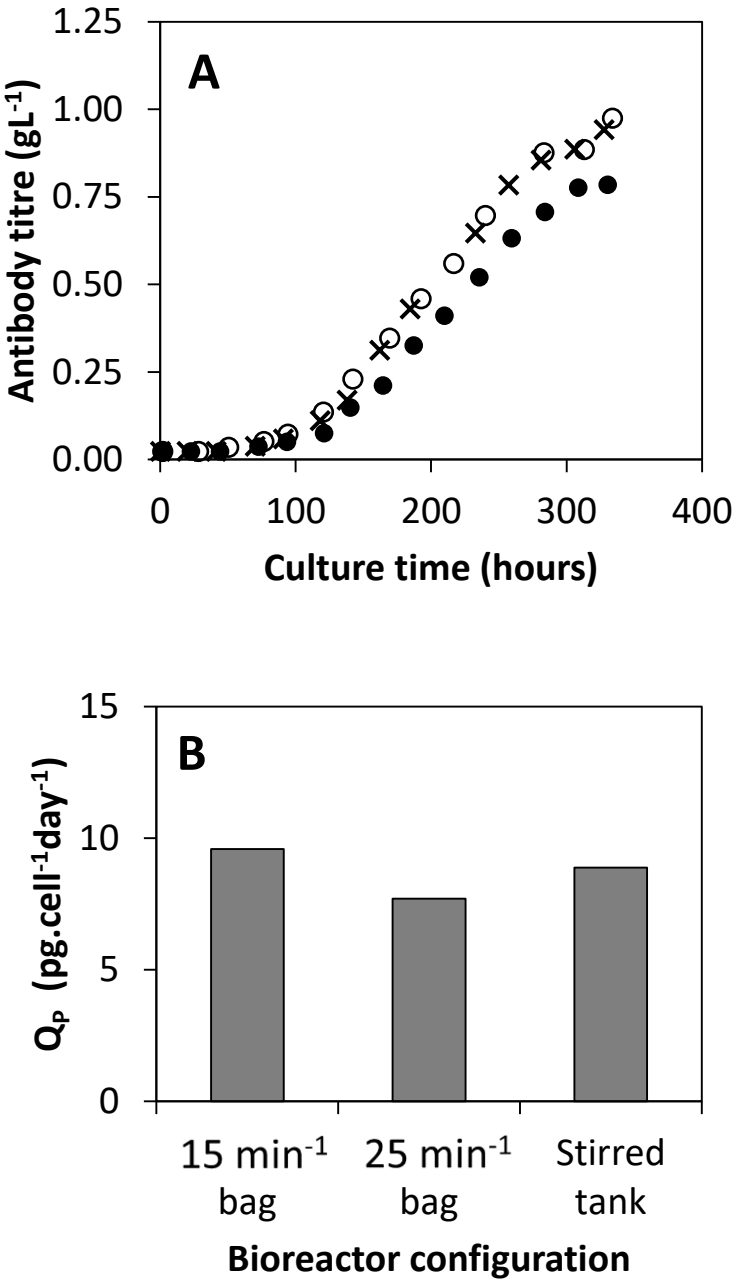

Figure 5.2: Antibody titre and productivity for surface aerated bag (open circles), dispersed gas phase bag (filled circles) and stirred tank (crosses) during the fed-batch cell culture described in Fig.5.1. (A) Antibody titre over the culture duration and (B) whole culture duration cell specific productivity. (N = 1) Cell culture kinetics described in Figure 5.1. Antibody concentration was measured as in section 2.3.2, cell specific productivity was calculated as in Section 2.3.3.2. Bioreactors operated as in section 2.2.1.1. and 2.2.1.2. and sampled as in Section 2.3.1.

5.2.3. Glucose Consumption and Lactate and Ammonium Production

High levels of EDR have been correlated with higher glucose consumption rates. Keane *et al.* (2003) reported a 42% increase in glucose consumption rate in response to 6.4 $x10^2$ Wm^{-3} and McDowell & Papoutsakis (1998) report a 40 % increase in response to impeller rotation rates of 300 compared to 80 rpm although no specific EDR were calculated. Godoy-Silva *et al.* (2009) measured no difference in glucose and lactate concentration trends for an industrial CHO cell line at EDR of up to 6.4 $x10^6$ Wm^{-3}. Fig.5.3 shows the cumulative glucose concentration, lactate concentration and ammonium concentration. Cumulative glucose consumption rate was found to be 7 % higher for the 25 min^{-1} bag and stirred tank than the 15 min^{-1} bag over the course of the cell culture. The 25 min^{-1} bag and stirred tank also had generally higher lactate concentrations after day 5, with peak values 20 % higher than in the 15 min^{-1} bag.

Greater lactate consumption in CHO cells has been associated with the expression of anti-apoptotic factors (Dorai *et al.* 2009), however this would contradict the lower viability seen towards the end of the culture in the 15 min^{-1} bag since anti-apoptotic proteins have been associated with longer maintenance of higher viability and cell counts (Kondragunta *et al.* 2012). Higher lactate consumption rates could also indicate a more productive metabolism (Martinez *et al.* 2013) given the increased antibody production of the 15 min^{-1} bag compared to the 25 min^{-1} bag (Figure 5.2B) and could, to some extent, explain the lower glucose consumption. Higher levels of lactate production has been theorised to be related to reduced oxidative metabolism within the mitochondria (Zagari *et al.* 2013).

The ammonium concentration profiles very similarly for all cultures up until day 7, where the 15 min^{-1} bag and tank trend upwards from ~1.2 mM to reach a peak of 2.8 mM at day 14, while the 25 min^{-1} bag only reaches 1.7 mM in the same period. The higher final peak in ammonium concentration at 15 min^{-1} and in the stirred tank may explain why they suffer the most rapid reduction in viability and viable cell density respectively in the final stages of the cell culture, although these values for ammonium are the 10mM level associated with toxicity in CHO cells (Lao & Toth

1997) they may be acting in association with other stressors to cause cell death (Zhu *et al.* 2005).

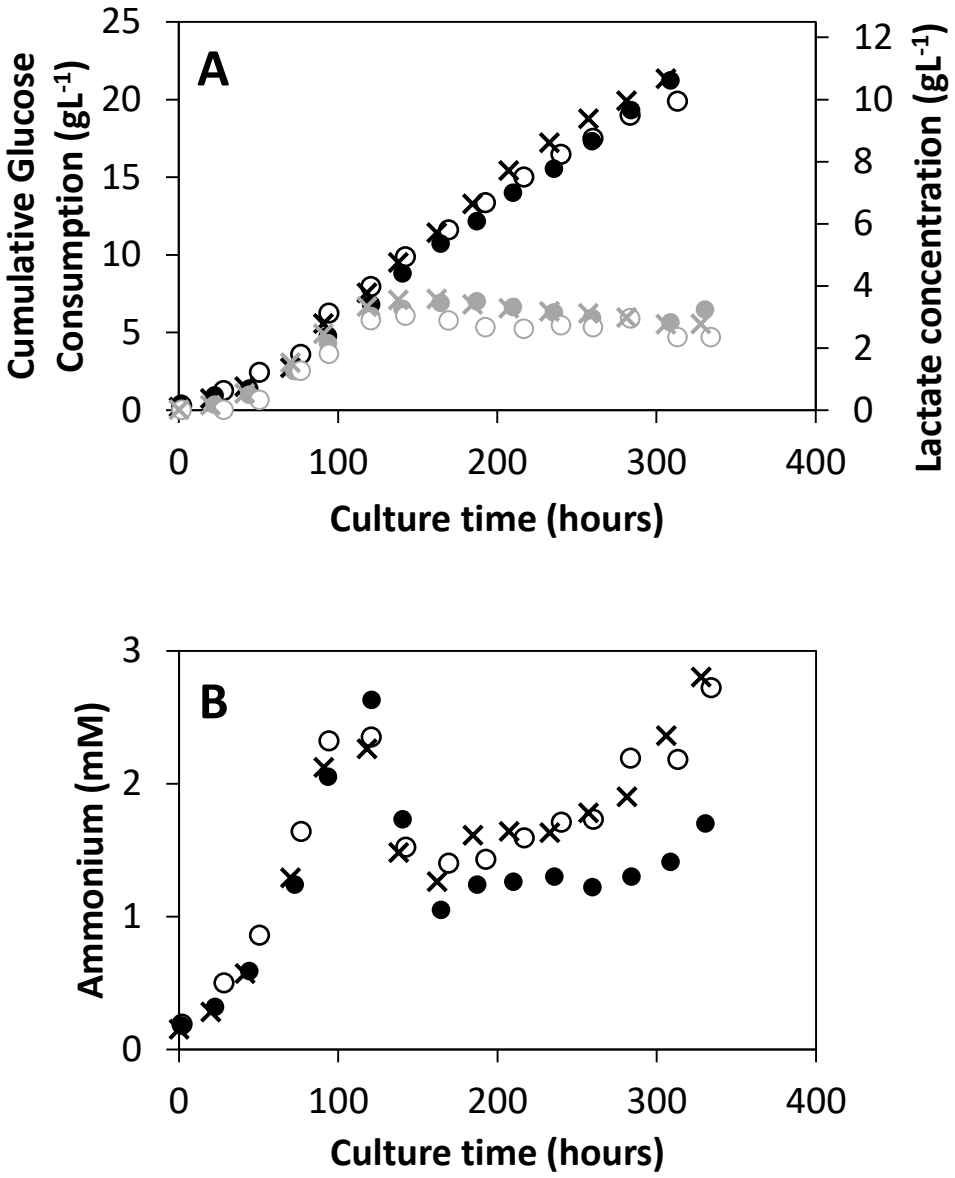

Figure 5.3: Extracellular cumulative glucose and daily lactate concentration for the surface aerated bag (open circles), dispersed gas phase bag (filled circles) and stirred tank (crosses) during the fed-batch cell culture described in Fig.5.1. The cumulative glucose consumption and lactate concentration (A) and daily ammonia ion concentration (B). (N = 1) Metabolite concentrations were obtained as in Section 2.3.2. Cumulative glucose concentration was calculated as in section 2.3.3.3. Cell culture kinetics are described in Fig.5.1 and 5.2.

5.2.4. Cell Diameter

Cell size changes in response to adverse cell culture conditions have been noted in Section 3.3 as well as by Godoy-Silva *et al.* (2009). Cell size has been theoretically related to shear stress in that cells may shrink in response to stress forces, or the shear stress would selectively damage larger cells due to the scale of turbulent eddies (Sections 1.4.1 & 3.3; Papoutsakis 1991). Modal cell sizes over the course of the cell culture for the three bioreactor configurations are shown in Fig.5.4. This technique counts cell aggregates as large particles, hence the modal average was used to filter out any upward bias of cell size measurement. Modal cell size showed very similar trends for all culture configurations, with the cell size falling from 14 to 13 µm over exponential phase as the cells rapidly multiply. For the remainder of the cell culture, modal cell size rose linearly from 13 to 18 µm as the cells. These results suggest that in this case, there is no clear effect on cell size in response to these different cell culture environments.

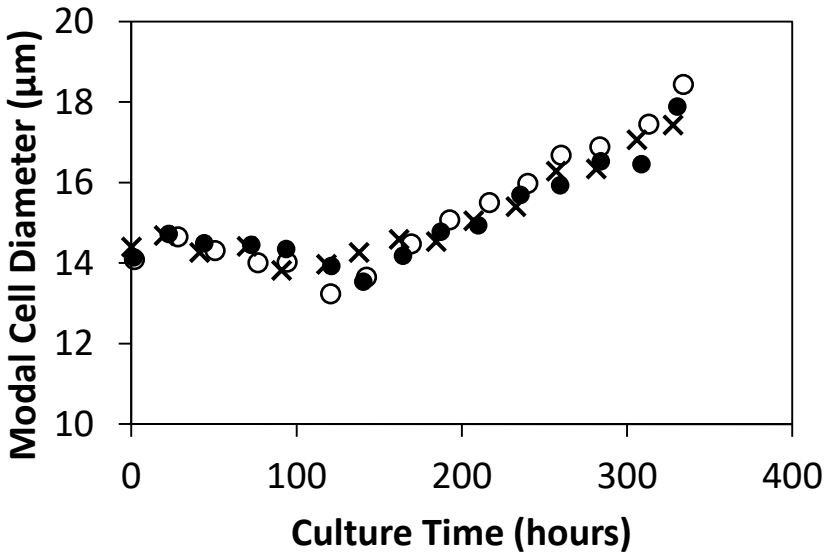

Figure 5.4: Modal cell diameter for surface aerated bag (open circles), dispersed gas phase bag (filled circles) and stirred tank (crosses) during fed-batch cell culture, kinetics described in Fig.5.1. (N = 1) Cell particle size distribution was determined by CASY TT (Roche) and the modal particle size was taken as the average viable cell size as described in Section 2.3.1. Cell culture kinetics are described in Fig.5.1 and 5.2.

5.3. Cell Phenotype Impacts

5.3.1. Filamentous Actin Intensity

Actin intensity was measured over the course of the cell cultures by flow cytometry to detect changes in response to the different cell culture environments as detailed in Section 2.4.6.2. Per cell average Filamentous actin (F-actin) intensities over the course of the cell culture for the three bioreactor configurations are shown in Fig.5.5. All cell culture systems followed similar trends over the course of the culture, with the 15 min^{-1} bag having significantly greater actin intensity for the majority of the first half of the cell culture duration. A two tailed t-test comparing the 25min^{-1} bag and stirred tank to the 15min^{-1} bag gave p-values of 0.03, 0.238, <0.001 and 0.06 for days 4,6,7 and 8 respectively. On days 12 and 14, the 15min^{-1} bag had significantly lower actin intensities ($p = 0.02$ and 0.01 respectively, *t*-test, Section 2.4.1) and was otherwise insignificantly different.

Changes in cell cytoskeleton have been previously reported in response to changes in the dispersed gas phase (Velez-Suberbie *et al.* 2012) as well as changes in the expression levels of genes relating to actin polymerisation (Kondragunta *et al.* 2012). Since F-actin provides mechanical support to the surface of the cell (Cooper, 2000) an increase in F-actin might be expected in response to an increase in shear stress. However, the opposite is being noted here, with the actin intensity falling in response to bubble related shear stress. Velez-Suberbie *et al.* (2012) noted the same when comparing suspended CHO cells cultured in a sparged stirred tank with those cultured a bubble free silicon membrane aerated stirred tank.

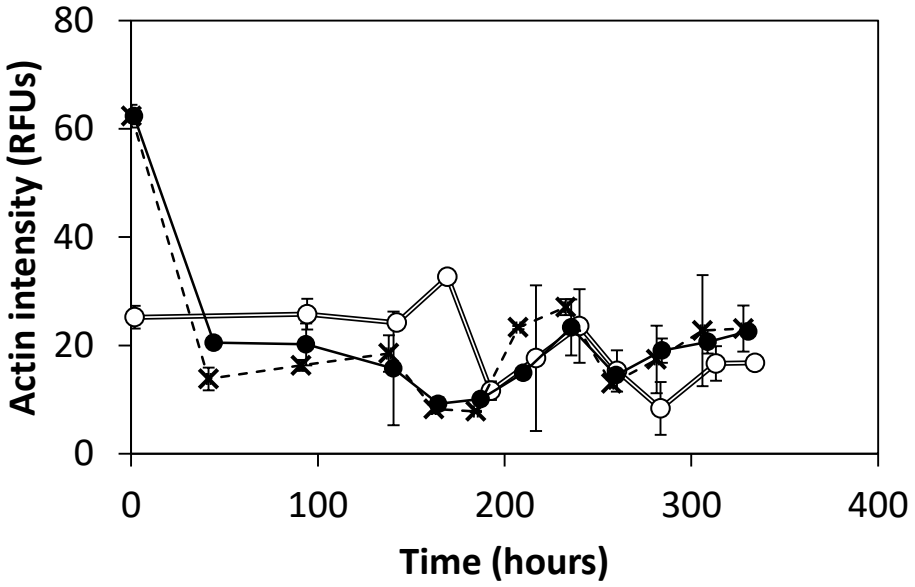

Figure 5.5: Filamentous actin intensity throughout the cell culture for surface aerated bag (open circles), dispersed gas phase bag (filled circles) and stirred tank (crosses). measured by flow cytometry. Cell culture kinetics described in Figure 5.1. Error bars represent one standard deviation (n = 2). Samples were stained by phalloidin and analysed by flow cytometry as described in Section 2.3.6.2. Cell culture kinetics are described in Fig.5.1 and 5.2.

5.3.2. Cell Cycle Distribution

Cell cycle arrest has been associated with oxidative stress in CHO cells (Bijur *et al.* 1999, Clopton *et al.* 1995). Cells currently in G1 are arrested in G1, while cells in S phase have been found to move to and then arrest in G2/M phase (Clopton *et al.* 1995). Cell cycle profiles show the proportion of cells residing in G1/0, S and G2 phase of the cell cycle based on the concentration of DNA in the cells.

The cell cycle distribution at four time points throughout the cell culture for the three bioreactor configurations are shown in Fig.5.6. All configurations show coarsely similar profiles, with the G0/G1 population increasing at the expense of the S population for the first 10 days of the culture followed by a reversal in this trend, while G2/M phase maintains a lower baseline level for the duration. Once the growth rate slows after day 5, there is a marked reduction in the proportion of cells in S phase (DNA replication) and increase in the proportion in G1/0 phase (cell growth), which is in line with the cell growth (Section 5.2.1) and cell size (Section

5.2.4) trends. The most evident difference between the culture configurations is in the relative populations in S phase and G2 phase. At 25 min^{-1} averaged over all sample time points, there are 2.9-fold as many cells in S phase compared to G2 phase, while at 15 min^{-1}, the ratio is 1.6-fold. Since cells progress from S phase into G2 phase and since cell growth rates have already been shown to be very similar (Fig.5.1), this suggests that at 15 min^{-1} the cells may be accumulating in G2/M phase.

S phase involves DNA replication and damage repair while G2/M phase contains a DNA damage checkpoint (Clopton *et al.* 1995), so arrest in G2/M phase may indicate significant DNA damage. Notably, at day 8, 28% of the cells cultured at 15 min^{-1} are in G2/M phase while only 8 and 10 % of cells from the 25 min^{-1} bag and stirred tank respectively are in G2/M phase. Data connecting cell cycle progression with shear stress by Motobu *et al.* (1998), found arrest in G0/G1 phase in response to shear stress in non-confluent adherent CHO cells, and also found a 50 % reduction in the proportion of cells in S phase. It was proposed by Motobu *et al.* (1998) that the shear stress response inhibited DNA replication. These data do not show a significant difference in the population in G0/G1 phase, or an associated growth rate effect, but do show consistent differences over the course of the cell culture in the proportions of cells in G2/M phase in different cell culture conditions. These results therefore suggest that the cells cultured in the bag rocked at 15 min^{-1} may be experiencing the highest levels of stress, contrasting with the expectation that the lack of a dispersed gas phase provides a less stressful cell culture environment.

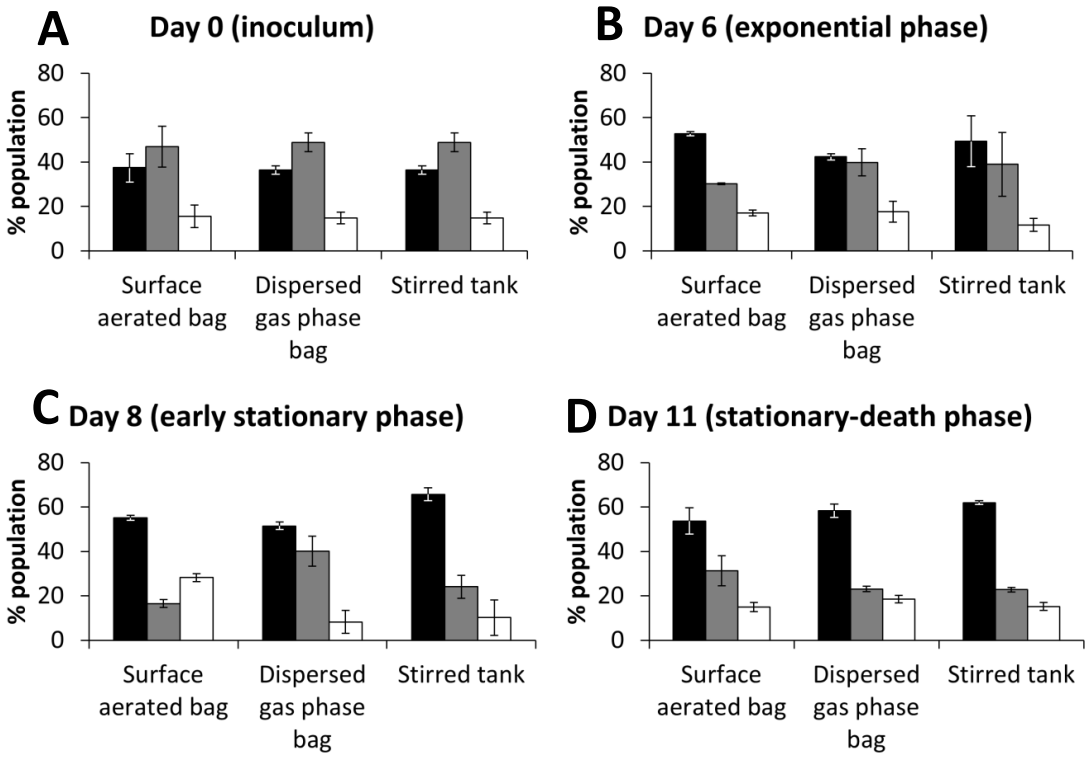

Figure 5.6: Cell cycle distribution at various time points throughout the cell culture for the three bioreactor configurations; (A) Day 0, (B) Day 6, (C) Day 8, (D) Day 11. G0/G1 phase (black bars), S phase (grey bars) and G2/M phase (white bars). Cell culture kinetics described in Fig.5.1. Error bars represent one standard deviation (n = 2). Samples were stained with propidium iodide and analysed by flow cytometry. Assay details can be found in Section 2.3.6.1. Cell culture kinetics are described in Fig.5.1 and 5.2.

5.3.3. Cell Viability Distribution

The 7-AAD/Annexin-V assay measures the presence or absence of apoptosis linked cell membrane proteins as well as the permeability of that membrane (Section 2.3.6.2). This is a more sensitive assay than trypan blue exclusion used by the ViCell to measure cell percentage viability (Section 2.3.1), because it differentiates between early and late apoptotic or secondary necrotic cells as well as quantifying necrotic cell debris. While the presence of necrotic cells is unlikely, this flow cytometric assay is not able to differentiate between cells in late apoptosis or secondary necrosis because in both cases membrane integrity has been lost by the cell (Dive et al. 1992). In all systems, there was a gradual reduction in the proportional viable cell population over the first 8 days of the cell culture,

combined with a small increase in late apoptotic and necrotic populations as shown in Figure 5.7. After day 8, there was a more rapid reduction in viable cells, which was most pronounced at 15 min^{-1}, with a 1:1 ratio of viable to late apoptotic cells by day 11 and 32 % of the cells being necrotic by day 13. In the stirred tank, the reduction in the relative viable cell population was more gradual but by day 14, the necrotic cells constituted 29 % of the total. The bag at 25 min^{-1} showed the least progression into apoptosis and necrosis, with the peak necrotic cell proportion being 22 % at day 13. This is in agreement with what was previously observed with the low actin intensity towards the end of the 15 min^{-1} bag cell culture (Section 5.3.1); apoptosis can result in small blebs being formed on the cell surface, which can fall off during fixation and then show up as low intensity traces on the actin flow cytometry (Velez-Suberbie *et al.* 2012). These findings contrast with Velez-Suberbie *et al.* but are in line with Kondragunta *et al.* (2012), in which a greater level of shear stress was found to maintain cell viability due to the expression of anti-apoptotic proteins. The significant proportion of necrotic cells which accumulate after day 8 in the 15 min^{-1} bag, coupled with the drop in viability suggest significant changes in cellular health after that point. The significantly greater proportion of cells in G2/M arrest at day 8 in Section 5.3.2 appears to precede the rapid reduction in cell health noted between day 8 and day 10, suggesting that the cells in the 15 min^{-1} bag are significantly stressed at day 8.

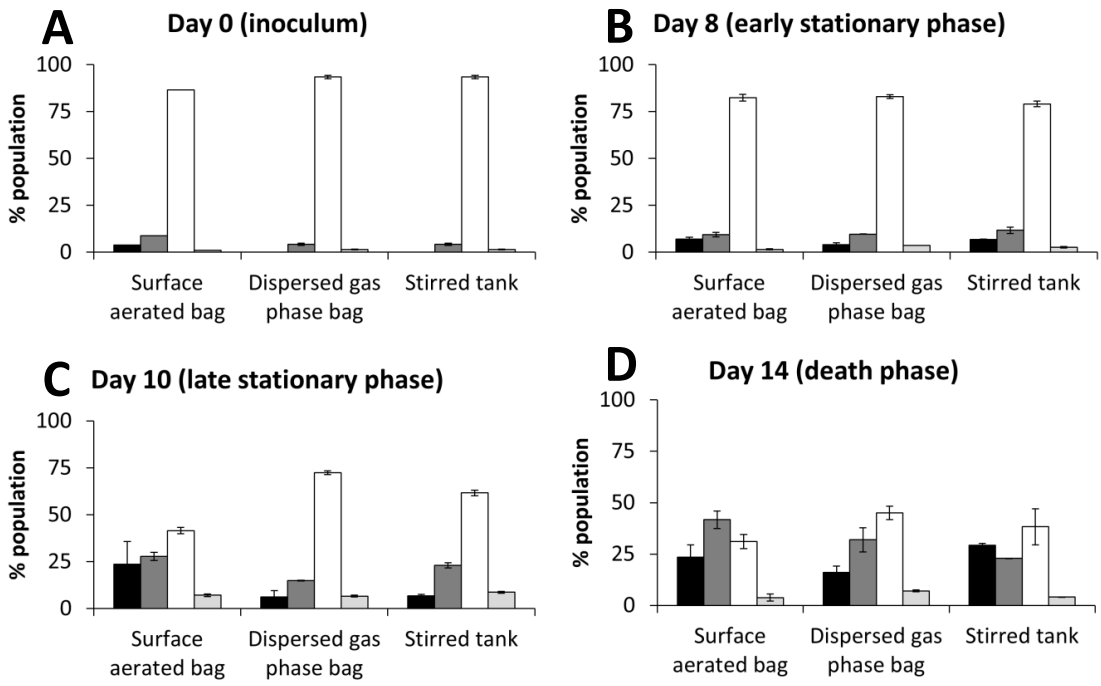

Figure 5.7: Cell viability distribution at various timepoints throughout the cell culture. (A) Day 0, (B) Day 8, (C) Day 10 and (D) Day 14. Necrotic debris (black bars), Late apoptotic/secondary necrotic cells (dark grey bars), viable cells (white bars) and early apoptotic cells (light grey bars). Cell culture kinetics described in Figure 5.1. Error bars represent one standard deviation (n = 2). Cells were stained with Annexin V-FITC and 7-ADD and analysed by flow cytometry. Assay details can be found in Section 2.3.6.3. Cell culture kinetics are described in Fig.5.1 and 5.2.

5.4. Transcriptomic impacts

As part of the experimental design, a set of genes were identified for a focussed transcriptomics study based, in part, on the previous work of Kondragunta *et al.* (2012); this revealed a subset of genes that were found to change in expression levels of oxidative stress related genes in response to different culture configuration. Actin polymerisation was measured, since this had been shown to change by Velez-Suberbie *et al.* (2012) as well as glycosylation since high EDR have been shown to have an effect by Godoy-Silva *et al.* (2009). Finally, cholesterol retention was measured due to its importance in controlling membrane fluidity and cell stress signalling (Zhang *et al.* 2011).

5.4.1. Cell Stress Response

SOD1 and APEX1 are both expressed in response to cellular stress, specifically oxidative stress. SOD1 encodes an enzyme which is responsible for destroying superoxide radicals to prevent further damage to the DNA (McCord & Fridovich 1969), while APEX1 encodes and enzyme which cleaves to the 5' end of the DNA error to start the process of base excision repair (Chiarini *et al.* 2000). Expression levels of both of these genes were found to rise over the course of the culture, with expression increasing by at least 4-fold for SOD1 and 1.5-fold for APEX1. This falls in line with the viability data shown in Figure 5.1, as the cells would express more defensive genes as cellular viability falls towards the end of the cell culture. In general, expression levels were similar but were slightly higher in the 15 min^{-1} bag and lower in the 25 min^{-1} bag, with expression levels in the stirred tank falling between the two. This correlates with the viability and apoptosis assays and also the cell cycle retention in phase G2/M in response to DNA damage. At the very least, it can be said that in this case, shear stress does not appear to be affecting the oxidative stress that the cell population is under. Expression of these genes has previously been associated with maintenance of cell count and cell viability (Kondragunta *et al.* 2012), however, in our case, the 15 min^{-1} bag actually suffers the most rapid viability drop following the increase in expression of these factors. It may be that the expression of these proteins is in response to detrimental changes in the culture chemistry rather than as a result of shear stress.

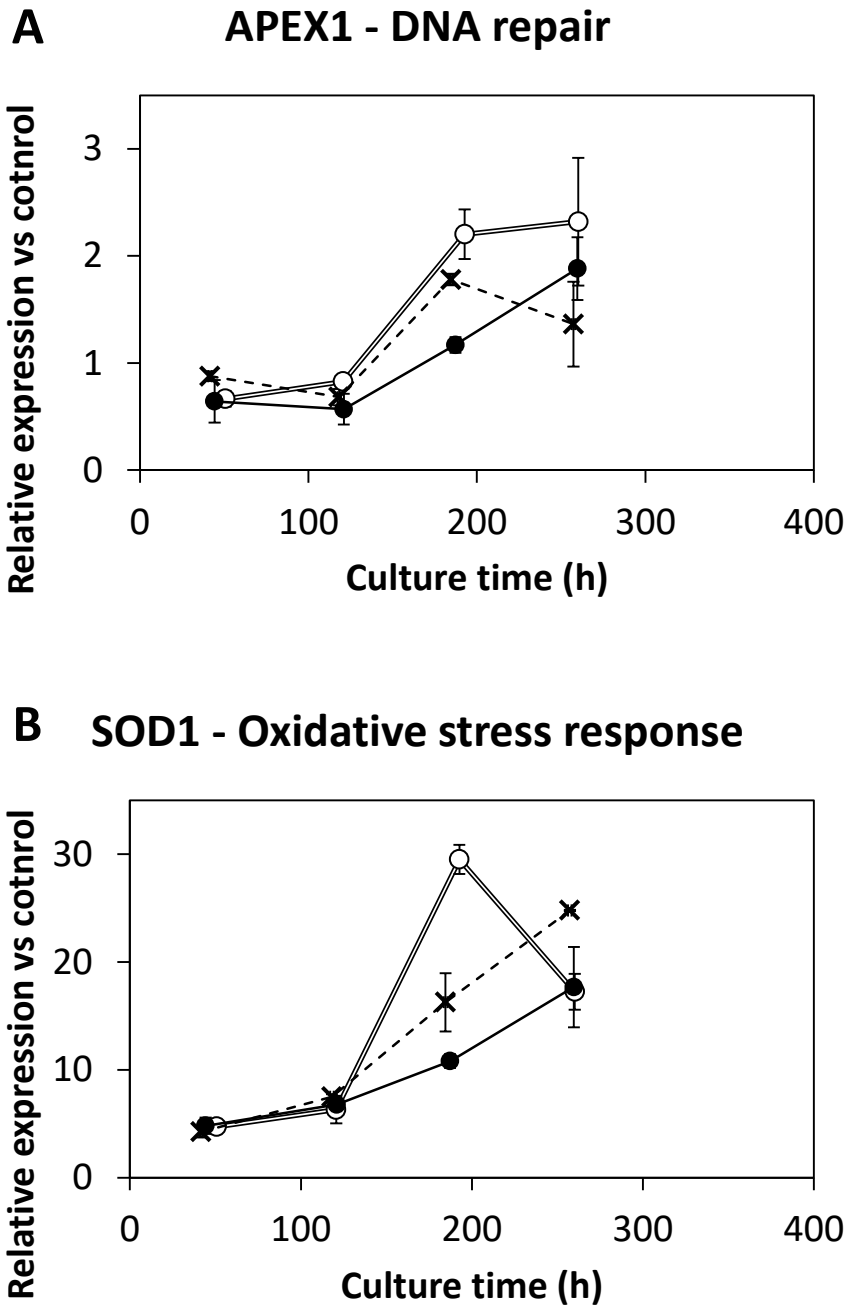

Figure 5.8: Intracellular mRNA expression levels of APEX1 and SOD1 at various timepoints throughout the culture. (A) DNA repair gene, APEX1, expression and (B) oxidative stress response gene, SOD1, expression. Surface aerated bag (open circles), dispersed gas phase bag (filled circles) and stirred tank (crosses). Cell culture kinetics described in Figure 5.1. Error bars represent one standard deviation (n = 3). Levels of intracellular mRNA were measured by qPCR and compared to ACTB expression as a control. For further assay details refer to section 2.3.5. Cell culture kinetics are described in Fig.5.1 and 5.2.

5.4.2. Cell Physiological Response

ARPC3 encodes a subunit of a protein complex involved in the control of actin polymerisation (Machesky *et al.* 1994). F-actin intensity reductions were previously observed in response to a dispersed gas phase by Velez-Suberbie *et al.* (2012). The expression levels measured here correlate with the F-actin intensity levels measured on the flow cytometer (Section 5.3.1). The 15 min^{-1} bag appeared to express lower levels than the 25 min^{-1} bag and stirred tank of ARPC3 in the early part of the culture when the F-actin levels were higher, however this was not statistically significant ($p = 0.54$ and 0.47 on day 2 and 5 respectively, Fig.5.5). The cells within the 15 min^{-1} bag increased the expression level of ARPC3, possibly in response to F-actin intensity reducing after day 8 which was followed by a rapid increase in F-actin intensity. On day 8 ARPC3 expression was significantly higher in the 15 min^{-1} bag than in the 25 min^{-1} bag, $p = 0.025$, however by day 12 the differences was no longer significant, $p = 0.25$. This analysis did not reveal any sustained differences in ARPC3 expression, however there was a weak inverse correlation with the filamentous actin measured by flow cytometry (Fig.5.5).

ABCA1 encodes a membrane associated ABC transport protein which is responsible for cholesterol efflux from the cell (Schmitz & Langmann 2001). Given cholesterol's importance in determining membrane fluidity (Sadava *et al.* 2011) and the theory of membrane fluidity being affected by shear stresses (Al-Rubeai *et al.* 1993), a study of the expression of this gene was included in the experimental design. For the majority of the culture, the bubble free cell culture at 15 min^{-1} exhibits significantly higher levels of ABCA1 expression, which would suggest that the cells are removing more cholesterol from the cytoplasm in a bubble free environment than they are in the presence of a dispersed gas phase. Cholesterol could be being retained inside the cell for the purposes of membrane reinforcement or as part of shear stress initiated signal pathways (Ramirez *et al.* 1990) but regardless, there does appear to be a measurable response to the cell culture environment, of which cholesterol is a part.

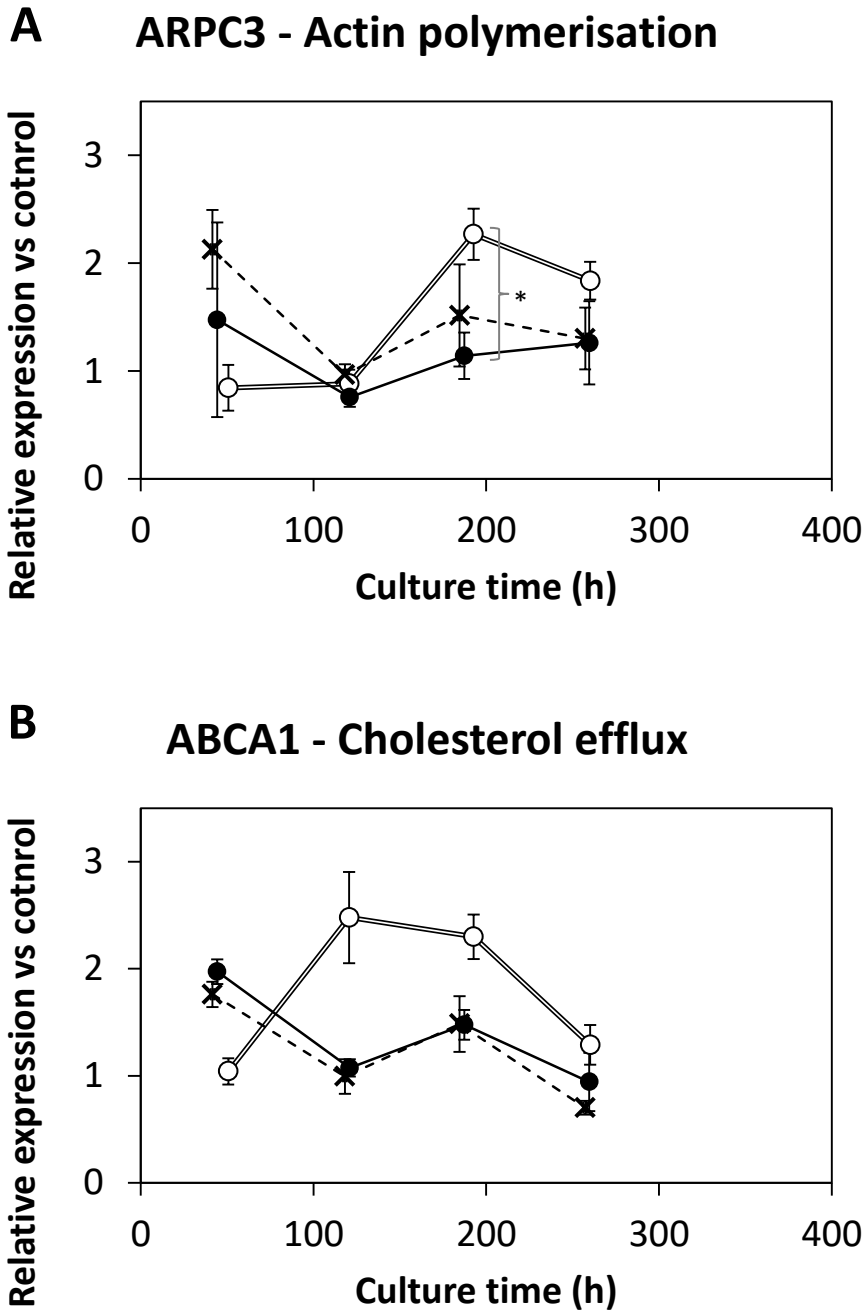

Figure 5.9: Intracellular RNA expression levels of (A) ARPC3 and (B) ABCA1 at various timepoints throughout the culture. Surface aerated bag (open circles), dispersed gas phase bag (filled circles) and stirred tank (crosses). Cell culture kinetics described in Figure 5.1. Error bars represent one standard deviation (n = 3). Levels of intracellular mRNA were measured by qPCR and compared to ACTB expression as a control. For further assay details refer to Section 2.3.5. Cell culture kinetics are described in Fig.5.1 and 5.2. * p = 0.025

DDOST encodes a 48 kDa subunit of the oligosaccharyltransferase complex that transfers the glycan chain from a lipid carrier to nascent proteins in the endoplasmic reticulum lumen known as Dolichyl-diphosphooligosaccharide--protein glycosyltransferase (Yamagata *et al.* 1998). Changes in the levels of N-linked glycosylation has been previously associated with differing levels of shear stress (Velez-Suberbie *et al.* 2012; Godoy-Silva *et al.* 2009) and DDOST expression has been found to change significantly in response to shear stress (Kondragunta *et al.* 2012). DDOST expression was very similar for all bioreactor configurations for the first 5 days of cell culture, however at the day 8 point there was significantly more expression in the bubble free bag and similarly lower values in the two environments with a dispersed gas phase. The generally higher expression in the bubble free bag correlates with the slightly higher cell specific productivity; therefore there is no clear change in the expression of this protein in response to the shear stress.

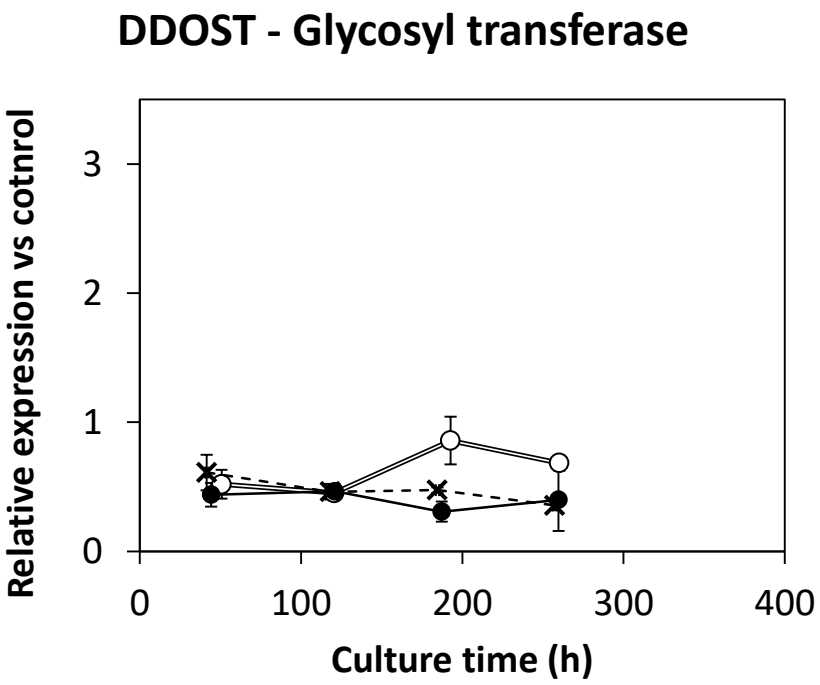

Figure 5.10: Intracellular RNA expression levels of DDOST at various timepoints throughout the culture. Surface aerated bag (open circles), dispersed gas phase bag (filled circles) and stirred tank (crosses). Cell culture kinetics described in Figure 5.1. Error bars represent one standard deviation (n = 3). Levels of intracellular mRNA were measured by qPCR and compared to ACTB expression as a control. For further assay details refer to section 2.3.5. Cell culture kinetics are described in Fig.5.1 and 5.2.

5.5. Summary

The aim of this chapter was to measure the response of the cells in terms of cell culture kinetics, cell physiology and transcription of key sentinel genes to cell culture in rocked bags at different rocking rates and a stirred tank. In comparing the results from the three different bioreactor configurations, there were clear differences between the bubble free rocked bag and the rocked bag with the dispersed gas phase in terms of the protein productivity (Figure 5.2B), which suggests that the presence of this dispersed gas is having a detrimental effect on the cells. This is in line with the finding in Section 3.3, Fig.3.6D. There is no evidence of this reduced productivity in the stirred tank however, which also has a dispersed gas phase (Fig.5.2B). There is also no measurable difference in cell growth in response to these differing culture environments so this reduced

productivity is not a function of lethal cell culture conditions, indeed the bag culture with a dispersed gas phase maintains the highest viability and viable cell count at harvest (Fig.5.1A) as was previously observed in Section 3.4.

Accordingly, when looking at the cell viability and cell cycle in more detail, the 25 min^{-1} bag, which was previously hypothesised to provide the most stressful cell culture conditions (Section 3.10), has the smallest proportion of apoptotic and necrotic cells as well as the fewest cells arrested in G2/M phase (Fig.5.6). A similar effect to this was noted in Hybridoma cells by Kondragunta *et al.* (2012), however this was attributed to increased expression levels of anti-apoptotic genes such as SOD1 and APEX1. In this case, measurement of the levels of SOD1, a key gene involved in the oxidative stress response, suggest no significant change between the different configurations over the time course of the cell culture (Fig.5.8B), while the expression of the DNA repair gene APEX1 was higher in the bubble free bag (Fig.5.8A). Physiologically, the cells appear to subtly respond to the dispersed gas phase; cellular F-actin levels and the expression of an actin polymerising subunit were very similar across the three culture configurations (Fig.5.9), but they were especially close for the two cultures with a dispersed gas phase.

By applying a hierarchical set of assays to investigate cellular response to culture environments, clear differences were noted between cultures. Indicators of cellular stress were not found to correlate with bubble mediated shear stress, indicating that all configurations provided conditions suitable for cell culture. Cell health and cell cycle distribution showed high similarity between the high rocking rate bag and stirred tank. This supports the similarity noted between the mechanical robustness of the harvest material noted in Section 3.3.1.

In the next chapter, the generic nature of these findings is investigated for a second industrial cell line and the impact of bioreactor operating conditions on antibody product quality will be investigated further.

Chapter 6. Impact of Dispersed Gas Phase on Product Quality Attributes [1]

6.1. Introduction and Aim

As shown in Chapter 5, the physical environment in which a mammalian cell is cultured can have a significant effect on cell viability and various markers related to cell phenotype in response to sub-lethal levels of stress. These also had an impact on antibody titre (Fig.5.2). In addition, the physical environment in which a mammalian cell is cultured can impact upon the quality attributes of the product (Hossler *et al*. 2009; Godoy-Silva *et al.* 2009), which is critical in relation to regulatory approval (Section 1.10). Working in collaboration with Eli Lilly, this final results chapter explored the translation of the earlier findings into industrial practice using a second industrial cell line to examine the generic nature of the previous findings and exploiting the resources of Eli Lilly (Kinsale) to assess product quality attributes in more detail. Given the commercially sensitive nature of the process it is necessary to omit certain proprietary information such as on medium formulation, product characteristics and critical product quality attributes, and to normalise the product quality assay data.

During the commercial development of a biopharmaceutical process, cell culture will be carried out at several different scales in different bioreactor designs. The challenge when moving between scales or designs lies in ensuring consistent cell culture performance, especially with regard to product quality attributes (Section 1.10). A challenge associated with the use of rocked bags will be transferring processes developed in stirred tanks into rocked bags or vice versa and operation on different sites with different capital equipment investment.

In Chapter 3, an overall engineering characterisation established that the rocking rate is the most important agitation input to manipulate when conducting cell culture in a rocked bag, since it is responsible for the most significant responses in

[1] This chapter is included as part of the UCL requirements for award of the EngD in Bioprocess Engineering Leadership.

volumetric oxygen mass transfer and mixing time. The rocking rate of the rocked bag has been found to have a significant effect on the $k_La(O_2)$, through the increase in the interfacial area because of the entrainment of gas into the liquid due to wave formation at the fluid surface (Section 4.11.1). Lower rocking rates can provide cell culture capable oxygen transfer rates in the absence of dispersed gas (Section 3.3). These findings suggest that cell culture can be performed over a wide range of rocking rates, but it is not known which of these will provide the closest match to STR performance and if this phenomenon occurs in different rocked bag bioreactor configurations.

In STR, technology transfer is typically achieved by considering mixing time, oxygen transfer and carbon dioxide removal (Xing *et al.* 2009). Additional inputs such as volumetric gas flow rate and tip speed can be conserved over scale changes to indicate comparable environments and input control (Berridge *et al.* 2009). Empirical equations to predict the power input and flow regime are also used (Nienow 2014). In rocked bags, it is possible to design conditions that approximately match stirred tanks in terms of oxygen and carbon dioxide transfer and mixing time (Fig.3.1 to 3.5) as well as the turbulence kinetic energy (Fig.4.13).

Product chemical modifications are of critical interest because they directly impact immunogenicity, efficacy and injected half-life of the molecule (Section 1.10). Several non-critical quality attributes are monitored as an indicator of process consistency. Chemical modification, such as deamidation or oxidation, of a critical complementarity-determining region (CDR) residue can affect target binding and therefore efficacy (Vlasak *et al.* 2009). N-terminal glycan composition can affect the immunogenicity and pharmacokinetics of the glycoprotein (Sethuraman & Stadheim 2006). Product chemistry is highly sensitive to the cell culture conditions and can be impacted by dissolved oxygen, nutrient levels, pH, feeding strategies, bioreactor configuration and EDR (Hsu et al 2012; Spearman *et al.* 2011; Godoy-Silva *et al.* 2009). As such, it was considered very important to quantify the effect of rocked bag operation on product quality.

Product quality impacts have been observed by other authors in response to adverse hydrodynamic conditions, most notably in the glycosylation profile (Sieck et al 2013, Velez-Suberbie et al 2012, Godoy Silva et al 2009). Godoy Silva (2009) noted a step increase in the proportion of G1 and G2 glycan species of the resultant mAb between EDRs of 90 and 600Wm^{-3}, which remained unchanged up to $6.4x10^{6}Wm^{-3}$. A higher fucosylation:non-fucosylation ratio was observed by Velez-Suberbie et al in response to a sparged gas phase versus bubble free stirred tank cultivation. Sieck et al (2013) observed higher proportions of high mannose glycan species in antibody produced in bioreactors with one or both of high agitator power input ($525W.m^{-3}$) and volumetric gas flowrate (0.18vvm) but no effect on aggregation, or charged heterogeneity.

An impact was previously noted on the cell specific productivity (Section 3.3) and cellular mechanical robustness (Section 3.3.1) and the cell cycle progression and stress response (Sections 5.3 & 5.4) from adjusting the rocking rate of rocked bags. In this chapter, the aim of this chapter is to compare the effect of rocking rate on the total product quality profile of a state-of-the-art industrial biopharmaceutical process.

The specific objectives of this chapter are:

- To characterise the mass transfer rates of an alternative rocked bag bioreactor, comparing these to previously obtained values (Section 3.2)
- To establish sensitivities associated with the use of single-use probes.
- To compare the product quality of a state-of-the-art manufacturing process executed in rocked bags operated at different rocking rates to control and historical 5 L STR operations.

6.2. Engineering Characterisation of Alternative Bioreactors

The rocked bags used in this chapter were from a different manufacturer to those used for previous cell cultures (Chapters 3 and 5). To determine the conditions at which to operate these rocked bags, initial work focussed on engineering characterisation. Work from Section 3.2 suggested that mixing times would not be a concern at 10 L scale, so the evaluation focussed on oxygen and carbon dioxide mass transfer. These values could also be compared to those previously obtained, to assess the applicability of the previous findings.

6.2.1. Oxygen Mass Transfer

The $k_La(O_2)$ was found to increase rapidly with respect to rocking rate. At or above 14 min^{-1}, interaction between the receding fluid and port recession on the upper side of the bag caused some entrainment of gas. As the rocking rate was increased further, the number of entrained bubbles increased, and their size was observed to reduce, resulting in a pseudo exponential increase in the $k_La(O_2)$ with respect to rocking rate (Fig.6.1A) as found previously found in Section 3.2.1 (Fig.3.1A). Operating the bag at 6^o was also found to produce $k_La(O_2)$ of 58-67 % at 15, 25 and 35 min^{-1} compared to those at 10^o (Fig.6.1C), suggesting the same linear proportional effect observed in Fig.3.2A. Fill volume was found to have a smaller but still very significant effect on $k_La(O_2)$ than in the other rocked bag used in Section 3.2.3, with a 5 % change in fill volume having an approximate 30 % inverse effect on the $k_La(O_2)$ (Fig.6.1B).

As noted in Section 3.2.1, there appeared to be a low response of $k_La(O_2)$ *to* rocking rate below a critical rocking rate and then a significant response of $k_La(O_2)$ above this critical value. This can be seen in bags of several differing designs (Fig.3.1A). Fitting the data presented in Fig.3.1A as two linear relationships with an inflection point at 20 min^{-1} gives a prediction for the $k_La(O_2)$ over a range of rocking rates at 50 % fill volume and 10^o rocking angle. The $k_La(O_2)$ displayed in Fig.3.1A are predicted by:

$$\text{When N} \leq 20\ min^{-1},\ k_La(O_2) = 0.3 \times N \qquad (6.1)$$

$$\text{When N} > 20\ \text{min}^{-1},\ k_L a(O_2) = 1.8 \times N - 30 \quad (6.2)$$

Where *N* is the rocking rate of the bag in min^{-1} and $k_L a(O_2)$ is the volumetric oxygen mass transfer coefficient in hours^{-1}. Equations 6.1 and 6.2 predict $k_L a(O_2)$ with an average prediction error of 32 % and a prediction R^2 value of 0.84. The prediction of Equation 6.1 is more accurate, with the average prediction error being 17 %, while once the $k_L a(O_2)$ increases more rapidly at rocking rates above 25 min^{-1}, the prediction becomes less accurate, with an average prediction error of 42 % of the correct value. It should be noted that some of this prediction error may be accounted for by the confidence in the measured value being lower at higher rocking rates with this bioreactor system (Table 2.2). This suggests that while reasonable predictions can be made of the $k_L a(O_2)$ in lab scale rocked bags, bag geometry may have a significant effect on fluid flow, and therefore impact on oxygen transfer, especially at higher rocking rates, as was previously theorised based on the fluid dynamic characterisation in Section 4.11.1.

In terms of OTR, the $k_L a(O_2)$ in the bag allowed a large range of rocking rates to be feasible for use of the proposed Eli Lilly cell line. Oxygen transfer can be calculated using $k_L a(O_2)$ by the equation;

$$OTR = k_L a \times (C_L^* - C_L) \quad [6.3]$$

where C_L^* is taken as the inlet gas oxygen saturation as a fraction of air saturation concentration and C_L is the liquid phase oxygen saturation as a fraction of air saturation. Given that the control system attached to the bag is capable of delivering pure oxygen to the headspace, and the operational setpoint for DO is 60%. Assuming that the liquid phase would be saturated with oxygen in air (20.95% O_2 v.v^{-1}) at a concentration of 176 µM, and therefore at 840 µM under pure O_2, based on the peak O_2 demand of this process being 1.5 $\text{mmol.L}^{-1}\text{.h}^{-1}$ (Eli Lilly data), any $k_L a(O_2)$ above 2.1h^{-1} can support this process.

Based on the oxygen transfer derived minimum $k_L a(O_2)$, rocking rates of 10 min^{-1} and above would be able to support the cell culture. A rocking rate of 13 min^{-1} in this system produced very similar oxygen transfer rates in the rocked bag and the

lab scale stirred tank (4 and 3 mmol.L^{-1}.h^{-1} respectively) but did so without a dispersed gas phase. A rocking rate of 28 min^{-1} had an evident dispersed gas phase but approximately 3-fold the maximum oxygen transfer rate of the stirred tank. This would help to establish whether a dispersed gas phase was important for comparable cell culture performance. These two rocking rates were chosen to provide the closest equivalence of OTR and gas entrainment to the different rocked bag system used in Chapters 3 and 5.

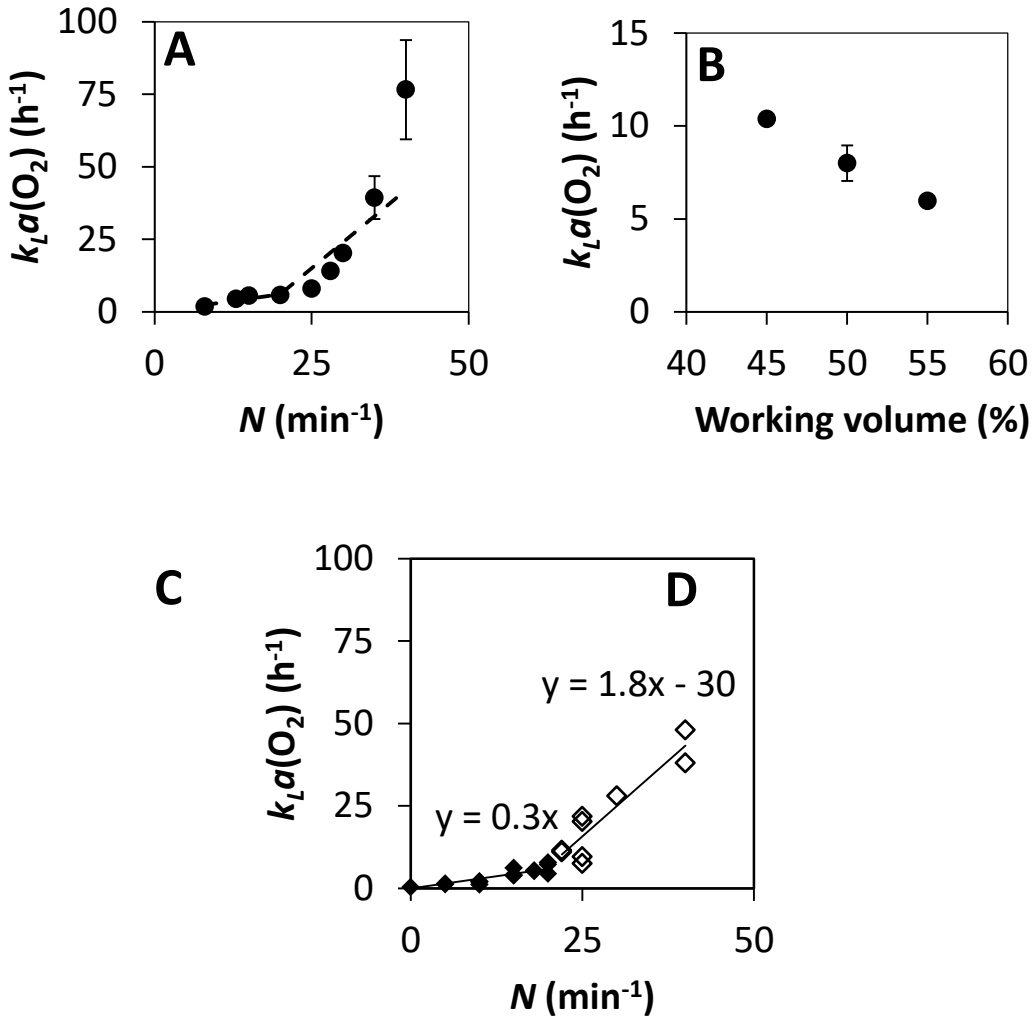

Figure 6.1: $k_La(O_2)$ response to changes in response to (A) Rocking rate; dashed line shows relationship derived from Fig.6.1D, Section 6.2.1, (B) working volume and (C) rocking angle data expresssed as % $k_La(O_2)$ at rocking angle of 6^o compared to 10^o. Values obtained in 10 L Sartorius CultiBag (Section 2.2.2.1). (D) reproduces data from various bioreactors shown in Fig.3.1A, with lines fitted by linear regression for data below (filled diamonds) and above (open diamonds) N = 20 min^{-1}, R^2 = 0.78 and 0.9 respectively. Error bars represent 95 % confidence (n = 3). $k_La(O_2)$ measured as described in Section 2.4.1.

6.2.2. Carbon Dioxide Mass Transfer

A brief evaluation of the CO_2 stripping was also conducted to ensure that the phenomena observed in the 10L Sartorius system agreed with those observed in 10-50 L Appliflex bag and Sartorius 50 L SUB in Fig.3.5C. CO_2 stripping findings fit well with those previously measured in Section 3 (Fig.6.2A). Comparing the $k_La(O_2)$

per gas flowrate in volume of gas per volume of liquid per hour (vvh) plotted against $k_La(O_2)$, shows that the two bag systems analysed compare very closely once differences in interfacial area, as estimated by the $k_La(O_2)$ evaluations (Section 3.2 & 6.2.1) are accounted for (Fig.6.2B). Increasing the airflow rate by 2.5-fold from 0.04 vvm to 0.1 vvm resulted in a 68 % increase in apparent CO_2 stripping rate. This suggests that in rocked bags, CO_2 stripping rate is less geometry dependent.

By using the same volumetric gas flow rate of 0.04 vvm for all configurations, comparable CO_2 stripping performance was ensured. Because of the buffered cell culture medium and controlled pH, changes in the gas flowrate are likely to only affect the addition of pH control substance, rather than the pH of the broth.

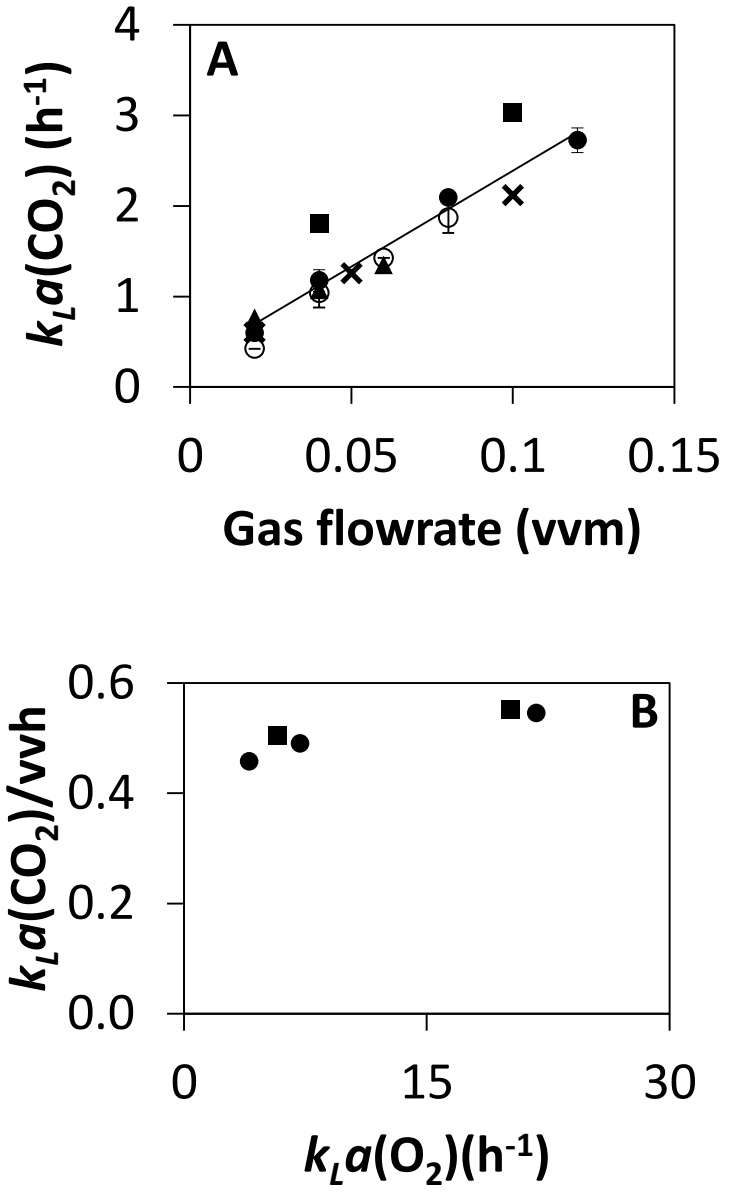

Figure 6.2: $k_La(CO_2)$ response to changes in (A) gas flowrate; 10L (filled circles) n=3, 20L (open circles), n=3 and 50L (filled triangles), n=1 Applikon rocked bag (Section 2.2.1.1), 70L SUB STR (Section 2.2.1.2) and Sartorius rocked bag (filled squares, Section 2.2.2.1) n=1, (B) Shows the comparison of previous $k_La(CO_2)$ values taken in an Appliflex 10L rocked bag (filled circles, Section 2.2.1.1 & 3.2) to the current 10L Sartorius rocked bag (filled squares, Section 2.2.2.1 & 6.2.2) once the difference in $k_La(O_2)$ has been accounted for. Applikon and 50 L SUB data in (A) from Fig.3.5C. $k_La(CO_2)$ determined as in Section 2.4.2.

6.3. Single-Use Probe Evaluations

Optical pH and DO probes are now widely used in single-use bioreactors and have been shown to be comparable to more traditional electrolytic and polarographic probes (Hanson *et al.* 2007). In spite of wide adoption, there remains limited knowhow around their routine use in bioreactors. Before the execution of parallel cell culture in the rocked bags, the basic technology around the single-use probes was characterised to identify potential failure points. pH probes are of particular interest, due to the potential for them to photo-bleach (Personal communication; Sartorius Application Specialist) and the high sensitivity of cells in culture to pH (Section 1.4.1). Covalently immobilised pH sensitive dye patches are attached to the inside of bioreactors and fibre optic cables are used to carry the light from the control tower to the probes and then carry the fluorescent response back. Further details of DO and pH probe mechanisms of detection can be found in Section 1.14.

The installation of the fibre optic cables was identified as a potential challenge, since the C-Flex (Cole-Parmer, London, UK) thermoplastic elastomer tubing into which they must be manually inserted exerts significant resistance during insertion, and the rocking of the bags could potentially work the cables loose. In terms of the cables themselves, there were several physical differences noted; their lengths differed slightly, they developed small bends where they entered their sleeves on the bags and at the end of the cable, the fibre optic centre protruded by differing amounts from the opaque outer protective sheath. These fibre optic (FO) cables were evaluated by successive reinstallation into the probe port of a CultiBag RM 10L (Section 2.2.2.1) filled with 5L of medium mimic (Section 2.4.1) followed by measurement from the control unit (Section 2.2.2.1). The absolute pH phase reading as well as the amplitude are important for accurate pH determination. The amplitude is proportional to the signal-to-noise ratio, with values above 10,000 being acceptable for cell culture (Personal communication; Sartorius Application Specialist).

The bends and length discrepancy (<60 mm over 2,600 mm) did not affect the reading or signal-to-noise ratio, however, the amount the probe protruded from

the opaque sheath that covered the length of the FO cable impacted upon both the signal-to-noise ratio and pH phase reading consistency (Fig.6.3). The pH phase reading is used by the system to calculate the pH, with the relationship between phase and pH being linear and patch specific. In this case, a change of 0.5 pH phase units related to a pH reading that differed by ~0.025. The greater exposure of the FO cable could allow more external sources of light to enter the FO and affect the reported readings. The longest protrusion had 4-fold the average variance in pH phase reading upon reinsertion, suggesting that signal transmission was more sensitive to the orientation relative to the fluorescent patch (Fig.6.3). The FO cable with a transparent core which protruded the furthest from the opaque sheath also had a significantly lower signal-to-noise ratio, although this was still above the recommended value of 10,000. It is not clear whether the protuberance is the cause of this, since there is no correlation over the 0.2-1.5 mm range. This does suggest that the fibre optic cables play an important role in the optical probe signal transmission system and should be evaluated prior to use to maximise their reliability.

Repeated testing of installation consistency also found that occasionally the fibre optic cables with the smallest protuberances (<0.5 mm) would also give especially low pH amplitudes (<1000). This installation sensitivity was further investigated. By deliberately installing the fibre optic a certain distance from the end of the sleeve, and therefore a certain distance from the pH sensitive patch, the effect of 'poor' installation could be quantified. It was found that compared to apparent contact with the end of the sleeve, a fibre optic positioned 0.5mm from the end of the sleeve would affect the pH reading by 0.11 % and at 1mm by 0.63 % (0.025 pH units). The pH amplitude (signal-to-noise) would fall significantly by 27 and 46 % at 0.5 and 1 mm respectively. This suggests that installation precision is not essential for an accurate pH reading but is desirable. This level of attenuation did not explain why some of the FO cables were so sensitive to installation.

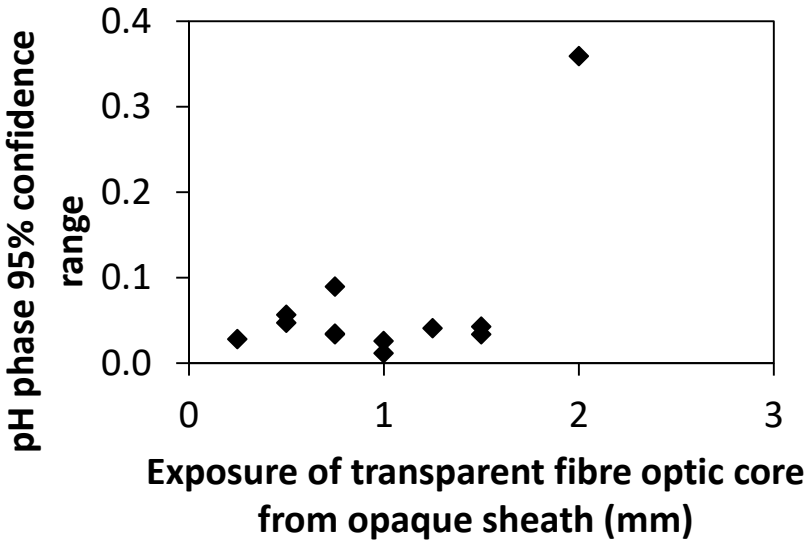

Figure 6.3: pH phase reading variability measured by 95 % confidence range compared to the exposure of the transparent core of the fibre optic cable from the opaque sheath. More details of these parameters can be found in Section 6.3.

During cell culture itself, the pH reading was found to be very stable and accurate, with the greatest drift recorded after the feed (Fig.6.4) as expected due to the significant increase in osmolality, to which pH patches are known to be cross-sensitive (Section 1.14.1). For all probes, during cell culture, the pH amplitude was found to start at 35-40,000 and trend downwards at approximately 200 per day, presumably as the patch photo-bleached. Over each of the six cell cultures operated in this rocked bag design, towards the beginning of each culture, the pH amplitude would also drop rapidly by >1,000 per day (Fig.6.4). FOs were reinstalled in this case and this was found to reliably stabilise the reading at pre-reduction levels (Fig.6.4). These drops did not appear to affect the online or offline (measured as in Section 2.3.1) pH reading accuracy (Fig.6.4). It is thought that this was reduction in pH amplitude was caused by the thermoplastic sleeves stretching due to the heat of the culture, the rocking of the bag and the tension of the fibre optic cable mounting and this could result in the displacement of the fibre optic with respect to the optical sensor patch. As noted above, even large changes in the pH amplitude do not necessarily result in significant changes in the pH reading being reported, but these inconsistent changes in signal-to-noise that are rectified

by re-installation suggest that probe reading and positioning should be monitored during cell culture to ensure reliable measurement and control of online parameters.

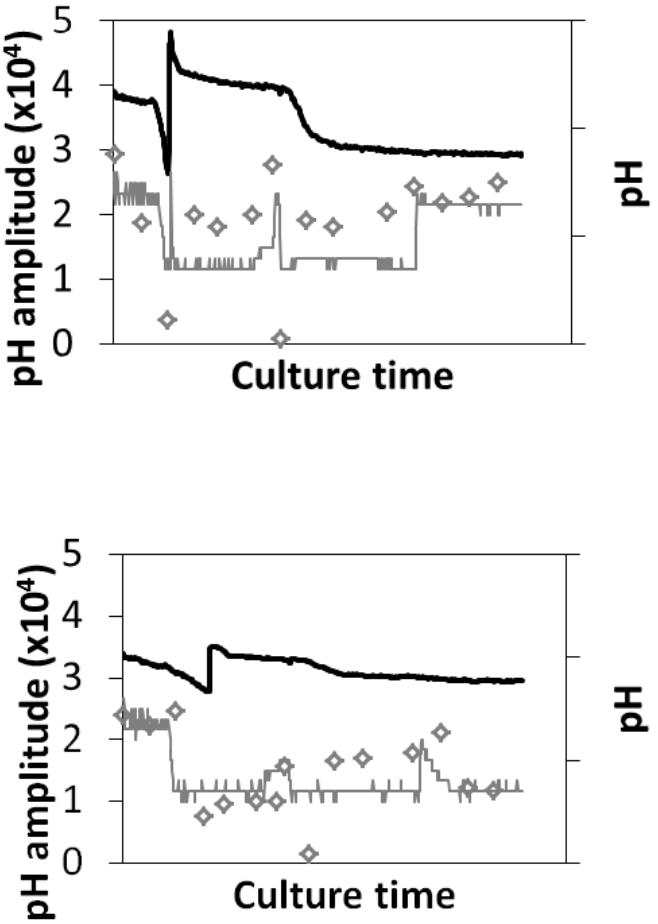

Figure 6.4: pH probe amplitude reading (black line), single-use pH probe pH reading (grey line) and offline pH readings (grey unfilled diamonds) over the course of two rocked bag cell cultures operated as in Section 2.2.2.1. pH amplitude and online pH reading were taken from the MFCS logging software (Sartorius Stedim), which logs values every 30 minutes. Offline pH readings were taken using a BioProfile 400 (Section 2.3.1).

6.4. Cell Culture Dissolved Oxygen Control

The higher rocking rate bag was found to have the better DO control during live cell culture, with minimal deviation from the DO setpoint at a rocking rate of 28 min^{-1} while several significant deviations can be observed in the bag operated at 13 min^{-1} in Fig.6.5. At 13 min^{-1}, the PID control loop for dissolved oxygen had to be adjusted to reduce overshoot and control oscillation. This required a significant reduction in the P term (from 100 % to 25 % of the error) to reduce the direct response to the error, as well as the introduction of a Derivative time, which acts to extrapolate the current rate of change of the process variable forwards to reduce rapid changes (from 0 to 1,000 s) to increase the period and therefore the controllability of the oscillations. Adjustments to the Integral time within the allowed range (0-1,000s) did not have any noticeable impact. In this way, the oscillations were reduced from approximately ±10 % DO to ±2 %.

At 28rpm, with the default settings there was no discernible oscillation (Fig 5.5). Unpublished work from within the department suggests that the mixing time at 13rpm would be in the ranger of 30-45 s, and the $k_La(O_2)$ was measured as 4.5h^{-1} (Fig.6.1). Neither of these values should represent much of a challenge for a DO control loop since lower $k_La(O_2)$ and higher mixing times are tolerated in larger scale in stirred tanks (Nienow 2006). The large gas headspace of rocked bags represents a challenge to gas based oxygen control loops because at a reasonably high cell culture gas flowrate of 0.1 vvm, it can take 30 s to change the composition of the gas phase by 1 %. This is as opposed to a stirred tank which can potentially change the composition of the majority of the gas phase by 100 % within the bubble residence time, which is <10 s (Sieblist *et al.* 2011). At higher rocking rates, the higher $k_La(O_2)$ and the lower mixing time would allow the different gas composition to more efficiently alter the oxygen saturation of the liquid phase and that liquid phase to more quickly reach homogeneity. Other solutions explored to try to solve the oscillatory gas control were to increase the gas flow rate to reduce headspace gas turnover time, and to also reduce the length and diameter of the gas inlet tubing to reduce dead volume between the gas mixer and rocked bag and

therefore the response time of the headspace gas composition beginning to change, however, neither of these had a significant beneficial effect.

The level of gas entrainment into the bulk fluid at 28 min^{-1} led to foaming, which has been previously observed with the previously used rocked bag in Section 2.4.1. Foaming is a significant problem for gas control in headspace aerated systems since it can significantly slow diffusion between the controlled gas phase and the liquid phase by adding several gas transfer resistant liquid films between the two. Antifoam had to be added on alternating days for the duration of the cell culture at 28 min^{-1}. Antifoam was also added at 13 min^{-1} to ensure comparability, although the very low total quantities added (80 ppm of active antifoam ingredient) were below the levels at which effects are reported in CHO cells.

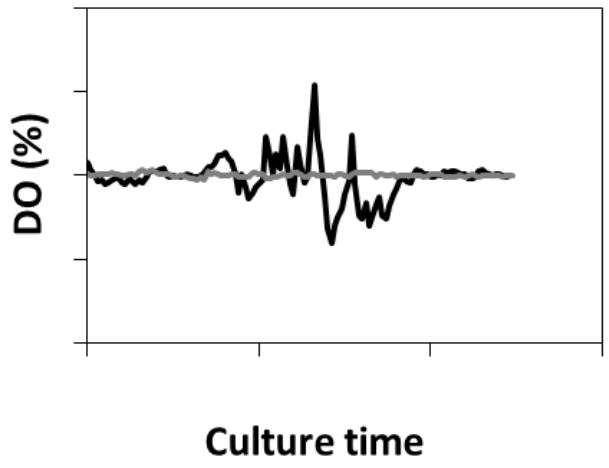

Figure 6.5: Online DO readings showing quality of DO control from the first 60hours of cell culture performed as described in Section 2.2.2.1 for the surface aerated bag (black line) and dispersed gas phase bag (grey line). Values taken from the MFCS logging software (Sartorius Stedim) which logs values every 30 minutes.

6.5. Comparison of Fed-Batch Cell Culture kinetics

The cell culture performance of the different bag configurations was evaluated by carrying out cell culture at different rocking rates. These rocking rates (13 and 28 min^{-1}) were selected on the basis of the engineering characterisation, as detailed in Section as in Section 6.4.1. Comparisons between the two bag configurations can

be used to build upon the understanding of the effect of rocking rate on cell culture performance, while comparisons with current and historical lab scale stirred tank (Section 2.2.2.2 and 2.3.7.1) performance can be drawn to indicate which configuration would provide the more successful technology transfer between bioreactors.

6.5.1. Cell Growth and Viability

Growth profiles for both the surface aeration and dispersed gas bag were very similar, with the cells growing to peak cell density over the first period of the cell culture and then remaining in stationary phase for the remainder of the culture duration (Fig.6.6A). This trend matched closely to that of the historic stirred tank data from Eli Lilly, with the bags generally achieving lower peak cell density (3.5-5.2 $x10^6$viable cells.mL^{-1}) than the tanks (4.0-7.0 $x10^6$viable cells.mL^{-1}). Within the bags, the low, 13 min^{-1}, rocking rate, surface aerated bags generally achieved and maintained higher cell densities than the high, 28 min^{-1}, rocking rate dispersed gas phase bags, but given the variability of the process peak cell density the differences are not statistically significant ($p=0.18$) tested by Tukey-Kramer HSD (Section 2.3.7.1). This contrasts with what was observed in Section 3.3, in which peak cell count tended to be slightly higher at the higher rocking rate (Fig.3.6) and in Chapter 5, where growth at either rocking rate was equivalent to the stirred tank (Fig.5.1A).

Viability profiles for both bag configurations were maintained above 95% for the first period of the cell culture (Fig.6.6B). After this point, the viability of the surface aerated bags falls at ~0.5 % per day, while the viability of the cells in the dispersed gas phase bags falls at approximately 1.5 % per day. In comparison to the historic stirred tank data, the late culture period viability trend of the surface aerated bags represents above average viability, while the dispersed gas phase bags were below the 5^{th} percentile for the final part of the cell culture. In spite of the more rapid decline in viability, the viable cell counts in the dispersed gas phase bags falls by 12±2 % from peak value over the latter part of the cell culture to harvest, compared to 22±3 % in the surface aeration bag. This suggests that the cells in the dispersed gas phase bag are dividing more rapidly later in the culture.

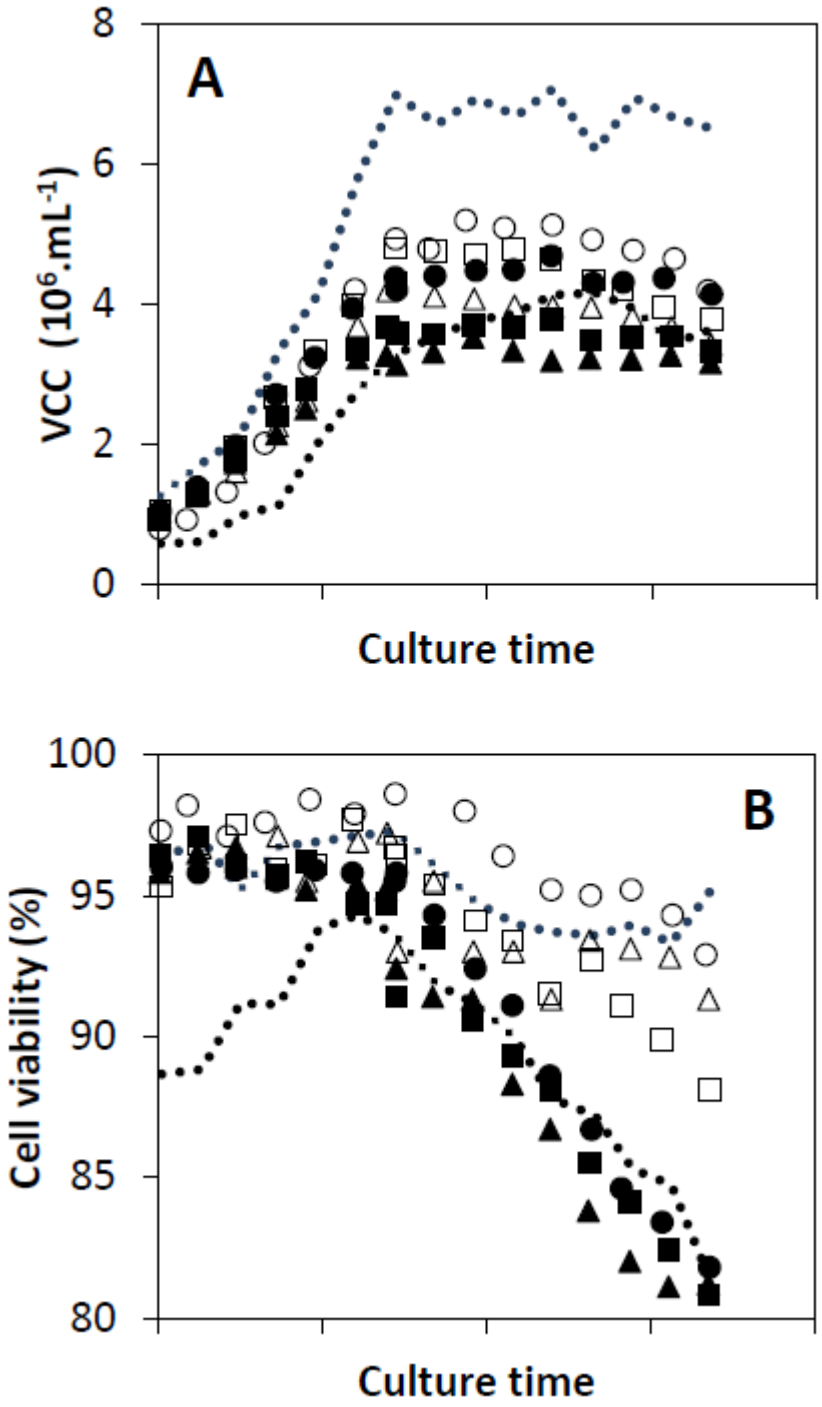

Figure 6.6: Cell culture (A) Viable cell count and (B) cell viability over the course of the cell culture for surface aerated bag biological repeats (open shapes), n =3 and dispersed gas phase bag biological repeats (filled shapes), n = 3 compared to 5 and 95 % confidence boundaries for historic and control stirred tanks operations (dotted lines), combined as described in Section 2.3.7. Viable cell count (A) and cell viability (B) against cell culture time. Bioreactors operated as in Section 2.2.2.1. and 2.2.2.2. and sampled as in section 2.3.1.

6.6. End point analysis of cell culture performance

6.6.1. Integral Viable Cell Count, Product Titre and Cell Specific Productivity

For a rigorous statistical analysis, the cell cultures conducted in bags were compared to historic stirred tank cell cultures with identical configurations (details of the basis for this can be found in Section 2.3.7.1). The larger sample size (n = 15) afforded by the historical dataset, combined with stirred tank controls run in parallel (n = 2), allowed comparison of the relatively small sample number of rocked bag runs at each rocking rate (n = 3) with good statistical confidence.

Cell growth, as quantified by culture duration IVC, appeared to be slightly lower than the control stirred tanks in the surface aerated bags and lower still in the dispersed gas phase bags (Fig.6.7). ANOVA found significant differences between the groups and these were further clarified using Tukey-Kramer Honest Significant Difference test (Section 2.3.7.1). The Tukey-Kramer HSD is similar to the t-test, but handles different sample sizes and corrects for experiment-wise error rate allowing multiple comparison (Tukey 1949). This test detected significant differences between the control stirred tank group and the dispersed gas phase rocked bags (P=0.0049), suggesting that a combination of the use of bags and the higher rocking rate was enough to significantly alter cell growth during cell culture. Harvest point titre was identical (<1 % difference) in the surface aerated rocked bags and control stirred tanks but was significantly (32 %, p = 0.0034) lower in the dispersed gas phase rocked bags than both of these groups (Fig.6.6).

Cell specific productivity was very closely matched between the dispersed gas phase rocked bags and control (1 % difference) suggesting that while the cell growth was significantly impacted by the entrained gas and foaming of the high rocking rate, the cell specific productivity was unaffected (Fig.6.7). At the surface aerated rocked bag, as has been previously observed in Section 3.3, the cell specific productivity appeared to be 16% higher than the control stirred tanks but statistically this could not be considered a significant difference (p=0.072). The

rocked bag was not found to perform significantly better in terms of product titre, the most important metric of cell culture performance.

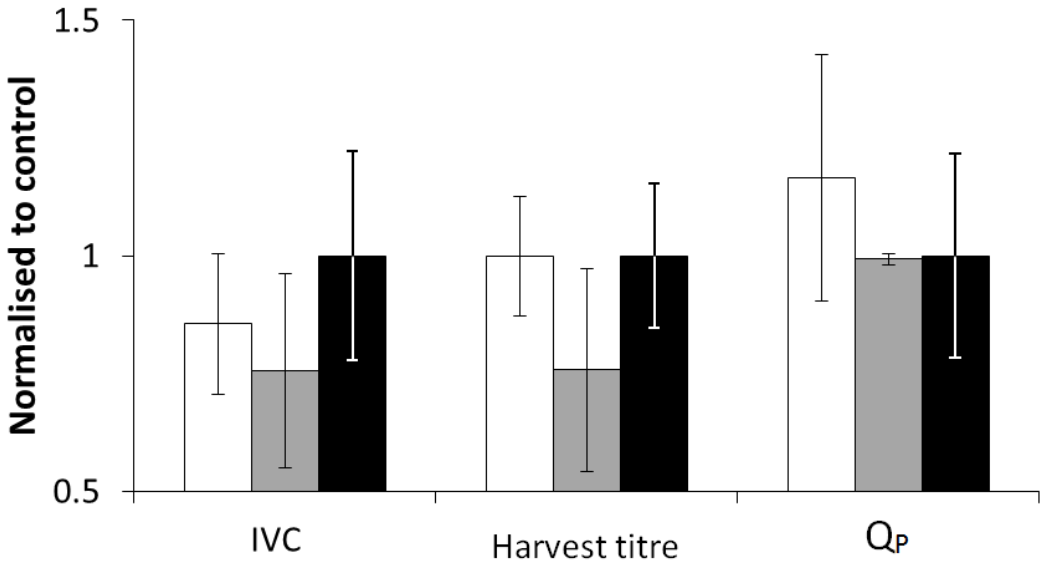

Figure 6.7: Summary cell culture performance comparison between surface aerated bag (white bars), dispersed gas phase bag (grey bars) and historic control stirred tanks (black bars); integral viable cell count (IVC), harvest point product titre and cell specific productivity (Q_P) Error bars represent 95 % confidence boundaries; n = 3 for the rocked bags and n = 2 and n = 15 for the combined control and historical stirred tanks respectively. Cell culture kinetics described in Fig.6.6.

6.6.2. Product Quality Attributes

The previous section demonstrates that the cells respond to the different environments produced in the rocked bags, with higher rocking rates, which produce a dispersed gas phase similar to a bioreactor, producing significantly lower growth and product titre than the stirred tank control and surface aerated bag. This finding is similar to what was found in Sections 3.3 & 5.2.1 in terms of the ~20 % reduction in Q_P. IVC, however, was not previously found to be significantly impacted by the rocking rate, so this may show that the growth response to the cell culture conditions is cell line or process specific.

Of crucial importance to the process is the quality attributes of the molecule produced. This molecule was known to be process responsive, so the product

quality would establish both the capability of the rocked bag as a mimic of stirred tanks and the effect of very different physical environments. With this product, Eli Lilly typically look at a range of product quality attributes over the process of production, recovery, purification and formulation, of which 12 are shown here. These cover specific chemical modifications, aggregation, charge heterogeneity and protein N-glycan profile.

The measured product quality attributes for each of the rocked bag bioreactor runs performed relative to the historical stirred tank data did not show significant differences ($p < 0.05$) between the configurations, with two exceptions (Fig.6.8).

PQA 4 showed significantly lower levels produced in the dispersed gas phase rocked bags compared to the control stirred tanks ($p = 0.0001$). There was also a noticeable but not statistically significant difference between the 13 rpm bags and the historic stirred tanks ($p = 0.075$). PQ4 is known to be sensitive to the seed bioreactor temperature and the inoculum age but since all systems were inoculated from the same seed train this does not explain the difference observed. The energetic reaction that results in this product quality attribute may be repressed in response to cellular stress brought on by culture in a more turbulent environment present at the higher rocking rate, as measured in Section 4.5.

PQA 6 levels were very significantly greater in the dispersed gas phase rocked bags compared to the control stirred tanks (1.67 and 0.94 respectively, $p = 0.0007$). No statistically significant differences could be detected between the other groups ($p > 0.05$). PQA 6 is responsive to dO_2 and dCO_2 concentration, pH and medium composition. Offline values taken during cell culture suggest, that bar dCO_2, none of these values was significantly different over the course of the cell culture. Offline dCO_2 levels measured over the course of the cell culture on the BioProfile 400 (NOVA) were found to be significantly different ($p = 1x10^{-13}$) with mean dCO_2 levels in the dispersed gas phase rocked bags, surface aerated rocked bag and the control STR being 11, 20 and 35mmHg respectively.

Lower CO_2 levels are thought to increase PQA 6 and are observed in the dispersed gas phase rocked bags for two reasons. Firstly, the lower total number of viable

cells present meant that once the culture acidified due to lactate production during the cell growth phase (Fig.6.13A) and the controller stopped adding CO_2, the concentration of dCO_2 within the culture was governed by the number and activity of viable cells, which was lower in the dispersed gas phase rocked bags, which had a lower IVC (Fig.6.7) and lower specific glucose consumption (Fig.6.12A). Secondly, the CO_2 stripping rate was 15 % higher at the higher rocking rate as a function of the greater gas interfacial area due to the dispersed gas phase (Fig.5.2), meaning that at a given level of CO_2 production, the CO_2 concentration in the culture broth would be 15 % lower.

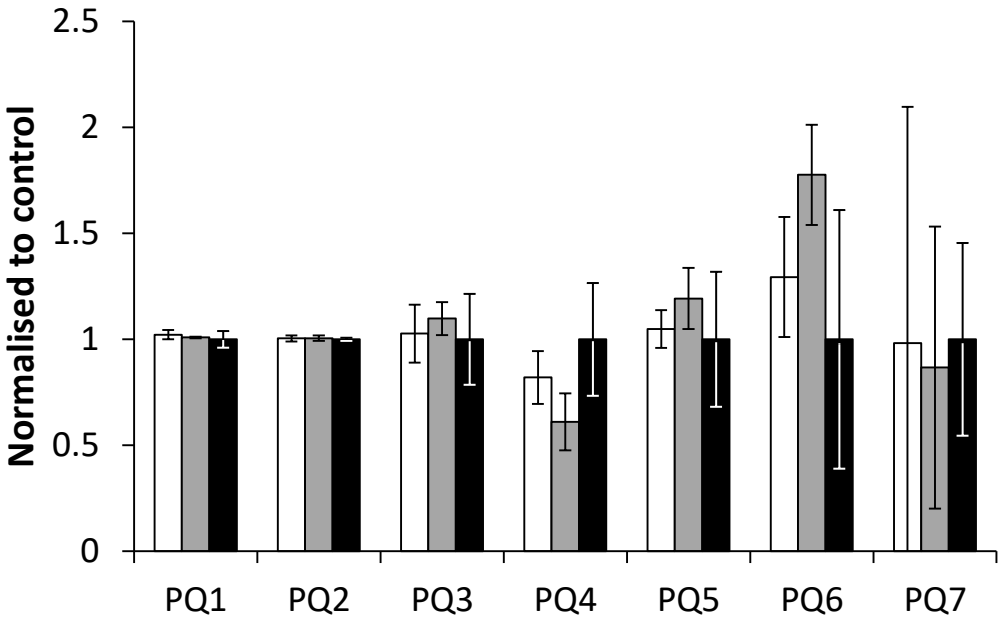

Figure 6.8: Quality attributes of the harvested product compared between surface aerated bag (white bars), dispersed gas phase bag (grey bars) and historic control stirred tanks (black bars). Error bars represent 95 % confidence boundaries; n = 3 for the rocked bags and n = 2 and n = 15 for the combined control and historical stirred tanks respectively. Cell culture kinetics described in Fig.6.6, details of the assays used are in Section 2.3.7.

N-terminal glycosylation was found to not be impacted by the bag configuration (Fig.6.9). No statistically significant differences were detected between the dispersed gas phase and surface aerated bags, with p-values ranging from 0.1 to 0.88, across tested areas. Differences in glycosylation profile have previously been

reported in response to changes in cell culture conditions, in the absence of any changes in cell growth (Velez-Suberbie *et al.* 2012; Godoy-Silva *et al.* 2009).

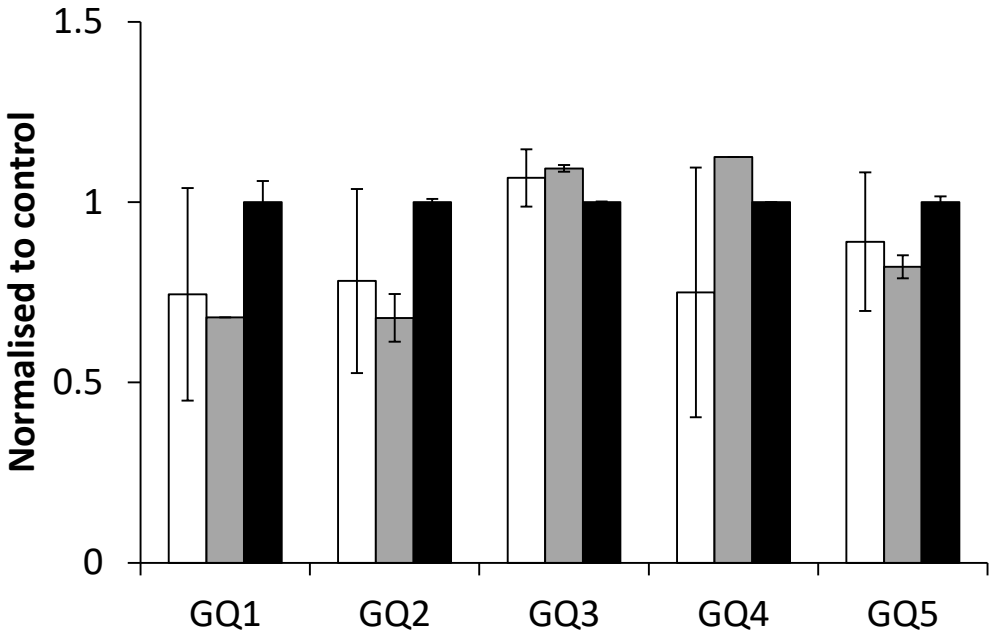

Figure 6.9: Gycosylation profile of the harvested product compared between surface aerated bag (white bars), dispersed gas phase bag (grey bars) and historic control stirred tanks (black bars). Error bars represent 95 % confidence boundaries; n=3 for the rocked bags and n = 2 and n = 15 for the combined control and historical stirred tanks respectively. Cell culture kinetics described in Fig.6.6, details of the assays used are in Section 2.3.7.

6.7. Rocked Bag Rocking Rate Comparison

To understand the difference in the growth and productivity between the high and low rocking rate bags, the cell culture kinetics were further investigated. There is a clear divergence in cell size in the latter part of the cell culture (Fig.6.10). The cells in the surface aeration bag expand from 18±0.7 µm to approximately 19±0.5 µm before ending the culture at ~18.5±0.1.5 µm, while in the dispersed gas phase bag, the cells shrink from 18±0.4 µm at feed to end the culture at 16.8±0.2 µm. Smaller cells were also observed in response to the dispersed gas phase in Section 3.3.

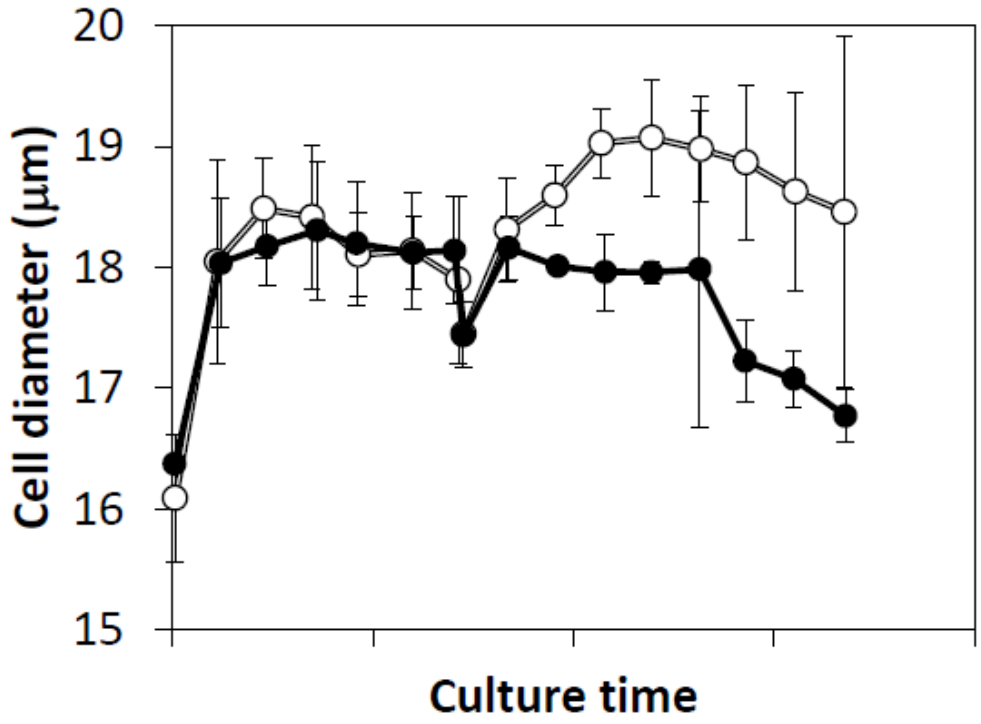

Figure 6.10: Mean cell diameter over the cell culture for surface aerated bag (open circles) and dispersed gas phase bag (filled circles). Error bars represent 95 % confidence boundaries, n = 3. Cell culture kinetics described in Fig.6.6, cell diameter measured by ViCell XR cell counter (Section 2.3.1).

Higher titre and a significantly higher rate of production was noted in the surface aerated bag compared to the dispersed gas phase bag over the latter part of the cell culture, 50 % higher Q_P over the last 30% of the culture duration for the surface aerated compared to the dispersed gas bags (Fig.6.11). The higher late culture productivity results in a 32 % higher final product titre for the surface aerated bags. The gradient of the plot of product titre against integral viable cell count (IVC) suggests that the rate of product expression is linear with respect to IVC in the dispersed gas phase bag but has accelerated post-feed in the surface aeration bag. Since the biphasic culture (Section 2.2.2) is designed to promote higher antibody productivity in the latter part, it appears that cells in the dispersed gas phase bag are not responding in a normal manner to the process parameter modifications and nutrient feed.

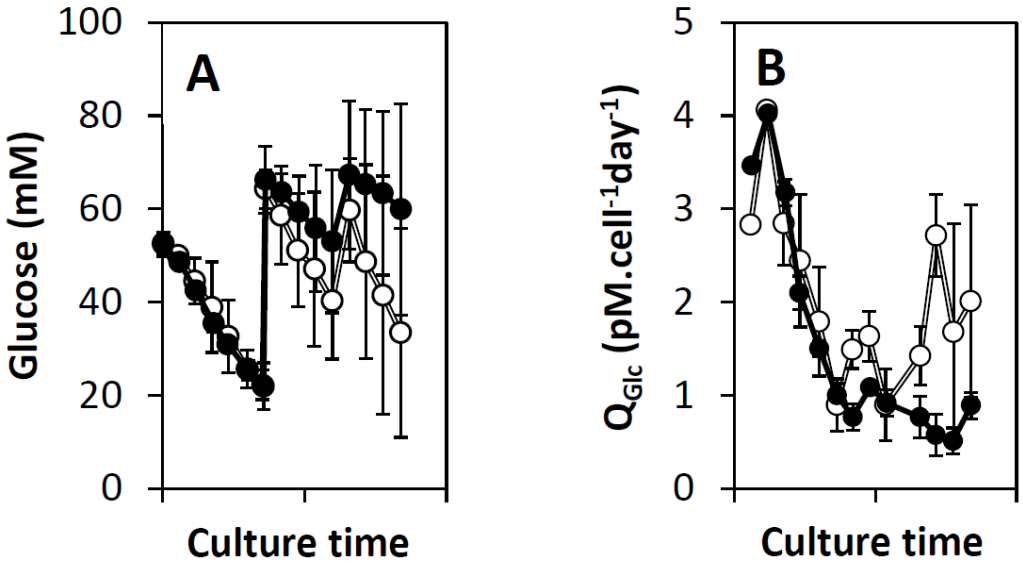

Figure 6.11: Product titre plotted against integral viable cell count for the surface aerated bag (open circles) and dispersed gas phase bag (filled circles). Error bars represent 95 % confidence boundaries, n = 3. Cell culture kinetics described in Fig.6.6, IVC calculated as in Section 2.3.3.1 and product titre measured by HPLC as in section 2.3.2.

Glucose consumption showed similar trends between the bag configurations, with the glucose concentration falling linearly at approximately 5 mM.day^{-1} for both bag configurations up until the feed at 40% of the culture duration. After this, glucose consumption accelerates in the surface aerated bag but decelerates in the dispersed gas phase bag, resulting in accumulation of glucose after the glucose supplementation. Cell specific glucose consumption calculation confirms that the per cell rate of glucose consumption drops rapidly over the first 40% of the culture duration from 4 to 1 pM.cell^{-1}.day^{-1} identically in both bag configurations before stabilising in the dispersed gas phase bag while rising to 2 pM.cell^{-1}.day^{-1} in the surface aerated bag. Higher levels of glucose consumption coupled with lower levels of cell division would suggest that the cells in the surface aerated bag have moved into a more productive state.

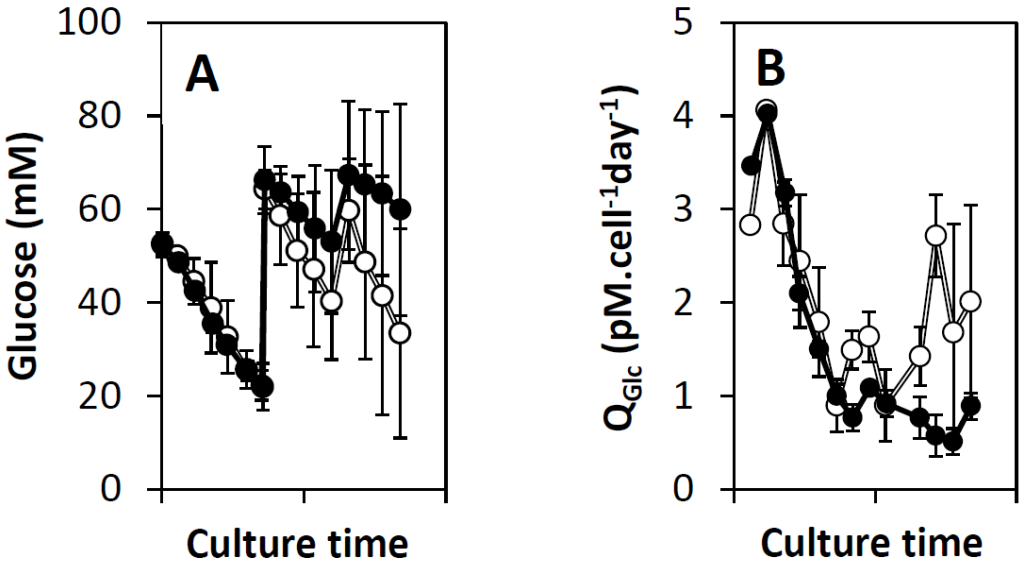

Figure 6.12: Cell culture glucose kinetics; (A) glucose concentration, (B) cell specific glucose consumption rate for the surface aerated bag (open circles) and dispersed gas phase bag (filled circles). Error bars represent 95 % confidence boundaries, n = 3. Cell culture kinetics described in Fig.6.6, glucose concentrations were measured as in Section 2.3.1 and cell specific glucose consumption rate calculated as in Section 2.3.3.3.

In terms of lactate concentration, both bag configurations follow a very similar profile, rising to 22 mM over the first third of the cell culture and plateauing thereafter (Fig.6.13A). At this point, the cells in the surface aerated bag appear to switch to net consumption, while cells in the dispersed gas phase bag do not (Fig.6.13B). This is likely due to the glucose supplementation, which due to the lower glucose consumption of the cells in the dispersed gas phase bag, results in a high glucose concentration (67 mM, Fig.6.12A), potentially leading to overflow metabolism and therefore higher lactate production (Wlaschin & Hu 2006). As with lactate, ammonium concentration is identical for the first 60% of the culture duration, with the concentration rising linearly from 2 to 14mM in both bag configurations (Fig.6.13C). At this point, the cells in the surface aerated bag again switch to net consumption of ammonia (-1 mM.day^{-1}), while those in the dispersed gas phase bag stabilise the concentration for the remainder of the culture (Fig.6.13D). The switch to ammonium consumption for the surface aerated bag is evident on the cell specific ammonium production rate. Since the peak values of

these potential toxins are very similar, it is unlikely that the slightly different flux alone would have any effects.

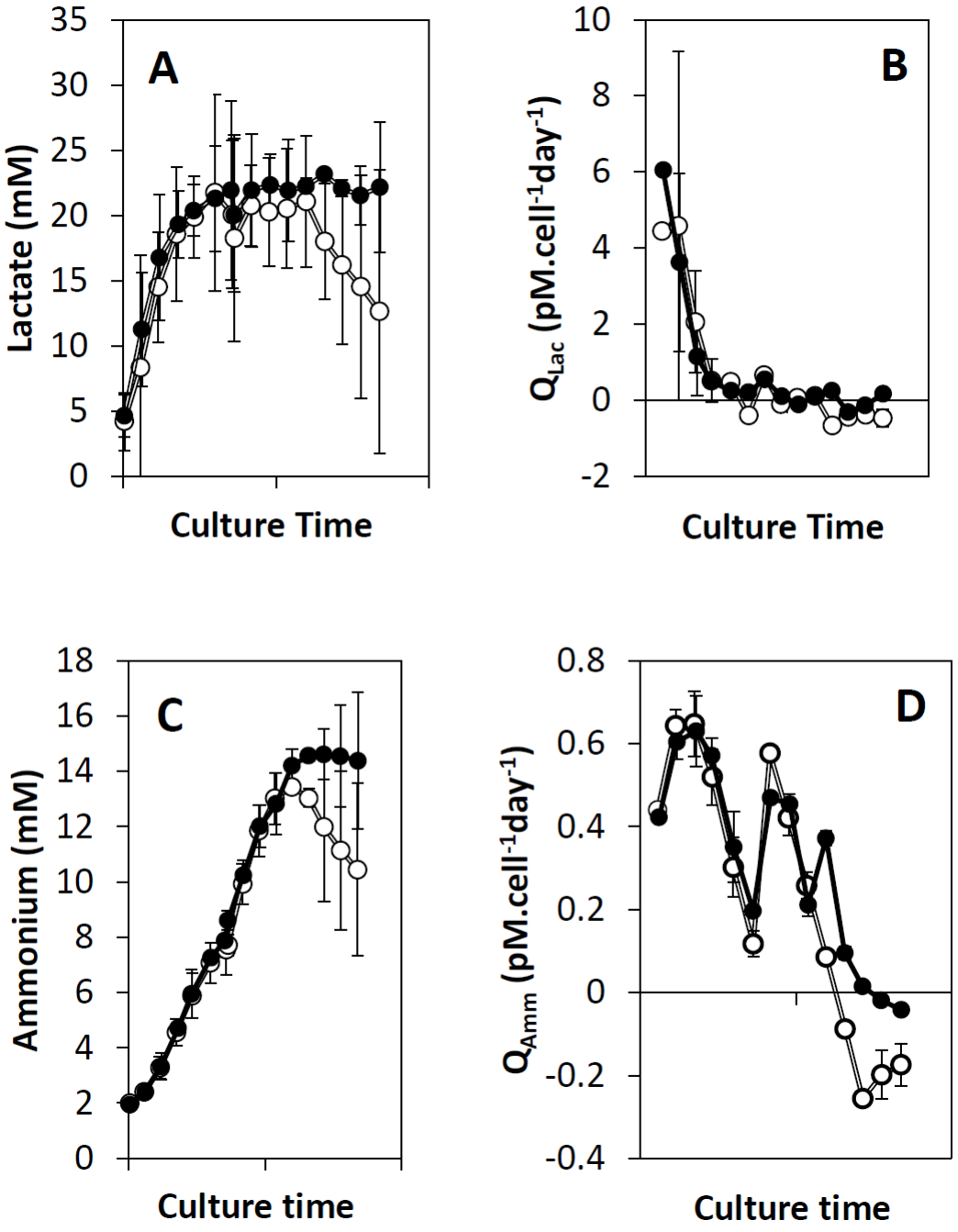

Figure 6.13: Cell culture lactate and ammonium cell culture kinetics; (A) lactate concentration and (B) cell specific lactate production rate, (C) ammonium concentration and (D) cell specific ammonium production rate for the surface aerated bag (open circles) and dispersed gas phase bag (filled circles). Error bars represent 95 % confidence boundaries, n = 3. Cell culture kinetics described in Fig.6.6, lactate and ammonium concentrations were measured as in Section 2.3.1 and cell specific production rates calculated as in Section 2.3.3.3.

Possibly due to the accuracy of the metabolite analyser for this metabolite, cell specific glutamine consumption rates do not show any significant trends, with values staying very close to 0 pM.cell^{-1}day^{-1} for the duration of the culture (Fig.6.14A). Despite the difference in specific ammonium rate consumption noted in the last 30% of the culture duration (Fig.6.13D), there is no significant difference in the specific glutamine consumption rate over the same period. Cell specific glutamate consumption shows consistently higher rates in the surface aerated bag throughout the cell culture (Fig.6.14B). This correlates with the lower ammonium and lactate production of the surface aerated bags, especially towards the end of the cell culture, since glutamate consumption is associated with lower accumulation of lactate and ammonium (Altamirano *et al.* 2000).

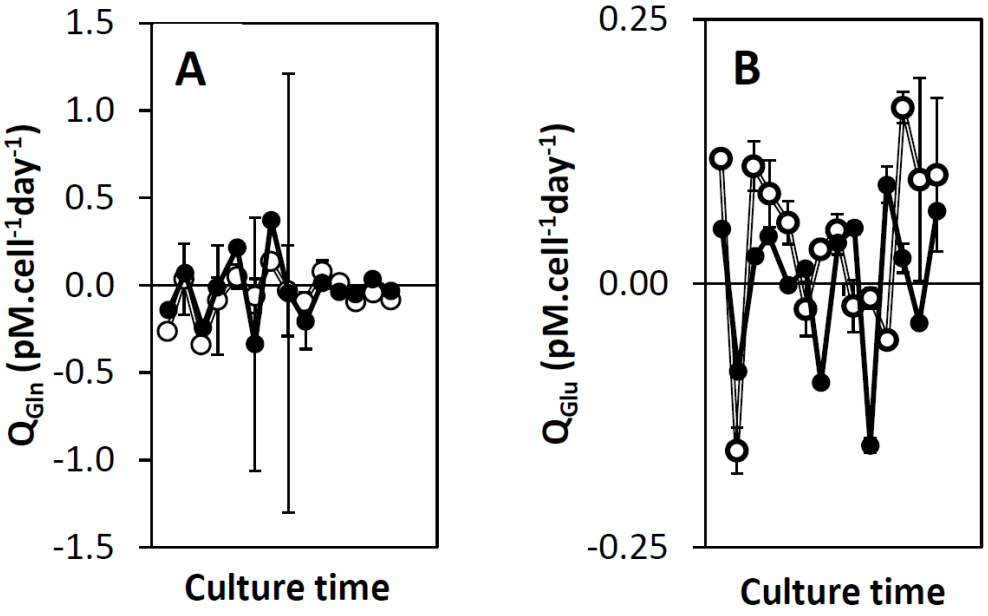

Figure 6.14: Cell culture glutamine and glutamate kinetics; (A) cell specific glutamine consumption rate and (B) cell specific glutamate consumption rate for the surface aerated bag (open circles) and dispersed gas phase bag (filled circles). Error bars represent 95 % confidence boundaries, n = 3. Cell culture kinetics described in Fig.6.6, glutamine and glutamate concentrations were measured as in Section 2.3.1 and cell specific consumption rates calculated as in Section 2.3.3.3.

6.8. Summary

The work described in this chapter was undertaken to explore the generic nature of the findings reported in Chapters 3 and 5 and to examine the impact of rocked bioreactor operating conditions on product quality in more detail using the resources available at Eli Lilly. Specific objectives were to compare the engineering characteristics of this rocked bag to the Applikon vessel used in chapters 3 and 5 and establish any sensitivity around the use of fluorescent sensors. These data were then used to conduct cell culture to evaluate the impact of rocking rate on the product quality using an alternative industrial cell line with comparison made to stirred tank controls and a large historical dataset.

In terms of general engineering performance, the alternative rocked bag geometry appears to follow the same trends for oxygen mass transfer response found in Section 3.2.1, with rocking rate and fill volume having the largest impact. Additionally, the presence of a dispersed gas phase was again noted above a critical rocking rate and this coincided with a more rapid increase in $k_La(O_2)$ in response to further increases in rocking rate (Fig.6.1). *A priori* precise predictions of of volumetric oxygen mass transfer coefficients are not possible in stirred tanks (Nienow *et al.* 2014, Van't Riet 1979), however the correlation established from the data collected in Section 3.2 predicted the performance of this rocked bag to within 32% over a rocking rate range of 8-40 min^{-1} (Section 6.2.1). CO_2 mass transfer rates were very predictable (Fig.6.2), which is due to the lower impact of interfacial area on carbon dioxide mass transfer due to the greater concentration gradient (Section 3.2.1).

Optical probes were found to work effectively provided their status was monitored. The signal-to-noise ratio of the pH probe appeared to be sensitive to minute changes in the relative position of the fibre optic cable and sensor patch (Fig.6.3). Probe readings were generally reliable over the course of cultures, but the signal-to-noise ratio was seen to drop significantly on several occasions, with reinstallation required to reverse this reduction (Fig.6.4). The design of fibre optic cable

retention mechanisms needs improvement in consistency and reliability for single-use sensors to achieve the same level of robustness as reusable probes.

For the industrial cell line used in this chapter, rocking rate clearly impacted upon cell growth and late culture viability with higher rocking rates leading to lower integral viable cell counts and more rapid cell viability reduction (Fig.6.6). There was also a small but statistically significant effect on cell specific productivity, which in conjunction with the lower IVC resulted in a significantly lower harvest product titre at gas entraining rocking rates (Fig.6.7). However, there does not appear to be a significant effect on the product quality profile (Fig.6.8 & 6.9). In five out of seven cases there is no statistically significant difference, and in one of the two cases in which differences were observed this appears to be as an indirect result of the low cell growth on the dCO_2 concentration.

As previously noted in Section 3.2.1, this alternative rocked bag design elicited the same phenomenon of gas entrainment above a critical rocking rate. This caused the same more rapid increase in oxygen mass transfer rate in response to higher rocking rates (Fig.6.1). Cell culture operated above and below this point was seen to impact on the growth and productivity of the cells as seen previously in Sections 3.3 and 5.2. With this alternate cell line the impact on growth was a small absolute reduction in peak cell density, which contrasts to what was seen previously Fig.3.6 & 5.1. However, the cell specific productivity again showed a measurable increase at lower rocking rates, being 16 % higher than at the high, gas entraining, rocking rate (Fig.6.7). This clearly suggests that the change in the fluid dynamic environment in response to rocking rate as measured in Section 4.10 is sufficient to affect cellular phenotype, but some of these effects may be cell line specific. In terms of the overall effect on product quality, there was not a significant response to rocking rate observed, with both bag configurations providing product quality profile very similar to that of control and historic stirred tanks (Fig.6.8 & 6.9).

Chapter 7. Conclusions and Future Work

7.1. Conclusions

This thesis describes the detailed physical and fluid dynamic characterisation of the rocked bag bioreactor design, which is used to describe a rational basis for configuring rocked bags for production cell culture. This has been achieved by applying traditional engineering characterisation alongside state-of-the-art fluid dynamic measurement techniques to understand the physical environment inside the rocked bag under different agitation regimes. Cell cultures were then carried out in two different cell lines and the effects on cell culture kinetics, harvest material, cell phenotype and transcriptome and product quality were measured.

The initial objective was to undertake a thorough engineering characterisation of a rocked bag bioreactor from lab to pilot scale. This was carried out as described in Chapter 3 to assess the impact of adjustments to the physical configuration of the bioreactor on oxygen and CO_2 transfer rate and liquid mixing time. Under typical operating conditions, rocked bags produced $k_La(O_2)$ values of 3-22 h^{-1} (Fig 3.1), $k_La(CO_2)$ values of 0.6-2.8 h^{-1} (Fig 3.3) and mixing times of 9-23 s (Fig 3.2) demonstrating the capability to meet the demands of current mammalian cell culture. This investigation revealed that mixing time and volumetric oxygen mass transfer coefficient were most sensitive to rocking rate, while the volumetric CO_2 mass transfer coefficient was sensitive to volumetric gas flowrate (Section 3.2.6). Within the ranges investigated, increasing the rocking rate led to an apparent exponential increase in $k_La(O_2)$ (Fig.3.1A) and an apparent linear reduction in mixing time (Fig.3.1B). It was observed that above a critical rocking rate (18 min^{-1} at 10 L), the liquid phase would entrain gas due to wave formation as it interacted with each end of the bag. The observed quantity of gas increased, while the bubble size decreased as rocking rate increased, explaining the rapidly increasing $k_La(O_2)$.

Bioreactor scales of 10, 20 and 50 L were also investigated (Section 3.2.7). While $k_La(CO_2)$ was found to not be affected by scale (Fig.3.5C), $k_La(O_2)$ reduced linearly with the reduction in surface area to volume ratio as scale was increased (Fig.3.1A).

Mixing time increased proportionately with the increase in volume (Fig.3.3B). This suggests that higher rocking rates may be necessary at larger scale, potentially precluding bubble-free operation.

Operating fed-batch cell culture for cell line A (Section 2.2.1) at below and above this critical rocking speed revealed differences in cell culture kinetics and harvest broth shear sensitivity (Section 3.3). At a rocking rate of 15 min^{-1}, with no gas entrainment, cell specific productivity was 19 % higher than at 25 min^{-1} (Fig.3.6D). However, the harvested cells from the bag rocked at 15 min^{-1} showed an increased tendency to lyse compared to those cultured at 25 min^{-1} under typical centrifuge levels of shear stress (Fig.3.10). This suggests that while cells are more productive when cultured in the bubble free conditions possible at lower rocking rates, the subsequent primary recovery operation may have a lower yield due to a higher concentration of cell debris.

Given the significant impact of rocking rate on mass transfer, mixing time, cell culture kinetics and cell mechanical robustness, the following objective was to characterise the fluid dynamic environment within the rocked bag as described in Chapter 4. A transparent, rocked bag mimic and rocking platform were fabricated in house (Fig.4.2). Angle resolved Particle Image Velocimetry (PIV) was used to measure the fluid velocities, turbulence kinetic energy and shear stress in response to rocking rate. Measured fluid velocities increased with rocking rate (Fig.4.13) from average values of 0.10-0.17 ms^{-1} as rocking rate was increased from 25-42 min^{-1}. Spatially, fluid velocities were highest towards the longitudinal centre and base of the bag (Fig.4.3-4.5) as it passes the horizontal point in the rocking cycle (Fig.4.8).

At 33.5 and 42 min^{-1}, it was noted that the liquid that pooled in the end of the bag as the platform angle increased interacted with the fluid still flowing into the end of the bag, generating 15 Pa of shear stress at the interface at 42 min^{-1} (Fig 4.7). This phenomenon was associated with the bubble entrainment initially observed in Chapter 3 (Section 3.2.1) as the high velocity fluid running into and under the low velocity fluid was observed to entrain gas. High speed photography combined with

purpose built software for visual analysis was further used to quantify the bulk fluid behaviour (Fig.4.10). It was found that the fluid moved progressively out of phase with respect to the rocking platform at higher rocking rates (Fig.4.12). The fluid being behind the platform phase at higher rocking rates meant that it reaches the far end of the bag when the platform is more inclined (Fig.4.3D & 4.5F). This allows the fluid that has yet to pool to move at higher velocity and consequently interact with the already pooled fluid as described above.

Equation 4.8 was subsequently derived from first principles, to predict the average longitudinal fluid velocity (R_P) and bulk fluid position within a rocked bag on the basis of the volumetric displacement of fluid by the base of the bag as the platform changes angle (Section 4.6). Comparison to the fluid dynamics within an ungassed stirred tank of equivalent scale (Gabriele *et al.* 2009) indicated that at rocking rates of 33.5 min^{-1} the rocked bag had comparable fluid velocities but produced a greater range of turbulence kinetic energy, possibly due to the long rock period (Fig.4.13).

The objective of Chapter 5 was to investigate the cell biological impact of the fed-batch cell culture of cells with and without a dispersed gas phase in rocked bags and compare this to an STR control. The surface aerated bag and stirred tank produced identical final titres with a 20 % higher day 14 antibody concentration than the dispersed gas phase bag. Specific productivities in the surface aerated bag, stirred tank and dispersed gas phase bag were 9.6, 8.9 and 7.7 $pg.cell^{-1}day^{-1}$ respectively. Cell cycle and apoptosis assays revealed that the cells in the surface aerated bag appeared to be under the most stress: From day 10 onwards, a greater proportion of necrotic and late apoptotic cells were present in the surface aerated bag compared to the stirred tank and dispersed gas phase bag (Fig.5.7). There was also a greater accumulation of cells in the G2/M and S phase after day 8, suggesting DNA damage in the surface aerated bag (Fig. 5.6). Transcriptomic analysis confirmed that the cells in the surface aerated bag were under increased levels of oxidative stress and were undergoing higher levels of DNA repair from day 8 to the end of the culture (Fig.5.8). The cells cultured in the dispersed gas phase bag had very similar values and trends to the stirred tank in the flow cytometric and transcriptomic assays. These measured biological responses paired the dispersed

gas phase bag and stirred tank together, however the cell culture productivity paired the surface aerated bag and stirred tank together. This suggests that the negative impact on the specific productivity of the cells when cultured at higher rocking rates, which entrain gas, was not mediated through any of the pathways assayed. The more closely matched physical environment of the 25 min^{-1} rocked bag and the stirred tank resulted in more closely matched cellular health but this did not translate to a specific productivity match.

The objective of Chapter 6 was to evaluate the effect of the rocked bag configuration on the product quality. This work would establish whether the differences in productivity observed in Chapters 3 and 5 were cell line or rocked bag design specific. This cell line (cell line B, Section 2.2.2) responded to the higher rocking rate, with a measurable negative effect on IVC and a statistically significant negative effect on specific productivity when a dispersed gas phase was generated by the rocking rate (Fig.6.7). However, product quality and glycosylation were statistically unaffected in 10 out of 12 analyses, with the dispersed gas phase bag being more deviant from the control and historic values than the surface aerated bag where differences arose (Fig.6.8 & 6.9). Investigating the metabolic cell culture kinetics revealed that the cells in the dispersed gas phase bag did not achieve the expected switch into a more productive state in the latter part of the cell culture and remained less metabolically active for the remainder of the cell culture (Fig.6.12). The cells cultured in the rocked bag under surface aerating conditions produced identical final product titre and product quality to the stirred tank (Section 6.6.2).

Overall, this work has shown that rocked bags tend to achieve cell culture growth, antibody productivity and antibody product quality most similar to stirred tanks when operated at rocking rates which provide surface aeration (Chapters 3 and 6). However, this occurs under conditions where the physical environment is significantly different between the rocked bioreactor and the Stirred tank (Chapter 4), resulting in measurably different cell physiology and gene expression (Chapter 5). The work has also shown that when rocked bag bioreactors are operated with a dispersed gas phase, the mechanical stability of the harvested cells is more akin to

that of an aerated SUB (Chapter 2). These finding have important consequences for the design of antibody manufacturing processes using single-use technologies employing rocked or other non-standard agitation mechanisms.

While stirred tank equivalent performance was achieved with two different CHO cell lines (Section 5.5.2 and 6.6), the rocked bag was not found to outperform the stirred tank in terms of final product concentration.

7.2. Future Work

As mentioned at a number of points throughout this thesis there are areas where the work could be improved and extended. These are described further below.

Given the number of factors involved in determining the engineering characteristics of the rocked bag in Chapter 3, a design of experiments approach would have been a superior approach to the one-factor-at-a-time approach pursued. This would have allowed the quantification of any interactions between terms and would have required far fewer experimental runs. The most efficient approach would have been a factorial screening design, which would have quickly identified the most significant factors, followed by a response surface to estimate curvature of response and factor interactions.

There are two measurements of the fluid flow within the rocked bag that would allow more precise approximation to existing scaling criteria for mammalian bioreactors. Clay particle floc systems are available which can used to compare the mean energy dissipation rate between a reference and investigated systems (Hoffmann *et al.* 1992). The reduction in floc size over time can be correlated to the power input ($P.V^{-1}$) of a system by comparing this to the reduction in a reference system of known power input such as a coquette shear gap device (Pilz & Hempel 2005). Such a technique could be used to experimentally determine an estimate for the mean energy dissipation rate within a rocked bag at lab scale. Secondly, a high speed photography system (Vazquez *et al.* 2005) with a limited focal depth could be used to estimate the volume of gas entrained and the range of bubble sizes produced during rocking at various energy dissipation rates.

Differences were noticed in the oxygen transfer and bubble entrainment characteristics of rocked bags from different manufacturers as described in Section 3.2.7. The effect of changes in bag length, width, depth and bag end geometry could be investigated using a large bag coupled with adjustable bag retention brackets. These could be relocated in conjunction with a flexible bag to simulate various bag scales, end geometries and aspect ratios which, in conjunction with the above techniques, could be used to experimentally determine the key dimensions which predict energy dissipation rate and the extent of gas entrainment in rocked bags over a range of scales.

To provide insight of the fluid dynamics at larger scale, CFD could be employed. CFD has previously been applied to rocked bags (Oncul *et al.* 2009) under laminar conditions. Using the existing PIV data, it would be of interest to develop a 2 phase CFD model of a rocked bag under a transitional-turbulent fluid flow regime at small scale. This could then be used to simulate what would happen at larger scale or with differing geometry. CFD models can be used to predict fluid position, velocity vectors and shear and energy dissipation.

Extending the engineering characterisation carried out in Chapter 3 to a pilot scale rocked bag would act to measure the validity of the above predictions. This could be followed by cell culture at this scale to evaluate whether controlled, stirred tank equivalent, fed-batch cell culture was possible at pilot scale in rocked bags.

In terms of the mechanism by which the cells are affected when cultured in rocked bags (Chapter 5), a more holistic transcriptomic approach could be used to locate the cause of the productivity and growth impact of cell culture at higher rocking rates seen in Chapters 3, 5 & 6. Additionally, while evidence of different broth characteristics were found in Chapter 3, a full evaluation of the downstream impact of cells cultured under different physical environments would provide broad insights into the whole bioprocessing effect of the physical cell culture environment on recovery and purification.

Rocked bags, when operated at rocking rates which do not entrain gas, provide a higher oxygen transfer to shear stress ratio compared to stirred tanks, with bubble

free aeration feasible at 25L scale (Chapter 3). This suggests that rocked bags may be better suited to the culture of shear sensitive cells such as those attached to microcarriers. Further investigation of the potential for rocked bags for culturing variously shear sensitive cell types could lead to the development of more efficient growth and screening platforms.

Chapter 8. Appendix 1: Materials and Methods

Supplementary Figures.

8.1. HPLC Example Calibration Curve

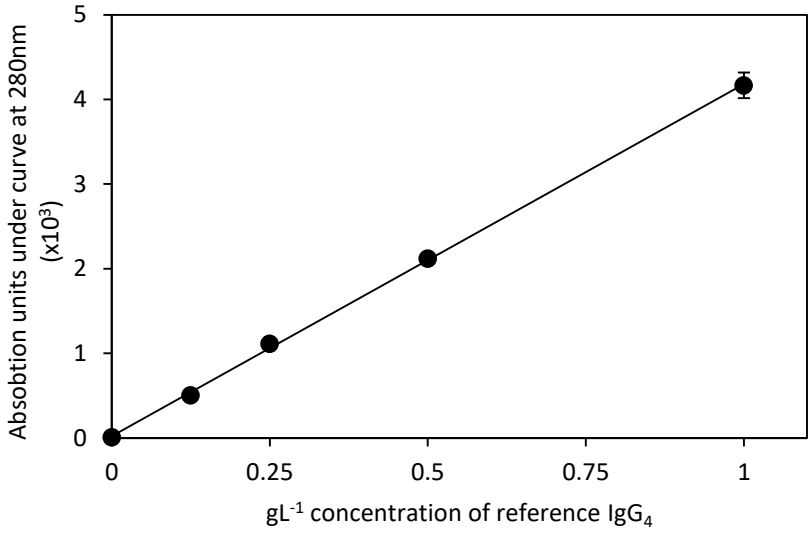

Figure 8.1: Calibration curve for HPLC as described in Section 2.3.2.

8.2. Medium Mimic $k_La(O_2)$ Compared to Cell Culture Medium

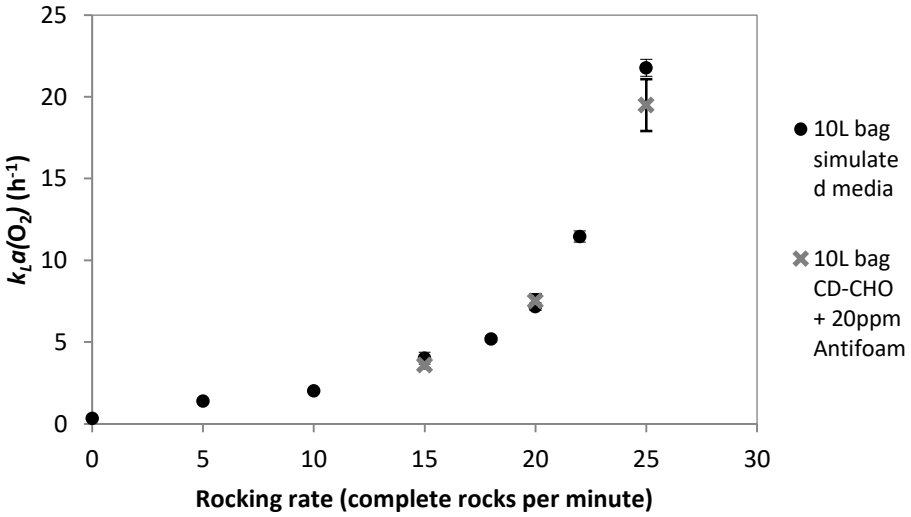

Figure 8.2: Oxygen mass transfer rate for CD-CHO + 20ppm Antifoam compared to media mimic. As in Section 2.4.1.

8.3. $k_La(O_2)$ Static Gassing-Out Example Raw Data

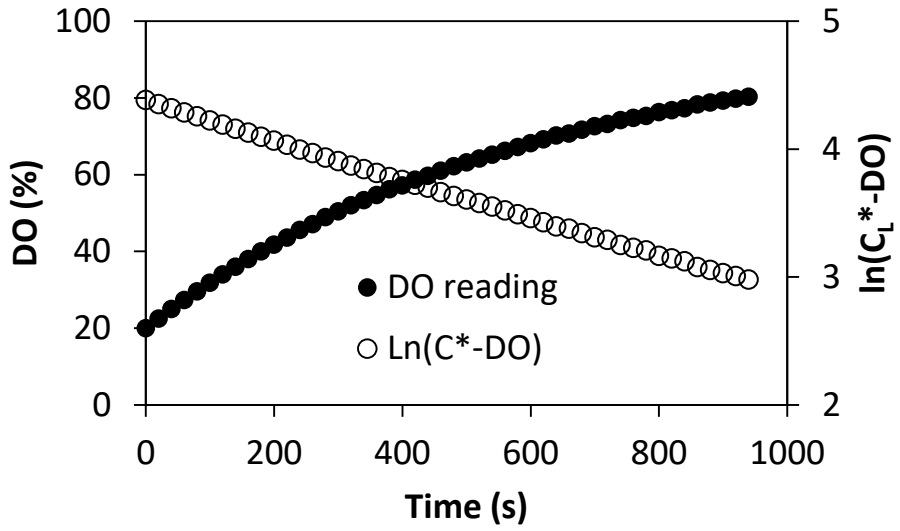

Figure 8.3: Example kLa(O2) experimental raw data. As the oxygen in the air saturated gas phase moves into the liquid phase, the DO reading (filled circles) increases proportionally to the driving force (C*-DO). Plotting ln(C*-DO) on the same time axis produces a straight line of gradient $-k_La$ (open circles). As in Section 2.4.1.

8.4. CO_2 Partial Pressure to pH Reading Calibration Curve

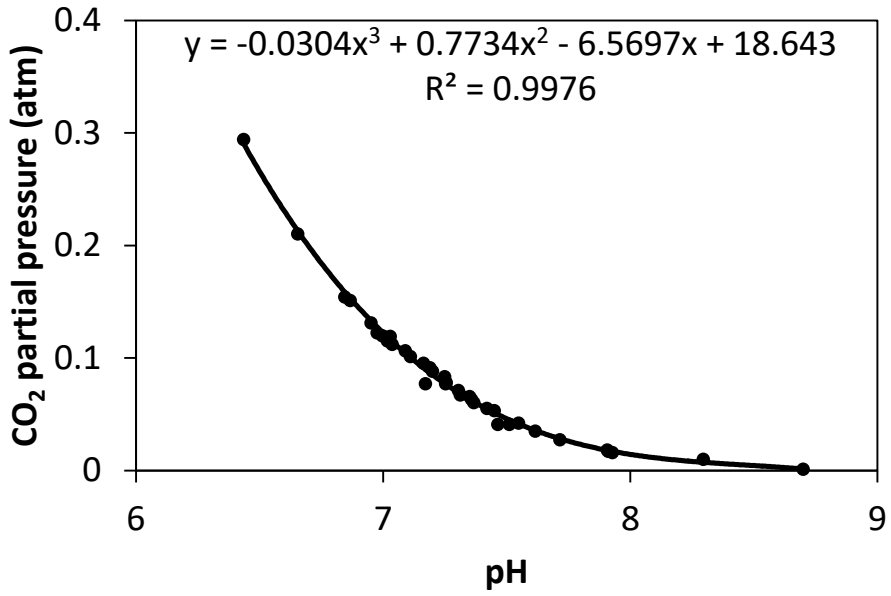

Figure 8.4: Calibration curve between online pH measured by electrolytic probe (Applikon) and offline dCO2 partial pressure readings measured on a Bioprofile 400 (NOVA Biomedical) as in Section 2.4.2.

8.5. Mixing Time Evaluation Example Raw Data

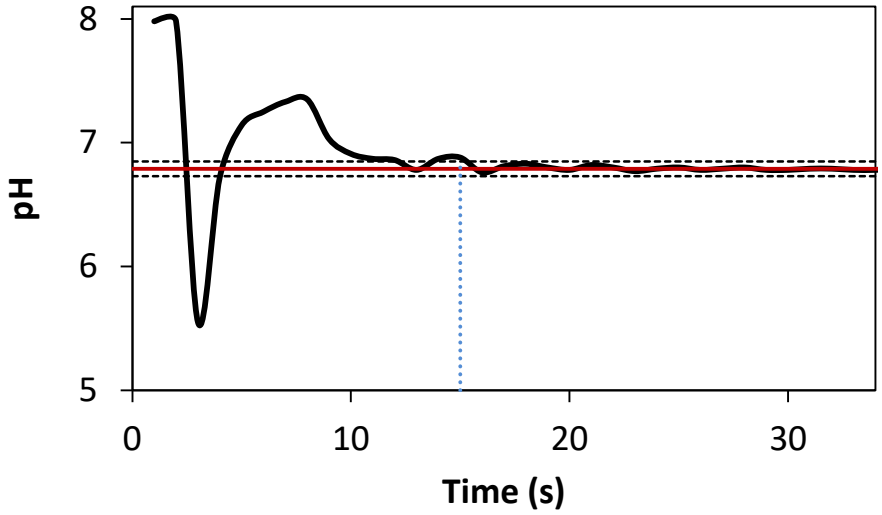

Figure 8.5: Example mixing time experimental data. Initial 2M HCl addition causes rapid downward movement as bolus of acid passes probe followed by reducing oscillation towards the steady final state. 95% mixing is measured as the time taken for the pH to pass and remain within 5% (Dashed black line) of the final steady reading (solid red line). As in Section 2.4.3.

8.6. qPCR Primer Product Evaluation

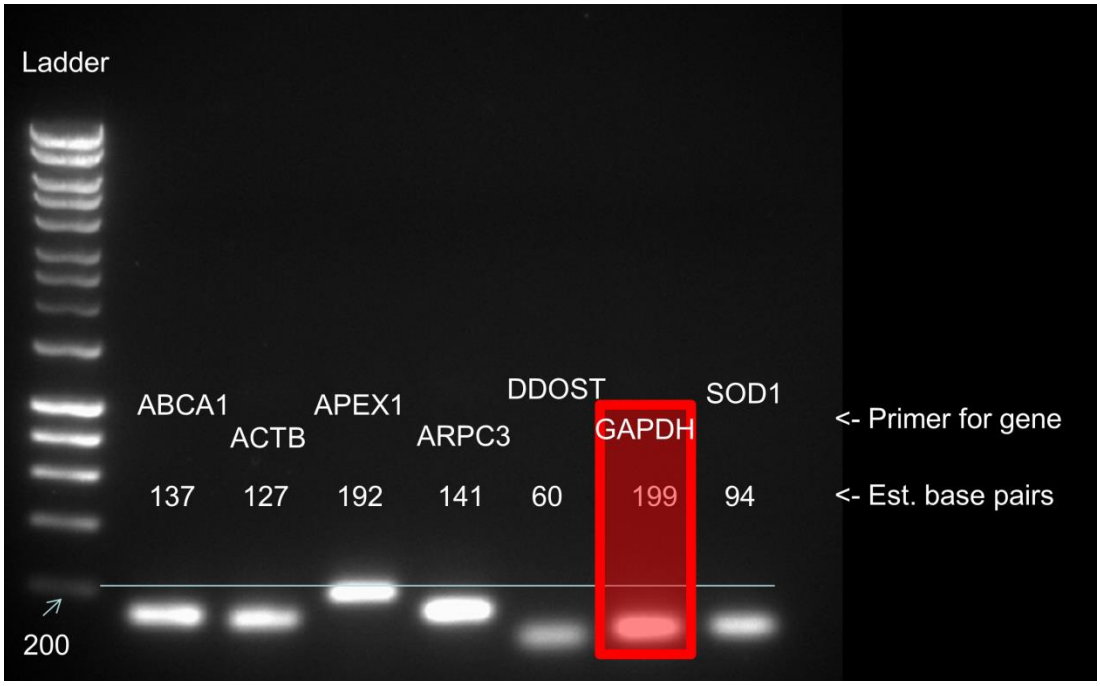

Figure 8.6: qPCR products tested for specificity by 1 % w.v^{-1} agarose gel electrophoresis against a BIOLINE HyperLadder 1kb Ladder for 1 hour at 120 volts and 400mA (Section 2.3.5.4). The GAPDH primer was to be a secondary control but was unused.

Chapter 9. Appendix 2: *MatLab* Scripts

9.1. PIV Raw Data Extraction and Calculation Script

MatLab script used to extract and post-process data from DynamicStudio software into fluid dynamic variables on a per field-of-view, per reading basis.

```
%read version 1.18

%reads the csv files exported from dynamic studios, needs to be told
%dimensions of vector map

function R = read

clear all

tic

timestarteda=fix(clock);

timestarted=timestarteda(1,4:6)

%title1 = '1.0L, 200rpm, Time Resolved,';

%title1 = '25rpm, 8^o, 50% fill, 0^o descending, end';


%READ NAMES/GET SIZE/GET TITLE (SOME BLOAT HERE)

sslist = dir ('*.csv');

ssn=size(sslist,1) ;

for i=1:ssn;
   sslist2{i,1}=sslist(i).name ;
end

str = sslist2{1,1};
[a b c d]= strread(str, '%s %s %s %s', 'delimiter', '.');

%GENERATE TITLE

title1=a;

%GENERATE FILE LIST

bingle=strcat(a,'.',b);

bingle2=strcat(bingle,'.00000%i.csv');
bingle3=strcat(bingle,'.0000%i.csv');
bingle4=strcat(bingle,'.000%i.csv');
```

```
clear a
clear b
clear c
clear d
clear sslist
clear bingle
clear i
clear str



% counts and specifies number of rows, also records mask and X and Y
% coordinates
pu=sprintf(bingle2{1,1},1);
r=csvread(pu,9,4);
nrows=size(r,1);

X=zeros(nrows,1);
Y=zeros(nrows,1);
Masked=zeros(nrows,1);

Masked(:,1)=r(:,8);
X(:,1)=r(:,1);
Y(:,1)=r(:,2);

%big SS prep

U=zeros(nrows,ssn,'single');
V=zeros(nrows,ssn,'single');
u=zeros(nrows,ssn,'single');
v=zeros(nrows,ssn,'single');
uv=zeros(nrows,ssn,'single');

%CSV READER

for i=0:9
  pu=sprintf(bingle2{1,1},i);
  r=csvread(pu,9,4);
  U(:,(i+1))=r(:,5);
  V(:,(i+1))=r(:,6);
end


for i=10:99
   pu=sprintf(bingle3{1,1},i);
   r=csvread(pu,9,4);
   U(:,(i+1))=r(:,5);
   V(:,(i+1))=r(:,6);
end

for i=100:(ssn-1)
   pu=sprintf(bingle4{1,1},i);
   r=csvread(pu,9,4);
   U(:,(i+1))=r(:,5);
   V(:,(i+1))=r(:,6);
```

```
end

Mreshape=reshape(Masked,127,156); % reshapes Masked (list of vector statuses) to a 127x156
matrix

Umean=zeros(nrows,1);
Umean = nanmean(U,2);

Vmean=zeros(nrows,1);
Vmean = nanmean(V,2);

%Vorticity

omegaX = zeros(127,156);
omegaY = zeros(127,156);
Xmetres = (nanmean(X,2))./1000;
Ymetres = (nanmean(Y,2))./1000;
vorticity = zeros(127,159);
Xmreshape = reshape(Xmetres,127,156);
Ymreshape = reshape(Ymetres,127,156);
Umeanreshape = reshape(Umean,127,156);
Vmeanreshape = reshape(Vmean,127,156);

for i = 1:127
   for j = 1:155
      omegaX(i,j) = (Vmeanreshape(i,(j+1)) - Vmeanreshape(i,j)) / (Xmreshape(i,(j+1)) -
Xmreshape(i,j));
   end % dv/dx. j is 1 to 158  rather than 1 to 159, given that if j = 159 then Vmeanreshape(i,(159+1))
would be erroneous. Also, the edges of the graph does not contain relevant information, so this is
OK.
end

for j = 1:156
   for i = 1:126
      omegaY(i,j) = (Umeanreshape((i+1),j) - Umeanreshape(i,j)) / (Ymreshape((i+1),j) -
Ymreshape(i,j));
   end % du/dy. i is 1 to 126 because if i = 127 then Vmeanreshape((127+1),j) would be erroneous.
Also, the edges of the graph does not contain relevant information, so this is OK.
end

for i = 1:127
   for j = 1:156
      vorticity(i,j) = omegaX(i,j) - omegaY(i,j);
   end
end

for j=1:nrows
   for i=1:ssn
      u(j,i)=(U(j,i)-Umean(j,1));
      v(j,i)=(V(j,i)-Vmean(j,1));
   end
end

clear omegaX
clear omegaY
clear pu
```

```
clear pv
clear ru
clear rv
clear uU
clear i
clear j
clear py
clear ry
clear px
clear rx
%clear U
%clear V

Su = zeros(nrows,ssn,'single'); % S denotes "squared", M denotes "mean" and R denotes "root"
Sv = zeros(nrows,ssn,'single');
Suv = zeros(nrows,ssn,'single');

% Coefficient of Correlation: R
UV = zeros(nrows,1); % u is the velocity fluctuations (difference of instantaneous velocity from the
mean)
UV = Umean.*Vmean; % U * V element by element


for j=1:nrows
   for i=1:ssn
      Su(j,i)=(u(j,i))^2;
      Sv(j,i)=(u(j,i))^2;
   end
end %squares each element of velocity fluctuations (u) where u = U - Umean


Suv = Su.*Sv;


MSuv = zeros(nrows,1);
MSuv = nanmean(Suv,2); % calculated the mean of (u^2)*(v^2) in each row
                % u may also be written as u'

clear Suv

RMSuv = zeros(nrows,1);
for i=1:nrows
   RMSuv(i,1)=(MSuv(i,1))^(0.5);
end

R = zeros(nrows,1);
for i=1:nrows
   R(i,1)=(UV(i,1))/(RMSuv(i,1));
end % Coefficient of correlation

Rreshape=reshape(R,127,156); % reshapes R(nrows,1) to a 127x156 matrix

% Turbulent Kinetic Energy: k

MSu = zeros(nrows,1);
```

```
MSu = nanmean(Su,2); % calculated the mean (u^2)*(v^2) in each row
                     % u may also be written as u'

MSv = zeros(nrows,1);
MSv = nanmean(Sv,2);

RMSu=zeros(nrows,1);
RMSv=zeros(nrows,1);
RMS=zeros(nrows,1);

for i=1:nrows
RMSu(i,1)=(MSu(i,1))^0.5;
RMSv(i,1)=(MSv(i,1))^0.5;
RMS(i,1) = (((RMSu(i,1))^2) + ((RMSv(i,1))^2))^(0.5);
end

RMSreshape=reshape(RMS,127,156);

clear RMSu
clear RMSv
clear Su
clear Sv

k = zeros(nrows,1);

k = (3/4) * (MSu + MSv); % Equation for turbulent kinetic energy in 2D

kreshape=reshape(k,127,156); % reshapes R(nrows,1) to a 127x156 matrix

clear UV
clear Su
clear Sv
clear Suv
clear i
clear j
clear MSuv
%RMSuv
%clear Rreshape
clear R
%clear MSv
%clear MSu
clear k


meanLength = zeros(nrows,1);

for i = 1:nrows
   meanLength(i,1) = (((Umean(i,1))^2) + ((Vmean(i,1))^2))^(0.5);
end

Lengthreshape = reshape(meanLength, 127, 156);

clear i

Ymean = zeros(nrows,1);
```

```
Ymean = ((nanmean(Y,2))/1000); % Convert Y from mm to meters

taoLam=zeros(nrows,1);
for i=1:nrows
   taoLam(i,1)=(8.9e-4)*(Umean(i,1)/Ymean(i,1));
end % Units in Pascals


Muv = zeros(nrows,1);

uv=(u.*v); % Element by element multiplication of velocity fluctuations (U-Umean)
Muv = nanmean(uv,2);
taoTurb = (-1000).*Muv;

clear uv


Shear = zeros(nrows,1);
for i=1:nrows
   Shear(i,1) = (taoLam(i,1))+(taoTurb(i,1));
end

taoTurbReshape=reshape(taoTurb,127,156);

clear Ymean
clear taoLam

clear Muv
clear taoTurb
clear Shear
clear i
clear j

FullA = zeros(nrows,ssn,'single');
FullB = zeros(nrows,ssn,'single');
FullC = zeros(nrows,ssn,'single');
FullD = zeros(nrows,ssn,'single');
FullE = zeros(nrows,ssn,'single');

% Smagorinsky Scale

dvbydx = zeros(127,156);
dubydy = zeros(127,156);
dvbydy = zeros(127,156);
dubydx = zeros(127,156);
A = zeros(127,156);
B = zeros(127,156);
C = zeros(127,156);
D = zeros(127,156);
LinA = zeros(nrows,1);
LinB = zeros(nrows,1);
LinC = zeros(nrows,1);
LinD = zeros(nrows,1);

kinvisc = ((8.9e-4)/1000); % Kinematic viscosity (m2/s) is dynamic viscosity divided by density.
```

```
vturb = zeros(nrows,1);
uturb = zeros(nrows,1);
vturbreshape = zeros(127,156);
uturbreshape = zeros(127,156);


for sheet = 1:ssn
   vturb = v(:,sheet);
   vturbreshape = reshape(vturb, 127, 156);
   uturb = u(:,sheet);
   uturbreshape = reshape(uturb, 127, 156);
   for i = 1:127
      for j = 1:155
         dvbydx(i,j) = (vturbreshape(i,(j+1)) - vturbreshape(i,j)) / (Xmreshape(i,(j+1)) - Xmreshape(i,j));
      end % dv/dx. j is 1 to 155  rather than 1 to 156, given that if j = 156 then
Vmeanreshape(i,(156+1)) would be erroneous. Also, the edges of the graph does not contain
relevant information, so this is OK.
   end
   for j = 1:156
      for i = 1:126
         dubydy(i,j) = (uturbreshape((i+1),j) - uturbreshape(i,j)) / (Ymreshape((i+1),j) - Ymreshape(i,j));
      end % du/dy. i is 1 to 126 because if i = 127 then Vmeanreshape((127+1),j) would be erroneous.
Also, the edges of the graph does not contain relevant information, so this is OK.
   end
   for j = 1:156
      for i = 1:126
         dvbydy(i,j) = (vturbreshape((i+1),j) - vturbreshape(i,j)) / (Ymreshape((i+1),j) - Ymreshape(i,j));
      end
   end
   for i = 1:127
      for j = 1:155
         dubydx(i,j) = (uturbreshape(i,(j+1)) - uturbreshape(i,j)) / (Xmreshape(i,(j+1)) - Xmreshape(i,j));
      end
   end
   for i = 1:127
      for j = 1:156
         A(i,j) = ((dubydx(i,j))^2);
         B(i,j) = ((dvbydy(i,j))^2);
         C(i,j) = ((dubydy(i,j))^2);
         D(i,j) = ((dvbydx(i,j))^2);
      end
   end

   LinA = reshape(A, nrows, 1);
   LinB = reshape(B, nrows, 1);
   LinC = reshape(C, nrows, 1);
   LinD = reshape(D, nrows, 1);

   for h = 1:nrows
      FullA(h,sheet) = LinA(h,1);
      FullB(h,sheet) = LinB(h,1);
      FullC(h,sheet) = LinC(h,1);
      FullD(h,sheet) = LinD(h,1);
   end
end
   clear vturb
```

```
   clear vturbreshape
   clear uturb
   clear uturbreshape
   clear dvbydx
   clear dubydy
   clear dvbydy
   clear dubydx
   clear A
   clear B
   clear C
   clear D
   clear LinA
   clear LinB
   clear LinC
   clear LinD



   vturb = zeros(nrows,1);
   uturb = zeros(nrows,1);
   vturbreshape = zeros(127,156);
   uturbreshape = zeros(127,156);
   dvbydx = zeros(127,156);
   dubydy = zeros(127,156);
   dvbydy = zeros(127,156);
   dubydx = zeros(127,156);
   A = zeros(127,156);
   B = zeros(127,156);
   C = zeros(127,156);
   D = zeros(127,156);
   LinA = zeros(nrows,1);
   LinB = zeros(nrows,1);
   LinC = zeros(nrows,1);
   LinD = zeros(nrows,1);

meanA = nanmean(FullA,2);
meanB = nanmean(FullB,2);
meanC = nanmean(FullC,2);
meanD = nanmean(FullD,2);

EpsilonSGS=zeros(nrows,1) ;

for h = 1:nrows
   EpsilonSGS(h,1) = ((0.17*0.001065332)^2) * (4*meanA(h,1) + 4*meanB(h,1) + 2*meanC(h,1) +
2*meanD(h,1))^(3/2);
end

ReshapeEpsilonSGS = reshape(EpsilonSGS, 127, 156);

KolmogorovSpaceSGS=zeros(127,156);

for i = 1:127
   for j = 1:156
      KolmogorovSpaceSGS(i,j) = ((kinvisc^3) / ReshapeEpsilonSGS(i,j)) ^ (1/4);
   end
end
```

```
% The following code will calculate the energy dissipation rate via direct
% evaluation (DE)
dvbydx = zeros(127,156);
dubydy = zeros(127,156);
dvbydy = zeros(127,156);
dubydx = zeros(127,156);
A = zeros(127,156);
B = zeros(127,156);
C = zeros(127,156);
D = zeros(127,156);
E = zeros(127,156);
LinA = zeros(nrows,1);
LinB = zeros(nrows,1);
LinC = zeros(nrows,1);
LinD = zeros(nrows,1);
LinE = zeros(nrows,1);

Xmetres = (mean(X,2))./1000;
Ymetres = (mean(Y,2))./1000;
Xmreshape = reshape(Xmetres,127,156);
Ymreshape = reshape(Ymetres,127,156);
Umeanreshape = reshape(Umean,127,156);
Vmeanreshape = reshape(Vmean,127,156);
kinvisc = ((8.9e-4)/1000); % Kinematic viscosity (m2/s) is dynamic viscosity divided by density.
KolmTime = zeros(127,156);
KolmSpace = zeros(127,156);
vturb = zeros(nrows,1);
uturb = zeros(nrows,1);
vturbreshape = zeros(127,156);
uturbreshape = zeros(127,156);

%clear X
%clear Y


for sheet = 1:ssn
   vturb = v(:,sheet);
   vturbreshape = reshape(vturb, 127, 156);
   uturb = u(:,sheet);
   uturbreshape = reshape(uturb, 127, 156);
   for i = 1:127
      for j = 1:155
         dvbydx(i,j) = (vturbreshape(i,(j+1)) - vturbreshape(i,j)) / (Xmreshape(i,(j+1)) - Xmreshape(i,j));
      end % dv/dx. j is 1 to 155  rather than 1 to 156, given that if j = 156 then
Vmeanreshape(i,(156+1)) would be erroneous. Also, the edges of the graph does not contain
relevant information, so this is OK.
   end
   for j = 1:156
      for i = 1:126
         dubydy(i,j) = (uturbreshape((i+1),j) - uturbreshape(i,j)) / (Ymreshape((i+1),j) - Ymreshape(i,j));
      end % du/dy. i is 1 to 126 because if i = 127 then Vmeanreshape((127+1),j) would be erroneous.
Also, the edges of the graph does not contain relevant information, so this is OK.
   end
   for j = 1:156
      for i = 1:126
```

```
        dvbydy(i,j) = (vturbreshape((i+1),j) - vturbreshape(i,j)) / (Ymreshape((i+1),j) - Ymreshape(i,j));
      end
    end
    for i = 1:127
      for j = 1:155
        dubydx(i,j) = (uturbreshape(i,(j+1)) - uturbreshape(i,j)) / (Xmreshape(i,(j+1)) - Xmreshape(i,j));
      end
    end
    for i = 1:127
      for j = 1:156
        A(i,j) = ((dubydx(i,j))^2);
        B(i,j) = ((dvbydy(i,j))^2);
        C(i,j) = ((dubydy(i,j))^2);
        D(i,j) = ((dvbydx(i,j))^2);
        E(i,j) = (dubydy(i,j) * dvbydx(i,j));
      end
    end

    LinA = reshape(A, nrows, 1);
    LinB = reshape(B, nrows, 1);
    LinC = reshape(C, nrows, 1);
    LinD = reshape(D, nrows, 1);
    LinE = reshape(E, nrows, 1);

    for h = 1:nrows
      FullA(h,sheet) = LinA(h,1);
      FullB(h,sheet) = LinB(h,1);
      FullC(h,sheet) = LinC(h,1);
      FullD(h,sheet) = LinD(h,1);
      FullE(h,sheet) = LinE(h,1);
    end
end
    clear vturb
    clear vturbreshape
    clear uturb
    clear uturbreshape
    clear dvbydx
    clear dubydy
    clear dvbydy
    clear dubydx
    clear A
    clear B
    clear C
    clear D
    clear E
    clear LinA
    clear LinB
    clear LinC
    clear LinD
    clear LinE
    vturb = zeros(nrows,1);
    uturb = zeros(nrows,1);
    vturbreshape = zeros(127,156);
    uturbreshape = zeros(127,156);

meanA = nanmean(FullA,2);
```

```
meanB = nanmean(FullB,2);
meanC = nanmean(FullC,2);
meanD = nanmean(FullD,2);
meanE = nanmean(FullE,2);

clear FullA
clear FullB
clear FullC
clear FullD
clear FullE
clear u
clear v

Epsilon=zeros(nrows,1);

for h = 1:nrows
   Epsilon(h,1) = kinvisc * (2*meanA(h,1) + 2*meanB(h,1) + 3*meanC(h,1) + 3*meanD(h,1) +
2*meanE(h,1));
end

ReshapeEpsilon = reshape(Epsilon, 127, 156);


KolmogorovSpace=zeros(127,156);

for i = 1:127
   for j = 1:156
      KolmogorovSpace(i,j) = ((kinvisc^3) / ReshapeEpsilon(i,j)) ^ (1/4);
   end
end

LengthM=zeros(127,156);
kM=zeros(127,156);
taoTurbM=zeros(127,156);
MEpsilonSGS=zeros(127,156);
KolmogorovSpaceM=zeros(127,156);
UmeanM=zeros(127,156);
VmeanM=zeros(127,156);
RMSM=zeros(127,156);
vorticityM=zeros(127,156);

for i=1:127;
   for j=1:156;
      if Mreshape(i,j) == 0;
         LengthM(i,j)=Lengthreshape(i,j);
         kM(i,j)=kreshape(i,j);
         taoTurbM(i,j)=taoTurbReshape(i,j);
         MEpsilonSGS(i,j)=ReshapeEpsilonSGS(i,j);
         KolmogorovSpaceM(i,j)=KolmogorovSpace(i,j);
         UmeanM(i,j)=Umeanreshape(i,j);
         VmeanM(i,j)=Vmeanreshape(i,j);
         RMSM(i,j)=RMSreshape(i,j);
         vorticityM(i,j)=vorticity(i,j);

      elseif Mreshape(i,j) == 16;
         LengthM(i,j)=Lengthreshape(i,j);
```

```
        kM(i,j)=kreshape(i,j);
        taoTurbM(i,j)=taoTurbReshape(i,j);
        MEpsilonSGS(i,j)=ReshapeEpsilonSGS(i,j);
        KolmogorovSpaceM(i,j)=KolmogorovSpace(i,j);
        UmeanM(i,j)=Umeanreshape(i,j);
        VmeanM(i,j)=Vmeanreshape(i,j);
        RMSM(i,j)=RMSreshape(i,j);
        vorticityM(i,j)=vorticity(i,j);

      else LengthM(i,j)= 0;
          kM(i,j)= 0;
          taoTurbM(i,j)= 0;
          MEpsilonSGS(i,j)= 0;
          KolmogorovSpaceM(i,j)= 0;
          UmeanM(i,j)= 0;
          VmeanM(i,j)= 0;
          RMSM(i,j)= 0;
          vorticityM(i,j)=0;

      end
   end
end

clear Umeanreshape
clear Vmeanreshape
clear RMSreshape
clear kolmogorovSpace
clear Lengthreshape
clear kreshape
clear taoTurbReshape
clear ReshapeEpsilonSGS
clear vorticity

% XM=zeros(nrows,1);
% YM=zeros(nrows,1);
%
% for i=1:nrows
%       if Masked(i) == 0;
%          XM(i)=X(i);
%          YM(i)=Y(i);
%
%       elseif Mreshape(i) == 16;
%          XM(i)=X(i);
%          YM(i)=Y(i);
%
%       else
%          XM(i)=NaN;
%          YM(i)=NaN;
%
%       end
% end

UM=zeros(nrows,ssn,'single');

for i=1:nrows
   for j=1:ssn
```

```
      if Masked(i) == 0;
         UM(i,j)=U(i,j);

      elseif Mreshape(i) == 16;
         UM(i,j)=U(i,j);

      else
         UM(i,j)=0;

      end
   end
end

clear U

VM=zeros(nrows,ssn,'single');

 for i=1:nrows
   for j=1:ssn
      if Masked(i) == 0;
         VM(i,j)=V(i,j);

      elseif Mreshape(i) == 16;
         VM(i,j)=V(i,j);

      else
         VM(i,j)=0;

      end
   end
 end

clear V

%clear all bar useful variables

clearvars -except title1 kM LengthM taoTurbM MEpsilonSGS KolmogorovSpaceM UmeanM VmeanM
RMSM UM VM X Y Mreshape Masked nrows vorticityM

%Generate variable name friendly general title

title2=strrep(title1{1,1},' ','_');
title3=genvarname(title2);

%Generate detailed titles such Length_general title

titleL=strcat('Length_',title3);
titleR=strcat('RMS_',title3);
titleT=strcat('TKE_',title3);
titlev=strcat('Vorticity_',title3);
titleS=strcat('Shear_',title3);
titleU=strcat('Umean_',title3);
titleV=strcat('Vmean_',title3);

%rename plots with detailed titles
```

```
eval([titleL, '=LengthM']);
eval([titleR, '=RMSM']);
eval([titleT, '=kM']);
eval([titlev, '=vorticityM']);
eval([titleS, '=taoTurbM']);
eval([titleU, '=UmeanM']);
eval([titleV, '=VmeanM']);

clear LengthM
clear RMSM
clear kM
clear vorticityM
clear taoTurbM
clear UmeanM
clear VmeanM

title6 = strcat('Keyvar_',title1{1,1},'.mat'); % save key variables for reprocessing.
save (title6) %,'title1', 'kM', 'LengthM', 'taoTurbM', 'MEpsilonSGS',
'KolmogorovSpaceM','UmeanM','VmeanM','RMSM','UM','VM','X','Y','Mreshape','Masked','nrows','vo
rticityM');

% xlswrite((strcat('Length_',title1{1,1})),LengthM)
% xlswrite((strcat('RMS_',title1{1,1})),RMSM)
% xlswrite((strcat('TKE_',title1{1,1})),kM)
% xlswrite((strcat('Vorticity_',title1{1,1})),vorticityM)
% xlswrite((strcat('Shear_',title1{1,1})),taoTurbM)

timefinisheda=fix(clock);
timefinished=timefinisheda(1,4:6)
timetaken=toc

% %SOUND FLOURISH
% Done=zeros(nrows,2);
% for i=1:nrows
%     Done(i,1)=meanLength(i,1);
%     Done(i,2)=RMS(i,1);
% end
%
% sound(Done);

%clear all
```

9.2. Calculated Data Compilation Step 1 Script

MatLab script used to combine the above output from the two field of views into a single dataset.

```
%adder version 1.02

%adds two array exports together and then calls cont to plot and save these

function D = adder(rpm)

close all

%rpm = input('rpm?')

fillist=what;

load(fillist.mat{1,1});
load(fillist.mat{2,1});

list{1} = who ('Length*');
list{2} = who ('RMS*');
list{3} = who ('TKE*');
list{4} = who ('Vorticity*');
list{5} = who ('Shear*');
list{6} = who ('Umean*');
list{7} = who ('Vmean*');
%list{8} = who ('Mask*');

%Length Figure

%Length end and mid addition and NaNing

Length1=eval(list{1}{1,1});
Length2=eval(list{1}{2,1});
Length3=Length1+Length2;
Length4=NaN(size(Length3,1),size(Length3,2));
for i=1:size(Length3,1);
   for j=1:size(Length3,2);
      if any(Length3(i,j))==1;
         Length4(i,j)=Length3(i,j);
      end
   end
end

%Umean end and mid addition and NaNing

Um1=eval(list{6}{1,1});
Um2=eval(list{6}{2,1});
Um3=Um1+Um2;
Um4=NaN(size(Um3,1),size(Um3,2));
for i=1:size(Um3,1);
   for j=1:size(Um3,2);
      if any(Um3(i,j))==1;
```

```
        Um4(i,j)=Um3(i,j);
      end
   end
end

%Vmean end and mid addition and NaNing

Vm1=eval(list{7}{1,1});
Vm2=eval(list{7}{2,1});
Vm3=Vm1+Vm2;
Vm4=NaN(size(Vm3,1),size(Vm3,2));
for i=1:size(Vm3,1);
   for j=1:size(Vm3,2);
      if any(Vm3(i,j))==1;
         Vm4(i,j)=Vm3(i,j);
      end
   end
end

%Quiver plot

% svx=NaN(size(Length4,1),size(Length4,2));
% svy=NaN(size(Length4,1),size(Length4,2));
% svu=NaN(size(Length4,1),size(Length4,2));
% svv=NaN(size(Length4,1),size(Length4,2));

for i=1:25
   for j=1:31
    svx(i,j) = (5*j)-2; % generates vector x location
    svy(i,j) = (5*i)-2; % ditto for y
    svu(i,(j))=mean(mean(Um4(((5*i-4):(5*i)),((5*j-4):((5*j))))); %gets spatial mean over 7x7 vector
grid in U dir
    svv(i,(j))=mean(mean(Vm4(((5*i-4):(5*i)),((5*j-4):((5*j))))); %ditto for V
   end
end

%Length contour plot

cont(Length4./(.315/(60/rpm)*2),list{1}{1,1},0.0,0.5)

%Attachment of quiver plot to contour plot

hold on
quiver(double(svx),double(svy),double(svu),double(svv),'Color',[0 0
0],'AutoScaleFactor',1.2,'LineWidth',1); %plots quiver plot onto contour plot
hold off

print (gcf,'-painters', '-dtiff', '-r300',strcat((list{1}{1,1}),'.tiff'));

%print (gcf,'-painters', '-dpng', '-r300',strcat((list{1}{1,1}),'.png'));

close all
```

```
%TKE end and mid addition and NaNing

TKE1=eval(list{3}{1,1});
TKE2=eval(list{3}{2,1});
TKE3=TKE1+TKE2;
TKE4=NaN(size(TKE3,1),size(TKE3,2));
for i=1:size(TKE3,1);
   for j=1:size(TKE3,2);
      if any(TKE3(i,j))==1;
         TKE4(i,j)=TKE3(i,j);
      end
   end
end

%TKE contour plot

cont(TKE4./(.315/(60/rpm)*2),list{3}{1,1},0,.1)

close




%Vorticity end and mid addition and NaNing

Vorticity1=eval(list{4}{1,1});
Vorticity2=eval(list{4}{2,1});
Vorticity3=Vorticity1+Vorticity2;
Vorticity4=NaN(size(Vorticity3,1),size(Vorticity3,2));
for i=1:size(Vorticity3,1);
   for j=1:size(Vorticity3,2);
      if any(Vorticity3(i,j))==1;
         Vorticity4(i,j)=Vorticity3(i,j);
      end
   end
end

%Vort contour plot

cont((Vorticity4./(rpm/60)),list{4}{1,1},-100,100)

close



%Shear end and mid addition and NaNing

Shear1=eval(list{5}{1,1});
Shear2=eval(list{5}{2,1});
Shear3=Shear1+Shear2;
```

```
Shear4=NaN(size(Shear3,1),size(Shear3,2));
for i=1:size(Shear3,1);
   for j=1:size(Shear3,2);
      if any(Shear3(i,j))==1;
         Shear4(i,j)=Shear3(i,j);
      end
   end
end

%Shear contour plot

cont(((Shear4.^2).^.5),list{5}{1,1},0,15)

close
```

9.3. Calculated Data Compilation Step 2 Script

MatLab script written to call 'adder' (Appendix 2.2) for an experiments worth of readings – 8 (1 at each angle investigated).

```
function D = mastadder(rpm)

tic

timestarteda=fix(clock);

timestarted=timestarteda(1,4:6) %#ok<NOPTS>

follist=dir;

for i=1:size(follist,1)
runlist{i,1}=strcat(pwd,'\',follist(i,1).name); %#ok<SAGROW>
end

for i=1:size(follist,1)
   Approximate_progress=i/size(follist,1) %#ok<NOPTS>
try cd(runlist{i,1});
   adder(95.23809524)
   %men(i,1)=ans
catch 'could not run function in this folder, trying next folder'
end
end

toc
```

9.4. Calculated Data Plotting Script

MatLab script written to plot graphs for velocity, turbulent kinetic energy and shear from the above collated data.

```
tic

%GRAPH PLOTTER to be used after READ in the same directory

clear all
```

```
fillist=what

load(fillist.mat{1,1})
load(fillist.mat{2,1})

%load ('*.mat')

list{:,1} = who ('Length*')
list{:,2} = who ('RMS*')

%Choose title

title1 = '1.0L, 350rpm, Angle Resolved, 00^o, 300IPs,';
%title1 = '2.4L, 200rpm, Time Resolved,';


%Set x and y axis limits for all plots

xl=11;
xh=159;
yl=1;
yh=127;


close all









%TURBULENCE KINETIC ENERGY PLOT

kmax = max(kreshape(60:125,1:90));
maxK = max(kmax);
kmin = min(kreshape(60:125,1:90));
minK = min(kmin);

kreshapeD=double(kreshape);
figure(1);
contourf(kreshapeD,15,'LineStyle','none');
colorbar;
title2 = ' TKE (m^2s^-^2)'; %specific graph title to be added onto global title
title3 = strcat(title1, title2); % concatenates specific and global graph title
title4= strcat(title3,'.png');
ylabel('z/H','FontSize',13);
xlabel('r/R','FontSize',13);
title(title3,'FontSize',14); %sets graph title
%caxis ([0, 0.15000001]) %impeller zone scaled colourbar axis
axis equal %believed to in some way maintains aspect ratio
axis vis3d %also maintains aspect ratio
%axis fixed
```

```
xlim ([xl xh]) %sets axis and data limits
ylim ([yl yh])
set (figure(1), 'PaperPosition', [1 1 25 25]) % sets PRINTED paper aspect ratio MAYBE IMPORTANT IF
FIGURE ASPECT RATIO CHANGES
set(gca, 'XTick', [11:28.8:159]); %sets notch distance on x axis
set(gca, 'XTickLabel', [1:-0.2:0],'fontsize',12); % sets notch labels on x axis and font size on both axes
set(gca, 'YTick', [1:23.27531:127]);
set(gca, 'YTickLabel', [0:0.05:0.270673]);
set(figure(1), 'color', 'white'); % sets the bground color to white
c2=colorbar;
ylabel(c2,title2,'fontsize',15);

print (figure(1),'-painters', '-dpng', '-r300',title4);
```

```
%RMS PLOT

Rmax = max(RMSreshape(60:125,1:90));
maxR = max(Rmax);
Rmin = min(RMSreshape(60:125,1:90));
minR = min(Rmin);

RMSreshapeD=double(RMSreshape./1.39);
figure(2);
contourf(RMSreshapeD,15,'LineStyle','none');
colorbar;
title2 = ' Normalised Fluid RMS velocity (RMSV.V_t_i_p ^-^1)'; %specific graph title to be added onto
global title and caxis label
title3 = strcat(title1, title2); % concatenates specific and global graph title
title4= strcat(title3,'.png');
ylabel('z/H','FontSize',13);
xlabel('r/R','FontSize',13);
title(title3,'FontSize',14); %sets graph title
%caxis ([0, 0.090000001]) %impeller zone scaled colourbar axis
 axis equal %believed to in some way maintain aspect ratio
axis vis3d %also maintains aspect ratio
%axis fixed
xlim ([xl xh]) %sets axis and data limits
ylim ([yl yh])
set (figure(2), 'PaperPosition', [1 1 25 25]) % sets PRINTED paper aspect ratio MAYBE IMPORTANT IF
FIGURE ASPECT RATIO CHANGES
set(gca, 'XTick', [11:29.6:159]); %sets notch distance on x axis
set(gca, 'XTickLabel', [1:-0.2:0],'fontsize',12); % sets notch labels on x axis and font size on both axes
set(gca, 'YTick', [1:23.27531:127]);
set(gca, 'YTickLabel', [0:0.05:0.270673]);set(gca, 'YTickLabel', [0:0.1:1.0]);
set(figure(2), 'color', 'white'); % sets the bground color to white
c2=colorbar;
ylabel(c2,title2,'fontsize',15);
```

```
print (figure(2),'-painters','-dpng','-r300',title4);
```

```
%LENGTH PLOT

lmax = max(Lengthreshape(60:125,1:90));
maxL = max(lmax);
lmin = min(Lengthreshape(60:125,1:90));
minL = min(lmin);

LengthreshapeD=double(Lengthreshape./1.39);
figure(3);
contourf(LengthreshapeD,15,'LineStyle','none');
colorbar;
title2 = ' Normalised Fluid velocity (V.V_t_i_p ^-^1)'; %specific graph title to be added onto global
title and caxis label
title3 = strcat(title1, title2); % concatenates specific and global graph title
title4= strcat(title3,'.png');
ylabel('z/H','FontSize',13);
xlabel('r/R','FontSize',13);
title(title3,'FontSize',14); %sets graph title
caxis ([0, 0.3000001]) %impeller zone scaled colourbar axis
 axis equal %believed to in some way maintains aspect ratio
axis vis3d %also maintains aspect ratio
%axis fixed
xlim ([xl xh]) %sets axis and data limits
ylim ([yl yh])
set (figure(3), 'PaperPosition', [1 1 25 25]) % sets PRINTED paper aspect ratio MAYBE IMPORTANT IF
FIGURE ASPECT RATIO CHANGES
set(gca, 'XTick', [11:29.6:159]); %sets notch distance on x axis
set(gca, 'XTickLabel', [1:-0.2:0],'fontsize',12); % sets notch labels on x axis and font size on both axes
set(gca, 'YTick', [1:23.27531:127]);
set(gca, 'YTickLabel', [0:0.05:0.270673]);
set(figure(3), 'color', 'white'); % sets the bground color to white
c2=colorbar;
ylabel(c2,title2,'fontsize',15);
%set (figure(3),'alpha',(0.2))

%Extra step to add vector map to figure

for i=1:25
   for j=1:31
    svx(i,j) = (5*j)-2; % generates vector x location
    svy(i,j) = (5*i)-2; % ditto for y
    svu(i,(j))=mean(mean(Umeanreshape(((5*i-4):(5*i)),((5*j-4):((5*j))))); %gets spatial mean over
7x7 vector grid in U dir
    svv(i,(j))=mean(mean(Vmeanreshape(((5*i-4):(5*i)),((5*j-4):((5*j))))); %ditto for V
```

```
   end
end

hold on
quiver(double(svx),double(svy),double(svu),double(svv),'Color',[0 0
0],'AutoScaleFactor',1.2,'LineWidth',1); %plots quiver plot onto contour plot
hold off
%set(fc2,'position',[700 00 500 850])

print (figure(3),'-painters','-dpng','-r300',title4);









%SHEAR PLOT

smax = max(taoTurbReshape(60:125,1:90));
maxS = max(smax);
smin = min(taoTurbReshape(60:125,1:90));
minS = min(smin);

taoTurbReshapeD=double(taoTurbReshape);
figure(4);
contourf(taoTurbReshapeD,15,'LineStyle','none');
colorbar;
title2 = ' Shear Stress (Pa)'; %specific graph title to be added onto global title
title3 = strcat(title1, title2); % concatenates specific and global graph title
title4= strcat(title3,'.png');
ylabel('z/H','FontSize',13);
xlabel('r/R','FontSize',13);
title(title3,'FontSize',14); %sets graph title
%caxis ([0, 0.15000001]) %impeller zone scaled colourbar axis
 axis equal %believed to in some way maintains aspect ratio
axis vis3d %also maintains aspect ratio
%axis fixed
xlim ([xl xh]) %sets axis and data limits
ylim ([yl yh])
set (figure(4), 'PaperPosition', [1 1 25 25]) % sets PRINTED paper aspect ratio MAYBE IMPORTANT IF
FIGURE ASPECT RATIO CHANGES
set(gca, 'XTick', [11:29.6:159]); %sets notch distance on x axis
set(gca, 'XTickLabel', [1:-0.2:0],'fontsize',12); % sets notch labels on x axis and font size on both axes
set(gca, 'YTick', [1:23.27531:127]);
set(gca, 'YTickLabel', [0:0.05:0.270673]);
set(figure(4), 'color', 'white'); % sets the bground color to white
c2=colorbar;
ylabel(c2,title2,'fontsize',15);

print (figure(4),'-painters', '-dpng', '-r300',title4);
```

```
%SMAGORINSKY PLOT

smagmax = max(ReshapeEpsilonSGS(60:125,1:90));
maxSMAG = max(smagmax);
smagmin = min(ReshapeEpsilonSGS(60:125,1:90));
minSMAG = min(smagmin);

ReshapeEpsilonSGSD=double(ReshapeEpsilonSGS);
figure(5);
contourf(ReshapeEpsilonSGSD,15,'LineStyle','none');
colorbar;
title2 = ' Local Energy Dissipation Rate, Smagorinsky (W)'; %specific graph title to be added onto
global title
title3 = strcat(title1, title2); % concatenates specific and global graph title
title4= strcat(title3,'.png');
ylabel('z/H','FontSize',13);
xlabel('r/R','FontSize',13);
title(title3,'FontSize',14); %sets graph title
%caxis ([0, 0.15000001]) %impeller zone scaled colourbar axis
axis equal %believed to in some way maintains aspect ratio
axis vis3d %also maintains aspect ratio
%axis fixed
xlim ([xl xh]) %sets axis and data limits
ylim ([yl yh])
set (figure(5), 'PaperPosition', [1 1 25 25]) % sets PRINTED paper aspect ratio MAYBE IMPORTANT IF
FIGURE ASPECT RATIO CHANGES
set(gca, 'XTick', [11:29.6:159]); %sets notch distance on x axis
set(gca, 'XTickLabel', [1:-0.2:0],'fontsize',12); % sets notch labels on x axis and font size on both axes
set(gca, 'YTick', [1:23.27531:127]);
set(gca, 'YTickLabel', [0:0.05:0.270673]);
set(figure(5), 'color', 'white'); % sets the bground color to white
c2=colorbar;
ylabel(c2,title2,'fontsize',15);

print (figure(5),'-painters', '-dpng', '-r300',title4);
```

```
%KOLMOGOROV PLOT

ksmax = max(KolmogorovSpace(60:125,1:90));
maxKS = max(ksmax);
```

```
ksmin = min(KolmogorovSpace(60:125,1:90));
minKS = min(ksmin);

KolmogorovSpaceD=double(KolmogorovSpace);

for i=1:159
   for j=1:127
      if KolmogorovSpaceD(j,i) == inf;
            KolmogorovSpaceD(j,i)= 0;
      end
   end
end


figure(6);
contourf(KolmogorovSpaceD,15,'LineStyle','none');
colorbar;
title2 = ' Kolmogorov Spatial Scale (m)'; %specific graph title to be added onto global title
title3 = strcat(title1, title2); % concatenates specific and global graph title
title4= strcat(title3,'.png');
ylabel('z/H','FontSize',13);
xlabel('r/R','FontSize',13);
title(title3,'FontSize',14); %sets graph title
%caxis ([0, 0.15000001]) %impeller zone scaled colourbar axis
axis equal %believed to in some way maintains aspect ratio
axis vis3d %also maintains aspect ratio
%axis fixed
xlim ([xl xh]) %sets axis and data limits
ylim ([yl yh])
set (figure(6), 'PaperPosition', [1 1 25 25]) % sets PRINTED paper aspect ratio MAYBE IMPORTANT IF
FIGURE ASPECT RATIO CHANGES
set(gca, 'XTick', [11:29.6:159]); %sets notch distance on x axis
set(gca, 'XTickLabel', [1:-0.2:0],'fontsize',12); % sets notch labels on x axis and font size on both axes
set(gca, 'YTick', [1:23.27531:127]);
set(gca, 'YTickLabel', [0:0.05:0.270673]);
set(figure(6), 'color', 'white'); % sets the bground color to white
c2=colorbar;
ylabel(c2,title2,'fontsize',15);

print (figure(6),'-painters', '-dpng', '-r300',title4);


%clear all

timetaken=toc
```

9.5. Bulk Fluid Tracking and Quantification Script

MatLab Script written to interpret and quantify the angle of the fluid surface and position of the fluid from video photography of the rocked bag.

```
close all
clear all

tic
```

```
%list all files in dir

list=dir;

%find only *.!
piclist=cell(size(list),1);

for i=1:length(list);
   [pathstr, name, ext] = fileparts(list(i).name);
   if strcmp(ext, '.bmp')==1;
   piclist{i}=list(i).name;
      %else piclist(i)=[];
   end
end

%# find empty cells
emptyCells = cellfun(@isempty,piclist);
%# remove empty cells
piclist(emptyCells) = [];


% keeperIndexes = find(allBlobAreas > 2000);  % Take the larger objects.
% % Note how we use ismember to select the blobs that meet our criteria.
% nickelBinaryImage = ismember(labeledImage, keeperIndexes);


%read, crop and put into 3d array
%generates frames in greyscale big 3d array

pics=uint8(zeros(499,1046,360));

for i=1:360
   pic=imread(piclist{i});
   pic2=imcrop(pic, [215,162,1045,498]);
   %easyendtemp=pic2;
   %pic=imread(piclist{i+180});
   %pic2=imcrop(pic, [215,162,1045,498]);
   %hardendtemp=fliplr(pic2);
   pics(:,:,i)=pic2;
   %pics(:,:,i)=cat(2,hardendtemp,easyendtemp);
   %pics(:,:,i+180)=cat(2,fliplr(easyendtemp),fliplr(hardendtemp));
end

meanintense1=mean(mean(mean(pics)))
meanintense=mean(pics,3);
darkbit=pics(373,48,2)
lightbit=pics(221,303,2)

makepics=toc
tic

%failed attempt at motion detection

%base=single(zeros(size(pics,1),size(pics,2)));
% mot=single(zeros(size(pics,1),size(pics,2)));
```

```
% mot2=single(zeros(size(pics,1),size(pics,2)));
% mot3=single(zeros(size(pics,1),size(pics,2)));
%
% for i=1:size(pics,1)
%     for j=1:size(pics,2)
%         %for k=size(pics,3)/10:size(pics,3)/10:size(pics,3);
%           mot=mot2;
%            %if pics(i,j,k)-pics(i,j,k+1-size(pics,3)/10) >10 ;
%            if abs(pics(i,j,36) -- pics(i,j,1)) >10 ;
%               mot2(i,j)=mot(i,j)+5;
%
%                       end
%       end
%    end
% %end
%
%


% %split into two halfs
% pics_l=uint8(zeros(size(pics,1),size(pics,2)/2,size(pics,3)));
% pics_r=uint8(zeros(size(pics,1),size(pics,2)/2,size(pics,3)));

%flicker adjust

%pics_fa=uint8(zeros(size(pics,1),size(pics,2),size(pics,3)));

pics_fa=pics;

% for i = 1:size(pics,3)
% temppics=single(pics(:,:,i));
% temppics2=temppics./mean(mean(temppics))*meanintense(498,1045);
% pics_fa(:,:,i)=temppics2;
% end


% work out thresholds
cutoffabs=single((lightbit-darkbit)/5+darkbit); %.8*(meanintense1+1)/256
cutoff=(cutoffabs+1)/256

%free up memory

clearvars -except pics_fa cutoff

angs=double(zeros(size(pics_fa,3),2));

stats=single(zeros(2,size(pics_fa,3)));
%macs=uint16(zeros(size(pics_fa,2),size(pics_fa,3)));


%make video object
vidObj=VideoWriter('bulkline.avi');

%open video object
open (vidObj);
```

```
%record video

for i = 1:size(pics_fa,3)
   tic
   %pic_bw=~im2bw(pics_fa,cutoff);

   if i<181
   frame_a=pics_fa(:,:,i);
   frame_b=fliplr(pics_fa(:,:,i+180));

   else
   frame_a=pics_fa(:,:,i);
   frame_b=fliplr(pics_fa(:,:,i-180));

   end

   frame=horzcat(frame_b,frame_a);

   %make binary and invert
   frame2=~im2bw(frame,cutoff);

 %interpolate across o-ring and bolts

 %o-ring

 frame3=frame2;
     for j=1:size(frame2,2);
        if mean(frame2(255:260,j)) > 0.5 ;
              frame3(257:285,j)=1;
        end
        if mean(frame2(305:310,j)) > 0.5 ;
              frame3(285:307,j)=1;
        end
     end

     %left bolt

        frame4=frame3;
     for k=1:size(frame3,1);
        if mean(frame3(k,695:700)) > 0.5 ;
              frame4(k,642:697)=1;
        end
        if mean(frame3(k,590:595)) > 0.5 ;
              frame4(k,593:642)=1;
        end
     end

      %right bolt

        frame5=frame4;
     for k=1:size(frame4,1);
        if mean(frame4(k,1392:1397)) > 0.5 ;
              frame5(k,1395:1450)=1;
        end
```

```
        if mean(frame4(k,1497:1502)) > 0.5 ;
            frame5(k,1450:1499)=1;
        end
    end


  %morphological image smoothing
  frame6 = imfill(frame5,'holes');
  frame7=bwmorph(frame6,'clean');
  frame8=bwmorph(frame7,'close');
  frame9=bwmorph(frame8,'open');


%blob location and area filtering

%label blobs
labelledimage=bwlabel(frame9);

%find blob properties
blobmes=regionprops(labelledimage, frame9, 'all');

%take out just blob areas
allBlobAreas = [blobmes.Area];
% Get a list of the blobs that meet our criteria and we need to keep.
allowableAreaIndexes = allBlobAreas > 15000;
%turn binary location map into location index
keeperIndexes = find(allowableAreaIndexes);
%keep only blobs that fit spec
keeperBlobsImage = ismember(labelledimage, keeperIndexes);
%re-lable interesting blobs
%labeledbigblobImage = bwlabel(keeperBlobsImage);

%find centres of 'fluid blob'
cents = regionprops(keeperBlobsImage, 'centroid');

%just show flicker adjusted video frame
hold off
imshow(frame,'InitialMagnification',50)

%then put line round 'fluid blob'
hold on
contour(keeperBlobsImage, [1, 1],'r')

%mark estimated 'fluid blob' centre point
scatter(cents.Centroid(1,1),cents.Centroid(1,2),200,'+','r')


  for j=1:size(keeperBlobsImage,2)

    [binme,macs(1,j)]=max(keeperBlobsImage(:,j));
    macs2=macs;
    for l = 1:size(macs,2)

      if macs(1,l)==1;
        macs2(1,l)=NaN;
```

```
        end
      end

   end


%plot(macsnow)


validdata = ~isnan(macs2);
angnow = macs2(validdata);

where=find(validdata,1);
[howhi,wherehi]=min(angnow);

   if mean(angnow) - howhi >75 && wherehi <(size(angnow,2)/2);
   start=wherehi;
   else
      start=where;
   end

   if start<where
      start=where;
   end

   if mean(angnow) - howhi >75 && wherehi >(size(angnow,2)/2)
      ender=wherehi;
   else
      ender=size(angnow,2);
   end

%linearfit=polyfit((start-where+1:ender),angnow(:,start-where+1:ender),1);

angnow2=angnow(:,start-where+1:ender);
linearfit=polyfit(1:size(angnow2,2),angnow2(1,:),1);

angs(i,:)=linearfit;

liner(1,1)=linearfit(1,1)+linearfit(1,2);
liner(2,1)=((size(angnow2,2))*linearfit(1,1))+linearfit(1,2);
liner(1,2)=start;
liner(2,2)=ender+where;

%plot([x1 x2], [y1 y2])
plot([liner(1,2) liner(2,2)], [liner(1,1) liner(2,1)],'g','linewidth',2);
hold off


   %render and capture frame to video object
   %imshow(labeledbigblobImage,'InitialMagnification',50);
   currframe=getframe;
   writeVideo(vidObj,currframe);

   %put each centre points into variable
   intmed=cents.Centroid;
```

```
    stats(1:2,i)=intmed;
   %put each fluid blob size into variable
    stats(3,i)=max(allBlobAreas);


frame_time=toc;
est_time_left=frame_time*(size(pics_fa,3)-i)
end

close (vidObj);

%transpose stats
stats2=stats';


save('centsizesurfang.mat','stats2','macs','angs')

close all

%potentially more efficient video code, not yet implemented

% avi = avifile('/path/to/output');
% figure_handle = figure('visible', 'off');
%
% % ...
% for something = 1:1000
%     cla
%     % (draw stuff...)
%     avi = addframe(avi, figure_handle);
%end

%repository

toc
```

References

Adrian RJ, 2005. Twenty years of particle image velocimetry. *Exp Fluids* 39(2):159-69.

Adrian RJ. 1984. Scattering particle characteristics and their effect on pulsed laser measurements of fluid flow: speckle velocimetry vs. particle image velocimetry. *Appl Opt* 23:1690–1.

Adrian RJ. 1987. Measurement Potential of Laser Speckle Velocimetry in Hunter WW & Foughner JT. *Flow Visualization and Laser Velocimetry for Wind Tunnels: Proceedings of a NASA Workshop Held at Langley Research Center*. NASA:219-26.

Adrian RJ. 1991. Particle-Imaging Techniques For Experimental Fluid-Mechanics. *Annual Review of Fluid Mechanics*, 23(1):261-304.

Adrian, R.J., 1986. Image shifting technique to resolve directional ambiguity in double-pulsed velocimetry. Applied Optics 25 (21), 3855–3858.

Aggarwal S. 2014. What's fueling the biotech engine—2012 to 2013. *Nat Biotechnol* 32:32-9.

Al-Fageeh MB & Smales CM. 2006. Control and regulation of the cellular responses to cold shock: the responses in yeast and mammalian systems. *Biochem J* 397(2):247-59.

Al-Rubeai M, Emery AN, Chalder S, Goldman MH. 1993 A flow cytometric study of hydrodynamic damage to mammalian cells. *J Biotechnol* 31(2):161-77.

Altamirano C, Paredes C, Cairo JJ, Godia F. 2000. Improvement of CHO Cell Culture Medium Formulation: Simultaneous Substitution of Glucose and Glutamine. *Biotechnol Prog* 16:69−75.

Alves SS, Maia CI, Vasconcelos JMT. 2002. Experimental and modelling study of gas dispersion in a double turbine stirred tank. *Chem Eng Sci* 57(3):487-96.

Arathoon, W.R. Birch, J.R., 1986. Large-scale cell culture in biotechnology. *Science* 232(4756):1390-5.

Atta CV. 1991. Local Isotropy of the Smallest Scales of Turbulent Scalar and Velocity Fields. *Proceedings of the Royal Society A: Mathematical, Physical and Engineering Sciences*, 434(1890):139-47.

Aubin J, Le Sauze N, Bertrand J, Fletcher DF, Xuereb C. 2004. PIV measurements of flow in an aerated tank stirred by a down- and an up-pumping axial flow impeller. *Experimental Thermal and Fluid Science* 28(5):447-56.

Baldi S & Yianneskis M. 2003. On the Direct Measurement of Turbulence Energy Dissipation in Stirred Vessels with PIV. *Industrial & Engineering Chemistry Research*, 42(26):7006-16.

Barbaroux M, Gerighausen S, Hackel H. 2014. An Approach to Quality and Security of Supply for Single-Use Bioreactors. In Eibl R & Eibl D. *Disposable Bioreactors II*. Series: Adv Biochem Eng Biotechnol. Springer, Heidelberg.

Barker DB & Fourney ME. 1977. Measuring fluid velocities with speckle patterns. *Opt Lett* 1:135–7.

Barnes D & Sato G, 1980. Methods for growth of cultured cells in serum-free medium. *Analytical biochemistry* 102(2):255-70.

Barrett T, Wu A, Zhang H, Levy MS, Lye GJ. 2010. Microwell engineering characterization for mammalian cell culture process development. *Biotechnol Bioeng* 105(2):260–75.

Bebbington CR. 1991. Expression of antibody genes in non-lymphoid mammalian cells. *Methods Enzymol* 2:136-45.

Beer C, Buhr P, Hahn H, Laubner D, Wirth M. 2003. Gene expression analysis of murine cells producing amphotropic mouse leukaemia virus at a cultivation temperature of 32 and 37 degrees C. *J Gen Virol* 84(7):1677-86.

Berridge J, Seamon K, Venugopal S. A-Mab: a Case Study in Bioprocess Development. 2009. *CMC Biotech Working Group; CASSS, an International Separation Science Society: Emeryville, CA.*

Bijur GN, Briggs B, Hitchcock CL, Williams MV. 1999. Ascorbic acid-dehydroascorbate induces cell cycle arrest at G2/M DNA damage checkpoint during oxidative stress. *Environ Mol Mutagen* 33(2):144-52.

Borth N, Mattanovich D, Kunert R, Katinger H. 2005. Effect of increased expression of protein disulfide isomerase and heavy chain binding protein on antibody secretion in a recombinant CHO cell line. *Biotechnol Prog* 21(1):106-11.

Bosch P, Lundgren B, Kaisermayer C. 2008. How to construct a monoclonal antibody factory: A comparison of production costs in fed batch and perfusion culture with microcarriers - Part two. *Bioprocess J* 7(2):30–43.

Boychyn M, Yim SSS, Bulmer M, More J, Bracewell DH, Hoare M. 2004. Performance prediction of industrial centrifuges using scale-down models. *Bioprocess Biosys Eng* 26(6):385-391.

Brecht, R., 2009. Disposable Bioreactors: Maturation into Pharmaceutical Glycoprotein Manufacturing. In Scheper T. *Adv Biochem Eng Biotechnol*. Springer, Heidelberg.

Brühlmann D, Jordan M, Hemberger J, Sauer M, Stettler M, Broly H. 2015.Tailoring recombinant protein quality by rational media design. *Biotechnol Prog* 31(3):615-29.

Bryant J. 1977 The characterization of mixing in bioreactors. *Adv Biochem Eng* 1977, 5, 101-123.

Butler M. 2006. Optimisation of the cellular metabolism of glycosylation for recombinant proteins produced by Mammalian cell systems. *Cytotechnol* 50(1-3):57-76.

Cabaret F, Bonnot S, Fradette L, Tanguy PA. 2007. Mixing Time Analysis Using Colorimetric Methods and Image Processing. *Ind Eng Chem Res* 46(14):5032–42.

Carvalhal AV, Marcelino I, Carrondo MJT. 2003. Metabolic changes during cell growth inhibition by p27 overexpression. *Appl Microbiol Biotechnol* 63(2):164–73.

Challener CA. 2014. Securing the Single-Use Supply Chain. *Pharma Technol* 38(12). Available from - http://www.pharmtech.com/securing-single-use-supply-chain *[Accessed: 10-Aug-2015]*

Chatel A, Kumpalume P, Hoare M (2014) Ultra Scale-Down Characterization of the Impact of Conditioning Methods for Harvested Cell Broths on Clarification by Continuous Centrifugation—Recovery of Domain Antibodies from rec *E. coli. Biotechnol Bioeng* 111(5): 913–24.

Chelius D, Rehder DS, Bondarenko PV. 2005. Identification and Characterization of Deamidation Sites in the Conserved Regions of Human Immunoglobulin Gamma Antibodies. *Anal Chem* 77(18):6004-11.

Chiarini LB, Freitas FG, Petrs-Silva H, Linden R. 2000. Evidence that the bifunctional redox factor / AP endonuclease Ref-1 is an anti-apoptotic protein associated with differentiation in the developing retina. *Cell Death Differ* 7(3):272-81.

Chisti Y. 1989. Airlift Bioreactors. Elsevier.

Chisti Y. 2000. Animal-cell damage in sparged bioreactors. *Trends Biotechnol* 18(10):420-32.

Chisti Y. 2001. Hydrodynamic damage to animal cells. *Crit Rev Biotechnol* 21(2):67-110.

Chmiel H. 2006. Bioreaktoren. In: Chmiel H. *Bioprozesstechnik*. Elsevier, München.

Clark LC, Wolf R, Granger D, Taylor Z.1953. Continuous recording of blood oxygen tensions by polarography. *J App Physiol* 6(3):189–93.

Clincke MF, Guedon E, Yen FT, Ogier V, Roitel O, Goergen JL. 2011. Effect of surfactant pluronic F-68 on CHO cell growth, metabolism, production, and glycosylation of human recombinant IFN-γ in mild operating conditions. *Biotechnol Prog* 26(1)*:*1-10.

Clincke MF, Mölleryd C, Zhang Y, Lindskog E, Walsh K, Chotteau V. 2013. Very high density of CHO cells in perfusion by ATF or TFF in WAVE bioreactor™. Part I. Effect of the cell density on the process. *Biotechnol Prog* 29(3):754-67.

Clopton DA, Saltman P. 1995. Low-level oxidative stress causes cell-cycle specific arrest in cultured cells. *Biochem Biophys Res Commun* 210(1):189-96.

Cooper GM. 2000. Structure and Organization of Actin Filaments. In *The Cell: A Molecular Approach*. (2nd edn.) Sunderland (MA): Sinauer Associates.

Cronin DG, Nienow AW, Moody GW. 1994. An Experimental Study of the Mixing in a Proto-Fermenter Agitated by Dual Rushton Turbines. *Food Bioprod Proc* 72:35-40.

Croughan MS, Hamel J-F, Wang DIC. 1987. Hydrodynamic effects on animal cells grown in microcarrier cultures. *Biotechnol Bioeng* 29(1):130-41.

Danckwerts PV. 1951. Significance of Liquid-Film Coefficients in Gas Absorption. *Ind Eng Chem* 43(6):1460-7.

DeMali KA, Wennerberg K, Burridge K. 2003. Integrin signaling to the actin cytoskeleton. Curr Opin Cell Biol 15:572–582.

Dimasi JA & Grabowski HG. 2012. R&D costs and returns to new drug development: A review of the evidence. In Danzon PM & Nicholson S. *The Oxford Handbook of the Economics of the Biopharmaceutical Industry*. Oxford Handbooks in Economics.

Dimotakis, P.E., 1993. Some issues on turbulent mixing and turbulence. *GALCIT Rep. FM93-1a*:22-23.

Ding W, Madsen G, Mahajan E, O'Connor S, Wong K. 2014. Standardized Extractables Testing Protocol for Single-Use Systems in Biomanufacturing. *Pharma Eng* 34(6).

Dinnis DM, James DC. 2005. Engineering mammalian cell factories for improved recombinant monoclonal antibody production: lessons from nature? *Biotechnol Bioeng* 91(2):180-9.

Dive C, Gregory CD, Phipps DJ, Evans DL, Milner AE, Wyllie AH. 1992. Analysis and discrimination of necrosis and apoptosis (programmed cell death) by multiparameter flow cytometry. *Biochim Biophys Acta* 1133(3):275-85.

Dorai H, Kyung YS, Ellis D, Kinney C, Lin C, Jan D, Moore G, Betenbaugh MJ. 2009. Expression of anti-apoptosis genes alters lactate metabolism of Chinese Hamster Ovary cells in culture. *Biotechnol Bioeng* 103(3):592-608.

Doran PM. 2009. Bioprocess Engineering Principles. Academic press.

Drakeman DL. 2014. Benchmarking biotech and pharmaceutical product development. *Nat Biotechnol* 32:621-25.

Ducommun P, Ruffieux P, Kadouri A, von Stockar U, Marison IW. 2002 Monitoring of temperature effects on animal cell metabolism in a packed bed process. *Biotechnol Bioeng* 77(7):838–42.

Ducoste J, Clark M. 1998. The influence of tank size and impeller geometry on turbulent flocculation: II. Model. Env Eng Sci 15:225–35.

Eibl R & Eibl D. 2006. Design and use of the wave bioreactor for plant cell culture. In Gutta Dupta S, Ibaraki Y. *Plant tissue culture engineering*. Springer Netherlands.

Eibl R & Eibl D. 2007. Design of bioreactors suitable for plant cell and tissue cultures. *Phytochem Rev* 7(3):593–8.

Eibl R, Kaiser S, Lombriser R, Eibl D. 2010. Disposable bioreactors: the current state-of-the-art and recommended applications in biotechnology. *App Microbiol Biotechnol* 86(1):41-9.

Eibl R, Werner S, Eibl D. 2009. Bag Bioreactor Based on Wave-Induced Motion: Characteristics and Applications. *Adv Biochem. Eng Biotechnol* 115:55-87.

Fan L, Kadura I, Krebs LE, Hatfield CC, Shaw MM, Frye CC. 2012. Improving the efficiency of CHO cell line generation using glutamine synthetase gene knockout cells. *Biotechnol Bioeng* 109(4):1007-15.

Fan Y, del Val IJ, Müller C, Sen JW, Rasmussen SK, Kontoravdi C, Weilguny D, Andersen MR. 2014. Amino acid and glucose metabolism in fed-batch CHO cell culture affects antibody production and glycosylation. *Biotechnol Bioeng* 112(3):521-35.

Farid, S.S., Washbrook, J. & Titchener-Hooker, N.J., 2005. Decision-support tool for assessing biomanufacturing strategies under uncertainty: stainless steel versus disposable equipment for clinical trial material preparation. *Biotechnol Prog* 21(2):486-97.

Figueredo-Cardero A, Chico E, Castilho L, de Andrade Medronho R. 2012. Particle image velocimetry (PIV) study of rotating cylindrical filters for animal cell perfusion processes. *Biotechnol Prog* 28(6):1491-8.

Flanagan W, Pietrzykowski M, Pizzi V, Brown A, Sinclair A, Monge M. 2014. An Environmental Lifecycle Assessment of Single-Use and Conventional Process Technology: Comprehensive Environmental Impacts. *BioPharm Int* 27(13). Available from - http://www.biopharminternational.com/environmental-lifecycle-assessment-single-use-and-conventional-process-technology-comprehensive-envi [Accessed: 10-Aug-2015]

Fleisehaker RJ & Sinskey AJ. 1981. Oxygen demand and supply in cell culture. *Appl Microbiol Biotechnol* 12(4)*:*193–7.

Fussenegger M. 2001. The impact of mammalian gene regulation concepts on functional genomic research, metabolic engineering, and advanced gene therapies. *Biotechnol Prog* 17(1):1-51.

Gabriele A, Nienow AW, Simmons MHJ. 2009. Use of angle resolved PIV to estimate local specific energy dissipation rates for up- and down-pumping pitched blade agitators in a stirred tank. *Chem Eng Sci* 64(1):126-143.

Genzel Y, Behrendt I, König S, Sann H, Reichl U. 2004. Metabolism of MDCK cells during cell growth and influenza virus production in large-scale microcarrier culture. *Vaccine* 22(17–18):2202-8.

Genzel Y, Olmer RM, Schäfer B, Reichl U. 2006. Wave microcarrier cultivation of MDCK cells for influenza virus production in serum containing and serum-free media. *Vaccine* 24(35-36):6074–87.

Gigout A, Buschmann MD, Jolicoeur M. 2008. The fate of Pluronic F-68 in chondrocytes and CHO cells. *Biotechnol Bioeng* 100(5):975-87.

Gill NK, Appleton M, Baganz F, Lye GJ.2008. Design and characterisation of a miniature stirred bioreactor system for parallel microbial fermentations. *Biochem Eng J* 39(1):164–176.

Glacken MW, Fleischaker RJ, Sinskey AJ. 1983. Large-scale production of mammalian cells and their products: engineering principles and barriers to scale-up. *Annals of the New York Academy of Sciences*, 413(1):355-72.

Glindkamp A, Riechers D, Rehbock C, Hitzmann B, Scheper T, Reardon KF. 2009. Sensors in Disposable Bioreactors Status and Trends. *Adv Biochem Eng Biotechnol* 115:145-169.

Godoy-Silva R, Chalmers JJ, Casnocha SA, Bass LA, Ma N. 2009. Physiological responses of CHO cells to repetitive hydrodynamic stress. *Biotechnol Bioeng* 103(6):1103-17.

Goudar CT, Piret JM, Konstantinov KB. 2011. Estimating cell specific oxygen uptake and carbon dioxide production rates for mammalian cells in perfusion culture. *Biotechnol Prog* 27(5):1347-57.

Gramer MJ, Eckblad JJ, Donahue R, Brown J, Shultz C, Vickerman K, Priem P, van den Bremer ET, Gerritsen J, van Berkel PH. 2011. Modulation of antibody galactosylation through feeding of uridine, manganese chloride, and galactose. *Biotechnol Bioeng* 108(7):1591-602.

Gray DR, Chen S, Howarth W, Inlow D, Maiorella. 1996. CO_2 in large-scale and high-density CHO cell perfusion culture. *Cytotechnol* 22(1-3):65-78.

Haldankar R, Li D, Saremi Z, Baikalov C, Deshpande R. 2006. Serum-free suspension large-scale transient transfection of CHO cells in WAVE bioreactors. *Mol Biotechnol* 34(2):191-9.

Hammond M, Nunn H, Rogers G, Lee H, Marghitoiu AL, Perez L, Nashed-Samuel Y, Anderson C, Vandiver M, Kline S. 2013. Identification of a leachable compound detrimental to cell growth in single-use bioprocess containers. *PDA J Pharm Sci Technol* 67(2):123-34.

Hanson MA, Brorson KA, Moreira AR, Rao G. 2009. Comparisons of optically monitored small-scale stirred tank vessels to optically controlled disposable bag bioreactors. *Microb Cell Fact* 5(8):44.

Hanson MA, Ge X, Kostov Y, Brorson KA, Moreira AR, Rao R. 2007. Comparisons of optical pH and Dissolved Oxygen sensors with traditional electrochemical probes during mammalian cell culture. *Biotechnol Bioeng* 97: 833-841.

Hart DP. 2000. PIV error correction. *Exp Fluids* 29:13–22.

Hegde S, Pant T, Pradhan K, Badiger M, Gadgil M. 2012. Controlled release of nutrients to mammalian cells cultured in shake flasks. *Biotechnol Prog* 28(1):188-95.

Hinze JO. 1970. Turbulent flow regions with shear stress and mean velocity gradient of opposite sign. In *App Sci Res 22(1):*163-75.

Hirt C. & Nichols B., 1981. Volume of fluid (VOF) method for the dynamics of free boundaries. *J Comp Phys* 39(1):201-25.

Hodge G. 2005. Media Development for Mammalian Cell Culture. *Biopharm Int* 18(5). Available from - http://www.biopharminternational.com/media-development-mammalian-cell-culture [Accessed: 10-Aug-2015]

Hoffmann J, Tralles S, Hempel SC. 1992. Test system for determination of mechanical stress of particles in bioreactors. *Chem Eng Sci* 64:953–6.

Hong P, Koza S, Bouvier ESP. 2012. Size-Exclusion Chromatography for the Analysis of Protein Biotherapeutics and their Aggregates. *J Liq Chromatogr Relat Technol* 35(20):2923-50.

Hossler P, Khattak SF, Li ZJ. 2009. Optimal and consistent protein glycosylation in mammalian cell culture. *Glycobiol* 19(9):936-49.

Hsu WT, Aulakh RP, Traul DL, Yuk IH. 2012. Advanced microscale bioreactor system: a representative scale-down model for bench-top bioreactors. *Cytotechnol* 64(6):667-78.

Hu W, Berdugo C, Chalmers JJ. 2011. The potential of hydrodynamic damage to animal cells of industrial relevance: current understanding. *Cytotechnol* 63(5):445–60.

Hu WS, Aunins JG. 1997. Large-scale mammalian cell culture. *Curr Opin Biotechnol* 8(2):148-53.

Huang HT, Fiedler HE, Wang JJ. 1993. Limitation and improvement of PIV. Part I. Limitation of conventional techniques due to deformation of particle image patterns. *Exp Fluids* 15:168–174.

Huang YM, Hu W, Rustandi E, Chang K, Yusuf-Makagiansar H, Ryll T. 2010. Maximizing productivity of CHO cell-based fed-batch culture using chemically

defined media conditions and typical manufacturing equipment. *Biotechnol Prog* 26(5):1400-10.

Hutchinson N, Bingham N, Murrell N, Farid S, Hoare M. 2006. Shear stress analysis of mammalian cell suspensions for prediction of industrial centrifugation and its verification. *Biotechnol Bioeng* 95(3):483-491.

Irani N, Wirth M, van Den Heuvel J, Wagner R. 1999. Improvement of the primary metabolism of cell cultures by introducing a new cytoplasmic pyruvate carboxylase reaction. *Biotechnol Bioeng* 66(4):238-46.

IUPAC, 1997. Compendium of Chemical Terminology - the Gold Book (2nd edn.) International Union of Pure and Applied Chemistry.

Jayapal KP, Wlaschin KF, Hu WS. 2007. Recombinant protein therapeutics from CHO cells-20 years and counting. *Chem Eng Prog* 103(10):40.

Jenke D & Barge VJ. 2014. Factors Affecting the Release of Extractable Acetic Acid from Multi-layered Plastic Films Containing Ethylene Vinyl Acetate (EVA) and Polyethylene (PE) Layers. *Pharma Outsourcing*. Available from - http://www.pharmoutsourcing.com/Featured-Articles/161922-Factors-Affecting-the-Release-of-Extractable-Acetic-Acid-from-Multi-layered-Plastic-Films-Containing-Ethylene-Vinyl-Acetate-EVA-and-Polyethylene-PE-Layers/ [Accessed: 15-Aug-2015]

Jenke D. 2007. Evaluation of the chemical compatibility of plastic contact materials and pharmaceutical products; safety considerations related to extractables and leachables. *J Pharm Sci* 96(10):2566-81.

Jiang Z, Sharfstein ST. 2008. Sodium butyrate stimulates monoclonal antibody over-expression in CHO cells by improving gene accessibility. *Biotechnol Bioeng* 100(1):189-94.

Kadwell SH, Hardwicke PI. 2007. Production of baculovirus-expressed recombinant proteins in wave bioreactors. *Methods Mol Biol* 388:247-66.

Kalmbach A, Bordás R, Öncül AA, Thévenin D, Genzel Y, Reichl U. 2011. Experimental Characterization of Flow Conditions in 2- and 20-L Bioreactors with Wave-Induced Motion. *Biotechnol Prog* 27(2):402-9.

Kawase Y, Moo-Young M. 1989. Mixing time in bioreactors. *J Chem Technol Biotechnol* 44(1):63–75.

Kayser K, Lin N, Allison D, Donahue L, Caple M. 2006. Cell line engineering methods for improving productivity. *BioProcess Int*. Available from - http://www.bioprocessintl.com/wp-content/uploads/bpi-content/0643ar01su_77541a.pdf [Accessed 11-Aug-2015]

Keane JT, Ryan D, Gray PP. 2003. Effect of shear stress on expression of a recombinant protein by Chinese hamster ovary cells. *Biotechnol Bioeng* 81:211–20.

Keane RD, Adrian RJ. 1992. Theory of cross-correlation analysis of PIV images. *App Sci Res* 49(3):191-215.

Kelley B. 2009. Industrialization of mAb production technology - The bioprocessing industry at a crossroads. *MAbs* 1(5):443-52.

Kermis HR, Kostov Y, Harms P, Rao G. 2002. Dual excitation ratiometric fluorescent pH sensor for noninvasive bioprocess monitoring: development and application. *Biotechnol Prog* 18(5):1047-53.

Kim do Y, Chaudhry MA, Kennard ML, Jardon MA, Braasch K, Dionne B, Butler M, Piret JM. 2013. Fed-batch CHO cell t-PA production and feed glutamine replacement to reduce ammonia production. *Biotechnol Prog* 29(1):165-75.

Kim MS, Kim NS, Sung YH, Lee GM. 2002. Biphasic culture strategy based on hyperosmotic pressure for improved humanized antibody production in Chinese hamster ovary cell culture. *Vitro Cell Dev Biol Anim* 38(6):314-9.

Khan FR. 2005. Investigation of tubrbulent flows and instabilities in a stirred vessel using particle image velocimetry. PhD Thesis. Loughborough University.

Kim SH, Lee GM. 2007. Down-regulation of lactate dehydrogenase-A by siRNAs for reduced lactic acid formation of Chinese hamster ovary cells producing thrombopoietin. *Appl Microbiol Biotechnol* 74(1):152-9.

Knevelman C, Hearle DC, Osman JJ, Khan M, Dean M, Smith M, Aiyedebinu Cheung K. 2002. Characterisation and Operation of a Disposable Bioreactor as a Replacement for Conventional Steam In Place Inoculum Bioreactors for Mammalian Cell Culture Processes. *Cell* 1050(1E):6.

Koetsier WT & Thoenes D. 1972. Coalescence of Bubbles in a Stirred Tank. *Proceedings of the Fifth European Symposium on Chemical Reactor Engineering.*

Kresta SM & Wood PE. 1993. The flow field produced by a pitched blade turbine: Characterization of the turbulence and estimation of the dissipation rate. *Chem Eng Sci*, 48(10):1761-74.

Krothapalli A. 1991. The development of laser speckle velocimetry for the study of vortical flows. *NASA STI/Recon Technical Report.* SuDoc NAS 1.26:177589.

Kumar N, Gammell P, Clynes M. 2007. Proliferation control strategies to improve productivity and survival during CHO based production culture. *Cytotechnol* 53(1-3):33-46.

Kunas KT & Papoutsakis ET. 1990. Damage mechanisms of suspended animal cells in agitated bioreactors with and without

Langheinrich C, Nienow AW, Eddleston T, Stevenson NC, Emery AN, Clayton TM, Slater NKH. 2002. Oxygen Transfer in Stirred Bioreactors Under Animal Cell Culture Conditions. *Food Bioprod Proc* 80(1):39-44.

Langheinrich C, Nienow AW, Eddleston T, Stevenson NC, Emery AN, Clayton TM, Slater NKH. 1998. Liquid homogenization studies in animal cell bioreactors of up to 8m^3 in volume. *Food and bioproducts processing: transactions of the Institution of Chemical Engineers, Part C* 76(2):107-16.

Lao MS & Toth D. 1997. Effects of ammonium and lactate on growth and metabolism of a recombinant Chinese hamster ovary cell culture. *Biotechnol Prog* 13(5):688-91.

Lau EC, Kong S, McNulty S, Entwisle C, McIlgorm A, Dalton KA, Hoare M. 2013. An ultra scale-down characterization of low shear stress primary recovery stages to enhance selectivity of fusion protein recovery from its molecular variants. *Biotechnol Bioeng* 110(7):1973–83.

Lavery M & Nienow A W. 1987. Oxygen transfer in animal cell culture medium. *Biotechnol Bioeng* 30(3):368-73.

Lee JS, Kallehauge TB, Pedersen LE, Kildegaard HF. 2015.Site-specific integration in CHO cells mediated by CRISPR/Cas9 and homology-directed DNA repair pathway. *Sci Rep* 5:8572.

Li F, Vijayasankaran N, Shen AY, Kiss R, Amanullah A. 2010. Cell culture processes for monoclonal antibody production. *MAbs* 2(5):466-77.

Lim JAC, Sinclair A. 2007. Process economy of disposable manufacturing: Process models to minimize upfront investment. *Am Pharm Rev* 10:114-21.

Liu C & Chang T. 2006. Rational development of serum-free medium for Chinese hamster ovary cells. *Proc Biochem* 41(11):2314-19.

Liu H, Gaza-Bulseco G, Faldu D, Chumsae C, Sun J. 2008. Heterogeneity of monoclonal antibodies. *J Pharm Sci* 97(7):2426-47.

Löffelholz C, Kaiser SC, Kraume M, Eibl R, Eibl D. 2014. Dynamic Single-Use Bioreactors Used in Modern Liter- and m3 - Scale Biotechnological Processes: Engineering Characteristics and Scaling Up. In Eibl R & Eibl D. *Disposable Bioreactors II.* Series: Adv Biochem Eng Biotechnol. Springer, Heidelberg.

Lucas BK, Giere LM, DeMarco RA, Shen A, Chisholm V, Crowley CW. 1996. High-level production of recombinant proteins in CHO cells using a dicistronic DHFR intron expression vector. Nucleic Acids Res 24(9):1774-9.

Ma N, Chalmers JJ, Auniņs JG, Zhou W, Xie L. 2004 Quantitative studies of cell-bubble interactions and cell damage at different pluronic F-68 and cell concentrations. *Biotechnol Prog* 20(4):1183-91.

Ma N, Koelling KW, Chalmers JJ. 2002 Fabrication and use of a transient contractional flow device to quantify the sensitivity of mammalian and insect cells to hydrodynamic forces. *Biotechnol Bioeng* 80(4):428-37.

Machesky LM, Atkinson SJ, Ampe C, Vanderckhove J, Pollard TD. 1994. Purification of a cortical complex containing two unconventional actins from Acanthamoeba by affinity chromatography on profiling-agarose. *J Cell Biol* 127:107–115.

Magelli F, Montante G, Pinelli D, Paglianti A. 2013. Mixing time in high aspect ratio vessels stirred with multiple impellers. *Chem Eng Sci* 101(20):712-20.

Mahajan E, Matthews T, Hamilton R, Laird MW. 2010. Use of disposable reactors to generate inoculum cultures for E. coli production fermentations. *Biotechnol Prog* 26(4):1200-3.

Marino M, Corti A, Ippolito A, Cassani G, Fassina G. 1997. Effect of bench-scale culture conditions on murine IgG heterogeneity. *Biotechnol Bioeng* 54(1):17-25.

Marks DM. 2003. Equipment design considerations for large scale cell culture. *Cytotechnol* 42(1):21-33.

Martínez VS, Dietmair S, Quek LE, Hodson MP, Gray P, Nielsen LK. 2013. Flux balance analysis of CHO cells before and after a metabolic switch from lactate production to consumption. *Biotechnol Bioeng* 110(2):660-66.

Mayinger F, Feldmann O. 2004. Bubble dispersion in aerated stirred vessels. In Sommerfeld M. *Bubble Flow.* Springer Berlin Heidelberg.

McCord JM & Fridovich I. 1969. Superoxide dismutase. An enzymic function for erythrocuprein (hemocuprein). *J Biol Chem* 244(22):6049-55.

McDowell CL & Papoutsakis ET. 1998. Increased agitation intensity increases CD13 receptor surface content and mRNA levels, and alters the metabolism of HL60 cells cultured in stirred tank bioreactors. Biotechnol Bioeng 60:239–250

Melling A. 1997. Tracer particles and seeding for particle image velocimetry. *Meas Sci Technol* 8(12):1406.

Michaels JD, Nowak JE, Mallik AK, Koczo K, Wasan DT, Papoutsakis ET. 1995. Interfacial properties of cell culture media with cell-protecting additives. *Biotechnol Bioeng* 47(4):420-30.

Micheletti M, Barrett T, Doig SD, Baganz F, Levy MS, Woodley JM, Lye GJ (2006) Fluid mixing in shaken bioreactors: Implications for scale-up predictions from microlitre-scale microbial and mammalian cell cultures. *Chem Eng Sci* 61(9):2939–49.

Mikola M, Seto J, Amanullah A. 2007. Evaluation of a novel Wave Bioreactor cellbag for aerobic yeast cultivation. *Bioproc Biosyst Eng* 30(4):231–41.

Mostafa SS & Gu X. 2003. Strategies for improved dCO2 removal in large-scale fed-batch cultures. *Biotechnol Prog*, 19(1):45-51.

Motobu M, Wang P-C, Matsumura M. 1998. Effect of shear stress on recombinant Chinese hamster ovary cells*. J Ferm Bioeng* 85(2):190-5.

Müthing J, Kemminer SE, Conradt HS, Sagi D, Nimtz M, Kärst U, Peter-Katalinić J. 2003. Effects of buffering conditions and culture pH on production rates and glycosylation of clinical phase I anti-melanoma mouse IgG3 monoclonal antibody R24. *Biotechnol Bioeng* 83(3):321-34.

Nienow AW, 2014. Letter to the Editor: Re "Development of a scale-down model of hydrodynamic stress to study the performance of an industrial CHO cell line under simulated production scale bioreactor conditions" [Sieck, J.B., Cordes, T., Budach, W.E., Rhiel, M.H., Suemeghy, Z., Leist, C., Villiger, T.K., Morbidelli, M., Soos, M., 2013. *J Biotechnol* 164:41-49]. *J Biotechnol* 171:82-4

Nienow AW, Rielly CD, Brosnan K, Bargh N, Lee K, Coopman K, Hewitt CJ. 2013. The physical characterisation of a microscale parallel bioreactor platform with an industrial CHO cell line expressing an IgG4. *Biochem Eng J* 76:25-36.

Nienow AW, Langheinrich C, Stevenson NC, Emery AN, Clayton TM, Slater NK. 1996. Homogenisation and oxygen transfer rates in large agitated and sparged animal cell bioreactors: Some implications for growth and production. *Cytotechnol*, 22(1-3):87-94.

Nienow AW. 1997. On impeller circulation and mixing effectiveness in the turbulent flow regime. *Chem Eng Sci* 52(15):2557-2565.

Nienow AW. 1998. Hydrodynamics of Stirred Bioreactors. *Appl Mech Rev* 51(1):3-32.

Nienow AW. 2006. Reactor engineering in large scale animal cell culture. *Cytotechnol* 50(1-3):9-33.

Nogueira J, Lecuona A, Rodriguez P. 1997. Data validation, false vectors correction and derived magnitudes calculation on PIV data. *Meas Sci Technol* 8:1493.

Novais JL, Titchener-Hooker NJ, Hoare M. 2001 Economic comparison between conventional and disposables-based technology for the production of biopharmaceuticals. *Biotechnol Bioeng* 75(2):143-153.

Novais JL, Titchener-Hooker NJ, Hoare M. 2001. Conventional and Disposables-Based Technology for the Production of Biopharmaceuticals. *Biotechnol Bioeng* 75(2):143-53.

Oberkampf W. 2002. Verification and validation in computational fluid dynamics. *Prog Aerosp Sci*, 38(3):209-72.

Odeleye AOO, Marsh DTJ, Osborne MD, Lye GJ, Micheletti M. 2014. On the fluid dynamics of a laboratory scale single-use stirred bioreactor. *Chem Eng Sci* 111:299-312.

O'Gorman S, Fox DT, Wahl GM. 1991. Recombinase-mediated gene activation and site-specific integration in mammalian cells. *Sci* 251(4999):1351-5.

Oh SKW, Nienow AW, Al-Rubeai M, Emery AN. 1989. The effects of agitation intensity with and without continuous sparging on the growth and antibody production of hybridoma cells. *J Biotechnol* 12(1):45-61.

Oh SKW, Nienow AW, Al-Rubeai M, Emery AN. 1992. Further studies of the culture of mouse hybridomas in an agitated bioreactor with and without continuous sparging. *J Biotechnology* 22:245-270.

Oncül A, Kalmbach A, Genzen Y, Reichl U, Thévenin D. 2010. Characterization of flow conditions in 2 L and 20 L wave bioreactors using computational fluid dynamics. *Biotechnol Prog* 26(1):101–110.

Oosterhuis NM & Kossen NW. 1984. Dissolved oxygen concentration profiles in a production-scale bioreactor. *Biotechnol Bioeng* 26(5):546-50.

Oosterhuis NMG & van der Heiden P. 2010. Mass Transfer in the CELL-tainer Disposable Bioreactor. In T.Noll. *Cells and Culture, ESACT Proceedings 4*. Springer Science+Business Media B.V.

Orlando SJ, Santiago Y, DeKelver RC, Freyvery Y, Boydston EA, Moehle EA, Choi VM, Gopalan SM, Lou JF, Li J, Miller JC, Holmes MC, Gregory PD, Umgy FD, Cost GJ. 2010. Zinc-finger nuclease-driven targeted integration into mammalian genomes using donors with limited chromosomal homology. *Nucleic Acids Re*s 38(15):152.

Osman JJ, Birch J Varley J, 2002. The response of GS-NS0 myeloma cells to single and multiple pH perturbations. *Biotechnol Bioeng* 79(4):398-407.

Otto R, Santagostino A, Schrader U. 2014. Rapid growth in biopharma: Challenges and opportunities. In *Science to Operations: Questions, Choices and Strategies for Success in Biopharma.* McKinsey&Company. Available from - http://www.mckinsey.com/insights/health_systems_and_services/rapid_growth_in_biopharma. [Accessed: 14-Aug-2015]

Pan H, Chen K, Chu L, Kinderman F, Apostol I, Huang G. 2009. Methionine oxidation in human IgG2 Fc decreases binding affinities to protein A and FcRn. *Protein Sci* 18:424–433.

Papoutsakis ET. 1991. Fluid-mechanical damage of animal cells in bioreactors. *Trends Biotechnol* 9(12):427-37.

Park JH, Noh SM, Woo JR, Kim JW, Lee GM. 2016. Valeric acid induces cell cycle arrest at G1 phase in CHO cell cultures and improves recombinant antibody productivity. *Biotechnol J* 11(4):487-96.

Pasloske BL. 2001. Nucleases Methods and Protocols. Humana Press Inc. 8:107.

Paul EL, Atiemo-Obeng VA, Kresta SM, 2004. Handbook of Industrial Mixing Science and Practice. John Wiley & Sons.

Pavlou AK & Reichert JM. 2004. Recombinant protein therapeutics--success rates, market trends and values to 2010. *Nat Biotechnol* 22(12):1513-9.

Peube JL. 2009. Fundamentals of Fluid Mechanics and Transport Phenomena. John Wiley & Sons, Inc.

Pilz RD, Hempel DC. 2005. Mechanical stress on suspended particles in two- and three-phase airlift loop reactors and bubble columns. *Chem Eng Sci* 60(22):6004-12

Pollock J, Ho SV, Farid SS. 2013. Fed-batch and perfusion culture processes: economic, environmental, and operational feasibility under uncertainty. *Biotechnol Bioeng* 110(1):206-19.

Quaranta M, Borisov SM, Klimant I. 2012. Indicators for optical oxygen sensors. *Bioanal Rev* 4(2-4):115-57.

R J Adrian. 1997. Dynamic ranges of velocity and spatial resolution of particle image velocimetry. *Meas Sci Technol* 8:1393–8.

Rao G, Moreira A, Brorson K. 2009. Disposable bioprocessing: the future has arrived. *Biotechnol Bioengineering* 102(2):348-56.

Rathore AS & Winkle H. 2009. Quality by design for biopharmaceuticals. *Nat Biotechnol* 27:26-34.

Rawlings B & Pora H. 2009. Environmental Impact of Single-Use And Reusable Bioprocess Systems. *Bioproc Online*. Available from - http://www.bioprocessonline.com/doc/environmental-impact-of-single-use-and-0001 [Accessed: 10-Aug-2015]

Reilley CN. 1965. Advances in Analytical Chemistry and Instrumentation. John Wiley & Sons Inc. New York.

Reinhart D, Damjanovic L, Kaisermayer C, Kunert R. 2015. Benchmarking of commercially available CHO cell culture media for antibody production. *Appl Microbiol Biotechnol* 99(11):4645-57.

Reinhart D, Sommeregger W, Debreczeny M, Gludovacz E, Kunert R. 2014. In search of expression bottlenecks in recombinant CHO cell lines - a case study. *Appl Microbiol Biotechnol* 98(13):5959-65.

Restelli V, Wang M-D, Huzel N, Ethier M, Perreault H, Butler M. 2006. The effect of dissolved oxygen on the production and the glycosylation profile of recombinant human erythropoietin produced from CHO cells. *Biotechnol Bioeng* 94(3):481-94.

Rice JW, Rankl NB, Gurganus TM, Marr CM, Barna JB, Walters MM, Burns DJ. 1993. A comparison of large-scale Sf9 insect cell growth and protein production: stirred vessel vs. airlift. *Biotechniques* 15(6):1052-9.

Ries C, John G, John C, Eibl R, Eibl D. 2010. A shaken disposable bioreactor system for controlled insect cell cultivations at milliliter-scale. *Eng Life Sci* 10(1)75-9.

Rodrigues ME, Costa AR, Henriques M, Azeredo J, Oliveira R. 2009. Technological Progresses in Monoclonal Antibody Production Systems. *Biotechnol Prog* 26(2):332-51.

Sadava D, Hillis DM, Heller HC, Berenbaum MR. 2011. Life: The Science of Biology (9th edn.) *Freeman.*

Sandstrom CE, Miller WM, Papoutsakis ET. 1994. Serum-free media for cultures of primitive and mature hematopoietic cells. *Biotechnol Bioeng* 43(8):706-33.

Sardeing R, Aubin J, Xuereb C. 2004. Gas–Liquid Mass Transfer: A Comparison of Down- and Up–pumping Axial Flow Impellers with Radial Impellers. *Chem Eng Res Des* 82(12):1589-96.

Sauerwald TM, Oyler GA, Betenbaugh MJ. 2003. Study of caspase inhibitors for limiting death in mammalian cell culture. *Biotechnol Bioeng* 81(3):329-40.

Schmalzriedt S, Jenne M, Mauch K, Reuss M. 2003. Integration of Physiology and Fluid Dynamics. *Adv Biochem Eng Biotechnol* 80:19-68.

Schmitz G, Langmann T. 2001. Structure, function and regulation of the ABC1 gene product. *Curr Opin Lipidol* 12(2):129–40.

Schröder M, Schäfer R, Friedl P. 2002. Induction of protein aggregation in an early secretory compartment by elevation of expression level. *Biotechnol Bioeng* 78(2):131-40.

Sethuraman N, Stadheim TA. 2006. Challenges in therapeutic glycoprotein production. *Curr Opin Biotechnol* 17(4):341-6.

Sharp KV, Adrian RJ. 2001. PIV Study of small-scale flow structure around a Rushton turbine. *Fluid Mech Trans Phenom* 47(4):766–78.

Sieblist C, Hägeholz O, Aehle M, Jenzsch M, Pohlsceidt M, Lübbert A. 2011. Insights into large-scale cell-culture reactors: II. Gas-phase mixing and CO_2stripping. *Biotechnol J* 6(12):1547-56.

Sieck JS. 2012. Scale-Down Modeling of CHO Fed-Batch Processes for Monoclonal Antibody Production. PhD Thesis. *ETH Zurich*.

Sieck JB, Cordes T, Budach WE, Rhiel MH, Suemeghy Z, Leist C, Villiger TK, Morbidelli M, Soos M. 2013. Development of a Scale-Down Model of

hydrodynamic stress to study the performance of an industrial CHO cell line under simulated production scale bioreactor conditions. *J Biotechnol* 164(1):41-9.

Siganporia CC, Ghosh S, Daszkowski T, Papageorgiou LG, Farid SS. 2014. Capacity planning for batch and perfusion bioprocesses across multiple biopharmaceutical facilities. *Biotechnol Prog* 30(3):594-606.

Sinclair A, Leveen L, Monge M, Lim J, Cox S. 2008. The Environmental Impact of Disposable Technologies. *Biopharm int* Available from: http://biopharmservices.com/wp-content/uploads/2014/04/EnvironmentImpactDisposables.pdf [Accessed - 10-Aug-2015]

Sinclair A. 2007. Process economy of disposable manufacturing: process models to minimize upfront investment. Presented at: *International Business Communications Life Sciences' Single-Use Bioprocess Systems and Applications Conference: La Jolla, CA.*

Singh V. 1999. Disposable bioreactor for cell culture using wave-induced agitation. *Cytotechnol* 30(1-3):149–158.

Sinnott, R. K. 2005. Coulson & Richardson's Chemical Engineering, Volume 6: Chemical Engineering Design. (4th edn.) Butterworth-Heinemann.

Sou SN, Sellick C, Lee K, Mason A, Kyriakopoulos S, Polizzi KM, Kontoravdi C. 2015. How does mild hypothermia affect monoclonal antibody glycosylation? *Biotechnol Bioeng* 112(6):1165-76.

Spearman M, Dione B, Butler M. 2011. The Role of Glucosylation in Therapeutic Antibodies in Al-Rubeai M. *Antibody Expression and Production*. 251-92. Springer Netherlands.

St. Amand MM, Hayes J, Radhakrishnan D, Fernandez J, Meyer B, Robinson AS, Ogunnaike BA. 2016. Identifying a Robust Design Space for Glycosylation

During Monoclonal Antibody Production. *Biotechnol Prog [Epub ahead of print].*

Stock R. 2010. A Significant and Growing Market: Single Use Technology in the Biopharmaceutical Industry. *Am Pharma Rev*.

Stothard P. 2000. The Sequence Manipulation Suite: JavaScript programs for analyzing and formatting protein and DNA sequences. *Biotechniques* 28:1102-4.

Sucosky P, Osorio DF, Brown JB, Neitzel GP. 2004. Fluid mechanics of a spinner-flask bioreactor. *Biotechnol Bioeng* 85(1):34-46.

Tait AS, Aucamp JP, Bugeon A, Hoare M. 2007. Ultra Scale-Down Prediction Using Microwell Technology of the Industrial Scale Clarification Characteristics by Centrifugation of Mammalian Cell Broths. *Biotechnol Bioeng* 104(2):321-31.

Tang YJ, Ohashi R, Hamel JFP. 2007. Perfusion Culture of Hybridoma Cells for Hyperproduction of IgG_{2a}Monoclonal Antibody in a Wave Bioreactor-Perfusion Culture *System Biotechnol Prog* 23(1)255–64.

Tanzeglock T, Soos M, Stephanopoulos G, Morbidelli M. 2009. Induction of mammalian cell death by simple shear and extensional flows. *Biotechnol Bioeng* 104(2):360-70.

Tharmalingam T & Goudar CT. 2015. Evaluating the impact of high Pluronic® F68 concentrations on antibody producing CHO cell lines. *Biotechnol Bioeng* 112(4):832-7.

Thyagarajan B, Calos MP. 2005. Site-Specific Integration for High-Level Protein Production in Mammalian Cells. In *Therapeutic Proteins Methods and Protocols*, Humana Press.

Tomasini E, Paone N, Rossi M. 2008. Overview on PIV Application to Appliances. In *Topics in Applied Physics*. Springer, Heidelberg.

Trinh K, Garcia-Briones M, Chalmers JJ, Hink F. 1994. Quantification of damage to suspended insect cells as a result of bubble rupture. *Biotechnol Bioeng.* 43(1):37-45.

Trummer E, Fauland K, Seidinger S, Schriebl K, Lattenmayer C, Kunert R, Vorauer-Uhl K, Weik R, Borth N, Katinger H, Müller D. 2006. Process parameter shifting: Part II. Biphasic cultivation-A tool for enhancing the volumetric productivity of batch processes using Epo-Fc expressing CHO cells. *Biotechnol Bioeng*. 94(6):1045-52.

Tukey J. 1949. Comparing Individual Means in the Analysis of Variance. *Biometrics* 5(2):99–114.

United States Pharmacopeia Convention. 2013a. <87> Biological Reactivity Tests, In Vitro. *United States Pharmacopeia and National Formulary (USP 37-NF 32)*. Rockville, MD.

United States Pharmacopeia Convention. 2013b. <88> Biological Reactivity Tests, In Vivo. *United States Pharmacopeia and National Formulary (USP 37-NF 32)*. Rockville, MD.

v B, Joshi BH, Han J, Brorson KA, Puri RK, Moreira AR, Rao G. 2012. Bioreactor environment-sensitive sentinel genes as novel metrics for cell culture scale-down comparability. *Biotechnol Prog* 28(5):1138-51.

Vallejos JR, Brorson KA, Moreira AR, Rao G. 2011. Integrating a 250 mL-spinner flask with other stirred bench-scale cell culture devices: a mass transfer perspective. *Biotechnol Prog* 27(3):803-10.

van Engeland M, Nieland LJ, Ramaekers FC, Schutte B, Reutelingsperger CP. 1998. Annexin V-affinity assay: a review on an apoptosis detection system based on phosphatidylserine exposure. *Cytometry* 31(1):1-9.

Van't Riet K. 1979. Review of Measuring Methods and Results in Nonviscous Gas-Liquid Mass Transfer in Stirred Vessels. *Ind Eng Chem Proc Des Dev* 18(3):357-64.

Varley J & Birch J. 1999. Reactor design for large scale suspension animal cell culture. *Cytotechnol* 29(3):177-205.

Vasquez A, Sanchez RM, Salinas-Rodriguez E, Soria A, Manasseh R. 2005. A look at three measurement techniques for bubble size determination. *Exo Ther Fluid Sci* 31(1):49-57.

Velez-Suberbie ML, Tarrant RDR, Tais AS, Spencer DIR, Bracewell DG. 2012. Impact of aeration strategy on CHO cell performance during antibody production. *Biotechnol Prog* 29(1):116-26.

Villiger TK, Scibona E, Stettler M, Broly H, Morbidelli M, Soos M. 2016. Controlling the time evolution of mAb N-linked glycosylation - Part II: Model-based predictions. *Biotechnol Prog [Epub ahead of print].*

Vlasak J & Ionescu R. 2008. Heterogeneity of Monoclonal antibodies revealed by charge-sensitive methods, *Curr Pharm Biotechnol* 481(14):468-81.

Vlasak J & Ionescu R. 2011. Fragmentation of monoclonal antibodies. *MAbs* 3(3):253-63

Vlasak J, Bussat MC, Wang S, Wagner-Rousset E, Schaefer M, Klinguer-Hamour C. 2009. Identification and characterization of asparagine deamidation in the light chain CDR1 of a humanized IgG1 antibody. *Anal Biochem* 392:145–54.

Vrábel P, van der Lans RGJM, Luyben KCAM, Boon L, Nienow AW. 2000. Mixing in large-scale vessels stirred with multiple radial or radial and axial up-pumping impellers: modelling and measurements. *Chem Eng Sci* 55(23):5881-96.

Walsh G & Jefferis R. 2006. Post-translational modifications in the context of therapeutic proteins. *Nat Biotechnol* 24(10):1241-52.

Wang H, Jia X, Wang X, Zhou Z, Wen J Zhang J. 2014. CFD modeling of hydrodynamic characteristics of a gas–liquid two-phase stirred tank. *App Math Model* 38(1):63-92.

Warnock JN, Al-Rubeai M. 2006. Bioreactor systems for the production of biopharmaceuticals from animal cells. *Biotechnol Appl Biochem* 45(1):1-12.

Weber W, Weber E, Geisse S, Memmert K. 2002. Optimisation of protein expression and establishment of the Wave Bioreactor for Baculovirus/insect cell culture. *Cytotechnol* 38(1-3):77–85.

Weheliye W, Yianneskis M, Ducci A. 2012. On the fluid dynamics of shaken bioreactors— flow characterization and transition. *AIChE* J 59(1):334-44.

Westerweel J. 1993. Digital Particle Image Velocimetry: Theory and application. PhD Thesis. *Delft University Press*.

Whitman WG. 1962. The Two Film Theory of Gas Adsorption. *Int J Heat Mass Trans* 5(5):429-33.

Wise WS. 1951. The Measurement of the Aeration of Culture Media. *J Gen Microbiol* 5:167-177.

Wlaschin KF & Hu WS. 2006. Fedbatch Culture and Dynamic Nutrient Feeding. *Biochem Eng Biotechnol* 101:43–74.

Wong VVT, Wong NSC, Tan HK, Wang DIC, Yap MGS. 2003. Enhancing Production of Recombinant Proteins from Mammalian Cells. *Molecular Engineering of Biological and Chemical Systems (MEBCS)* 2003-01. Available from - http://hdl.handle.net/1721.1/3782 [Accessed: 11-Aug-15]

World Health Organisation. 2010. Workshop on Technology Transfer for Local Manufacturing Capacity of Vaccines. Geneva, Switzerland

Wulf E, Debonben A, Bautz FA, Faulstich H, Wieldan TH. 1979. Fluorescent phallotoxin, a tool for the visualization of cellular actin. *Proc Natl Acad Sci* 76(9):4498-4502.

Wurm FM. 2004. Production of recombinant protein therapeutics in cultivated mammalian cells. *Nat Biotechnol* 22:1393-8.

Xing Z, Kenty B, Koyrakh I, Borys M, Pan S-H, Li ZJ. 2011. Optimizing amino acid composition of CHO cell culture media for a fusion protein production. *Process Biochem* 46(7):1423-9.

Xing Z, Kenty BM, Li ZJ, Lee SS. 2009. Scale-up analysis for a CHO cell culture process in large-scale bioreactors. *Biotechnol Bioeng* 103(4):733-46.

Yamagata T, Tsuru T, Momoi MY, Suwa K, Nozaki Y, Mukasa T, Ohashi H, Fukushima Y, Momoi T. 1998. Genome organization of human 48-kDa oligosaccharyltransferase (DDOST) *Genomics* 45(3):535–40

Yang JD, Lu C, Stasny B, Henley J, Guinto W, Gonzalez C, Gleason J, Fung M, Collopy B, Benjamino M, Gangi J, Hanson M, Ille E. 2007. Fed-Batch Bioreactor Process Scale-Up From 3-L to 2 , 500-L Scale For Monoclonal Antibody Production From Cell Culture. *Cell* 98(1):141-154.

Yoon SK, Kim SH, Lee GM. 2003. Effect of low culture temperature on specific productivity and transcription level of anti-4-1BB antibody in recombinant Chinese hamster ovary cells. *Biotechnol Prog* 19:1383-6.

Yoon SK, Kim SH, Song JY, Lee GM. 2006. Biphasic culture strategy for enhancing volumetric erythropoietin productivity of Chinese hamster ovary cells. *Enzyme Microb Technol* 39(3):362-5.

Yu X, Wood D, Ding X. 2008. Extractables and Leachables Study Approach for Disposable Materials Used in Bioprocessing. *Biopharm Int 21(2)*. Available from - http://www.biopharminternational.com/extractables-and-leachables-study-approach-disposable-materials-used-bioprocessing [Accessed: 11-Aug-15]

Yuk IH, Baskar D, Duffy PH, Hsiung J, Leung S, Lin AA. 2011. Overcoming challenges in WAVE Bioreactors without feedback controls for pH and dissolved oxygen. *Biotechnol Prog* 27(5):1397-406.

Zagari F, Jordan M, Stettler M, Broly H, Wurm FM. 2013. Lactate metabolism shift in CHO cell culture: the role of mitochondrial oxidative activity. *N Biotechnol* 30(2):238-345.

Zhang A, Tsang VL, Moore B, Shen V, Huang YM, Kshirsagar R, Ryll T. 2015. Advanced process monitoring and feedback control to enhance cell culture process production and robustness. *Biotechnol Bioeng* [Epub ahead of print].

Zhang X, Stettler M, De Sanctis D, Perrone M, Parolini N, Discacciati M, De Jesus M, Hacker D, Quarteroni A, Wurm F. 2009. Use of Orbital Shaken Disposable Bioreactors for Mammalian Cell Cultures from the Milliliter-Scale to the 1,000-Liter Scale. *Adv Biochem Eng Biotechnol* 115:33-53.

Zhang X, Hurng J, Rateri DL, Daugherty A, Schmid-Schönbein GW, Shin HY. 2011. Membrane cholesterol modulates the fluid shear stress response of polymorphonuclear leukocytes via its effects on membrane fluidity. *Am J Physiol Cell Physiol* 301(2):451-60.

Zhang Z & Thomas CR. 1993. Modeling of animal cell damage in turbulent flows. In: Nienow AW *Proc. 3rd int. conf. on bioreactor and bioprocesses fluid dynamics*. Mechanical Engineering Publications Ltd., London.

Zhou G, Kresta SM. 1996. Impact of tank geometry on the maximum turbulence energy dissipation rate for impellers. *AIChE* 42:2476-90.

Zhu J. 2012. Mammalian cell protein expression for biopharmaceutical production. *Biotechnol Adv* 30(5):1158-70.

Zhu MM, Goyal A, Rank DL, Gupta SK, Vanden Boom T, Lee SS. 2005. Effects of elevated pCO_2 and osmolality on growth of CHO cells and production of antibody-fusion protein B1: a case study. *Biotechnol Prog* 21(1):70-7.

Zhu Y, Cuenca JV, Zhou W, Varma A. 2008. NS0 Cell Damage by High Gas Velocity Sparging in Protein-Free and Cholesterol-Free Cultures. *Biotechnol Bioeng* 101(4):751-60.